Nanoparticle self-assembly and ultrafast nanomagnet switching dynamics

by

Longfei Ye

Bachelor of Arts
Fudan University, 2001

_____

Submitted in Partial Fulfillment of the Requirements

for the Degree of Doctor of Philosophy in

Physics

College of Arts and Sciences

University of South Carolina

2013

Accepted by:

Thomas M. Crawford, Major Professor

Richard A. Webb, Committee Member

Yaroslaw Bazaliy, Committee Member

Paul G. Huray, Committee Member

Lacy Ford, Vice Provost and Dean of Graduate Studies

Dedication

To my wife Yang Chen and my family

ACKNOWLEDGMENTS

First and foremost, I would like to thank my major principal research advisor, Dr. Thomas M. Crawford for teaching me how to conduct professional experimental research in solid state physics. I greatly appreciate his effort, ideas, and support that he contributed to make my research in the past few years interesting and productive. His vast knowledge and experience in various scientific fields gave me tremendous assistance in figuring out hard research problems and developing innovative ideas. I also appreciate he offered me much freedom in performing research and was very patient at times when my research progress was slow. His belief in me made my success in graduate school and scientific experimental research possible. It was an honor to be his Ph.D. student.

I would like to give my thanks to my co-advisor, Professor Richard A. Webb, for supporting my research and training me how to use all of his instruments and fix technical problems. His strong research experience in low temperature physics and nanodevice fabrication contributed to make the spin-transfer torque project move forward smoothly. What I learned from him will benefit my career throughout my lifetime. I also appreciate his continuous encouragement and assistance to me when I had tough moments in research projects and my life.

I want to give special thanks to Dr. Samir Garzon for his great assistance in getting me started with professional research in Dr. Crawford and Dr. Webb group. Skills in conducting both experimental research and theoretical calculations that I learned from him provided me a solid foundation in continuing my Ph.D. research.

I want to thank Dr. Mefford (Material Science and Engineering, Clemson Univer-

sity), the Mefford group and Dr. Carlos Rinaldi (Chemical Engineering, University of Florida) for their collaborations. The nanoparticle self-assembly project would not move smoothly or efficiently without their supplies of nanoparticles. Their active involvement and discussion broadened my knowledge and skills in the colloidal science and contributed to enhance the project progress and productivity. I also owe thanks to the dissertation members Dr. Yaroslaw Bazaliy and Professor Paul G. Huray for having taken the time to understand my work and supporting my project change.

I want to thank all my colleagues in Dr. Crawford and Dr. Webb group who contributed to make my research move forward and keep all lab machines running. In particular, Jason Henderson, Dr. Shifan Shi, and Brad Terry had worked on the nanoparticle self-assembly project before I joined. Their contributions with the knowledge transfer saved me a lot of effort in understanding the project and the technology involved. I could not make the further achievement in this project without standing on their shoulders. Tanner Pearson worked hard to take data using the nanoparticle fluid cell in the whole summer 2013. Bochen Zhong and Ning Lu had been taking care of the PPMS operation continuously. In addition, I want to acknowledge staff in the Electron Microscopy Center at USC, esp. Dr. Soumitra Ghoshroy and Jibin Zhao, for allowing me to access the facilities.

I want to thank Brad Knaus and Xurong Chen (my roommate) for assisting me to survive and get used to the life in a foreign country when I just landed in USC from China 2005. That moment was challenging for me, since it was my first time to come abroad to study and work in the environment with a completely new culture. I also want to thank my friends, inside or outside of the Physics department, for making the time outside the lab enjoyable. Without them, these years of study in USC would not have been so easy.

I must thank my family. Mom and Dad, who, millions of miles away, worked very hard to earn opportunities for me to go to college and then pursuit the Ph.D. degree

in USC. I owe great gratitude to my brother Shengbin Ye, sisters Yuying Ye and Yuzhen Ye for taking care of Mom since Dad passed away in 2009. My study in USC would not be possible without their constant encouragement and support.

Finally, I want to thank my wife, Yang Chen for everything she has done. She sacrificed her lawyer job in China to come over abroad for supporting my study. My life would be much more difficult without her being with me. And I would not be able to make it through without her love and strong encouragement and support.

ABSTRACT

A novel manufacturing technology that offers a low-cost alternative for creating more complex optical materials that are assembled with single-nanometer precision is demonstrated. Using the enormous magnetic field gradients up to 1×10^7 T/m present near the surface of magnetic recording media, colloidally suspended superparamagnetic nanopartilces are self-assembled into patterned microstructures. The position and shape of these microstructures are precisely controlled by magnetic patterns on the template. The template that can be reprogrammed and reused is magnetically recorded using commercial magnetic recording technology. These microstructures consisting entirely of self-assembled magnetic nanoparticles are then transferred to flexible polymer thin films with patterns maintained. In particular, all-nanoparticle diffraction gratings are fabricated by employing this technology and extensively studied.

Based on the nanomanufacturing technology, a versatile measurement technique is developed to study magnetic nanoparticle self-assembly dynamics. The self-assembly dynamics is monitored in real-time by detecting optical diffraction from an all-nanoparticle grating as it self-assembles. It is demonstrated the nanoparticle self-assembly not only strongly depends on the nanoparticle concentration and size, but also shows a dramatic change in the diffracted intensity as a result of the suspension pH that is not observed with static light scattering. Further, the diffracted signal not only has high sensitivity to the particle aggregation, but also detects different time dependence that depends on the colloidal stability of particles.

The diffraction efficiency can be strongly enchanted by mixing the nanoparticle

suspension with a small amount of phosphate buffer saline (PBS). While common dynamic light scattering and Zeta potential measurements do not show such a dramatic dependence on the PBS volume as this optical diffraction measurement shows. This demonstrates not only the nanoparticle self-assembly process is highly tunable, but also the optical diffraction is more sensitive to subtle changes in colloidal stability of particle suspensions than commonly used light scattering. This metrology has a strong potential as a complementary metrology for commonly used dynamic light scattering measurements.

In a second study, ultrafast magnetization dynamics are investigated by employing a pulse shaping scheme consisting of two ultrashort (~ 30 ps) spin-transfer torque (STT) pulses with variable delay, amplitudes and polarities. A coherent control of the magnetization dynamics is demonstrated to reliably manipulate the magnetization dynamics. Magnetic dynamics show strong asymmetrical dependence on the inter-pulse delay for oppositely polarized pulses. Experimental measurements suggest that appropriately-shaped spin transfer can be used to efficiently manipulate the orientation of a free layer nanomagnet, thus providing an alternative for spin torque driven spintronic devices. An additional 5 ns STT pulse with variable amplitudes are combined and precisely timed with the pair of picosecond pulses to cancel the magnetic damping. Although partial damping cancellation is possible with dc currents, the resulting trajectories are completely dephased, demonstrating that precisely-timed pulses are required to observe nearly complete damping cancellation with time-domain sampling experiments. Partial experimental work that attempts to uncover ultrafast demagnetization process by combining ~ 1ps STT pulses with femtosecond optical pulses has also been performed.

TABLE OF CONTENTS

LIST OF TABLES

List of Figures

Chapter 1

General Introduction

This thesis consists of two major experimental projects I have pursued in my graduate research. The first project (nanoparticle self-assembly: chapter 2 - 5) focuses on a novel nanomanufacturing technology and investigation of nanoparticle self-assembly dynamics.

The second project (spin-transfer torque: chapter 6 - 7) focuses mainly on ultrafast magnetic dynamics induced by ultrashort spin-transfer torque (STT) pulses in spin-valve nanostructures.

1.1 Motivation

As nanotechnology advances, nanoparticles appear one of the most prominent potential candidates for technological applications [94] [157]. Implementation of excellent functional materials or devices using nanoparticles requires not only nanostructures with desirable functions, but also a means to assemble those nanostructures to practical sizes while maintaining the nanostructure arrangement. The application of nanotechnology to areas such as photonics and electronics, chemical and biological sensors, energy storage, and catalysis requires this manipulation of these nanoparticles into functional materials and devices, and this remains a fundamental challenge.

Nanoparticle self-assembly, also known as bottom-up nanofabrication, utilizing nanoparticles as building blocks to construct larger, complex and functional structures such as sheets, tubes, wires, and shells needed as scaffolds and structures for catalysis, hydrogen storage, nanoelectronic devices, and drug delivery [201] [72] [246] [136] [21]

, is one of the most important, promising, and sustainable techniques for applications [80] [214] [180]. This process is similar to the biological technique of assembling small structural blocks at the atomic or molecular level to a large structure, such as DNA nanostructures self-assemble into proteins [233] [239].

This bottom-up nanofabrication has some advantages over the traditional top-down method. Nanofabrication using top-down technology not only requires precise growth techniques such as physical vapor deposition, chemical vapor deposition, molecular beam epitaxy, but also involves patterning techniques such as photolithography, electron beam lithography, and nanoimprint lithography. The above mentioned processes, though standard, are laborious, time-consuming, and costly. In contrast, the nanoparticle self-assembly approach is simple and cost effective [233] [154] [134] .

To date, although many nanoparticle assembly approaches have been demonstrated in the literature [170], [21] [38] [173] [149] [68] [145] [218], few offer a comprehensive, predictable, and generally applicable scheme. In this dissertation, I describe experimental research to develop a low-cost and reliable nanomanufacturing technology by employing magnetic nanoparticle self-assembly and a pattern transfer technique to create complex functional materials. One device that I have nanomanufactured and studied extensively is the diffraction grating. Diffraction gratings consisting of a large number of equally spaced parallel slits or grooves play an important role in many technologies, including spectroscopy [122], laser systems [86], and information communication [244], where, for example, gratings increase the capacity of fiber-optic networks using wavelength division multiplexing/demultiplexing [151]. High-resolution commercial diffraction gratings were originally fabricated with ruling engines, and the ruling process is slow and requires precise control of mechanical motion and external vibration [87]. Other fabrication methods include photographic recording of a stationary interference fringe field in photoresist to create a holographic grating [164], electron beam lithography [137], and focused ion beam etching [58]. Re-

cently, gratings have been fabricated using laser pulses to ablate metal nanoparticles or thin films, with interference to create the grating pattern [50, 98, 116]. Given the evolving need for control over optical element fabrication, lower cost and sustainable manufacturing technologies with nanometer precision are needed to create novel optical materials, and maintain the pace of technological innovation in optical technologies.

In addition, magnetic nanoparticles cover a broad spectrum in potential applications such as magnetic seals in motors, magnetic inks for bank cheques, and biomedical applications (e.g., magnetic resonance contrast media and therapeutic agents in cancer treatment) [14] [234] [152]. In particular, magnetic nanocrystals are promising building blocks for high-performance nanodevices for information storage [32] [159]. Well controlled magnetic particles have been fabricated and self-assembled into three dimensional superlattices. These assemblies are chemically and mechanically robust and have potential in application for high-density magnetic recording media [215] [214]. State-of-the-art spintronics devices require not only nanoscale designs and fabrication techniques, but also high-quality magnetic media that can support fast/ultrafast magnetic transitions.

Spintronics, i.e., spin-based electronics, focuses on devices and concepts that use the spin degree of freedom of electrons [248]. These are in strong contrast to conventional electronic devices that utilize the functionality of carrier charges. Using the spin together with the electronic charge or alone, spintronic devices have some advantages over the conventional electronic devices including non-volatility, faster speeds, higher device integration density and greater energy efficiency [235] [191].

Ferromagnetic materials possess a net spin imbalance at the Fermi level, which can be used to create spin polarized currents. When this spin current is injected into a ferromagnet, the spin angular momentum of the current interacts with local spins in the ferromagnet. This exchange interaction generate a mutual torque that is called

the spin-transfer torque [178] [210] [202] [13]. This spin-transfer torque can induce both switching and continuous procession of the local magnetization in a ferromagnet [209] [128]. The ability to switch ferromagnetic magnetization via the spin-transfer torque shows strong potential for technological applications.

First, the spin-transfer torque serves a very promising candidate for data storage technology. Disk drives, conventional data storage devices, employ the Oersted field of a current carrying wire to switch magnetic data. The stray field of the write head limits the data density. This difficulty could be overcome with spin-transfer torques, where device switching is achieved with STT currents directly. This storage architecture can be extended to 3-dimensions with each bit accessed independently providing a large density of stored data [42] [31] [96] [4].

Second, the down-scaling of Si transistors has been going on for many decades. Eventually the miniaturization of Si devices will come to an end. Although one technology will replace the logic elements of current computer processors is still unclear, spin-transfer torque devices could offer an alternative. STT devices are non-volatile and this inherent non-volatility is a dramatic advantage over Si transistors, since Si transistor-based logic elements need to save executed information in the processor memory [156]. This would allow the STT-based logic elements to refigure themselves in real-time so that the computational efficiency can be maximized. In addition, switching STT logic elements as fast as 30 ps have been achieved in spin-valve devices [66]. This switching efficiency together with the non-volatility of STT-based logic elements could increase overall computational speed, and thus STT technology could provide an alternative for current CMOS.

These two projects that I have undertaken are not independent, but correlated. Since the nanoparticle self-assembly can be employed to fabricate STT devices and biosensors at lower cost than commonly used techniques such as the electron-beam lithography and lift-off process [37] [83]. For instances, Dugay et al. has reported

4

room-temperature tunneling mangetoresistance in self-assembled Fe nanoparticles
[46]. Jia et al. has fabricated a horseradish peroxidase biosensor by self-assembling
gold nanoparticles to a thiol-containing sol-gel network [104]. Nanoparticle self-
assembly has been widely used to construct kinds of biosensors including acoustic
wave, optical, electrochemical biosensors [105].

1.2 Introduction to part I: the nanoparticle self-assembly project

Nanoparticle self-assembly has been demonstrated as a sustainable manufacturing
technology for construction of complex patterns including linear chains, and close
packed arrays [201]. For optical applications, self-assembly has been used to create
dynamic diffraction gratings in liquid from colloidal nanoparticles using electrophore-
sis [229]. Similarly, self-assembly via DNA and other surface anchoring techniques
has been employed to pattern diffraction gratings on surfaces [196].

Here, I describe research that is performed to develop a low-cost nanomanu-
facturing alternative to fabricate all-nanoparticle diffraction gratings. Nanoscale
magnetically-recorded templates are created on a disk drive medium using commercial
magnetic recording technology. The magnetic medium is longitudinal or perpendic-
ular. Colloidally suspended magnetic nanoparticles are pumped onto the magnetic
medium surface. These nanoparticles suspended in the fluid self-assemble onto the
magnetic medium surface by the ultra-high field gradients present near the magnetic
medium surface. The self-assembled nanoparticles form a diffraction grating since
the recorded template is programmed to create an array of magnetic fields with equal
spacing. After a time (coating time), the remaining fluid on top of the medium sur-
face is removed leaving the self-assembled grating behind on the medium surface. A
transparent liquid polymer is spun onto the medium surface and cured. The polymer-
nanoparticle assembly is then peeled from the medium surface, while maintaining
nanoparticle patterns, yielding an all-nanoparticle diffraction grating embedded in

the transparent polymer film.

To better understand this process the magnetic medium is placed at the bottom of a transparent fluid cell, and optical diffraction from the grating is monitored during assembly in real-time to study the nanoparticle self-assembly process. The dependence of the nanoparticle self-assembly process on the suspension concentration, pH and particle size, is investigated. In particular, the colloidal stability of nanoparticles is varied to compare the sensitivity of this measurement technique with the dynamic light scattering technique that is more commonly used to assess colloidal nanoparticles.

Chapter 2 provides an introduction to magnetic nanoparticles and nanoparticle self-assembly. Critical properties of magnetic nanoparticles and colloidal suspensions of these magnetic nanoparticles, together with their colloidal stability, are discussed. Techniques and methodologies that are used to drive the nanoparticle self-assembly, in particular, a magnetic field directed self-assembly, are introduced.

Chapter 3 discusses nanomanufacturing of all-nanoparticle diffraction gratings including the fabrication process and spectral measurements of the nanomanufactured gratings.

Chapter 4 focuses on real-time detection of nanoparticle self-assembly dynamics by employing optical diffraction from an all-nanoparticle grating as it self-assembles on a magnetic medium located in a fluid cell.

Chapter 5 discusses nanoparticle self-assembly dynamics caused by destabilizing the nanoparticle suspension. These destabilized nanoparticles are created by mixing a stable nanoparticle suspension, i.e., a base suspension, with a known volume of Phosphate Buffer Saline (PBS). Measurements show that the nanoparticle self-assembly dynamics depend strongly on the volume of added PBS. Dynamic light scattering measurements are also performed for comparison.

1.3 Introduction to part II: the spin-transfer torque project

Part II (chapters 6-7) reports coherent control of ultrafast nanomagnet switching dynamics via ultrafast spin-transfer torque (STT) pulses. Understanding ultrafast magnetic dynamics driven by STT is critical for achieving fast switching speed of these future memory devices. Here, by using a simple pulse shaping scheme consisting of two ultrafast spin torque pulses with variable amplitudes and delay, ultrafast magnetic switching dynamics in spin-valve nanostructures are investigated.

Chapter 6 introduces Giant Magnetoresistance (GMR). A discussion of spin current, STT, and magnetization dynamics is also provided. Experimental measurements demonstrating coherent control of nanomagnet dynamics using pairs of ultrafast STT pulses are presented. Theoretical simulations based on a Macrospin model of a nanomagnet to interpret these experimental results are also included.

Chapter 7 presents experimental work to extend the double pulse technique. A pair of oppositely polarized ultrafast pulses are generated to study delay dependence of nanomagnet dynamics. Ultrafast nanomagnet dynamics are investigated while the magnetic damping is partially canceled by an additional 5 ns STT pulse. Finally efforts towards combining picosecond STT pulses with femtosecond optical pulses is made.

Chapter 8 concludes this dissertation.

CHAPTER 2

MAGNETIC NANOPARTICLES AND SELF-ASSEMBLY

This chapter discusses the properties of magnetic nanoparticles. In particular, superparamagnetic nanoparticles with the size on the order of 10 nm are discussed. Colloidal stabilities, together with the inherent properties of these nanoparticles, are crucial for their technological applications. Common methods that are used to characterize nanoparticles including particle core sizes, magnetic properties, and colloidal stability, are introduced. An introduction to techniques and methodologies that are used to drive the nanoparticle self-assembly is also provided. In particular, magnetic field directed self-assembly is emphasized; A novel nanomanufacturing technology that can drive nanoparticle self-assembly using magnetically-recorded templates is discussed.

2.1 MAGNETIC NANOPARTICLES

2.1.1 Magnetism

Magnetism has been studied for decades. Magnetism originates from electrons in atoms or ions of solids whose orbitals are modified by their crystalline environment. Atomic nuclei also produce magnetism. However, magnetic moments arising from atomic nuclei are typically thousands of times smaller than those of electrons, and therefore are negligible in magnetic materials [27]. Materials are classified into five categories of magnetism depending on how they respond to external magnetic fields ($\mathbf{H}$), i.e., their bulk magnetic susceptibility χ: diamagnetism, paramagnetism, fer-

romagnetism, ferrimagnetism, and antiferromagnetism [27] [34]. χ is defined as the derivative of the magnetization ($\mathbf{M}$, i.e., the magnetic moment of the magnetic material divided by the volume) with respect to the applied magnetic field strength [5] [34]. χ can be determined by measuring $\mathbf{M}$ experimentally at a finite $\mathbf{H}$. Diamagnetic materials such as Cu and Au have negative χ, while paramagnetic materials such as Pd have positive χ. Some materials with positive χ such as Fe, Co and Ni, have a nonvanishing magnetic moment, even in the absence of a magnetic field. Magnetism in these materials is called ferromagnetism.

From a quantum-mechanical view, all electronic shells of a diamagnetic material are filled, and therefore this material has zero spin and orbital angular momentum. However when this diagmagnetic material is placed in an external field, a Lorentz force is exerted on electrons circling the nucleus, which modifies electrons' orbital motions and causes a decrease of magnetic moment in the external magnetic field direction. Therefore diamagnetism appears in all materials with a negative susceptibility.

In contrast, paramagnetism and ferromagnetism are caused by the presence of unpaired electrons. Paramagnetic materials have non-zero total electronic angular momentum induced by the external field and this angular momentum favors the alignment of the magnetic moment along the field. However, paramagnets do not retain the magnetization after the external field is removed, because thermal energy is large enough to randomize these orientations of the angular momentum.

The net magnetic moment of ferromagnets that sustains after removing the field must be caused by some spectacular consequence of magnetic interactions. If there were no such magnetic interactions, the individual magnetic moments of atoms would be thermally disordered similarly as paramagnets and thus cancel each other. This interaction, causing the magnetic ordering, is known as the exchange interaction, or exchange splitting and arises from the singlet-triplet energy splitting in a two-electron system [5] [188]. The overall wave function of the two-electron system consists of both

the spatial and spin wave functions. Since electrons having spin-1/2 are fermions, the overall wave function must be antisymmetric. Therefore, if the spatial wave function is symmetric, the spin wave function has to be antisymmetic. This state is called a singlet. Similarly if the spatial wave function is antisymmetic, the spin wave function has to be symmetric. This state is called triplet. These two states have different energies, and the energy difference is known as the singlet-triplet energy splitting. The energy splitting, in quantum mechanics, can be calculated using the spin Hamiltonian [5] [34] that is expressed as

$$\mathcal{H}^{spin} = -\sum J\mathbf{S_1} \cdot \mathbf{S_2}, \tag{2.1}$$

where J is the exchange constant, $\mathbf{S_1}$ and $\mathbf{S_2}$ are spin operators of the two electrons respectively. The system will favor parallel spins if $J > 0$, and antiparallel if J < 0. Similarly, for a system consisting of a large number of ions, the total exchange interaction (H^{spin}) equals

$$H^{spin} = -\sum J_{ij}\mathbf{S_i} \cdot \mathbf{S_j}, \tag{2.2}$$

which is the Heisenberg Hamiltonian [5]. J_{ij} are known as exchange coupling constants and $\mathbf{S_i}$ and $\mathbf{S_j}$ are spin operators of the electrons in ion i and j respectively.

Ferrimagnetic materials such as Fe_3O_4 also possess spontaneous magnetization in the absence of the field. However while the magnetic moments between nearest neighbor atoms favor antiparallel alignment, their moments do not cancel, thus yielding a net moment as a whole [5] [34]. Antiferromagnetic materials do not sustain a net magnetic moment due to alternating alignment of equal individual local moments in the crystalline lattice [5] [34].

2.1.2 Superparamagnetic Nanoparticles

Superparamagnetism appears in very small ferromagnetic or ferrimagnetic materials. In contrast to bulk ferromagnetic materials that consist of multiple-domains

and display hysteresis loops in **M** vs **H** measurements, superparamagnetic materials primarily consist of single domains. Finite magnetic moments of superparamagnetic materials are aligned with an external magnetic field and become zero after the field is removed [84] [166]. Let us consider an ensemble of identical superparamagnetic nanoparticles, each with a magnetic moment m and negligible anisotropy. Assuming
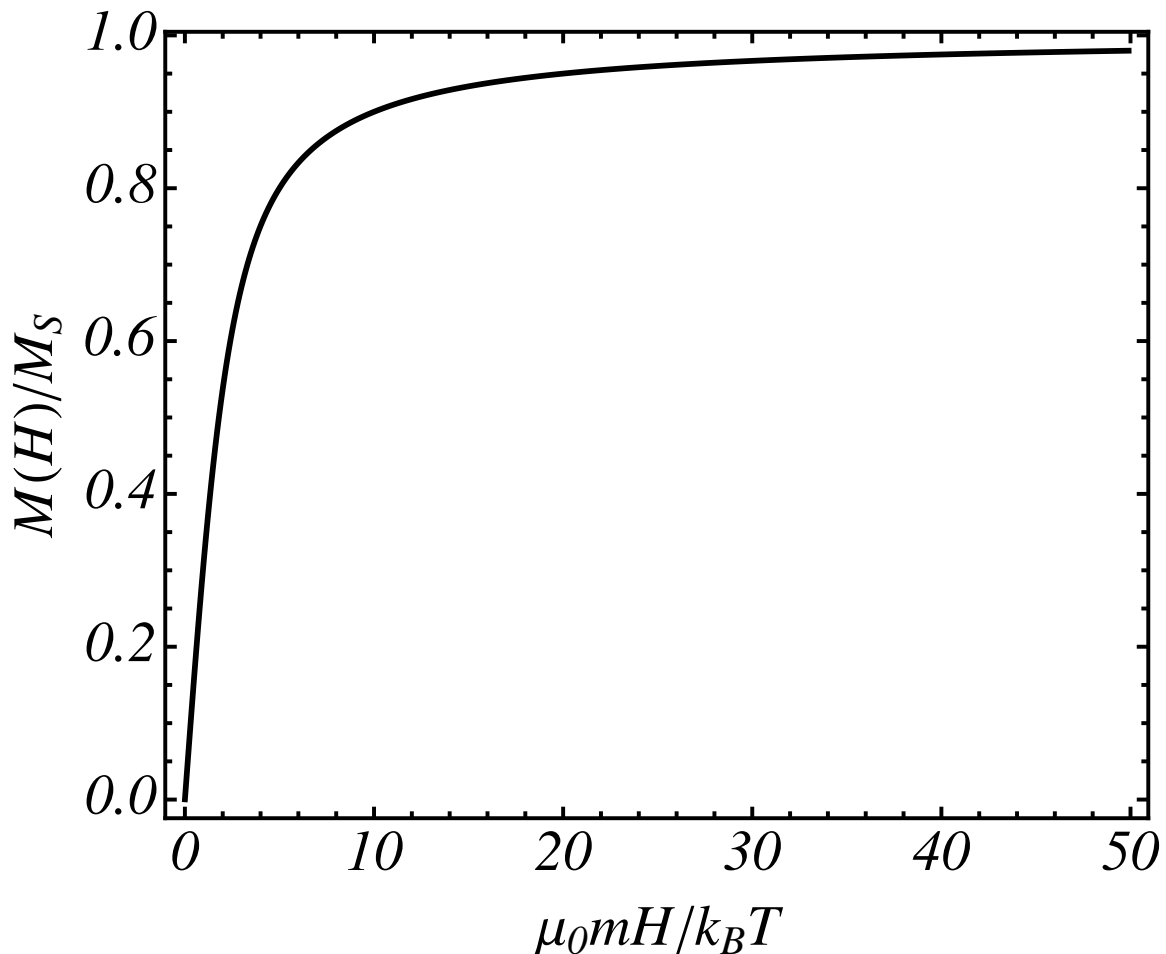
Figure 2.1 Plot of the theoretical Langevin equation of (2.3) as a function of $\mu_0 mH/k_B T$.

these nanoparticles do not interact with each other, the magnetization of the nanoparticle assembly $M(H)$ at a magnetic field H is expressed as [82]

$$\frac{M(H)}{M_S} = \coth\left(\frac{\mu_0 H}{k_B T}\right) - \frac{k_B T}{\mu_0 H} = L\left(\frac{\mu_0 mH}{k_B T}\right), \tag{2.3}$$

where L is known as the Langevin function [33] [57], $\mu_0 = 4\pi \times 10^{-7} H/m, k_B$, and T are the magnetic permeability of free space, Boltzmann constant, and temperature respectively.

Figure 2.1 shows the theoretical Langevin equation of (2.3) plotted as a function of $\mu_0 mH/k_B T$ at a finite temperature. $M = 0$ for $H = 0$ and increases monotonically as H is increased.

The reason superparamagnetic materials do not sustain spontaneous magnetization after removing the field is because their magnetic moments are extremely small. Let us consider a uniaxial and single-domain particle with anisotropy constant (per unit volume) K, and volume V, as shown in figure 2.2. **M** makes an angle θ with the direction of uniaxial easy axis (i.e, the z axis). The anisotropy energy $E_B = KV\sin^2\theta$. Thus the energy barrier (ΔE_B) that separates two energy minima at $\theta = 0 \ and \ \pi$ is KV. If KV is sufficient small, thermal fluctuations can overcome the energy barrier ΔE_B and spontaneously reverse **M** between two energy minima in the absence of **H**. For a 5nm diameter Fe_3O_4 nanoparticle, K is $\sim 4.7 \times 10^4 J/m^3$ [76] and ΔE_B is calculated as 3×10^{-21} J, which is smaller than $\sim 4 \times 10^{-21}$J, i.e., the thermal energy $k_B T$ at $T = 300$ K.

In 1949, Néel [165] proposed the the magnetization reversal process of superparamgenetic nanaoparticles is caused by thermal energy. This theory was further developed by Brown in 1973 [25], who suggested the nanoparticle magnetization fluctuates with a frequency f or a characteristic relaxation time $\tau = 1/(2\pi f)$. According to the Néel-Brown model [232],

$$\tau = \tau_0 \ exp\left(\frac{KV}{k_B T}\right), \tag{2.4}$$

where $\tau_0 = 10^{-10}$ s, is the inverse attempt frequency. τ increases as T decreases. When τ becomes comparable to the measurement time (τ_m) at a particular temperature T_b, the particle is said to be blocked and T_b is called the blocking temperature. By
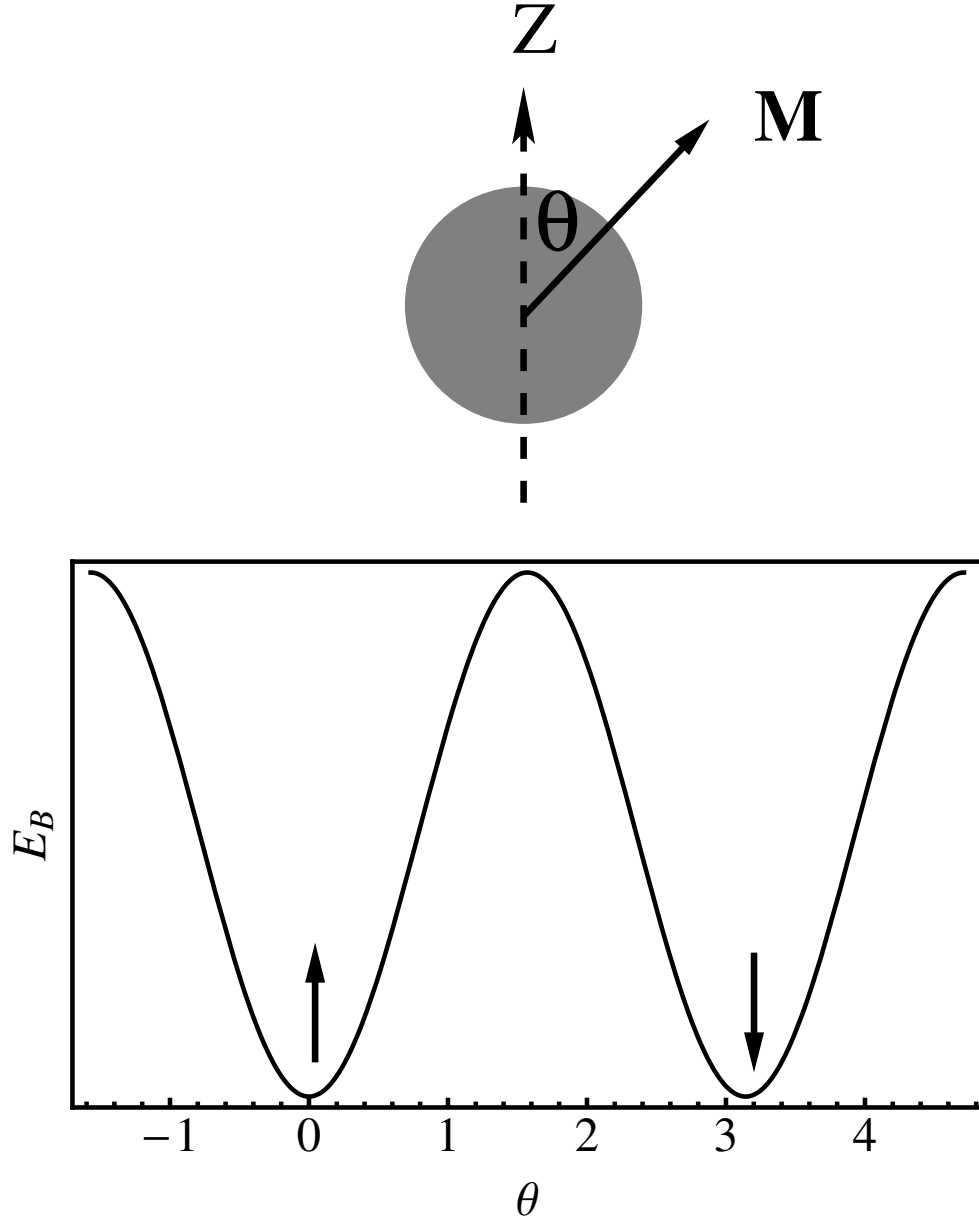
Figure 2.2 Schematic picture of the magnetic energy E_B of a single-domain particle with uniaxial anisotropy as a function of the magnetization direction. θ is the angle between the magnetization $\mathbf{M}$ and the easy axis.

equating $\tau = \tau_m$ in equation (2.4), one obtains

$$T_b = KV[k_B ln(\tau_m/\tau_0)]^{-1}. \tag{2.5}$$

Using equation (2.5) for a 5 nm diameter Fe_3O_4 nanoparticle and $\tau_m = 1$ ms, one

obtains $T_b = 18$ K.

2.1.3 Ferrofluid

A great deal of interest in suspensions of magnetic nanoparticles in carrier liquids is stimulated by the fact that such fluids possess both normal liquid behavior and the possibility to control their flow and properties with moderate magnetic fields [184] [176] [192]. These suspensions, also called ferrofluids [216, 140], contain superparamagnetic particles with a size of about 10 nm in diameter, and the carrier liquid is typically an oil or water base. The magnetic material most often used is magnetite (Fe_3O_4). These magnetic nanoparticles are protected appropriately against agglomeration and thus stably suspended in the fluid (section 2.2 describes how these nanoparticles are protected).

The control of flow and other properties of particles with external magnetic fields is possible because each particle can be treated as a thermally agitated single domain particle in the carrier liquid, i.e., each particle carries a magnetic moment in an applied magnetic field. A magnetic force can be exerted on the particle by applying a magnetic field gradient. This magnetic force is proportional to both the particle magnetic moment and the field gradient. Relatively strong magnetic forces can be generated for particles suspended in a ferrofluid with moderate magnetic fields and gradients [184]. Therefore, the motion of magnetic particles in a ferrofluid can be controlled and manipulated by applying external magnetic fields, and this field of study is known as the magnetophoresis [139] [187] [127].

Ferrofluids are different from the usual magnetorheological fluids that consist of micron sized particles dispersed usually in oil and are used for dampers, brakes and clutches. A magnetorheological fluid is different from a ferrofluid which has smaller particles. A magnetic field applied to a magnetorheological fluid causes an increase of the viscosity. Therefore, they tend to behave like solids under large fields. However,

the viscosity of a ferrofluid remains almost same even if subjected to strong magnetic fields [192] [107] [23].

2.2   Colloidal Stability

Colloids are particles microscopically dispersed in another substance with particle sizes ranging from 1 to 1000 nm [227] [146]. Ferrofluids are colloids. In most common colloidal systems, the dispersion medium is liquid. These suspended particles do not form sediment in a gravitational field and are subjected to Brownian motion [90] [228] [195]. For a ferrofluid, these magnetic particles also do not agglomerate under moderate magnetic field gradients. Nonetheless they can agglomerate in the liquid due to van der Waals interactions [184] [88] [132] [92]. To achieve a stable suspension, the particles are stabilized by coating surfactants on the particle surface to prevent agglomeration. These surfactants generate repulsive forces that prevent particles from coming in contact, and thus suppress the destabilizing effect of the van der Waals interaction. The repulsive force can be created by electric charge (see section 2.2.2) or long chain of organic molecules (see section 2.2.4 in detail) as shown in figure 2.3. Colloidal particles with surface charges are electrostatically stabilized. Long chains of polymers produce steric repulsions and hence these particles are sterically stabilized (see section 2.2.4). These types of particle stabilization are used for the majority of ferrofluids. They allow the suspension to remain stable over several months to years depending on how the particles are synthesized [184] [29] [177].

2.2.1   Van der Waals Forces

In the 19th century, the Dutch physicist Johannes Diderik van der Waals attempted to explain why real gases did not obey the ideal gas law by postulating the existence of long-range attractive forces in the ideal gas law equation. These attractive forces are now known as van der Waals forces. Van der Waals forces include both attractions
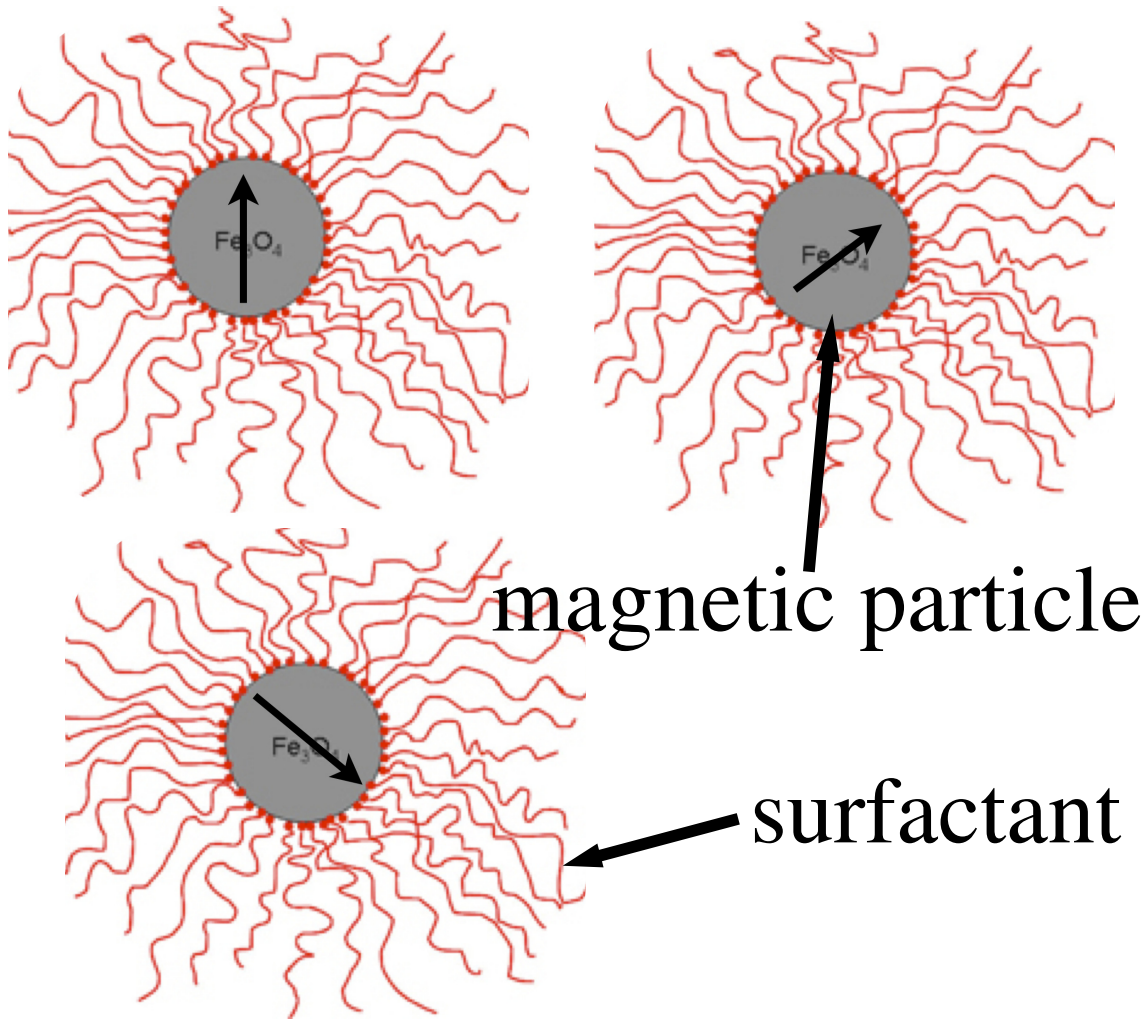
Figure 2.3   A schematic view of superparamagnetic Fe_3O_4 nanoparticles coated with surfactants.

and repulsions between atoms, molecules and other intermolecular forces. Later other scientists helped to reveal the origin of van der Waals forces.

The Lennard-Jones potential is often used to approximately describe the van der Waals interaction between two atoms or particles as a function of distance [30] [85]. The Lennard-Jones potential is defined as

$$w(r) = -Ar^{-6} + Br^{-12}, \tag{2.6}$$

where r denotes the distance between atoms, A and B are parameters in units of Jm^6 and Jm^{12} respectively. Figure 2.4 shows a representative plot of the Lennard-Jones
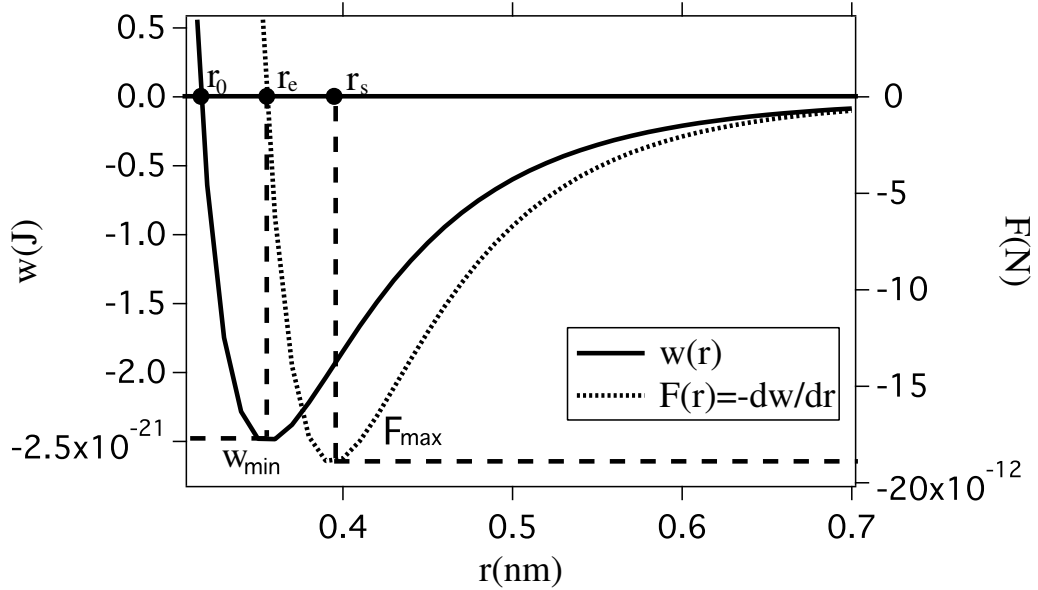
Figure 2.4 The Lennard-Jones potential and force vs particle distance using A = 10^{-77} Jm^6 and B = 10^{-134} Jm^{12} .

potential and force, i.e., $F(r) = -dw(r)/dr$, with respect to the atom separation r. The Lennard-Jones potential predicts a minimum energy w occurs at $r = r_e$, i.e., $F(r_e) = 0$. For atom separations smaller than r_e, the net force is repulsive and the r^{-12} term dominates. Its physical nature originates from the Pauli principle, i.e., the two atom system energy increases dramatically when their electronic clouds circling the atoms start to overlap. At large atom distances (i.e., $r > r_e$), the r^{-6} term dominates and this term represents the attractive van der Waals interaction. The attractive forces are not as strong as Coulomb or H-bonding interactions that arise from dipole-dipole interactions between the fluctuating electric dipole moments in atoms, yet they are responsible for the adhesion of atoms and the aggregation of nanoparticles [99]. For two identical spherical nanoparticles with radii R_p and a central seperation distance D, the van der Waals potential V_A is expressed as

$$V_A = -HR_p/6D, \tag{2.7}$$

where H is called Hamaker constant [99].

2.2.2 Electrostatic Repulsion

Electrostatically stabilized colloidal particles having charged surfaces form electrical double layers around their surfaces, arising from charged surfaces interact with electrolyte ions in the solution. These ions are present in the solvent, for example, the H_3O^+ and OH^- ions that exist in the deionized (DI) water. The surface charge is balanced by an equal amount of oppositely charged counterions, as shown in figure 2.5 (a). Some counterions are bound to the particle surface within a thin layer, which is called the Stern or Helmholtz layer [99] [183] [247]. Other ions diffuse away from the particle surface and remain in thermally agitated motion, creating a second electrical layer. This second layer, together with the Stern layer form the electric double layer around the particle. During particle transport, there is an artificial boundary, so-called slipping plane that separates the mobile fluid from the fluid that remains attached to the particle. This means the part that is bounded by the slipping plane moves as a single entity. The electrical potentials at the Stern plane and slipping plane are called the Stern and Zeta potential respectively. The cancellation of surface charges and ions in the electric double layer makes the particle electrically neutral.

For a surface charged particle with an electrical double layer, the potential ψ in the surrounding fluid is described by the Debye $-$ H$\ddot{u}$ckel equation [54] [205] [174]

$$\psi(x) = \psi_0 e^{-\kappa x}, \tag{2.8}$$

where x is the distance from the particle surface, ψ_0 is the electrical potential at the particle surface, and $1/\kappa$ is a characteristic decay length, known as the Debye length. The magnitude of the Debye length does not depend on the particle surface charge or potential, but solely the liquid and temperature. For example, the Debye length of NaCl aqueous solution at 25°C equals $0.304/\sqrt{[\text{NaCl}]}$ nm [99], where [NaCl] is the NaCl concentration in units of molarity (M). For 1mM and 1M [NaCl] solutions,
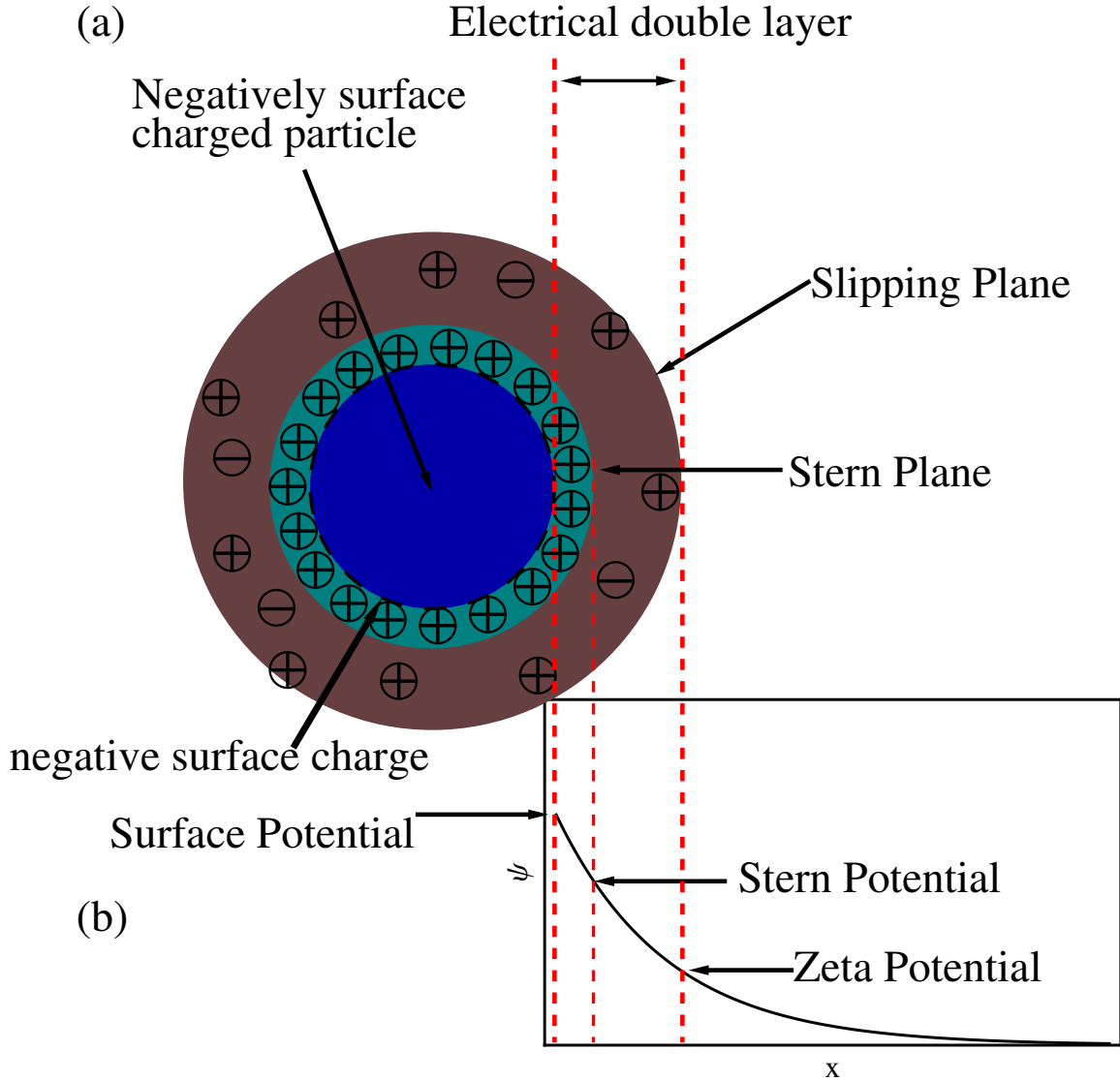
Figure 2.5 (a) Schematic illustration of an electrical double layer that surrounds a negatively surface charged particle. (b) Electrical potential around the particle.

the Debye lengths are 9.6 nm and 0.3 nm respectively. Figure 2.5 (b) shows ψ schematically as a function of the distance from a negatively surface charged particle. For two identical surface charged particles with radii R_p that are separated by a center to center distance D, the interaction free energy per unit area is given by [99]

$$V_R(D) = (64\pi k_B T R_p \rho_\infty \gamma^2 / \kappa^2) e^{-\kappa D}, \qquad (2.9)$$

where ρ_∞ is the ionic concentration in the bulk solution, and $\gamma = tanh(ze\psi_0/4k_BT)$

(z and e are ionic charge number and the electron charge respectively).

2.2.3   Colloidal Stability and DLVO Theory

In 1940s, Boris Derjaguin, Lev Landau, Evert Verwey and Theo Overbeek proposed that colloidal stability is determined by repulsive electrical forces surrounding the electrical double layer and attractive van der Waals forces, for particles that are electrostatic stabilized. This theory became known as the DLVO theory. The total potential $V_T(D)$ is written as

$$V_T(D) = V_A(D) + V_R(D). \tag{2.10}$$

Using equations (2.9) and (2.7), $V_T(D)$ is further written as

$$V_T(D) = (64\pi k_B T R_p \rho_\infty \gamma^2/\kappa^2)e^{-\kappa D} - HR_p/6D. \tag{2.11}$$

Figure 2.6 shows $V_A(D), V_R(D)$ and $V_T(D)$ as a function of particle separation. There is a net energy barrier as a result of the double-layer repulsive interaction which prevents particles from approaching each other and aggregating. On the contrary, if there is a sufficiently high repulsive barrier between particles, the repulsive force will prevent the particle flocculation from taking place and the colloidal system will be stable. However, if the repulsion is small or the particles collide with sufficient energy to overcome the energy barrier, Van der Waals attractive forces will pull them together, they then adhere strongly together and will not break apart again. Particle flocculation will occur.

In certain circumstances, e.g., colloids in solutions with high salt concentrations, $V_T(D)$ has a smaller primary barrier and "secondary minimum" as shown in figure 2.7. The large concentration salt decreases the primary barrier due to the electrostatic screening [112] [99]. Electrostatic screening is the damping of electric fields that are caused by the presence of mobile charge carriers [142] [207]. This "secondary
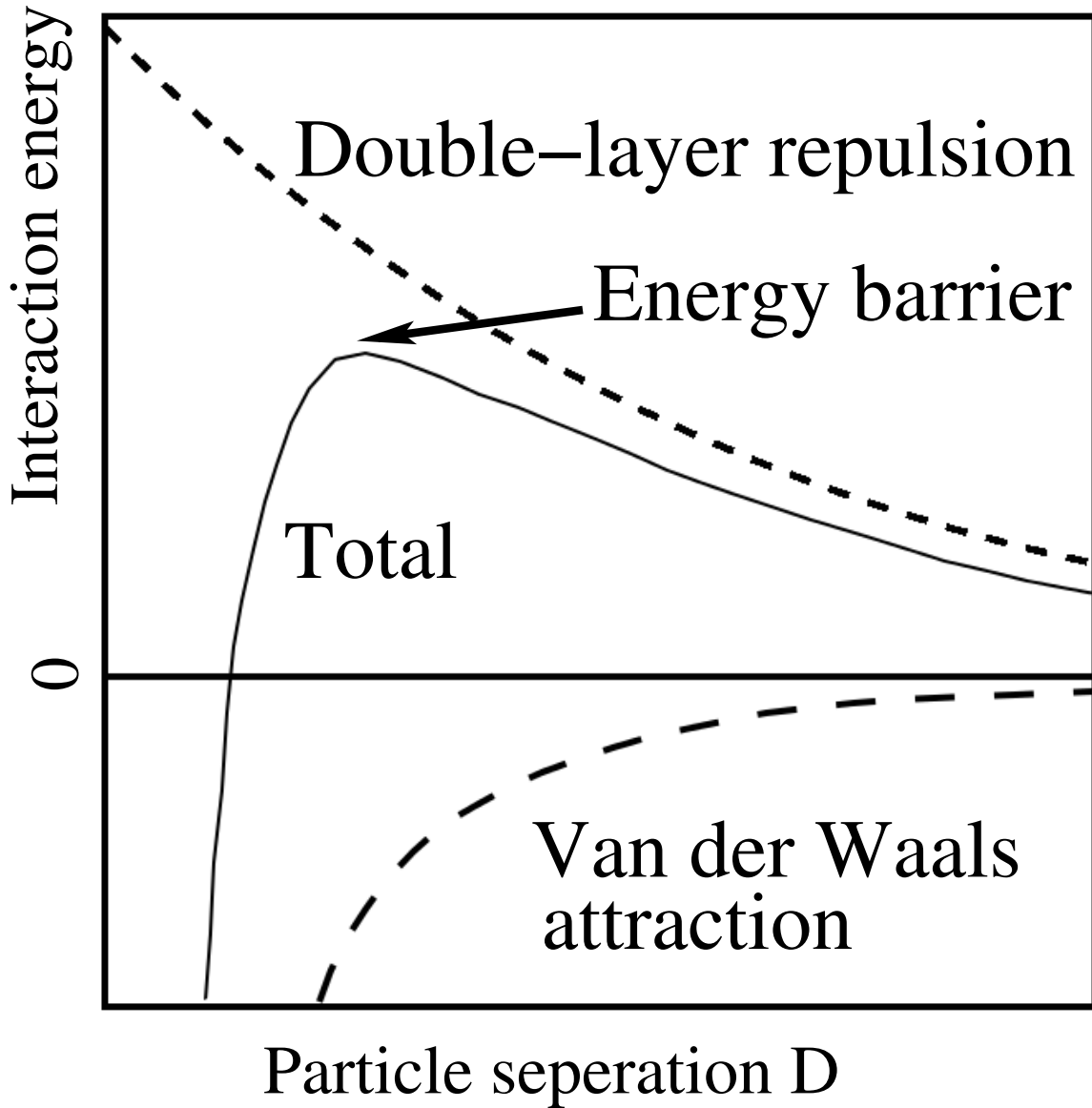
Figure 2.6   Schematic diagram of the variation of free energy with the particle separation according to DLVO theory. The net interaction energy is given by the sum of the double layer repulsion and van der Waals attraction that particles experience as they approach one another.

minimum" results in a weak and potentially reversible flocculation of particles. These flocculations could be sufficiently stable and thus can not be broken up by Brownian motions, but may dissociate under externally applied forces such as vigorous agitation.
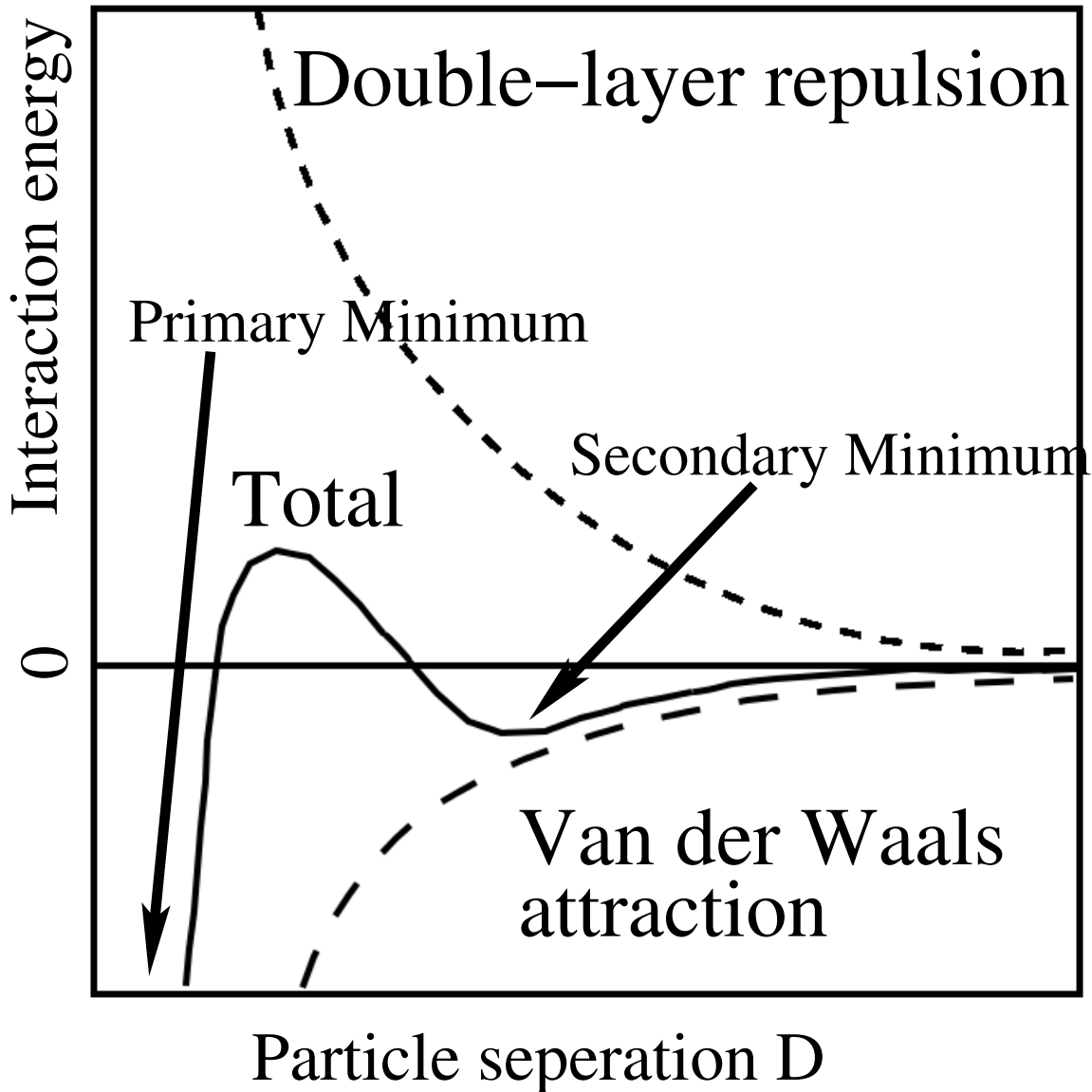
Figure 2.7   Schematic diagram of the variation of free energy with the particle separation according to DLVO theory, for colloids with high salt concentrations. The net interaction energy is given by the sum of the double layer repulsion and van der Waals attraction that particles experience as they approach one another. There is a secondary minimum of free energy, in addition to the primary minimum.

2.2.4   Steric Repulsion

As mentioned in the previous section, another method to achieve colloidal stability is

to add long polymer chains, such as polyethylene glycol (PEG), in the dispersion [155]

[73]. These long chains are absorbed on particle surfaces. If there are enough chains

of polymer absorbed, these layers will overlap when particles approach each other. This overlap makes the local polymer concentration increase, which results in higher free energy. Therefore, these polymer chains provide repulsion between particles and colloidal stability. This interaction is called steric repulsion.
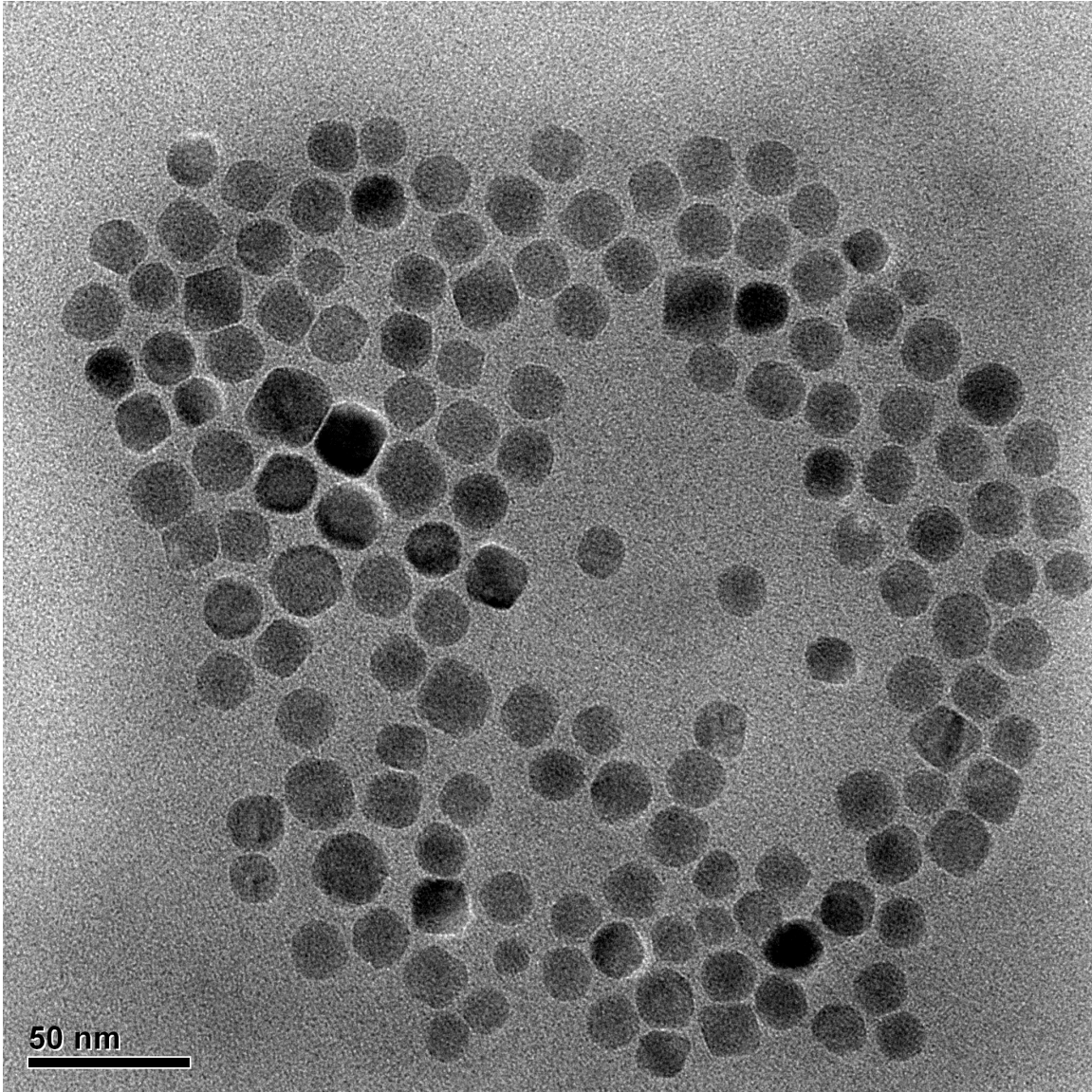
Figure 2.8   TEM image of Fe_3O_4 nanoparticles.

2.3.1   Transmission Electron Microscopy
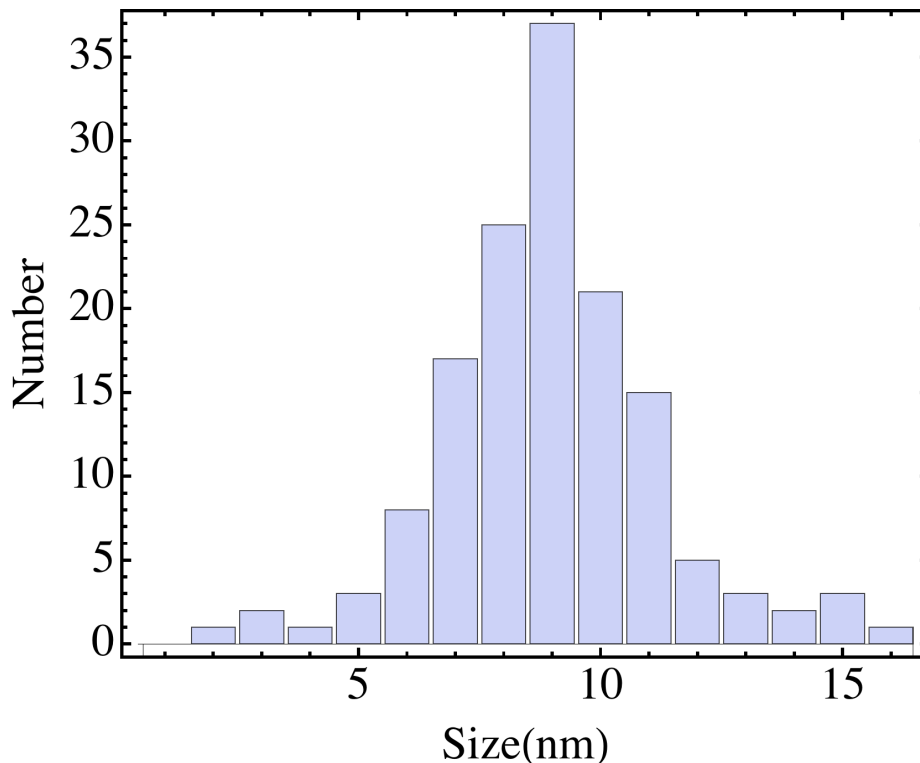
Figure 2.9   Core size distribution of particles that are shown in figure 2.8.

Transmission electron microscopy (TEM) can be used to characterize the particle core size [48]. In TEM, a high-energy (typically 40-400 kV) electron beam transmits through a thin sample film to image the material at atomic level resolution. TEM images are acquired and then analyzed to obtain a distribution of the particle core size. A typical measurement procedure is outlined as follows. First, a diluted colloidal solution is deposited onto a TEM sample grid and then dried. The TEM sample grid with a continuous silicon oxide film that is electron transparent is most often used. Second, the sample grid is loaded into the TEM chamber. TEM images of with enough particles are obtained. Typically > 200 particles are required, depending on the mean particle size. Figure 2.8 shows a TEM image of Fe_3O_4 nanoparticles.

Finally, the TEM images are analyzed to obtain mean particle size and distribution. For the particles displayed in figure 2.9 the mean particle size is 17.5 nm with a 2.2 nm standard deviation.

2.3.2   Vibrating Sample Magnetometer

The magnetic properties of nanoparticles are characterized with a vibrating sample magnetometer (VSM) [56]. The VSM contains a linear motor that drives sinusoidal vibrations of the sample in a particular frequency, e.g., 40 Hz. The sample oscillation amplitude varies depending on the machine used. The sample is placed in a uniform magnetic field to magnetize the sample. Our VSM vibrates the sample along the applied magnetic field that is created by injecting currents into superconducting coils. The oscillating magnetic moment of the sample induces a sinusoidal voltage in a nearby pickup coil according to the Faraday's law of induction [26] [55] . This induced voltage, which is measured with a lock-in amplifier, is proportional to the sample magnetic moment, but does not depend on the applied field.

Figure 2.10 shows the magnetic moment of Fe_3O_4 nanoparticles as a function of applied magnetic field as determined by the VSM. These nanoparticles have a mean size $\sim$13 nm in diameter, as determined by TEM. The sample is prepared by drop casting a nanoparticle suspension with a volume of 0.2 μL Fe_3O_4 nanoparticles onto a piece of Kapton tape. The curve displays zero coercivity, and the magnetic moment of the sample increases from zero as the external field is increased, decreases back to zero as the external field is removed. This m-H curve agrees with the prediction from the Langevin equation (2.3), demonstrating these nanoparticles are superparamagnetic. The dashed line as shown in figure 2.10 is the fit of the VSM data using the Langevin equation (2.3). The fit deviates from the VSM data because of several reasons including the nanoparticle polydispersity (i.e., the particle size has a distribution), a random anisotropy axis distribution, surface anisotropy, and interparticle
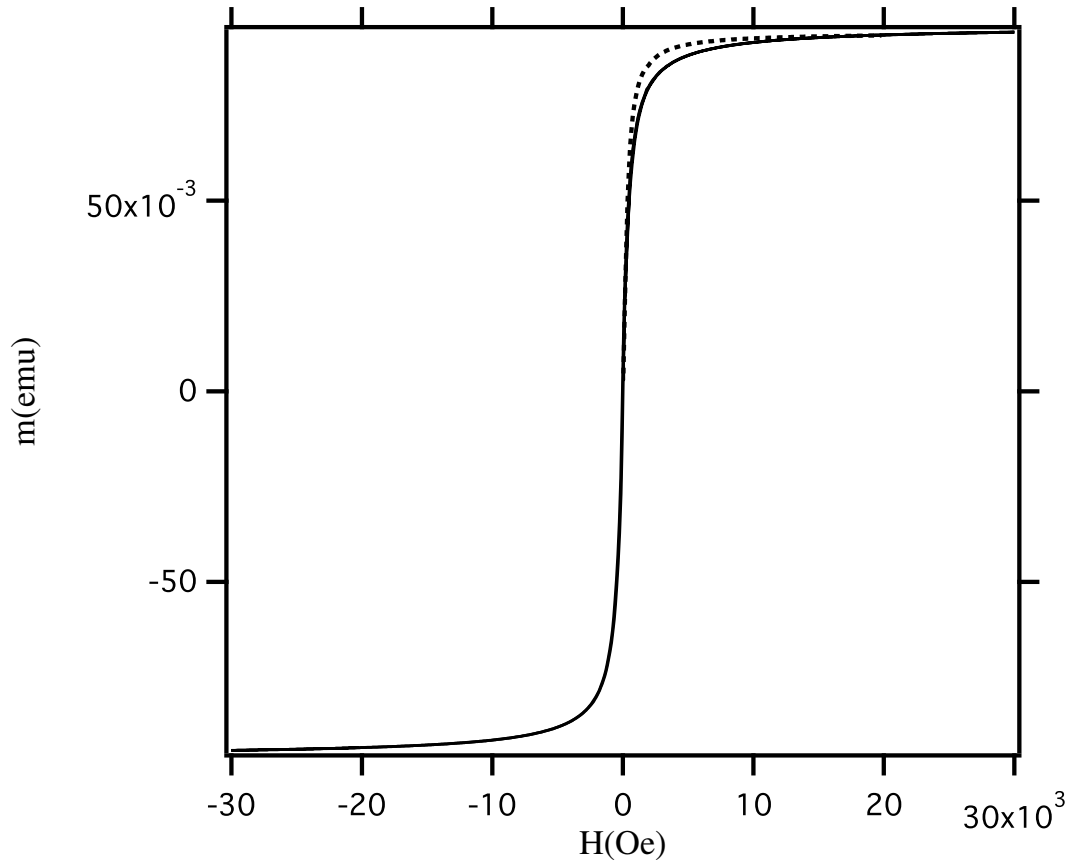
Figure 2.10 Magnetic moment vs applied field for 13nm diameter Fe_3O_4 nanoparticlces, as determined by the VSM.

magnetic interactions that are not incorporated into equation (2.3) [82]. From the fit, a saturation magnetic moment of 0.0941 emu is obtained, and a saturation magnetization (M_S) of 4.7 $\times 10^5$ A/m is calculated, which is close to the bulk value of 4.46 $\times 10^5$ A/m in the literature [184].

2.3.3 Dynamic Light Scattering

Any material illuminated by light reradiates electromagnetic energy, and this radiation is called scattering [97] [22]. Light scattering occurs because the electric field of the incident light induces oscillation of electrons in the material, and these acceler-

ated electrons radiate electromagnetic energy in all directions. Therefore, molecules in the material provide a secondary source of light. The intensity and angular distribution of scattered light depends on the size and shape of the scattering material. Light scattering falls into two categories, i.e., Rayleigh scattering and Mie scattering [115] [97]. Rayleigh scattering theory applies when the particle size is much smaller than the laser wavelength λ (typically $\leq \lambda/10$). In the Rayleigh approximation, the scattering intensity I $\propto$ d^6 and I $\propto 1/\lambda^4$, where d is particle diameter. Therefore, a 100 nm diameter particle scatters 10^6 times more light than a 10 nm diameter particle. This d^6 factor also indicates that it is difficult for a DLS instrument to measure extremely small particles in a mixture of variable size particles. This is because the total light scattering is dominated by large particles. Mie scattering occurs in the case where the particle size is $> \lambda/10$, and the scattering light intensity appears a complex function with respect to the scattering angle θ .

A laser, impinging onto a colloidal solution, is thus scattered by a collection of colloidally suspended particles that are subjected to the Brownian motion. The scattering light intensity measured with a detector at a given time is the superposition of all electrical fields radiated from the illuminated particles. Since all particles undergo Brownian motion, the scattered light intensity at the detector also fluctuates. With electromagnetic theory and time dependent statistical mechanics, it is possible to understand the molecular dynamics of these colloidally suspended particles from light scattering. This is known as the dynamic light scattering (DLS), Quasi Elastic Light Scattering or Photon Correlation Spectroscopy [1] [221].

DLS theory is based on two assumptions. The first assumption is that particles undergo Brownian motion and the probability density function P of a particle at position x and time t is given as [1] [15]

$$P(x,t|0,0) = (4\pi D_C x)^{-3/2} e^{-x^2/4D_C t}, \tag{2.12}$$

where D_C is the diffusion constant of the colloidal solution [74] [15] [217]. The second

assumption is that D_C relates to the particle hydrodynamic radius (R_H) by the Stokes-Einstein equation [171] [47], i.e.,

$$D_C = k_B T / 6\pi\eta R_H, \tag{2.13}$$

where η is the solution viscosity. The hydrodynamic radius is different from the particle core radius. The hydrodynamic radius of a non-spherical particle is the radius of a hypothetical spherical particle that has the same translational diffusion speed as the non-spherical particle. So if the particle changes shape and causes a change in translation diffusion speed, the hydrodynamic radius will change accordingly. A change in the particle surface that affects the particle translational diffusion speed also changes the hydrodynamic radius. For colloidally suspended monodisperse spherical nanoparticles, R_H is typically larger than the particle core radius, because the particle surface is coated with surfactants. Commonly, these surfactants contribute a several to 10′s of nm increase in R_H, depending on surfactants used [236] [155].

Figure 2.11 shows a schematic of a common DLS instrument that detects the hydrodynamic radius of colloids. The DLS instrument measures time-dependent scattering intensities I(t), which are used to compute D_C. Then R_H is calculated using the equation (2.13). To measure I(t), an autocorrelator is employed to construct the correlation function G(τ) of I(t) [15] [59] [171] , i.e.,

$$G(\tau) \;=\; < I(t) \cdot I(t + \tau) >, \tag{2.14}$$

where τ is the time difference between autocorrelator measurements. For a collection of colloidal monodisperse particles in the Brownian motion, G(τ) decays exponentially with respect to τ, and can be expressed as [15] [1]

$$G(\tau) = A_C[1 + B_C \exp(-2\Gamma\tau)], \tag{2.15}$$

where A_C and B_C are the baseline and intercept of the correlation function respec-

tively. Γ is given by

$$\Gamma = D_C q^2, \tag{2.16}$$

and

$$q = (4\pi n/\lambda) \sin(\theta/2), \tag{2.17}$$

where λ is the laser wavelength, n is the refractive index of the colloidal solution and θ is the scattering angle (figure 2.11). D_C is obtained by fitting $G(\tau)$ as a function of τ using equation (2.14). This algorithm is known as the Cumulants analysis [15] [1]. Finally a mean size with an estimate of the distribution width (also called the polydisparity index) is reported. The size distribution plots the relative intensity of
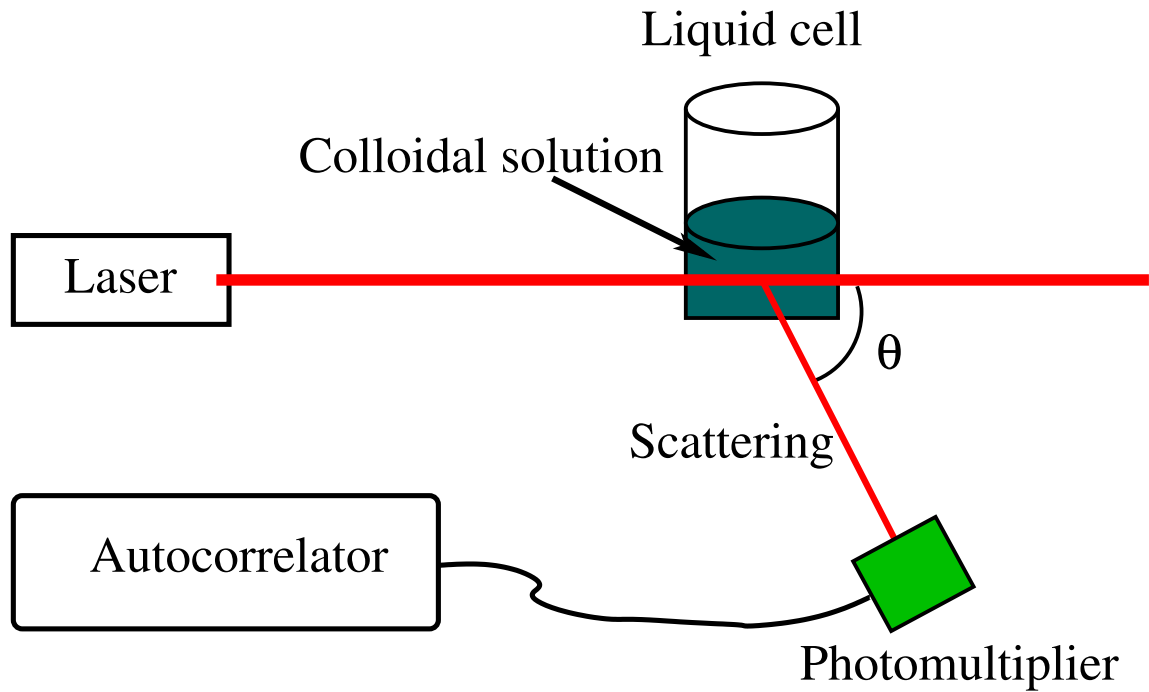
Figure 2.11   Schematic of a DLS instrument.

light scattered by various size particles, also known as the intensity size distribution. This distribution is converted to the volume and number size distributions according to the Mie theory [15]. The average of the three distributions is called the Z-average size distribution.

Self-assembly is a thermodynamically driven process in which a disordered system of pre-existing components (building blocks) forms an organized structure or pattern as a consequence of specific, local interactions among the components themselves [225] [233] [36]. In addition, a self-assembly process can be stimulated by evaporating solvent, applying a nanostructured surface (i.e., template) or external fields (i.e., field-directed assembly) [19] [81] [167] [99]. The field is employed to guide the nanoparticle assembly process and control the ultimate structure or pattern that these building blocks form, including their dimensionality and anisotropy. Self-assembly of magnetic nanoparticles has attracted great interest recently as it may offer a convenient tool for magnetic nanodevice fabrication [129] [19] [167] [186] [80].

2.4.1   Magnetic Nanoparticle Interaction

For a superparamagnetic nanoparticle with dipole moment $\mathbf{m}$ in an applied external field $\mathbf{H}$, the magnetic energy of the nanoparticle (U) is expressed as

$$U = -\mu_0 \mathbf{m} \cdot \mathbf{H}. \tag{2.18}$$

A magnetic force ($\mathbf{F}_m$) that is exerted on the nanoparticle equals the gradient of U [77] [100], i.e.,

$$\mathbf{F}_m = -\mu_0 \nabla(\mathbf{m} \cdot \mathbf{H}). \tag{2.19}$$

Here, $\mathbf{H}$ is the magnetic field at the nanoparticle center, and can be produced by another magnetic particle produces, applied externally, or be a superposition of both. A spherical magnetic nanoparticle 1, containing spatially homogeneous magnetic moment $\mathbf{m_1}$, produces a magnetic field at a position $\mathbf{r}$ where the nanoparticle center is considered as the origin of coordinates, and this magnetic field is expressed as [77] [100]

$$\mathbf{H} = \frac{3(\mathbf{m_1} \cdot \hat{\mathbf{r}})\hat{\mathbf{r}} - \mathbf{m_1}}{4\pi\mu_0 r^3}, \tag{2.20}$$

where $\hat{\mathbf{r}}$ is the unit vector of $\mathbf{r}$. Considering another spherical magnetic nanoparticle 2 that has a spatially homogeneous magnetic moment $\mathbf{m_2}$ at $\mathbf{r}$, the dipole-dipole energy U_{12} between these two magnetic nanoparticles is given by [77] [100]

$$U_{12} = \frac{\mathbf{m_1} \cdot \mathbf{m_2} - 3(\mathbf{m_2} \cdot \hat{\mathbf{r}})(\mathbf{m_2} \cdot \hat{\mathbf{r}})}{4\pi r^3}. \tag{2.21}$$

The dipole-dipole interaction could be repulsive or attractive depending on the relative orientation of these two dipole moments [100]. This dipole-dipole interaction results in an attractive force when $\mathbf{m_1}$, $\mathbf{m_2}$ are parallel, and a repulsive force when anti-parrallel. For a same $\mathbf{r}$, the attractive interaction is almost double the repulsion. The dipole-dipole interaction increases linearly with respect to both $\mathbf{m_1}$ and $\mathbf{m_2}$, but decays quickly as a function of $\mathbf{r}$ due to the $1/r^3$ term in equation (2.21).

External magnetic fields can help create nanoparticle arrays via dipole-dipole interactions. Structures with orientation anisotropies can be induced with applied magnetic fields too. Typically this field-assisted self-assembly process is reversible, i.e., the structure organized can be disassembled by removing the external magnetic field. For example, periodic arrays of photonic crystals with reversible tunability have been self-assembled by applying external fields to colloidally suspended superparamgnetic nanoparticles [71] [70] [117] [69].

2.4.2   Template-assisted Self-assembly

Recently, external fields have emerged as a key method to direct the assembly of colloidal nanoparticles. Particles with specific physical properties can be designed to maximize their interactions with external directing fields (e.g., magnetic, electric), or directing surfaces (e.g., confined geometries, interfaces) [19] [81] [186]. It is possible to create templates to produce the fields that assist magnetic particle assembly into desired patterned structures. This technique is called template-assisted field-directed self-assembly [80] [130]. Colloidal nanoparticle assembly in electric/magnetic fields

occurs due to induced interactions. Manipulation and control over these colloidal particles are provided by electrical/magnetic forces , as relatively strong forces are required to assemble particles. For magnetic particles, the magnetic force depends on the field gradient. Field gradients up to several 10 kT/m have been achieved using methods such as an array of permanent magnets [65] [64] [43]. However, higher field gradients are needed to achieve reliable and robust self-assembly of particles. Since particles are also subject to other forces such as the viscous drag force, Brownian force, and buoyancy force [64] [65]. Below I present evidence of ultra-high magnetic field gradients up to 1×10^7 T/m that are created on a template, i.e., a hard disk drive medium, via commercial magnetic recording technology. These field gradients can be employed to assemble magnetic nanoparticles and the template can be reprogrammed and reused.

2.5 Hard Disk Drives

We are in the information age and there are a variety of information data storage systems available on the market. These systems include magnetic tape drives, magnetic hard disk drives, magnetic floppy disk drives, magneto-optic (MO) disk drives, phase-change optical disk drives, semiconductor flash memory, magnetic random access memory (RAM), and holographic optical storage [231]. To date, specifically the hard disk drive is most widely used. This section provides an introduction to hard disk drives and how the magnetic medium on the disk drive is used to create ultra-high field gradients.

2.5.1 Overview

Hard disk drives have some advantages over other data storage systems such as large storage capacity, low-cost, fast access times and a relatively mature manufacturing infrastructure. Therefore, hard disk drives have dominated the mass information

storage devices for decades. Figure 2.12 shows a photograph of the hard disk drive with its key components:

1. Magnetic write/read heads and magnetic disks, also known as platters, which store the recorded data. The platters are made of a non-magnetic material, commonly aluminum alloy, glass or ceramic and are coated with a thin layer (10 - 30 nm) of magnetic material such as CoCrPt, with an outer protection layer. Each platter surface has a write/read head that is located on the trailing edge of a slider (a platter has two surfaces and thus two write/read heads).The head is too small to be visible to the eye. A slider is mounted to the end of a stainless steel gimbal-suspension, forming a so-called head-gimbal assembly (HGA). A pair of a write/read head and a recording disk surface is often called a head-disk assembly.

2. Data detection electronics and write circuit, are mostly located on a printed circuit board with many very-large-scale integration (VLSI) chips. These electronics and circuit control the disk rotation and actuator motion, and read/write magnetic data.

3. Mechanical servo and control system, including spindles, actuators, suspensions, and control chips. A spindle holds and spins the platters at varying speeds. An actuator is employed to move the heads roughly radially across the platters as they spin, and thus allows each head to access the entire surface of the platter.

4. Interface to microprocessor, located at one edge of the print-circuit board and through which the microprocessor input information from or output information to the disk drive.

Figure 2.13 shows the schematic principle of magnetic recording on longitudinal media where the magnetization is parallel to the disk drive surface. The longitudinal
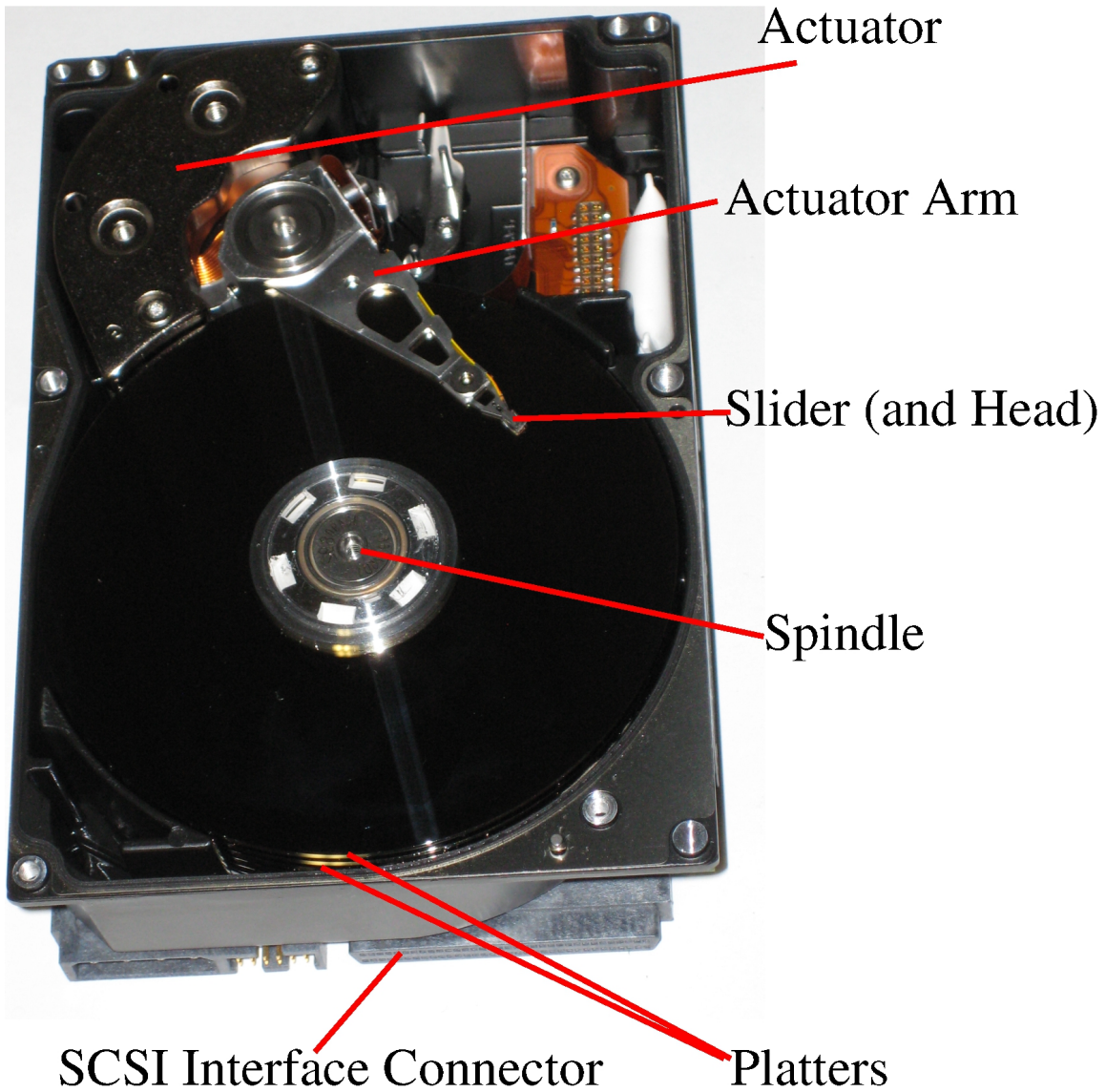
Figure 2.12   Photograph of a magnetic hard disk drive.

medium stores nonvolatile data using two distinctive magnetization states (i.e., thin arrows in figure 2.13). The medium magnetization directions can be modified back and forth with a magnetic write head at a localized storage site (i.e., a magnetic data "bit"). A write head is composed of yoke-shaped soft magnetic material which has an air gap (called head gap). The yoke has coils wound around it to magnetize a soft magnetic material with low coercivity and high permeability. During a write process, a current passes through the coils to create a write field in the medium near

the head gap. The write field is larger than the medium coercivity so that the bit underneath the write head is magnetized in the field direction. By changing the write current polarity, the other state can be written. There are junctions between the neighboring oppositely magnetized bits, called transitions. The transition length is ~ 10 nm for longitudinal magnetic recording media [231], but not shown in figure 2.13 for convenience.
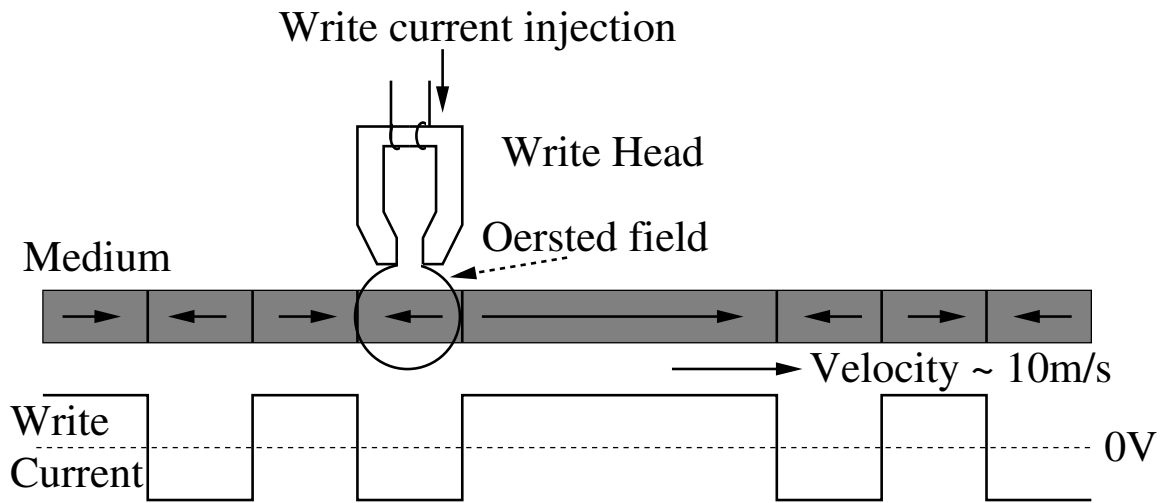
Figure 2.13   Schematic diagram showing the magnetic recording on longitudinal magnetic recording media.

During the disk drive operation, the disk spins at a constant speed ~ 10 m/s. The self-pressured air bearing existing between the spinning disk and the slider causes a constant separation (called the fly height) between them. The fly height is on the order of 25 nm. Data can be written in different data tracks by moving the slider in the radial direction.

2.5.2   Longitudinal Magnetic Recording Media

Magnetic recording medium in hard disk drives is composed of continuous magnetic thin films. The permanent magnets have coercivities large enough to maintain the

magnetization state for a long time after being written. A longitudinal magnetic recording medium has multiple layers stacked together as shown in figure 2.14.

~3nm Lubricant
~15nm Overcoat
~30nm Magnetic Thin Film

~150nm Cr

~10um NiP

~0.8mm Al Substrate
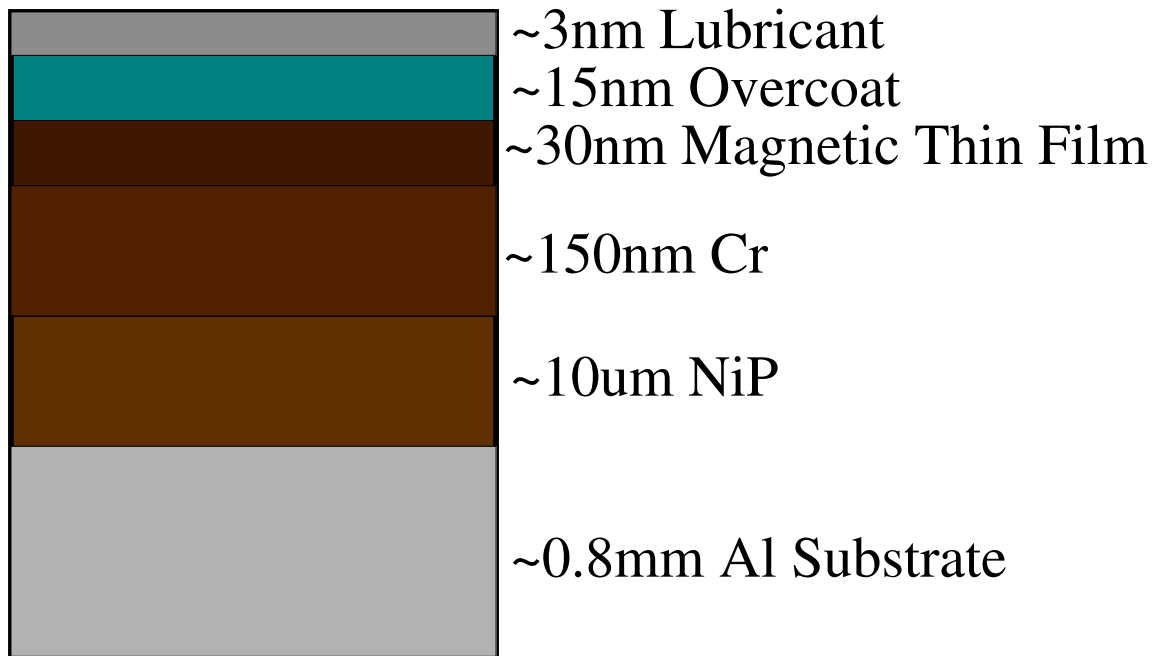
Figure 2.14 Schematic diagram a longitudinal magnetic medium on disk drives.

The aluminum substrate is plated with an amorphous NiP undercoat to make the disk rigid, smooth, and properly textured. A chromium underlayer is often used to control magnetic properties and microstructures of the magnetic recording layer. The magnetic layer (typically Co-based alloy) is covered by a carbon overcoat layer and lubricant. The last two layers are necessary for the tribological performance of the head-disk interface and for the protection of magnetic layer. Tribology is the science and engineering of interacting surfaces in relative motion [17]. The disk must rotate underneath the flying head at a high speed.Note that the fly height is the distance between the head air bearing surface to the disk top surface, while the magnetic spacing is the distance between head pole tips and the magnetic layer. The fly height is only a fraction of the magnetic spacing, and the latter is most relevant in the write and read processes.

2.5.3 Field and Field Gradients on Longitudinal Media

Figure 2.15 shows a schematic of a magnetic transition. The magnetization directions of the two data bits are parallel to the x axis, and the z axis is normal to the disk drive surface. The medium film has a finite thickness ($\delta \sim 30$ nm commonly) in the z direction.
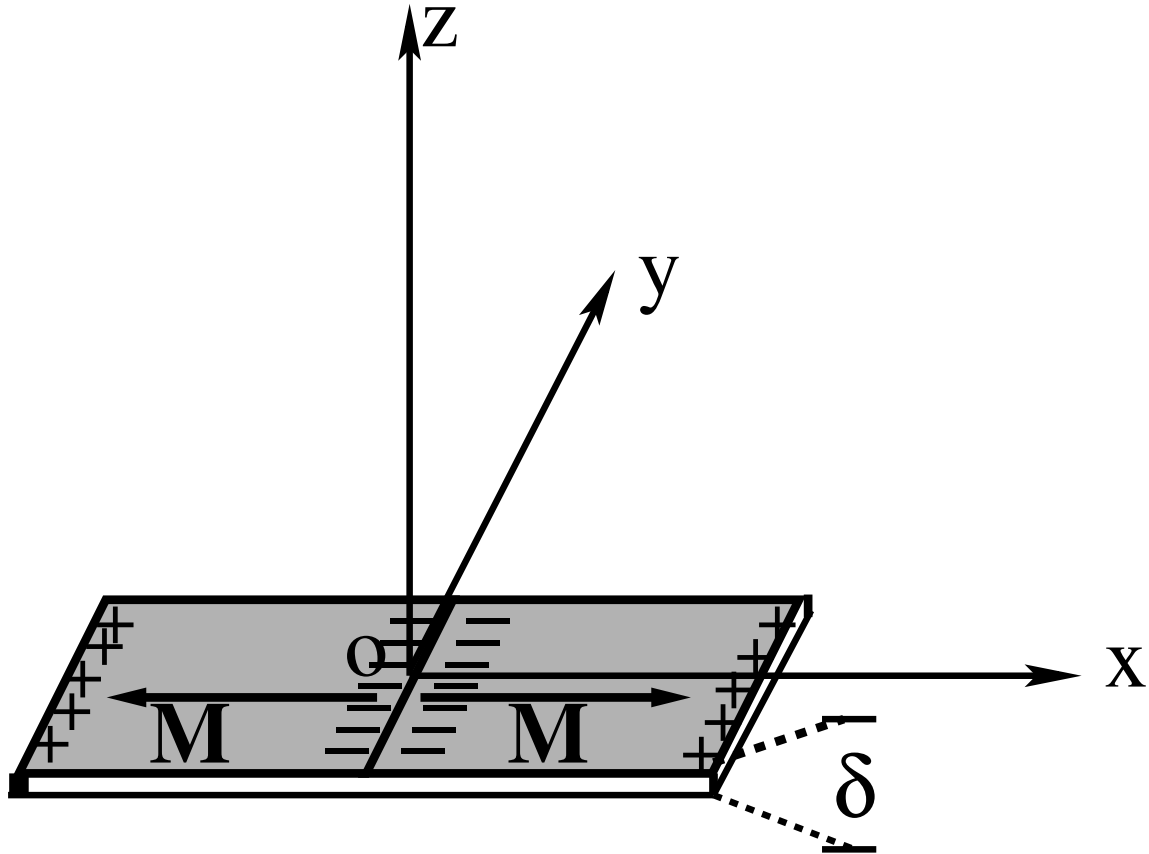
Figure 2.15   Schematic of magnetic transitions on a longitudinal magnetic medium.

Fields of Step Transitions

First, let us consider a single step transition on the longitudinal magnetic medium (figure 2.15). Therefore, the magnetization of the magnetic medium can be expressed as

$$M(x) = \begin{cases} -M_r, & x < 0 \text{ and} -\delta/2 \leq z \leq \delta/2, \\[2mm] M_r, & x > 0 \text{ and} -\delta/2 \leq z \leq \delta/2, \end{cases} \qquad (2.22)$$

where M_r is the remanence magnetization of the magnetic medium. Bound currents (in current picture) or magnetic charges (in charge picture) methods can be used to calculate the magnetic field H_{xz} at a point (x,z) that is produced by the transition [77] [100]. The charge picture is more convenient and thus widely used. This charge picture can be understood by superposing magnetic fields that are produced by all point magnetic charges in the whole space.

A point charge q_m at a position $\mathbf{r}'$ produces a field $\mathbf{H}$ at $\mathbf{r}$, which is written as [77] [100]

$$\mathbf{H} = \frac{q_m}{4\pi} \frac{\mathbf{r} - \mathbf{r}'}{|\mathbf{r} - \mathbf{r}'|^3}. \qquad (2.23)$$

Therefore, the magnetic field $\mathbf{H}(\mathbf{r})$ by superposing a distribution of volume charge with density ρ_m and surface charge with density σ_m is

$$\mathbf{H}(\mathbf{r}) = \frac{1}{4\pi} \left(\iiint \rho_m \frac{\mathbf{r} - \mathbf{r}'}{|\mathbf{r} - \mathbf{r}'|^3} d^3\mathbf{r}' + \iint \sigma_m \frac{\mathbf{r} - \mathbf{r}'}{|\mathbf{r} - \mathbf{r}'|^3} d^2\mathbf{r}' \right). \qquad (2.24)$$

Insert $\rho_m = \nabla \cdot \mathbf{M}(\mathbf{r}')$ and $\sigma_m = \mathbf{n}' \cdot \mathbf{M}(\mathbf{r}')$ [77] in equation (2.24), one obtains

$$\mathbf{H}(\mathbf{r}) = \frac{1}{4\pi} \left[\iiint \left(\nabla \cdot \mathbf{M}(\mathbf{r}') \right) \frac{\mathbf{r} - \mathbf{r}'}{|\mathbf{r} - \mathbf{r}'|^3} d^3\mathbf{r}' + \iint \left(\mathbf{n}' \cdot \mathbf{M}(\mathbf{r}') \right) \frac{\mathbf{r} - \mathbf{r}'}{|\mathbf{r} - \mathbf{r}'|^3} d^2\mathbf{r}' \right]. \qquad (2.25)$$

In the case of a transition given by equation (2.22), $\nabla \cdot \mathbf{M}(\mathbf{r}') = 0$ and there is a surface charge density $\sigma_m = -2M_r$ occurring at the transition center (i.e., x = 0) extending from $-\delta/2 \leq z \leq \delta/2$ in the z direction. Therefore, equation (2.25) reduces to

$$\mathbf{H}(\mathbf{r}) = -\frac{M_r}{2\pi} \iint \frac{\mathbf{r} - \mathbf{r}'}{|\mathbf{r} - \mathbf{r}'|^3} d^2\mathbf{r}'. \qquad (2.26)$$

Assuming the magnetic medium extends infinitely in the y direction and according to charge symmetry with respect to the x axis, the field in the y direction $H_y = 0$, i.e., $\mathbf{H}(\mathbf{r})$ lies in the x-z plane. Using equation (2.26), H_x and H_z are computed as

$$H_x(x, z) = -\frac{M_r}{2\pi} \int_{-\delta/2}^{\delta/2} \int_{-\infty}^{\infty} \frac{x}{\left(x^2 + (y - y')^2 + (z - z')^2\right)^{3/2}} dy' dz', \qquad (2.27)$$

and

$$H_z(x, z) = -\frac{M_r}{2\pi} \int_{-\delta/2}^{\delta/2} \int_{-\infty}^{\infty} \frac{z - z'}{\left(x^2 + (y - y')^2 + (z - z')^2\right)^{3/2}} dy' dz'. \qquad (2.28)$$

For simplicity and without losing the generality, y can be set $= 0$. Using the following integral equations (note that b and c are real numbers),

$$\int \frac{1}{(bx^2 + c)^{3/2}} dx = \frac{x}{c(bx^2 + c)^{1/2}}, \qquad (2.29)$$

$$\int \frac{1}{(x^2 + b^2)} dx = \frac{1}{b} \arctan \frac{x}{b}, \qquad (2.30)$$

and

$$\int \frac{x}{(bx^2 + c)} dx = \frac{1}{2b} \ln(bx^2 + c), \qquad (2.31)$$

one can show that equations (2.27) and (2.28) can be further simplified as

$$H_x(x, z) = -\frac{M_r}{\pi} \left[\arctan\left(\frac{z + \delta/2}{x}\right) - \arctan\left(\frac{z - \delta/2}{x}\right) \right], \qquad (2.32)$$

and

$$H_z(x, z) = -\frac{M_r}{2\pi} \ln \left[\frac{(z + \delta/2)^2 + x^2}{(z - \delta/2)^2 + x^2} \right]. \qquad (2.33)$$

Note the surface charge density at the transition $\sigma_m = -2M_r$, therefore, the magnetic field components at $\mathbf{r}$ for a unit surface charge at the step transition, i.e., H_x and H_z divided by σ_m, are expressed as respectively,

$$H_x^{ustep}(x, z) = \frac{1}{2\pi} \left[\arctan\left(\frac{z + \delta/2}{x}\right) - \arctan\left(\frac{z - \delta/2}{x}\right) \right], \qquad (2.34)$$

39

and

$$H_z^{ustep}(x, z) = \frac{1}{4\pi}\ln\left[\frac{(z + \delta/2)^2 + x^2}{(z - \delta/2)^2 + x^2}\right]. \tag{2.35}$$

Equations (2.34) and (2.35) are valid both inside and outside of the magnetic medium.

Fields and Field Gradients of Transitions with Finite Length

In reality, the transition is not single step, but has a finite length, also called a transition parameter(a) [231]. A real magnetization transition in the longitudinal medium is traditionally modeled by the arctangent function [16], i.e.,

$$M(x') = \frac{2M_r}{\pi}\arctan\left(\frac{x'}{a}\right). \tag{2.36}$$

Figure 2.16 shows the magnetization as a function of x' for a step and an arctangent transition with a 10 nm transition parameter (i.e., $a = 10$ nm). Assuming the finite transition does not change the fields in both y and z directions, the magnetic charge at each location x' can be regarded as an equivalent of a step transition with a surface charge density of $-\partial M(x')/\partial x'$. Therefore, equations (2.34) and (2.35) are used to calculate magnetic fields at (x,z) [i.e., $H_x^S(x - x', z)$ and $H_z^S(x - x', z)$] produced by such a step transition located at x'. One has

$$H_x^S(x - x', z) = \frac{-\partial M(x')/\partial x'}{2\pi}\left[\arctan\left(\frac{z + \delta/2}{x - x'}\right) - \arctan\left(\frac{z - \delta/2}{x - x'}\right)\right], \tag{2.37}$$

and

$$H_z^S(x - x', z) = \frac{-\partial M(x')/\partial x'}{4\pi}\ln\left[\frac{(z + \delta/2)^2 + (x - x')^2}{(z - \delta/2)^2 + (x - x')^2}\right]. \tag{2.38}$$

Using the superposition principle, one can compute the total magnetic field produced by a finite transition as

$$H_x(x, z) = \int_{-\infty}^{\infty} H_x^S(x - x', z)dx', \tag{2.39}$$

and

$$H_z(x, z) = \int_{-\infty}^{\infty} H_z^S(x - x', z)dx'. \tag{2.40}$$

40
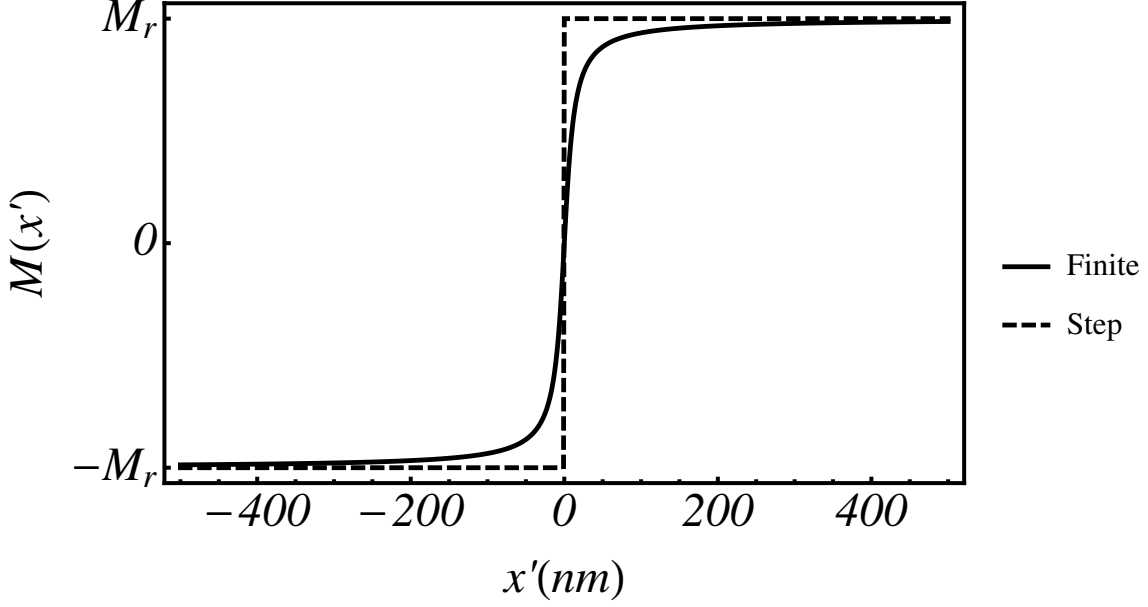
Figure 2.16   Arctangent (solid curve) and step (dotted curve) magnetization transtions.

Take the partial derivative of the equation (2.36) with respect to x', one obtains

$$\frac{\partial M(x')}{\partial x'} = \frac{2M_r}{\pi} \left(\frac{a}{x'^2 + a^2} \right).$$

(2.41)

Insert equation (2.41) into (2.39) and (2.40), finally, one obtains,

$$H_x^f(x, z) = \frac{M_r}{\pi} \left[\arctan \left(\frac{a + |z| + \delta/2}{x} \right) - \arctan \left(\frac{a + |z| - \delta/2}{x} \right) \right] (|z| \geq \delta/2),$$

(2.42)

and

$$H_z^f(x, z) = \pm \frac{M_r}{2\pi} \ln \left[\frac{(a + |z| - \delta/2)^2 + x^2}{(a + |z| + \delta/2)^2 + x^2} \right] (+ \text{ for } z \geq \delta/2 \text{ and } - \text{ for } z \leq -\delta/2).$$

(2.43)

Figure 2.17 (a) and (b) show magnetic fields H_x^f and H_z^f as function of x at different z positions respectively. H_x^f and H_z^f are computed using parameters $a = 10$ nm, $\delta = 30$nm, and $M_r = 4.5 \times 10^5$ A/m that is determined by VSM. Note the z position of the center medium plane is at zero. H_z^f is maximum at $x = 0$, and

41
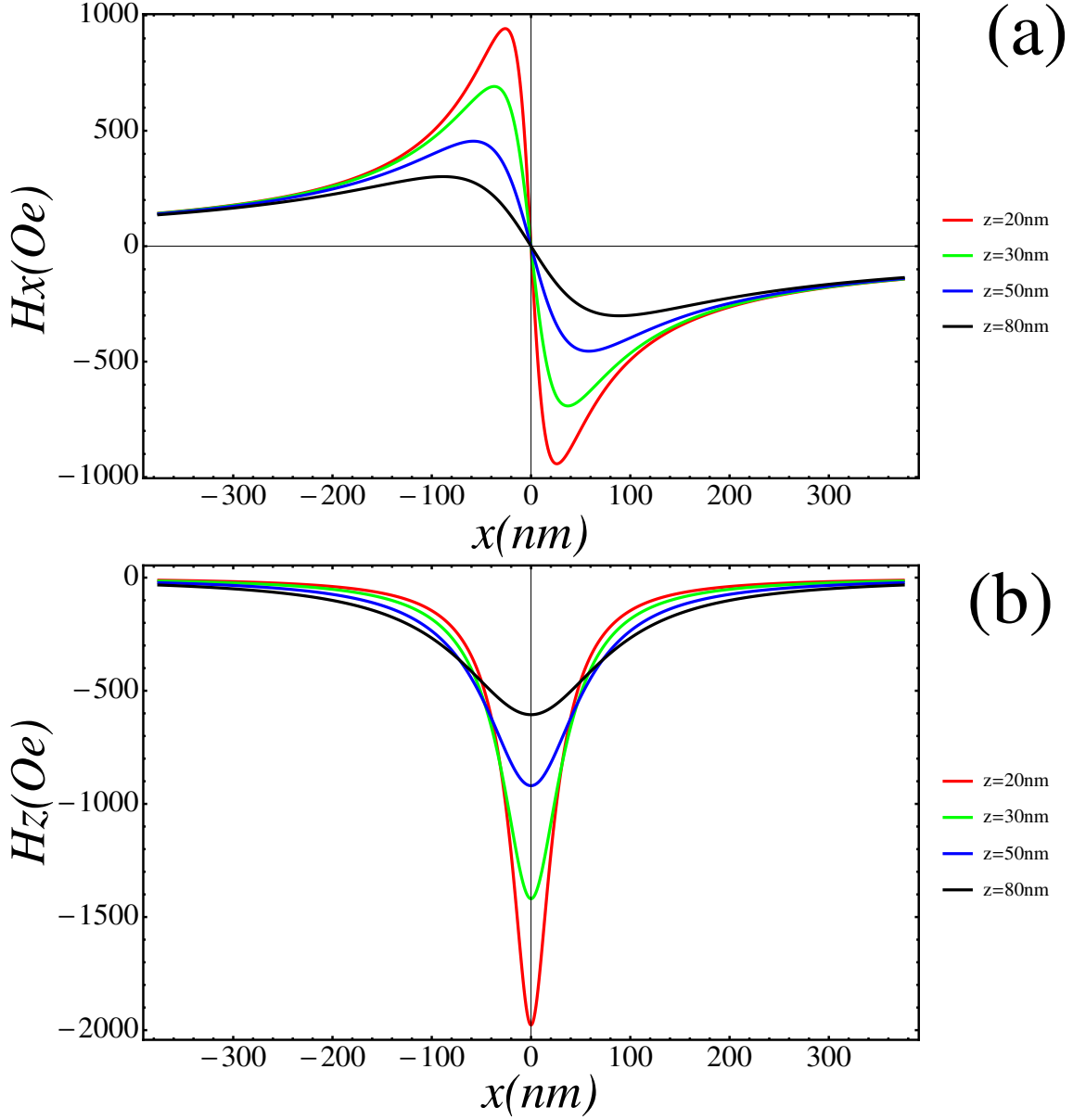
Figure 2.17 (a) H_x^f vs x at $z = 20, 30, 50$ and 80 nm. (b) H_z^f vs x at $z = 20, 30, 50$ and 80 nm.

decreases as x is increased. H_x^f displays a little different behavior, i.e., $H_x^f = 0$ at x $= 0$, increases first and then decreases as x is increased. Both H_x^f and H_z^f appear symmetric with respect to the x axis and decay with z. For example, above the transition, H_z^f is $\sim$ 2000 G at a 20 nm z and reduces to $\sim$100 G as z is increased to 500 nm. If there are superparamagnetic nanoparticles approaching the magnetic
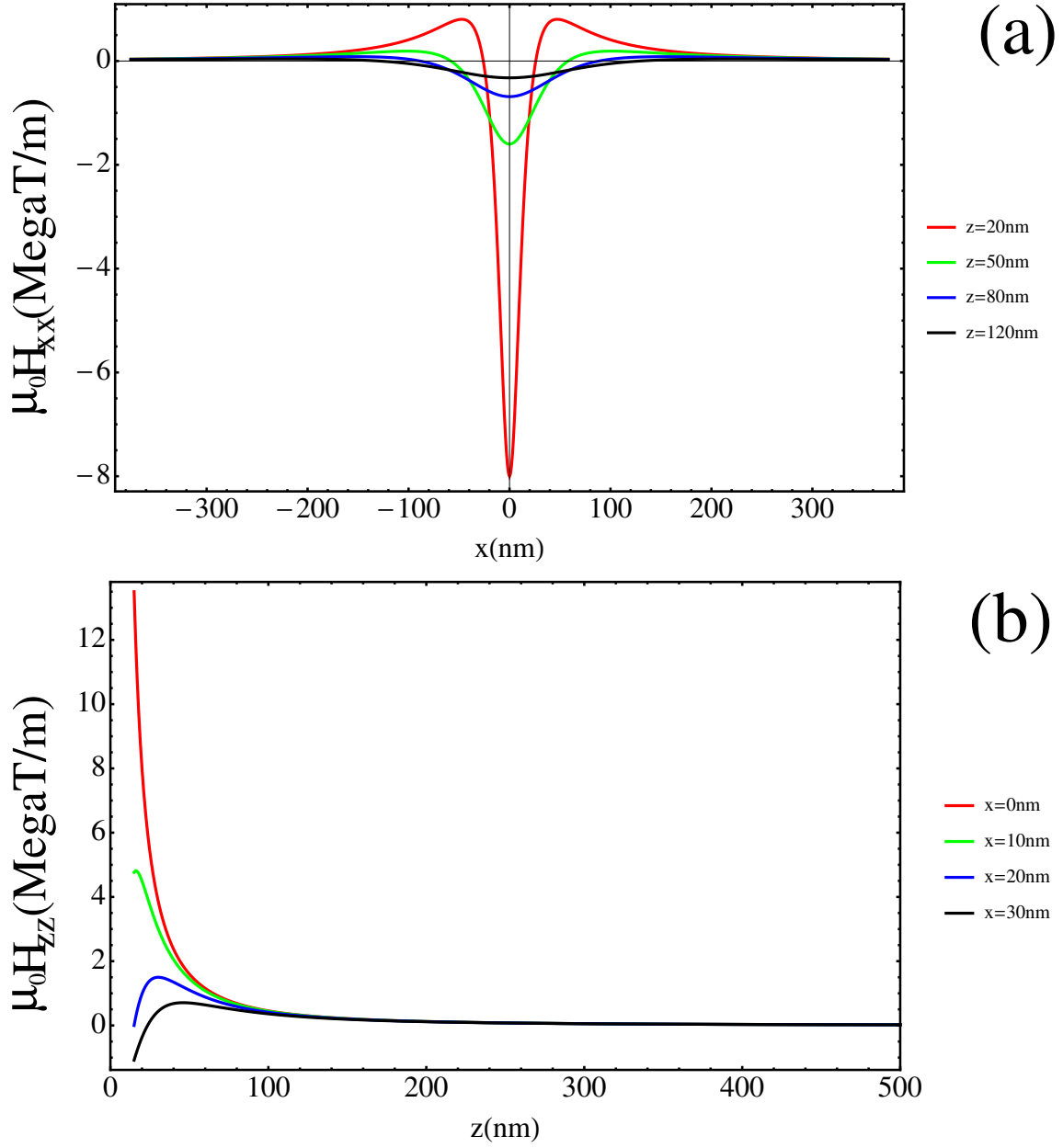
Figure 2.18 (a) H_{xx} vs x at $z = 20$, 30, 50 and 80 nm. (b) H_{zz} vs z at $x = 0$, 10, 20 and 30 nm.

medium surface, H_x^f and H_z^f will magnetize the nanoparticles in x and z directions respectively. The magnetic moment of the nanoparticle depends on the its position with respect to the medium surface and the transition.

Figure 2.18 shows field gradients H_{xx} as function of x at different z positions and

H_{zz} as function of z at different x positions, where H_{xx} and H_{zz} are respectively computed as

$$H_{xx} = \frac{\partial H_x^f(x,z)}{\partial x}, \tag{2.44}$$

and

$$H_{zz} = \frac{\partial H_z^f(x,z)}{\partial z}. \tag{2.45}$$

Ultra-high field gradients H_{xx} and H_{zz} up to $\sim 1 \times 10^7$ T/m exist above the magnetic medium surface around the transition. H_{xx} is largest at x = 0, and decreases quickly as x is increased [figure 2.18(a)]. H_{zz} is largest at z = 0, and decays quickly with respect to z [figure 2.18(b)]. These field gradients apply magnetic forces on the magnetized nanoparticles and thus direct the nanoparticle motion.

Figure 2.19 (a) and (b) show x and z components of the magnetic force (F_x and F_z) exerting on a 10 nm diameter Fe_3O_4 nanoparticle by the field gradients present near the magnetic medium surface. F_x and F_z are calculated using an effective dipole model [63] [64] and the equation (2.19). A product of x and F_x is negative as shown in figure 2.19 (a), meaning the nanoparticle moves towards the transition (i.e. x = 0). Similarly, F_z drives the nanoparticle towards the medium surface. Therefore, these field gradients direct the self-assembly of magnetic nanoparticles onto the transition.
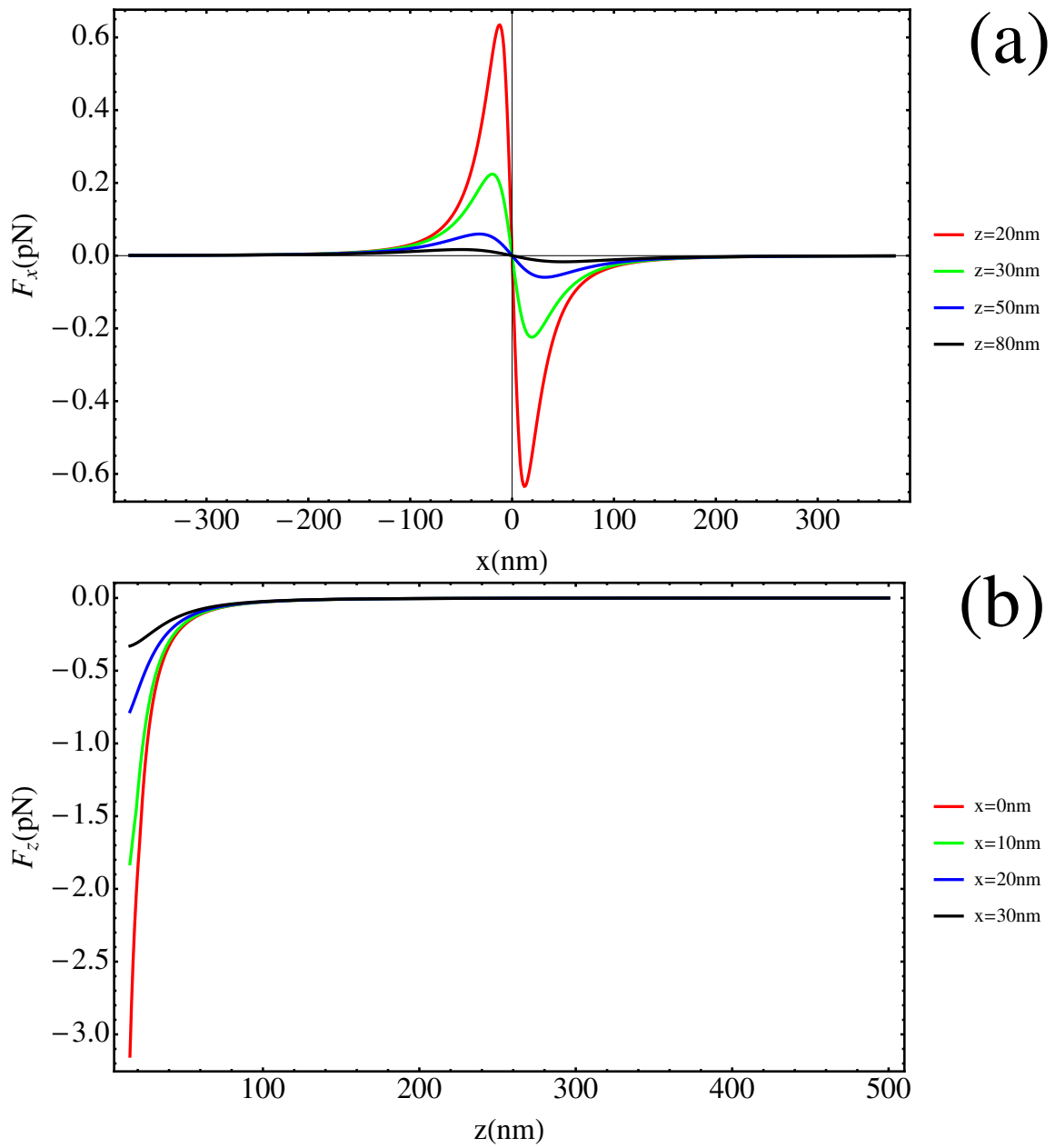
Figure 2.19   (a) F_x vs x at z = 20, 30, 50 and 80 nm for a 10nm diameter magnetite nanoparticle. (b) F_z vs z at z = 0, 10, 20 and 30 nm for a 10nm diameter magnetite nanoparticle.

Chapter 3

Self-assembly of All-nanoparticle Diffraction
Gratings

The previous section described the ultra-high field gradients present above magnetic transitions on longitudinal magnetic media. These field gradients can direct self-assembly of magnetic nanoparticles onto transitions. Therefore, magnetic nanoparticles can be self-assembled into patterned microstructures on the magnetic medium by patterning magnetic transitions. In this chapter, I demonstrate this technology can be employed to nanomanufature all-nanoparticle diffraction gratings using longitudinal media [243]. Perpendicular media are also employed and yield similar results. First I show the nanomanufacturing process. Second, I provide results of spectral measurements and calibration of these nanomanufactured gratings. Third, I present evidence for existence of a useful property that these gratings possess. Finally, I discuss the repeatability of the nanomanufacturing technique, demonstrating commercial potential of this technique for fabricating diffraction gratings and complex functional materials for future technological applications.

3.1.1   Grating Self-assembled onto Magnetic Medium Surface

Using magnetic recording to create nanoscale templates, magnetic nanoparticles are self-assembled onto disk drive magnetic media. Equally-spaced, oppositely-magnetized regions (i.e., magnetic bits) are recorded onto a 95 mm diameter longitudinal disk drive medium (i.e., a disk) via magnetic recording with a conventional read write head. The length of these regions are precisely controlled during the recording process to yield equal spacing lines patterned on the disk surface. Enormous magnetic field gradients exist above transitions. These field gradients exert a force on colloidally suspended superparamagnetic nanoparticles, i.e., a ferrofluid, deposited on the media. This spatially-localized magnetic force attracts the nanoparticles to these transitions, and by creating arrays of transitions over the disk surface, nanoparticles are precisely assembled into large-area patterned materials.

Pattern sizes and shapes are controlled by magnetic recording, with the magnetic medium acting as a template for nanoparticle assembly that can be both reused and reprogrammed with different patterns. For the diffraction gratings that are manufactured using the template, the lines lie parallel to the disk radius with the grating spacing along the disk circumference. Our gratings are written at a 28 mm radius, and over a 0.65 x 0.65 mm^2 illuminated area [e.g. 0.65 mm Gaussian full width at half maximum (FWHM) of our HeNe laser beam], the saggita for a 0.65 mm long chord is 2 μm. Therefore, relative to a 0.65 mm wide band, the deviation of our grating from square along the circumferential direction is ∼0.3% and can be neglected. Moreover, xy rectilinear recording can also be performed using a contact write read tester [144]. Figures 3.1(a)-3.1(d) show the entire process schematically.

As shown in figure 3.1 (a), magnetic recording media are diced into ∼12 mm di-

ameter circular coupons. After cleaning a coupon, $\sim$0.5 mL of diluted ferrofluid ($\sim$10 - 20 nm diameter cobalt ferrite ($CoFe_2O_4$) nanoparticles with $\sim$10 μg/mL nanoparticle concentration) is pipetted onto the coupon. These $CoFe_2O_4$ nanoparticles are provided by the Rinaldi group at University of Florida. The nanoparticles suspended in the ferrofluid just above the coupon surface are magnetized by the transitions' fields, and are then attracted to the transition region ["T" in figure 3.1(a)-3.1(c)], by the field gradient. The ferrofluid solution remains on the coupon for a length of time, e.g., 60 minutes, and is then removed by tilting the coupon slowly. Nanoparticles coat the transitions on the coupon [figure 3.1(b)]. A representative dark-field microscope image of the nanoparticle patterns assembled on the coupon is shown in figure 3.1(e).

3.1.2   Pattern Transfer of Gratings

After imaging the assembled nanoparticles a liquid polymer solution is spin-coated onto the coupon surface [figure 3.1(c)]. The polymer (Diskcoat 4220 from General Chemical Corp., Brighton, MI) is diluted with DI water (Diskcoat:DI water = 4:1) and spun at 2000 rpm for 20 s, and the resulting film is ~ 1.1 μm thick as determined using both stylus and optical profilometry. Varying the ratio of Diskcoat to DI water enables different polymer film thicknesses. After curing the polymer thin film for 15 minutes in air at room temperature, the polymer-nanoparticle assembly is peeled from the coupon surface with adhesive tape [figure 3.1(d)]. This peeling transfers the nanoparticle patterns to the polymer film. The adhesive tape has a 5 mm diameter central hole, yielding a window of suspended film containing patterned nanoparticles [figure 3.1(f)]. Figure 3.1(g) shows a dark-field image of the patterned nanoparticles as embedded in the suspended film after peeling. Grating spacing (d) is optically measured using a 100X objective lens, and, assuming equal spacing for these features, multiple measurements of 50 μm patterned regions ($L = 50$ μm) yield 742 $\pm$ $\sim$12 nm. Similar measurements on the peeled patterns yield 750 $\pm$ $\sim$12 nm. The 12 nm
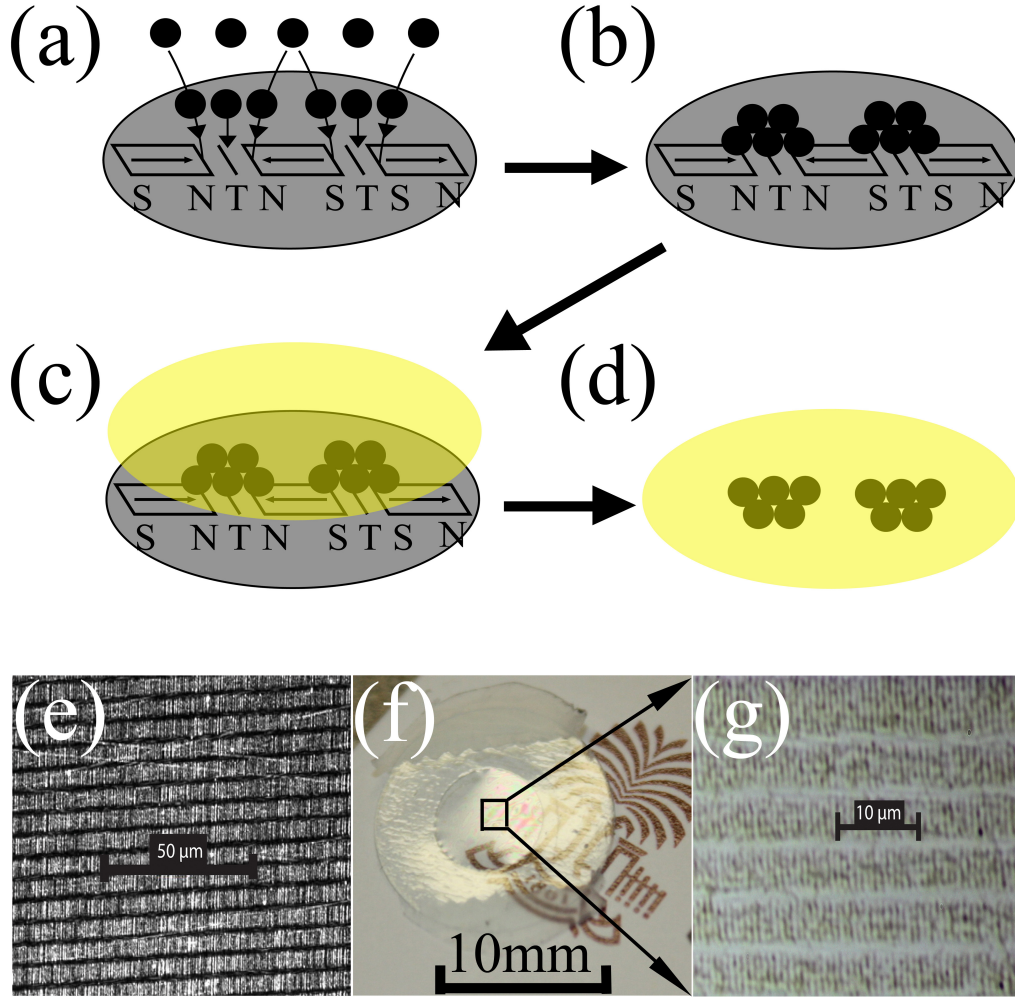
Figure 3.1 Diffraction grating nanomanufacturing using programmable magnetic recording and pattern transfer. (a)-(d) Schematic diagrams showing entire nanomanufacturing process. Gray ellipses: projections of coupons. Parallelograms: projections of magnetized regions on coupons and arrows enclosed denote magnetization directions. T: magnetic transition. Black dots: superparamagnetic nanoparticles. Yellow ellipses: projections of polymer thin films. (e) Dark-field optical image of nanoparticle arrays assembled on a coupon. (f) Polymer film containing patterned nanoparticles after peeling. (g) Dark-field optical image of the black square in (f) showing the assembled nanoparticle grating lines embedded in the polymer film.

error bars (σ) are obtained via

$$\sigma = \frac{L\delta N}{N^2}, \tag{3.1}$$

where N is the average groove number within the 50 μm patterned regions and δN is the standard deviation in N measurements. For peeled patterns, $N = 66.4$ and $\delta N = 1.03$. As no nanoparticles are observed on the coupon after peeling, and with the same pattern spacing after transfer within experimental error, this approach yields near-perfect transfer of the assembled grating from the coupon to the film.

3.1.3 Alternative Methods for Removing fluid off Coupon Surfaces

In addition to using slow tilting to remove the remaining fluid on the coupon by a slow tilting, other methods include a water rinse (WR), and stirring + WR. Table 3.1 lists experimental results obtained using these methods. In these experiments, both perpendicular and longitudinal magnetic media, and three kinds of nanoparticle suspensions are employed. One is the "EMG" nanoparticle suspension, created by diluting 10 μL stock solution of commercial ferrofluid (Ferrotec, Nashua, NH, EMG-707) with 20 mL deionized (DI) water. The EMG ferrofluid has a 0.001% volume concentration of $\sim$13 nm diameter Fe_3O_4 nanoparticles. The second is a filtered EMG suspension, which is made by filtering the EMG suspensions with a VWR syringe filter containing 200 nm polytetrafluoroethylene membrane. The third is a nanoparticle suspension ("mixture") that is generated by mixing 2 mL EMG suspensions with 87.5 uL phosphate buffer saline (PBS). PBS is a buffer solution commonly used in biology research. It is a water-based salt solution containing sodium chloride, sodium phosphate, potassium chloride and potassium phosphate. The buffer's phosphate groups help to maintain a constant pH. The ion concentrations of the solution usually match those of the human body. The reason for using the PBS will be clear shortly.

The "Med." column denotes which magnetic medium is used, where P and L abbreviate perpendicular and longitudinal medium respectively. The "Method" column indicates the method that is employed. WR represents the nanoparticle suspension is

Table 3.1 Experimental results for self-assembling nanoparticles onto the magnetic medium surface using different methods. Med.: abbreviation for medium. P: perpendicular magnetic medium. L: longitudinal magnetic medium. EMG: dilute EMG 707 suspension. Mixture: 2 mL EMG suspension mixed with 87.5uL PBS. WR: Water Rinse.

Run	Med.	Time	Suspension	Method	Image	Results
1	P	200s	Mixture	WR	SEM	Yes, Clean
2	L	200s	Mixture	WR	SEM	Yes, Clean
3	P	200s	EMG	WR	DF	No
4	L	200s	EMG	WR	DF	No
5	L	200s	EMG	Tilting	DF	No, 3 droplets
6	L	200s	EMG	WR	DF	No, 1 droplet
7	L	200s	Mixture	WR	DF	Yes, Clean
8	L	15min	EMG	WR	DF	No, 2 droplets
9	L	20min	EMG	WR	DF	No, 4 droplets
10	L	60s	Mixture	WR	DF+SEM	Yes, Clean
11	P	60s	Mixture	Stirring+WR	DF+SEM	Yes, Clean
12	L	15min	Mixture	Tilting	SEM	Yes, Fairly Dirty
13	P	15min	Mixture	Tilting	SEM	Yes, Dirty
14	L	15min	EMG	Tilting	SEM	Yes, Fairly Dirty
15	L	15min	EMG	Tilting	SEM	Yes, Fairly Dirty
16	L	15min	EMG	WR	SEM	No, 1 droplet

pipetted onto the coupon. After a length of coating time, most of the fluid remaining on the coupon is removed by vacuuming the fluid off with a pipette. Then the coupon is rinsed with DI water for 30 s and dried in a clean hood. "Stirring + WR" means the coupon is dipped and stirred in the nanoparticle suspension. After a coating time, the coupon is taken out of the suspension and a WR procedure is followed. The "Image" column illustrates how the self-assembled patterns are observed. DF and SEM denote dark-field optical imaging and scanning electron microscopy respectively. In the "Results" column, "yes" indicates nanoparticle patterns are observed on the coupon. "Droplets" means the coupon surface mainly has no patterns of nanoparticles except some small isolated areas (typically < 1 mm^2) that originate from the fluid droplets remaining on the surface as shown in figure 3.2. These two droplets are obtained in run 8. For the WR method and EMG suspension, both longitudinal and perpendicu-
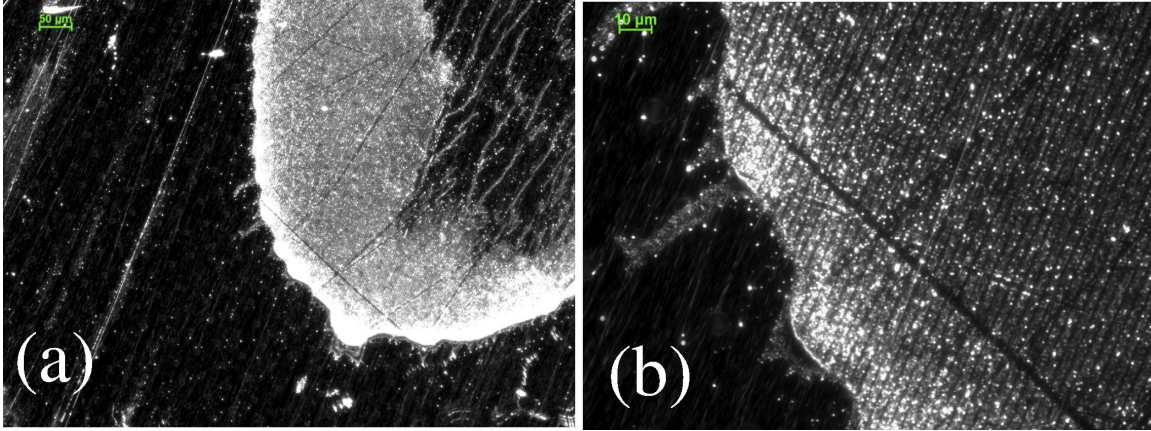
Figure 3.2 Two representative dark-field optical images, illustrating droplets that remain on the coupon surface after nanoparticle coating.

lar magnetic media do not generate patterns on the medium surface. For the tilting method and EMG suspension, some runs create patterns, others do not. Another run is conducted to investigate the nanoparticle coating in a fluid cell for filtered EMG suspensions. A laser diffraction signal is detected from the nanoparticle grating as assembled on the magnetic medium that is located in a fluid cell (chapter 4 discusses this technique in detail). These filtered nanoparticles have a 50 nm hydrodynamic diameter with $\pm$ 10 nm standard deviation as determined by dynamic light scattering, and have the smallest hydrodynamic diameters among all suspensions used. These filters remove large aggregates of nanoparticles. This diffraction measurement shows filtered EMG nanoparticles are attracted onto the medium surface. Therefore, unfiltered EMG nanoparticles coat on the medium surface too. It is deduced experimental runs that do not produce patterns are because of the method used, i.e., the method removes the coated nanoparticles during processing. This indicates that, in general, EMG suspensions assemble, but do not stick well to the medium surface. Here patterns observed in droplets appear to originate from nanoparticles that remain in fluid droplets during the solvent evaporation, while the originally attracted nanoparticles are removed during the processing. All experiments performed with the mixture suspension show patterns, demonstrating nanoparticles in the mixture
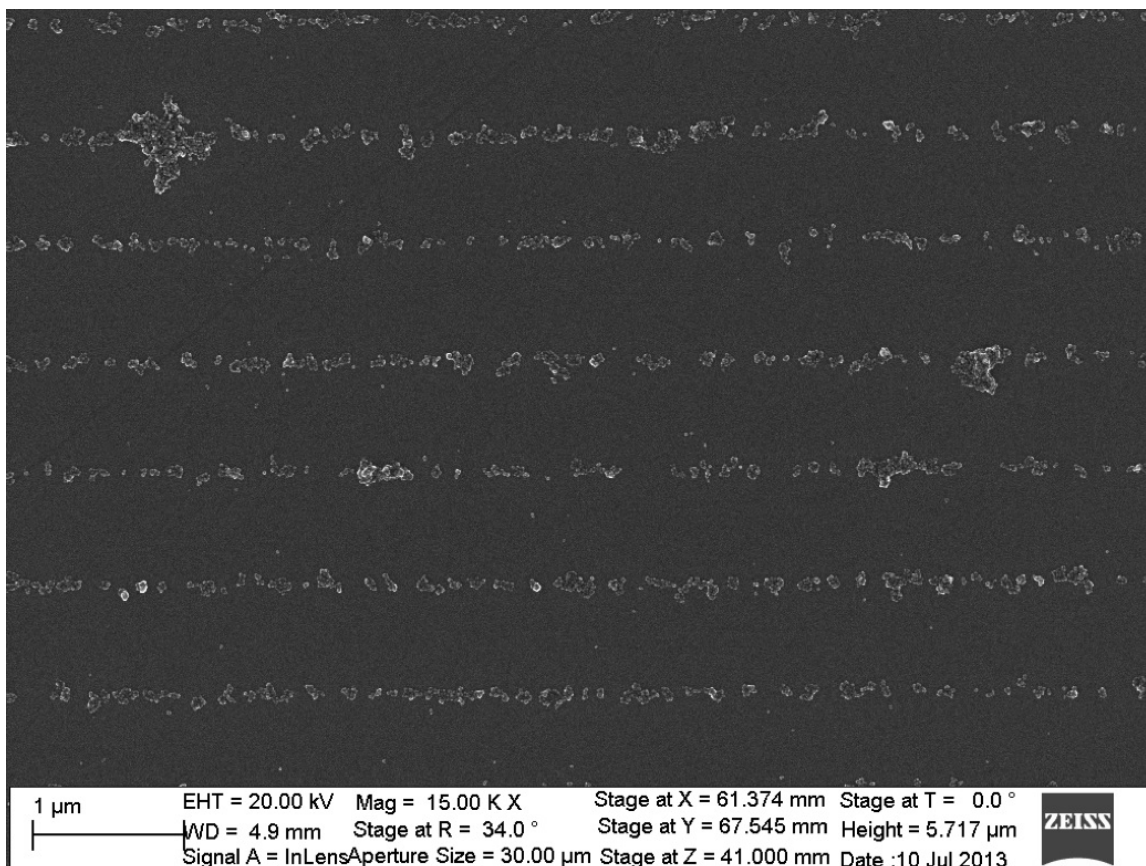
Figure 3.3   A representative SEM image for run 1.

suspension stick well to the coupon. For example, the disturbance occurring in the water rinse procedure removes coated particles from the EMG suspension, but not the mixture.

Figure 3.3 and 3.4 show representative SEM images of patterns that are created using the mixture suspension and tilting method. Note the pattern width in figure 3.4 is larger than that in figure 3.3, which is mainly caused by a longer coating time (900 s vs. 200 s). Figure 3.3 uses WR, while figure 3.4 doesn't. There are nanoparticles or nanoparticle aggregates existing between the grating lines, which may be called defects, in both figure 3.3 (rare) and 3.4 (plenty). Defects may originate from nanoparticles that remain in the fluid during the tilting. These nanoparticles remain on the coupon surface randomly, since they are not attracted onto the grating
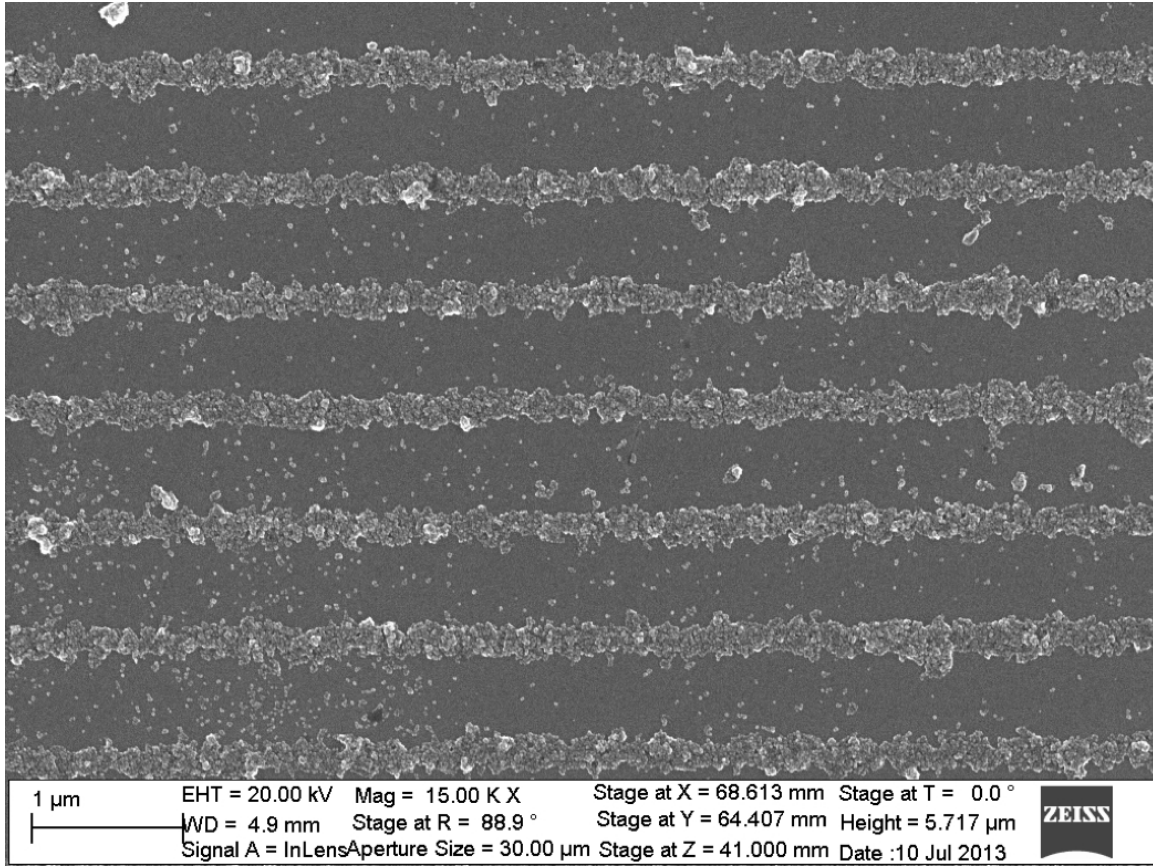
Figure 3.4   A representative SEM image for run 13.

lines (i.e., transitions) during the short drying time (in the order of 10 - 30 s). This problem does not occur in the water rinse method nearly, since the coupon is rinsed with the DI water before dying. The WR removes most nanoparticles that do not stick well on the surface. This demonstrates a WR leads to a clean grating fabrication.

3.2   Spectral Measurement and Calibration of Nanomanufactured Diffraction Gratings

This section discusses how these nanomanufactured diffraction gratings are characterized using an experimental apparatus built in the laboratory. The grating efficiency and spectral resolution of these gratings are also discussed.

3.2.1 Experimental Apparatus

Figure 3.5 demonstrates operation of our nanomanufactured gratings in an optical spectrograph. A grating is mounted on a rotation stage with the lines of nanoparticles in the y-z plane [front view in figure 3.5]. The rotation stage can orient the grating
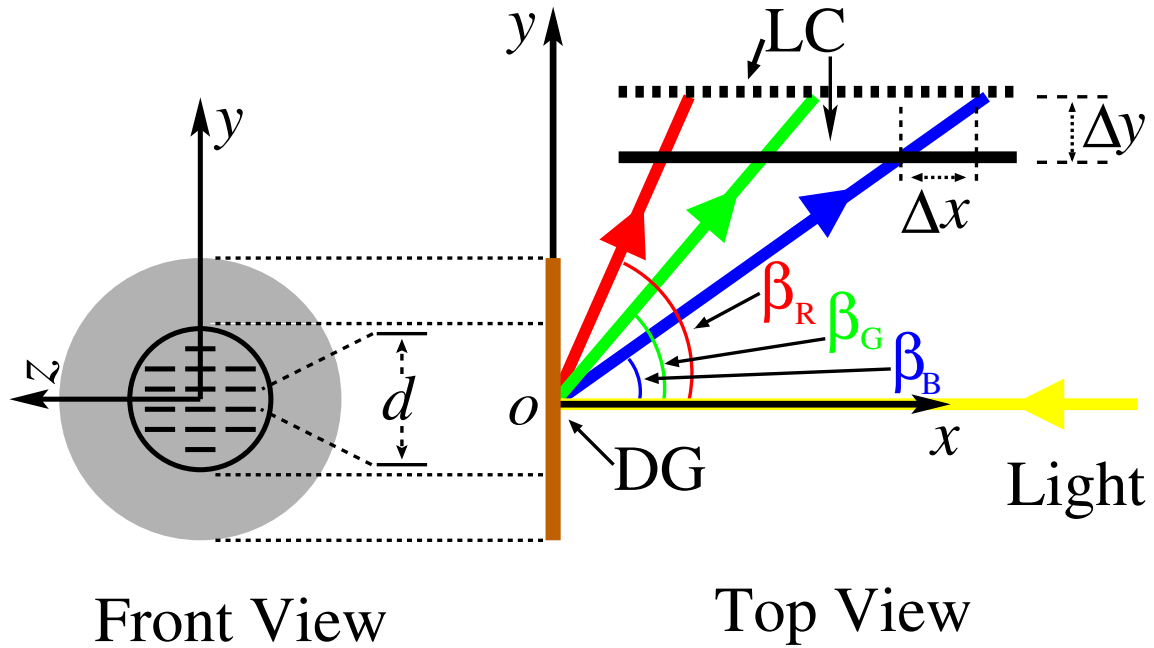
Figure 3.5   Schematic of experimental apparatus for Spectral measurements. Left panel: schematic diagram of polymer diffraction grating (DG) in front view. Right panel: schematic diagram of the measurement apparatus in top view. Light illuminates DG center (O) at normal incidence and diffraction spectra are recorded using a line camera (LC) in reflection mode. Red (green and blue) solid lines depict the diffracted red (green and blue) beam.

such that the nanoparticle lines are parallel to the z-axis. Diffraction spectra are obtained using the experimental geometry shown in figure 3.5 (Top View), with light incident onto the grating surface at normal incidence. Four optical sources [HeNe gas laser (632 nm), green (532 nm) and blue (405 nm) diode lasers and a tungsten-halogen bulb are aligned with the x-axis for illuminating the grating identically at the origin (O). A photodetector is used to monitor the intensity of laser transmission and verify power stability. A charge-coupled device (CCD) line camera (LC) is mounted on a

xy-translation stage. The LC incorporates a 3045 pixel CCD array (7 μm horizontal pixel size and ~21.3 mm long in total) with 350 - 1100 nm spectral range. For all spectral measurements the pixel line array is parallel to the *x*-axis and vertically aligned to be in the same plane as the incident light.
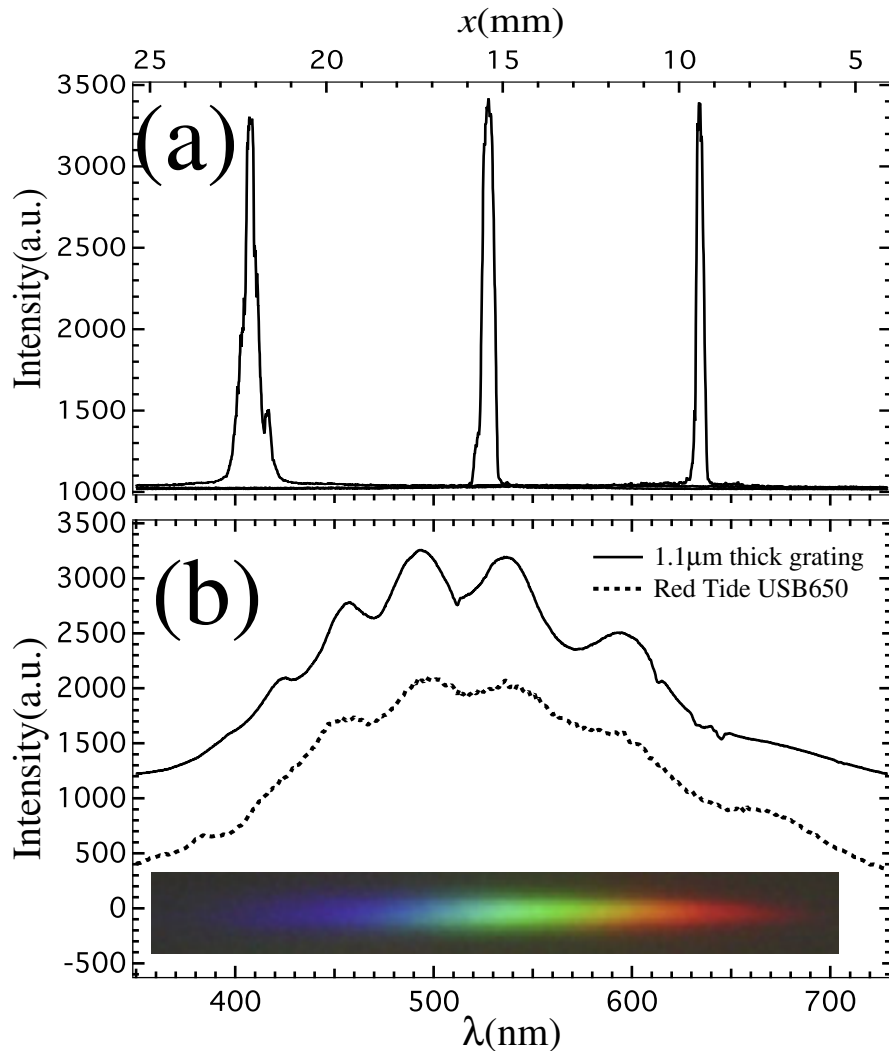
Figure 3.6 Representative spectra measured from a nanomanufactured diffraction grating in reflection mode. (a) Diffraction spectra of 405 nm, 532 nm and 632 nm lasers that are used to calibrate the diffraction grating spectrum (LC is at $x = 4.0$ mm and $y = 13.7$ mm). Top axis denotes LC pixel positions, and bottom axis calibrated to yield wavelength in nm. (b) Solid line: diffraction spectrum for a tungsten-halogen bulb measured with a 1.1 μm thick grating. Dotted line: diffraction spectrum for the tungsten-halogen bulb measured with a commercial spectrometer. Inset: photograph of tungsten-halogen spectrum measured with the 1.1 μm thick grating.

3.2.2 Results of Spectral Measurements

Figure 3.6(a) shows representative first-order diffraction spectra for a 1.1 μm thick polymer grating for 405, 532, and 632 nm laser lines, which are employed for calibrating the spectrograph. The calibration is performed by finding the angle of diffraction for the three reference laser lines as follows. The LC is translated by a known Δy and the corresponding peak position shift Δx is recorded. This calculation for the three lines is performed to determine absolute x and y positions of LC pixels. Both absolute and relative x and y LC positions are related to the angle of diffraction β, via

$$\tan \beta = \frac{\Delta y}{\Delta x} = \frac{y}{x}. \tag{3.2}$$

The diffraction angle is related to grating spacing and wavelength by the diffraction grating equation [172]

$$d(\sin \alpha + \sin \beta) = m\lambda, \tag{3.3}$$

where α is the incident angle, $= 0$ in our geometry, λ is the wavelength and m is the order number, $= 1$. λ is fitted as a function of β obtaining $d = 770 \pm 10$ nm. This result agrees within error bars with the 50 μm scale bar measurements discussed in section 3.1.2. Using $y = 13.7$ mm and $d = 770$ nm, Eq. (3.2) and Eq. (3.3) allow us to convert an arbitrary x-position on the LC into units of wavelength to generate the lower axis in figure 3.6(a)-3.6(b). The error in this spectral calibration is $\sim$13 nm, which is calculated using the pixel positions that correspond to the 550 nm center wavelength of our detection window. This 13 nm error arises from combining the 10 nm uncertainty in our measurement of d with 7 μm and 12 μm uncertainties in LC pixel position and y-stage translation respectively. The solid line in figure 3.6(b) shows the diffraction spectrum for a tungsten-halogen bulb recorded with our spectrograph. Five peaks at $\sim$425 nm, 455 nm, 495 nm, 535 nm, and 595 nm are

57

observed. The inset to figure 3.6(b) shows a photograph of the tungsten-halogen spectrum displayed on a white card for reference. The diffraction spectrum for the tungsten-halogen bulb recorded with a commercial spectrometer (Ocean Optics, Red Tide USB650 with ∼2.0 nm optical resolution) is also shown [the dotted line in figure 3.6(b)] for comparison. The two spectra match closely, however the solid line peaks for the nanomanufactured grating are more prominent (∼2x).

3.2.3   Efficiency of Nanomanufactured Diffraction Grating

The absolute efficiency of these nanomanufactured gratings measured with the HeNe laser (10 mW) is $0.071 \pm 0.002\%$. An asymptotic theory predicts our gratings, assuming the lamellar grating with ∼88 nm groove width as determined by analyzing the line profile of high resolution scanning electron microscopy images and 30 nm groove depth, have a 0.45% absolute efficiency in first-order Littrow mounts for the HeNe laser [143]. While the measured absolute efficiency is only ∼16% of that predicted, the absolute efficiency can be enhanced by tuning the groove width to the pitch ratio [143]. Note that the gratings have no reflectivity enhancing layers and still the diffracted signal is easily detected with our CCD line camera. By sputtering 20 nm of Au on a grating, an order of magnitude efficiency improvement is achieved, suggesting that further optimization of the fabrication process could yield better diffraction efficiency.

3.3   Concave Diffraction Gratings

3.3.1   Curvature Measurements and Control

While calibrating the spectra discussed above, a y-translation also causes a change in spectral peak intensity and width. Figure 3.7 shows a representative set of diffraction peaks on the LC during a series of y translations using the 532 nm laser. Starting at x

= 6 mm, the peak intensity first increases until $x = 12.7$ mm and then decreases until $x = 18.5$ mm. Similarly the spectral width decreases and then increases as x increases with the minimum peak width corresponding to the maximum intensity. Figure 3.7 labels the corresponding y-position in millimeters above each peak. Changing peak intensity and width as a function of x and y lead to the hypothesis that the grating is focusing the spectrum, and that our gratings are not planar but concave. As the LC records a projection parallel to the incident beam and β remains the same regardless of LC position, the peak center position is accurately detected by the LC. Therefore,
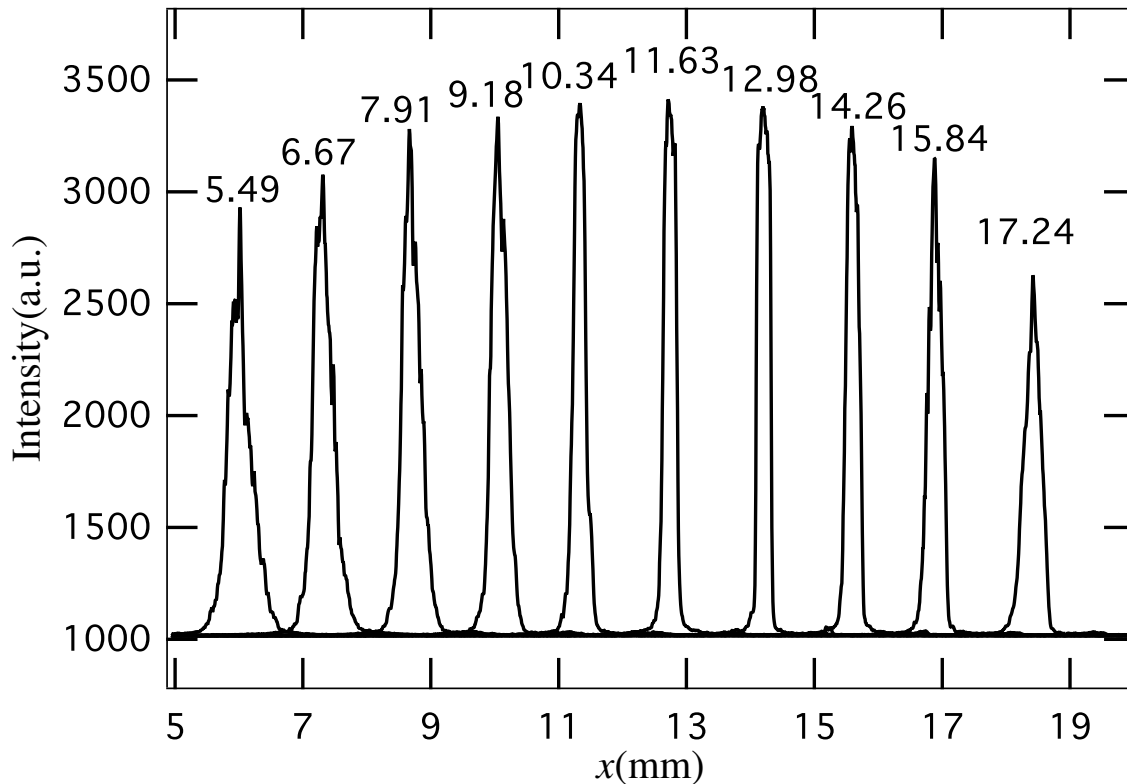
Figure 3.7   Representative 532 nm laser diffraction spectra obtained from nanomanufactured concave gratings demonstrating the grating is concave. The spectra are recorded while translating the LC in the y direction demonstrate changes in both peak intensity x-position (bottom axis) and width (corresponding y positions in millimeters are shown above each peak).

the spectral focus as a function of x and y can be precisely obtained by recording spectral profiles while translating the y stage. This measurement configuration is

known as the Wadsworth geometry [230, 45].

Figure 3.8 shows a concave grating geometry, where the origin O of the Cartesian system is at the center of the grating, the x-axis is the grating normal and the z-axis is parallel to the grating grooves. As for the plane grating, the light path difference for neighboring grooves must be an integral multiple of λ so that the diffracted waves are in phase. The light path difference for any two grooves of the concave grating separated by w is $(w/d)m\lambda$. Thus for light from point $A(x_0, y_0, z_0)$ with incident angle α on any point $P(u, w, l)$ of the concave grating, where w/d is an integral number, forms a spectral image at point $B(x, y, z)$ with diffraction angle β, light has
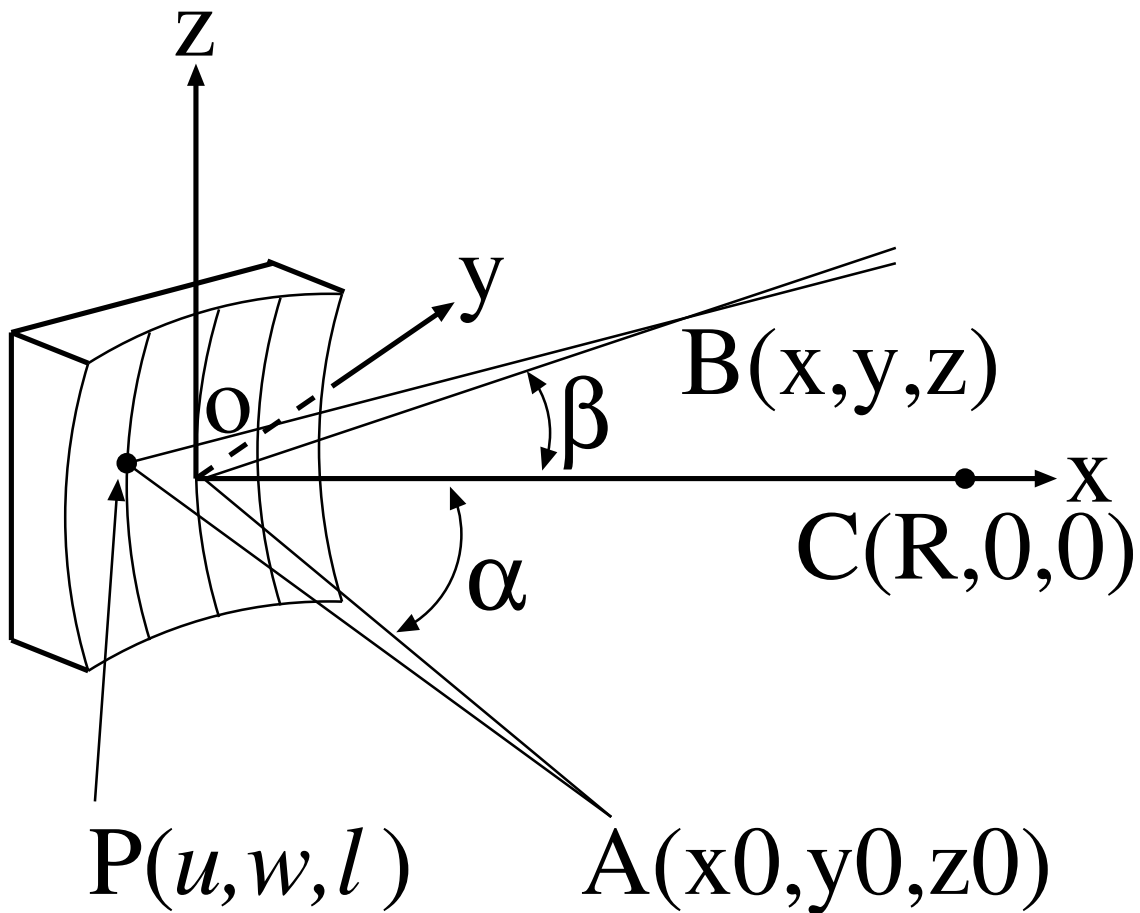
Figure 3.8   Schematic diagram of an optical system showing image formation with a concave grating.

to satisfy the light path function (F) [163]

$$F = <AP> + <PB> + \frac{mw\lambda}{d}, \qquad (3.4)$$

where $<AP>$ ($<PB>$) is the distance between points A and P (P and B). According to Fermat's principle of least time, point B is located such that F is an extreme for any point, P, and all extremes for focusing light from A at B must be equal[163]. Thus the condition for focusing light that diffracts from grating points along w [i.e., y direction in figure 3.8] is

$$\frac{\partial F}{\partial w} = 0. \qquad (3.5)$$

Since the LC pixel array records spectra only along the x-axis, one expands Eq. (3.4) in a series with respect to w [163], and inserts Eq. (3.4) into Eq. (3.5) using $\alpha = 0$ and $<AP> = \infty$ (Wadsworth geometry). Ignoring orders above first in w [163], one finds y as a function of x and for convenience this function is expressed in terms of y and β using Eq. (3.2)

$$y = R \frac{\sin\beta\cos^2\beta}{1 + \cos\beta}, \qquad (3.6)$$

where R is the radius of curvature of the grating.

Eleven gratings, 3 are 0.45 μm thick, 5 are 1.1 μm thick, and 3 are 6.25 μm thick, are nanomanufactured. Their focal positions measured with 632 nm, 532 nm, and 405 nm lasers are shown in figure 3.9 as triangles, dots, and crosses for each thickness respectively. These data are then fitted with Eq. (3.6) obtaining $R = 43.1 \pm 0.7$ mm, 57.1 ± 1 mm, and 71.6 ± 0.8 mm for 0.45 μm, 1.1 μm, and 6.25 μm thick gratings respectively [solid lines in figure 3.9]. Thicker films have larger radii of curvature, meaning the films are flatter, while thinner films have smaller radii of curvature, meaning the films are more curved [inset to figure 3.9]. The focal positions of the images diffracted by these three different curvatures as indicated in figure 3.9 show nearly equal diffraction angles [β in Eq. (3.3)] for each laser. This result further

61
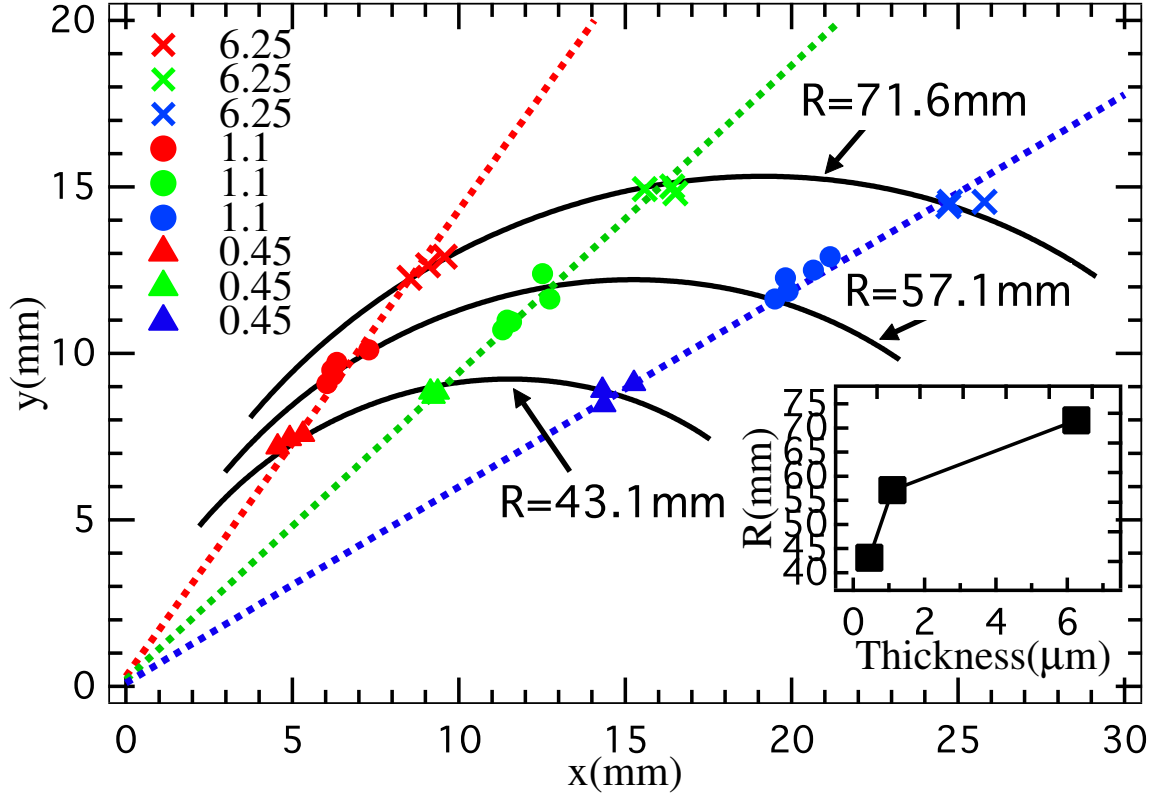
Figure 3.9 Curvature inherent in our nanomanufactured concave gratings. Red, green and blue dots (crosses and triangles) show focal positions for 632 nm, 532 nm and 405 nm lasers respectively. Polymer film thicknesses are indicated in the legend. Three solid lines show fitted trajectories of focal positions for the three grating thicknesses with fitted radii of curvature, R, as indicated. Red (green and blue) dashed lines display linear fits of diffraction angles for the 632, 532, and 405 nm lasers. Inset: R vs grating thickness.

confirms that our gratings have nearly identical spacings for differing polymer film curvatures [dotted lines drawn along a constant angle in figure 3.9]. Further, the zeroth-order term of an expansion of F with respect to w leads to the diffraction grating equation [i.e. Eq. (3.3)], demonstrating that grating curvature does not affect the diffraction angle, only the focused spectrum position. The nearly identical spacings and $< 2\%$ variations in R measurements show these nanomanufactured gratings are highly reproducible. These measurements demonstrate that not only does our nanomanufacturing process create repeatable concave gratings, but also

allows control of the radius of curvature. This inherent curvature eliminates a second curved mirror that is found in the Czerny-Turner [197], Ebert-Fastie [51], and Littrow monochromators [150].

3.3.2 Spectral Resolution of Nanomanufactured Diffraction Gratings

The spectral bandpass (B_S) of our concave grating spectroscopic system in the Wadsworth geometry is imaging limited, since there is no entrance slit and the line camera pixel size is 7μm,

$$B_S = P_F W_S, \tag{3.7}$$

where P_F and W_S are the plate factor for concave gratings and the entrance slit width respectively[169]. Using 0.65 mm for our entrance slit, i.e. $W_S = 0.65$ mm, and with ~2 x 2 mm^2 grating size, i.e. much smaller than R, the Rowland circle concave grating P_F [131] with an extra factor of $\sin\beta$ to account for the orientation of the LC pixels parallel to the x-axis is employed. Thus one has

$$B_S = \frac{dW_S \cos\beta \sin\beta}{mR}. \tag{3.8}$$

For 57.1 mm radius gratings, Eq. (3.8) predicts $B_S = 4.1$ nm for the HeNe laser, and the measured FWHM of the HeNe diffraction peak is 4.2 nm, i.e. suggesting our measured resolution agrees closely with that predicted for our particular imaging geometry. The measured and predicted resolutions agree closely for all three radii of curvature.

3.4 Repeatability of Nanomanufactured Diffraction Gratings

Figure 3.10(a) shows tungsten-halogen spectra for 5 nominally identical 1.1 μm thick polymer film gratings. The spectra are plotted with a vertical offset for clarity. Concave gratings focus different wavelength light at different y positions, and therefore
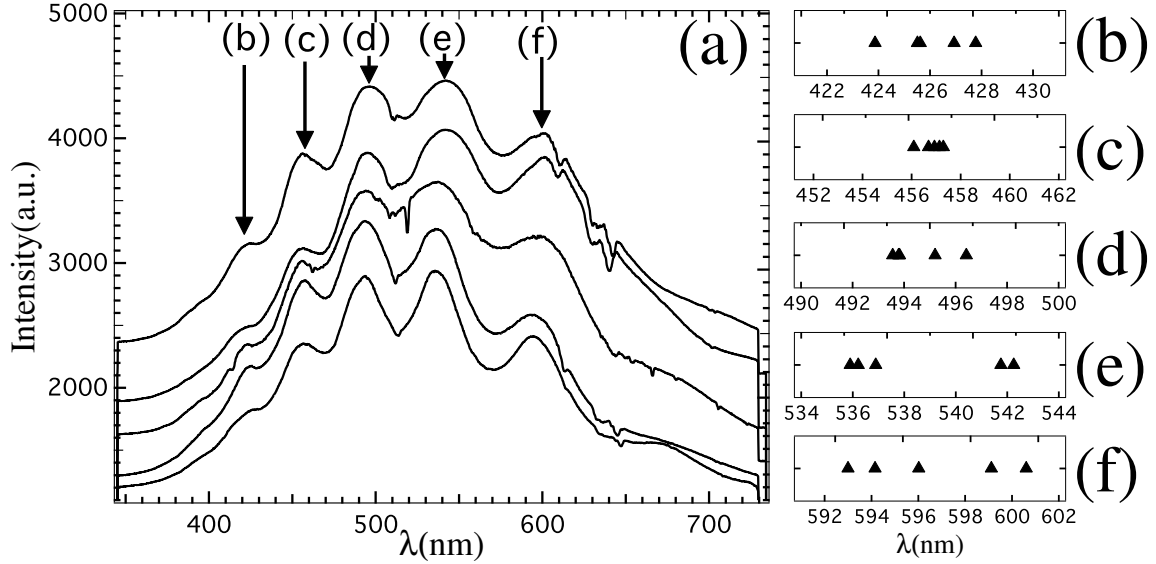
Figure 3.10   Repeatability of tungsten-halogen spectra. (a) Tungsten-halogen spectra obtained from 5 nominally identical 1.1 μm thick concave gratings. All spectra have 5 peaks and show similar spectral peak positions, demonstrating the high repeatability of tungsten-halogen spectra. (b)-(f) 10 nm peak-peak dot plot showing fitted peak positions for 5 gratings, demonstrating ∼ 3 nm average standard deviation.

spectra recorded on the LC are not linearly scaled with respect to y. For the 532 nm laser the diffraction foci for these 5 gratings are slightly different, and therefore tungsten-halogen spectra are recorded with the LC located at the average position, y = 11.33 mm. Each spectrum has 5 peaks, and each peak's position is fitted using the Lorentzian function [44], as displayed in figure. 3.10(b)-3.10(f). Figure 3.10(b) shows that the first peak of 5 identical gratings occurs at nearly the same spectral position with <10 nm variation. Figure 3.10(c)-3.10(f) show almost same behavior as Fig. 3.10(b) with ∼ 3 nm average standard deviation. Thus multiple grating studies both for differing radii of curvature and of tungsten-halogen spectra together demonstrate that our nanomanufacturing process is highly repeatable.

The polymer film curvature can be observed under optical microscopy. Figure 3.11 shows a representative dark-field optical image of grating lines embedded in a polymer film. After focusing on the center part of the patterns in the polymer film, outer parts appear slightly out of focus, demonstrating the polymer film is not planar, but curved. This curvature may occur during the peeling process as the outer portion of the
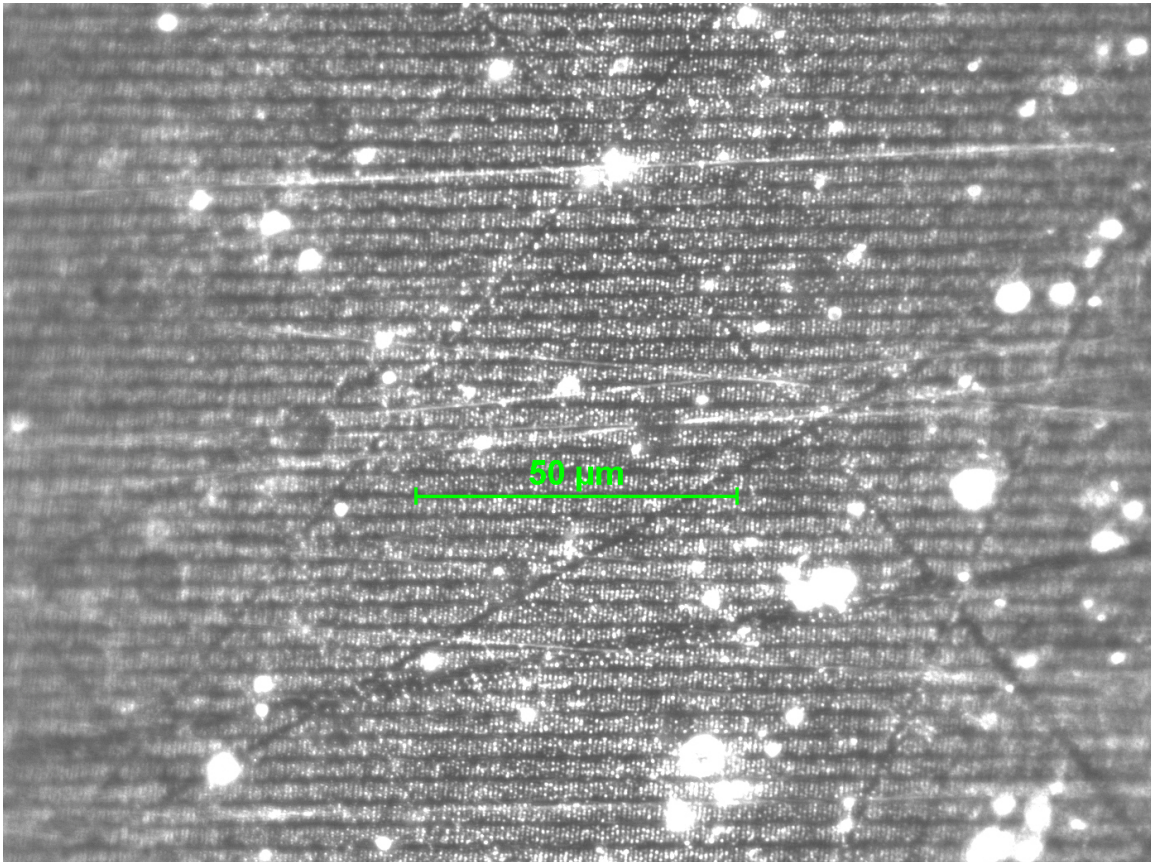
Figure 3.11   A dark-field optical image of grating lines embedded in a polymer film demonstrating the film curvature.

polymer film is attached to the tape, but not the inner portion. The peeling enlarges slightly the inner portion. After the polymer film is peeled off from the coupon surface, the enlarged portion relaxes into a curved film. Local curvatures may not occur because the polymer film is thin (on the order of a few microns) and possesses

a stress relaxation property [208] [198]. If local curvatures occur, the curvature radii of multiple polymer films will not be same. This would produce measurement data with much larger error bars than those as shown in figure 3.9. Therefore, the polymer film can be treated as concave and the experimental apparatus as shown in figure 3.5 is approximate to the Wadsworth configuration.

CHAPTER 4

REAL TIME MONITORING OF SUPERPARAMAGNETIC

NANOPARTICLE SELF-ASSEMBLY ON SURFACES OF

MAGNETIC RECORDING MEDIA

The previous chapter discussed the fabrication of all-nanopartice diffraction gratings using the field directed self-assembly and pattern transfer technology. However, the diffraction efficiency is lower than theoretically predicted, and a high efficiency diffraction grating is extremely important for its technological applications [169]. We need to better understand the nanoparticle self-assembly process to the improve the diffraction efficiency and the assembly and nanomanufacturing technology. In this chapter, I present evidence that the nanoparticle self-assembly dynamics can be monitored in real-time by detecting optical diffraction from the all-nanoparticle grating as it self-assembles on a grating pattern recorded on a magnetic medium located in a fluid cell. The nanoparticle self-assembly process can be highly tuned using knobs such as the particle pH and colloidal stability of nanoparticles [242].

4.1   EXPERIMENTAL

Figure 4.1 (a) shows a schematic of the fluid cell ($\sim 25 \times 15 \times 0.5$ mm^3) with a glass window to provide optical access. To provide better understanding, a photograph of a real fluid cell is also shown in figure 4.2 (a). The fluid cell is made by milling a piece of acrylic sheet (a Personal CNC milling machine is used). Six tapped holes are used to hold a piece of glass slide ($\sim 35 \times 25 \times 1$ mm^3) on top of the fluid cell. The
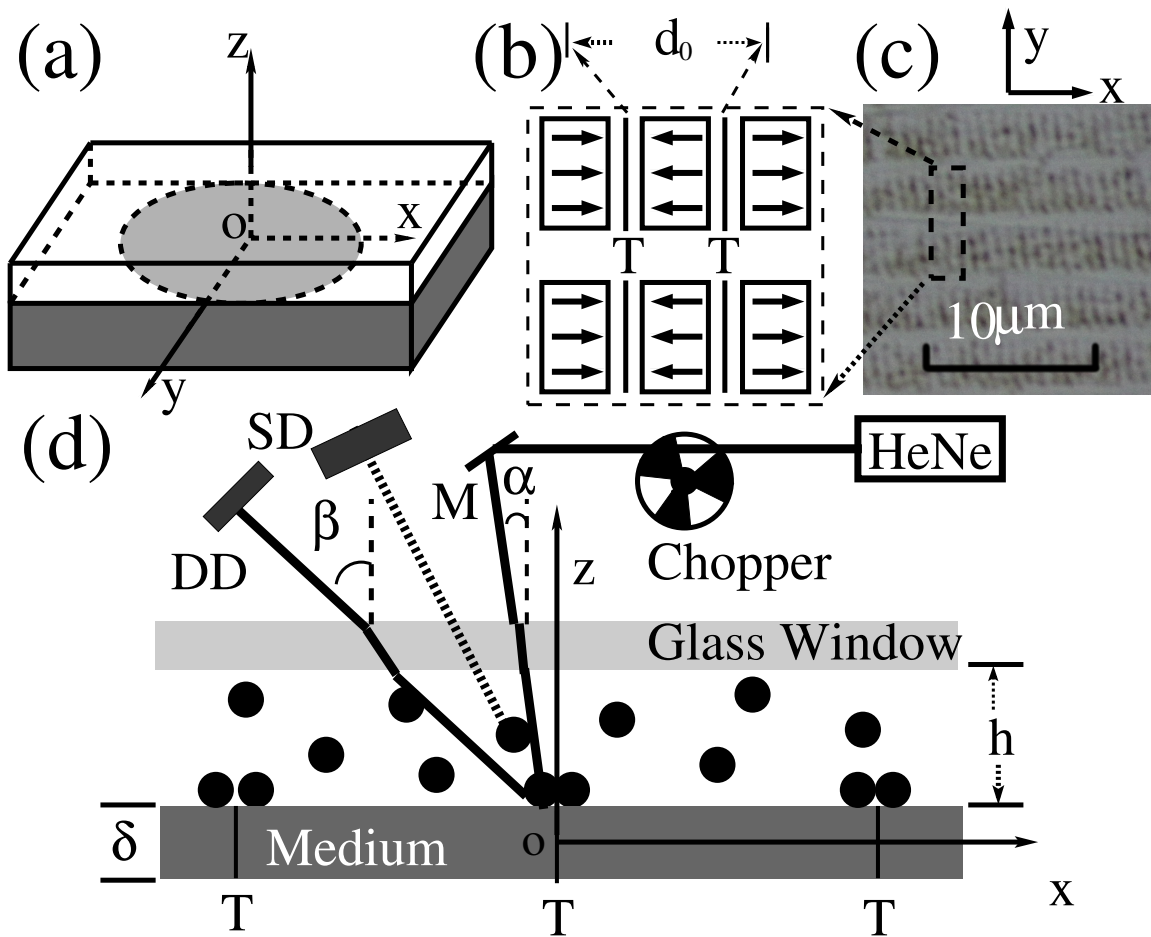
Figure 4.1   (a) Schematic of the fluid cell. (b) Schematic of magnetic patterns and transitions. Arrows: magnetization directions. (c) Dark-field optical image of grating lines. (d) Experimental apparatus and signal detection method. M: mirror.
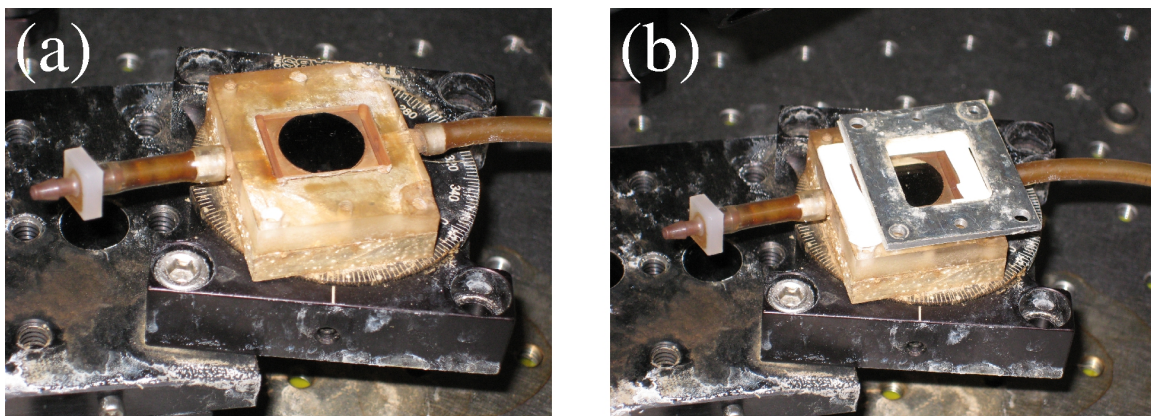
Figure 4.2   (a) Photograph of a real fluid cell. (b) Photograph of the fluid cell with a glass slide and top cover.

edge of the glass slide on both sides is wrapped with two layers of Teflon tape to seal the fluid cell [figure 4.2 (b)]. A 15 mm diameter longitudinal disk drive medium with thickness δ is located at the bottom of the cell and has $\sim$0.5 mm vertical distance (h) to the glass window bottom [figure 4.1 (d)].

Oppositely magnetized and interchanged pattern (i.e.,"bit") arrays with a width (d_0) were magnetically recorded on the medium [figure 4.1 (b)]. Ultrahigh field gradients exist above transitions ["T" in figure 4.1 (b)]. Colloidally suspended superparamagnetic nanoparticles in the fluid above the medium surface are magnetized and attracted onto the transitions yielding patterned arrays, i.e, an all-nanoparticle diffraction grating with grating spacing d_0. Figure 4.1 (c) shows a dark-field optical image of grating lines (along the y axis). These magnetic pattern arrays have a total area of $\sim 2 \times 2$ mm^2.

Dilute suspensions of magnetic nanoparticles are injected into the fluid cell by a syringe pump and the fluid stops flowing immediately after the fluid is pumped into the whole fluid cell (figure 4.2). An all-nanoparticle grating then self-assembles on the magnetic medium surface [figure 4.1 (d)]. A HeNe laser (wavelength $\lambda = 632.8$nm) is incident on the grating with a $\sim 5°$ angle (α) to avoid multiple light reflections between the glass window and disk drive. The diffraction angle β is related to d_0 and λ by the diffraction grating equation [91]

$$\mathrm{m}\lambda = \mathrm{d}_0(\sin\alpha + \sin\beta), \qquad (4.1)$$

where m is the diffraction order. The grating spacing d_0 is 750 nm, which has been verified by optical measurements on nanoparticle patterned arrays. A photodetector (DD), located in the x-z plane, is used to measure the first order diffraction, i.e., m = 1 and hence $\beta \sim 49°$. A second photodetector (SD), located in the y-z plane, is also employed to measure the laser scattering from the cell. The DD (SD) is $\sim$7 cm (5cm) away from the laser spot in the particle suspension. The laser beam is chopped at 2.5kHz and two lock-in amplifiers read the DD and SD outputs respectively with a

69
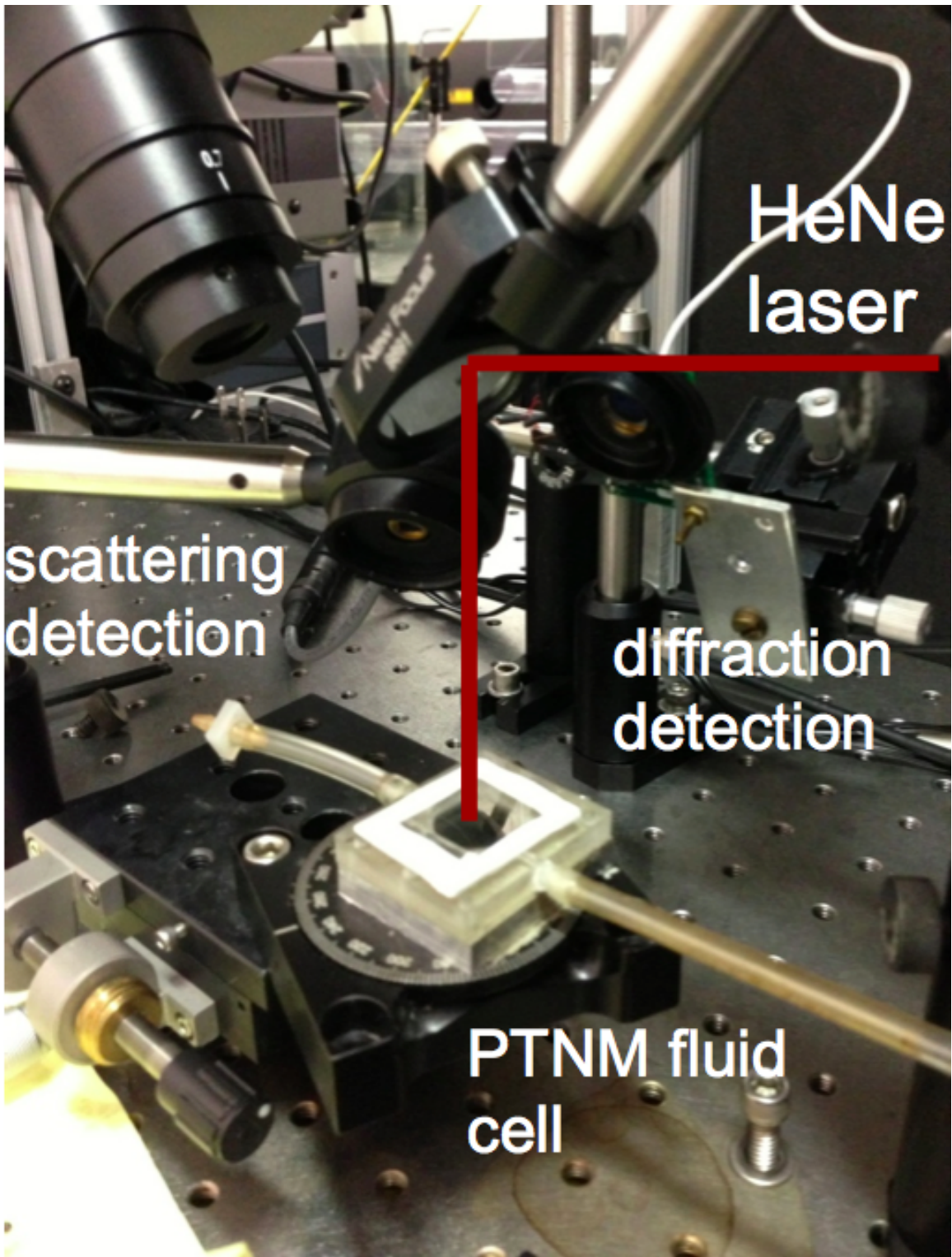
Figure 4.3 Photograph of the real experimental setup for real-time diffraction and scattering measurements.

10ms average time. Figure 4.3 shows a photograph of the real experimental apparatus. The fluid cell is mounted on a rotation stage that is stacked on a xy stage. The rotation stage, together with a video microscope (0.7 - 4.5x variable magnification) that monitors cross marks on the medium surface, is used to align grating lines with the laser beam. The xy stage is to locate the laser spot on the grating area.

4.2 Concentration, pH and Particle Size Dependence

First, we measure the light scattering (figure 4.4) and diffraction (figure 4.5) for nanoparticle suspensions with different concentrations and pHs. The light intensity that the DD monitors (I_d) includes the scattering from the cell ($I_{s,DD}$), and the first order diffraction ($I_{d,DD}$) from the grating. $I_{s,DD}$ is found to be linear with the scattering intensity that the SD detects ($I_{s,SD}$) and $I_{s,DD}/I_{s,SD} = 1.25 \pm 0.08$. Therefore, the diffraction intensity is calculated by subtracting the scattering signal from I_d via $I_{d,DD} = I_d - 1.25\ I_{s,SD}$. Note a $\sim 3\ \mu V$ scattering background from the cell containing no fluid is subtracted in all measurements. Figure 4.4 and 4.5 (a) show the scattering and first order diffraction as a function of time t up to 10 minutes for 4 particle suspensions (C1, C0.5, C0.25, C0.125) with relative concentrations 1, 0.5, 0.25 and 0.125 respectively. C1 has a 0.002% volume concentration of nanoparticles. These suspensions are created by diluting stock solutions of a commercial ferrofluid (Ferrotec, Nashua, NH, EMG-707) with de-ionized (DI) water. The EMG-707 stock solution contains Fe_3O_4 nanoparticles with an average size of 13 nm diameter dispersed in DI water. The time for the fluid to start flowing over the laser spot is defined at $t = 0$. All curves have spikes that occur after 0 s and remain $\sim$ 3-5 s, which is caused by the laser scattering from the wave front of flowing fluids [inset1 to figure 4.4]. After the spike, $I_{s,SD}$ remains constant (figure 4.4) and the average $I_{s,SD}$ is a linear function of the suspension concentration [inset2 to figure 4.4]. As shown in figure 4.5 (a), the diffracted intensity increases monotonically with time. At the same

71
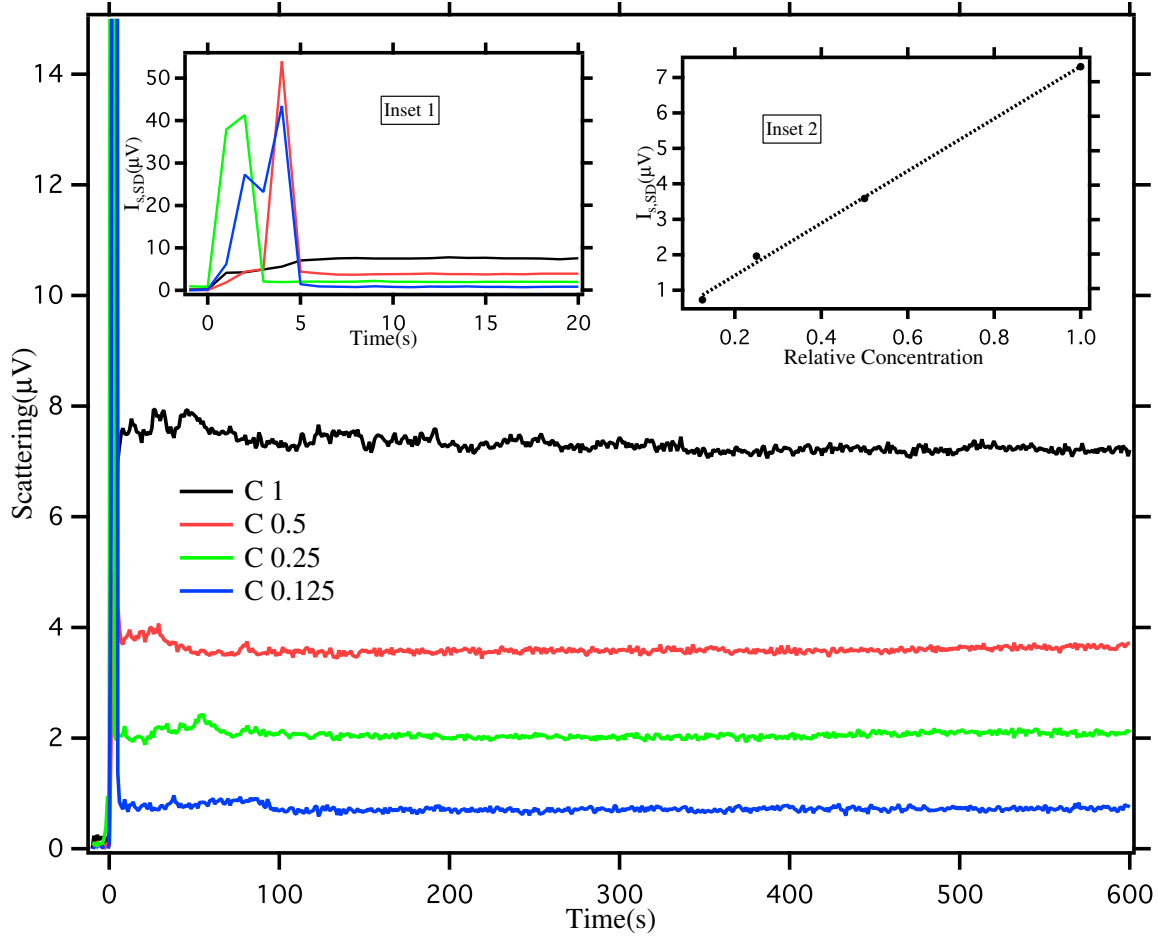
Figure 4.4 First order scattering vs time for different concentration particle suspensions. Inset 1: scattering signals showing spikes. Inset 2: scattering intensity vs particle concentration.

t, larger concentrations produce larger diffracted intensities (doubling concentration produces almost doubled $I_{d,dD}$ for $t > 100$s). Laser attenuation measurements on all suspensions used here show $< 10\%$ light attenuation, which can be ignored when comparing diffraction efficiencies.

Figure 4.5 (b) shows first order diffraction as a function of t for C0.5 at pH $=$ 7, 8, 9, 10 and 11. At the same t, we observe that as the pH value increases, $I_{d,DD}$ decreases and then increases [inset in figure 4.5 (b)]. In addition, at $t = 600$s, the pH7 suspension produces a $I_{d,DD}$ that is ~ 3 times larger than the pH9 suspension. Note we do not observe a similar pH dependence for average hydrodynamic diame-
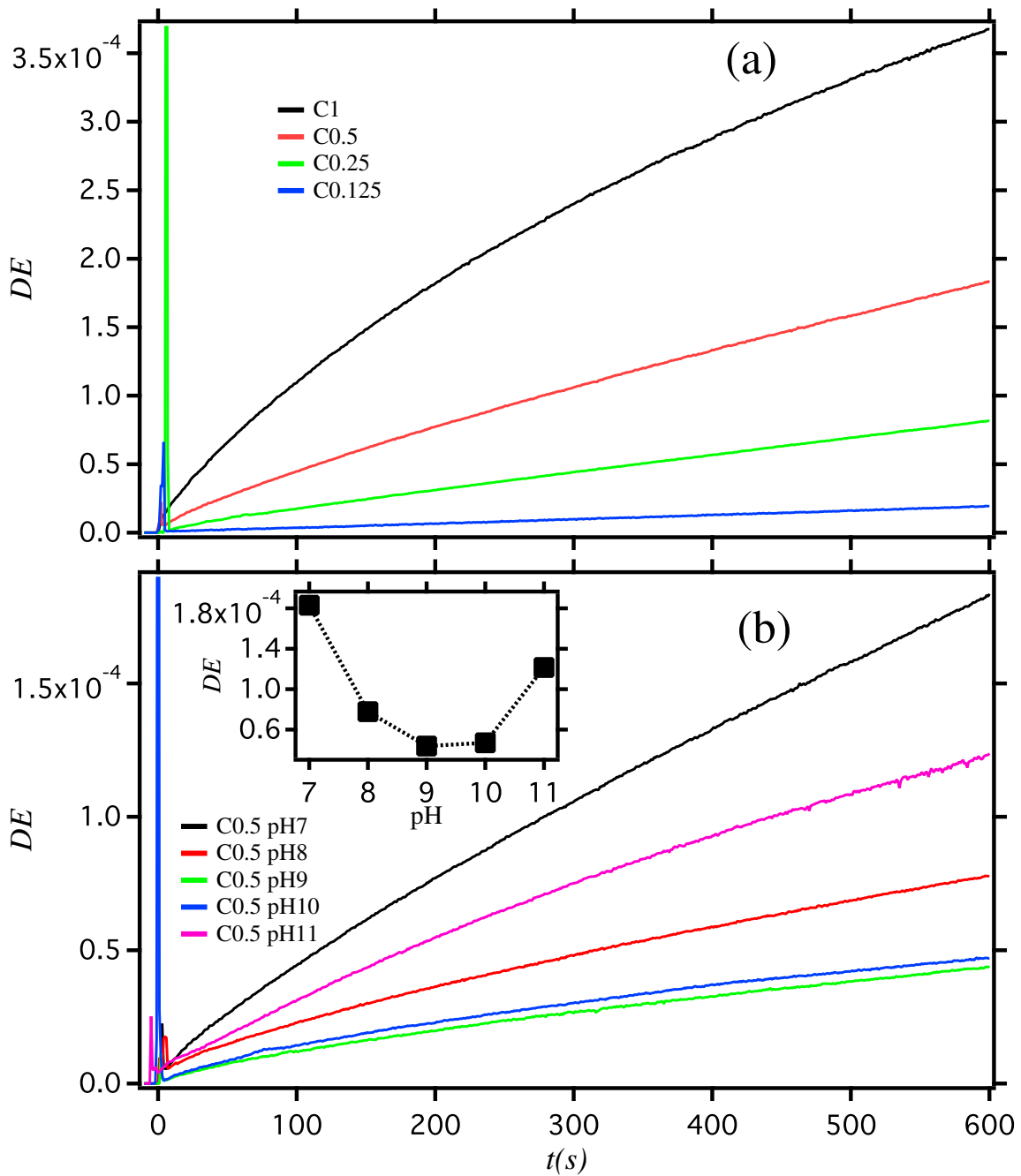
Figure 4.5 (a) First order diffraction vs time for different concentration particle suspensions. (b) First order diffraction vs time for different pH suspensions. Inset: diffraction at 600s vs pH.
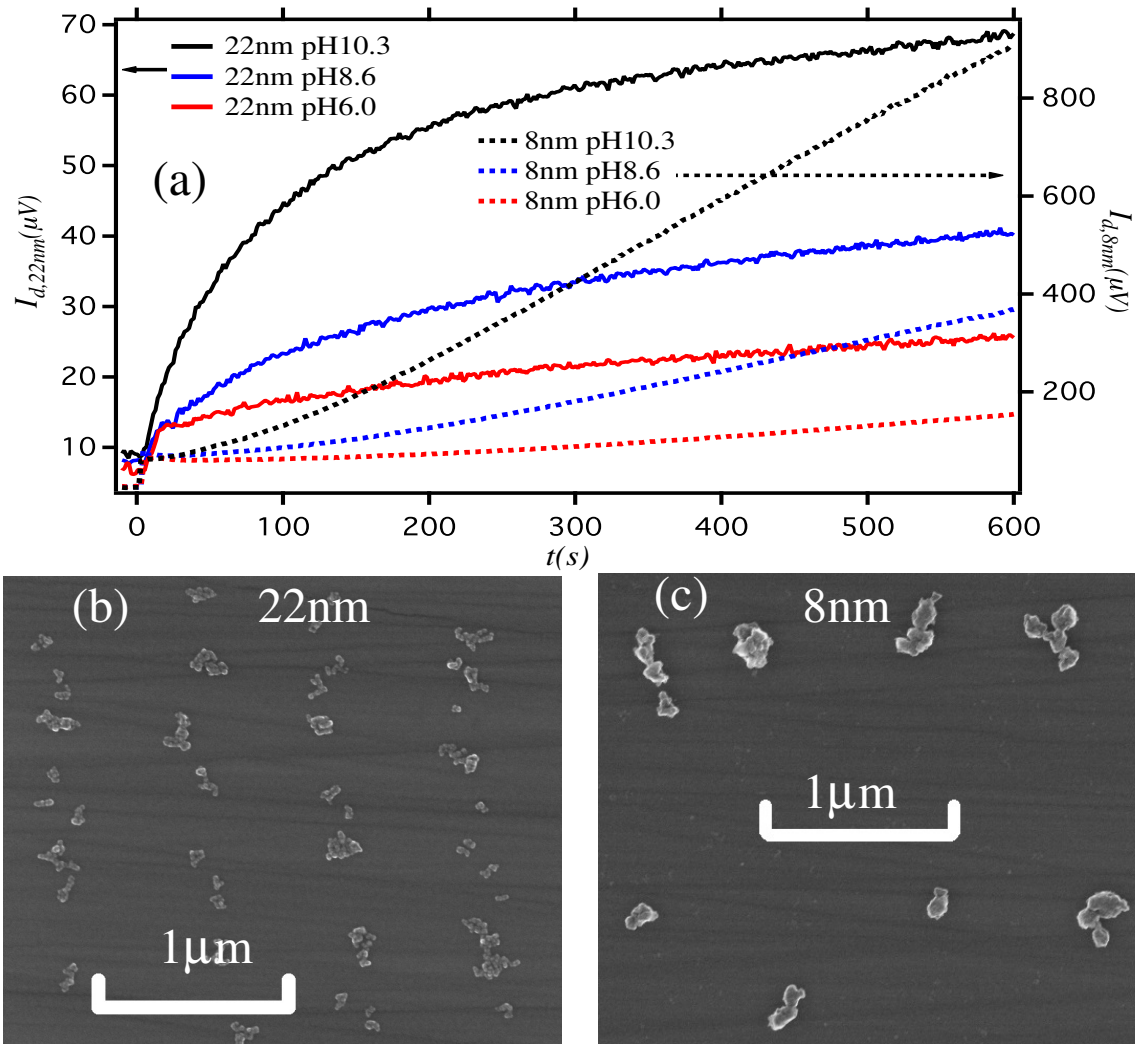
Figure 4.6 (a) First order diffraction vs time for different pHs, for 8nm and 22 nm core size nanoparticles. (b) and (c) SEM images of nanoparticle aggregates attracted on the magnetic medium that is dipped in the 8 nm and 22 nm particle suspensions respectively.

ters (d_{hydro}) of these nanoparticles. We determine d_{hydro} of these nanoparticles (i.e, the Z-average particle diameter) using a commercial dynamic light scattering (DLS) tool (Malvern, Zetasizer Nano ZS) and obtain hydrodynamic diameters between 95 - 125nm largely independent of pH. In these DLS measurements, correlation functions behaved reasonably and the software analysis converged properly to d_{hydro} that were largely independent of our suspension pH (in strong contrast to our diffraction intensity's dependence on the suspension pH).

Second, we measure light scattering and diffraction for nanoparticle suspensions with different core particle sizes and colloidal stabilities. Figure 4.6 (a) shows first order diffraction as a function of t for equal concentration suspensions with pH 6.0, 8.6 and 10.3, and made from 8 nm and 22 nm diameter nanoparticle species. These two nanoparticle suspensions are synthesized via thermal decomposition of iron oleate-oleic acid mixtures and then an oxidation procedure rendering these nanoparticles hydrophilic [175]. The 8 nm nanoparticles have significantly weaker colloidal stability as indicated by the larger d_{hydro} (250 nm vs 50 nm for the 22 nm nanoparticles). Both particles remain colloidally suspended over the timescale of measurements. For both particle species, pH makes strong impact on the diffracted signal and larger pHs yield larger diffraction intensities, which is a different behavior from that as shown in figure 4.5 (b). For the same pH and $t > 100$s, the 8 nm particles produce diffraction intensity 10 times larger than the 22 nm particles. Further, the 8 nm particles display dramatically different time dependence than both the 22 nm particles and EMG-707 particles. All 22 nm and EMG-707 particles [figure 4.5 and 4.6 (a)] display similar curve shapes which have negative curvatures [185]. However, 8 nm particles show "inverted" curve shapes, i.e., their curvatures are positive. Both 22 nm and EMG-707 particles have stronger colloidal stabilities than 8nm particles, as suggested by smaller d_{hydro} than 8nm particles (≤ 125 nm compared as 250nm for 8nm particles). This indicates large aggregates of particles with significantly weak colloidal stabilities yield the inverted curve shape. Figure 4.6 (b) and (c) show representative scanning electron microscopy (SEM) images of the 8 nm and 22 nm particles that are coated on the medium surface respectively. A statistical analysis of SEM images shows nanoparticle aggregates attracted from the 8 nm particle suspensions are more periodically distributed than those from the 22 nm particles. In addition, the 8 nm particles show significantly larger aggregates than the 22 nm particles. This further suggests that particle aggregation affects the time dependence of diffracted intensity.

While larger aggregates explain the 10 x difference in $I_{d,DD}$ between the two particle species, since particles scatter light with the intensity proportional to b^6 , where b is the particle diameter [115], it is not clear how the aggregation changes the curve shape. Likely it is due to the nanoparticle self-assembly process, not the diffraction.

4.3 INITIAL THEORETICAL CALCULATIONS

Particle transport in a magnetophoretic system (e.g., in the fluid cell) is governed by various forces including (a) the magnetic force due to all field sources, (b) viscous drag, (c) inertia, (d) gravity, (e) buoyancy, (f) thermal kinetics, (g) particle/fluid interactions (perturbations to the flow field), and (h) interparticle effects including (i) magnetic-dipole interactions, (ii) electric double-layer interactions, and (iii) van der Walls force [63] [64] [65]. For the nanoparticles used in the fluid cell, magnetic forces and viscous forces dominate, and all other effects can be ignored. However, it is instructive to estimate the magnitude of the other forces for this application. The gravitational (F_g) and buoyant (F_b) forces are respectively calculated as

$$F_g = \frac{4\rho\pi R_p^3 g}{3} \tag{4.2}$$

and

$$F_b = \frac{4\rho_f\pi R_p^3 g}{3}. \tag{4.3}$$

For a 10 nm diameter Fe_3O_4 particle ($R_p = 5$ nm) in water ($\rho = 5000\text{kg/m}^3$, $\rho_f = 1000$ kg/m3 , and $g = 9.8$ m/s). $F_g = 3 \times 10^{-5}$ fN and $F_b = 6 \times 10^{-6}$ fN are obtained, which are more than several orders of magnitude smaller than the magnetic force ($\sim$ 0.1 - several pN as shown in figure 2.19). The other forces can also be neglected, since the particle volume concentration is $\ll 1$.

Thus the nanoparticle transport is mainly governed by the magnetic ($\mathbf{F_m}$) and viscous drag force ($\mathbf{F_d}$). Since the fluid does not flow, the drag force can be calculated

as

$$\mathbf{F_d} = -6\pi\eta R_p \mathbf{v}, \tag{4.4}$$

using Stoke's law [8] [133], where $\mathbf{v}$ is the particle velocity and η is the viscosity of the fluid. The magnetic force ($\mathbf{F_m}$) is expressed as

$$\mathbf{F_m} = \mu_0 V_p (\mathbf{M_p} \cdot \nabla)\mathbf{H_a} \tag{4.5}$$

by inserting $\mathbf{m} = V_p \mathbf{M_p}$ in equation (4.5), where $\mathbf{H}_a$ is the magnetic field at the particle center, V_p and $\mathbf{M}_p$ are the particle volume and magnetization respectively. To determine the magnetic force $\mathbf{F_m}$, a linear magnetization model with saturation is employed to predict $\mathbf{M_p}$, in which $\mathbf{M_p}$ is a linear function of the field up to a saturation value $\mathbf{M_{sp}}$ [64] [65]. For a $|\mathbf{M_p}| < |\mathbf{M_{sp}}|$,

$$\mathbf{M_p} = \chi_p \mathbf{H_{in}}, \tag{4.6}$$

where μ_p and $\chi_p = \mu_p/\mu_0 - 1$ are permeability and susceptibility of the particle, and $\mathbf{H_{in}} = \mathbf{H_a} - \mathbf{H_{demag}}$, where $\mathbf{H_{demag}} = \mathbf{M_p}/3$ is the self-demagnetization field in the particle [77] [65]. If the particle is suspended in a magnetically linear fluid of permeability μ_f ($\chi_f = \mu_f/\mu_0 - 1$), the magnetic force is [108]

$$\mathbf{F_m} = \mu_f V_p \frac{3(\chi_p - \chi_f)(\mathbf{H_a} \cdot \nabla)\mathbf{H_a}}{(\chi_p - \chi_f) + 3(\chi_f + 1)}. \tag{4.7}$$

For a water based ferrofluid, $|\chi_f| \ll 1$, i.e. $\mu_f \approx \mu_0$, therefore, (4.7) reduces to

$$\mathbf{F_m} = \mu_0 V_p \frac{3(\chi_p - \chi_f)(\mathbf{H_a} \cdot \nabla)\mathbf{H_a}}{(\chi_p - \chi_f) + 3}, \tag{4.8}$$

and it also follows that

$$\mathbf{H_{in}} = \frac{3}{(\chi_p - \chi_f) + 3}\mathbf{H}_a, \tag{4.9}$$

and

$$\mathbf{M_p} = \frac{3(\chi_p - \chi_f)}{(\chi_p - \chi_f) + 3}\mathbf{H}_a. \tag{4.10}$$

Therefore, for an arbitrary $\mathbf{H}_a$,

$$\mathbf{M_p} = f(H_a)\mathbf{H}_a, \qquad (4.11)$$

where

$$f(H_a) = \begin{cases} \frac{(\chi_p - \chi_f) + 3}{3(\chi_p - \chi_f)}, & H_a < \frac{3(\chi_p - \chi_f)}{(\chi_p - \chi_f) + 3} M_{sp}, \\[2em] M_{sp}/H_a, & H_a \geq \frac{3(\chi_p - \chi_f)}{(\chi_p - \chi_f) + 3} M_{sp}, \end{cases} \qquad (4.12)$$

and $H_a = |\mathbf{H_a}|$.

The magnetic force can be decomposed into components, i.e.,

$$\mathbf{F_m}(x, z) = F_{mx}(x, z)\hat{x} + F_{mz}(x, z)\hat{z}, \qquad (4.13)$$

where

$$F_{mx}(x, z) = \mu_0 V_p f(H_a)\left[H_{ax}(x, z)\frac{\partial H_{ax}(x, z)}{\partial x} + H_{az}(x, z)\frac{\partial H_{ax}(x, z)}{\partial z}\right], \qquad (4.14)$$

and

$$F_{mz}(x, z) = \mu_0 V_p f(H_a)\left[H_{ax}(x, z)\frac{\partial H_{az}(x, z)}{\partial x} + H_{az}(x, z)\frac{\partial H_{az}(x, z)}{\partial z}\right], \qquad (4.15)$$

where

$$H_a = H_{ax}(x, z)\hat{x} + H_{az}(x, z)\hat{z}. \qquad (4.16)$$

$H_{ax}(x, z)$ and $H_{az}(x, z)$ above magnetic transitions of a longitudinal magnetic medium are given by equations (2.42) and (2.43) respectively. Note coordinates are shown in figure 2.15. Finally, particle trajectories can be calculated using Netwon's second law, i.e.,

$$m\frac{dv_x}{dt} = F_{mx}(x, z) - 6\pi\eta R_p v_x, \qquad (4.17)$$

and

$$m\frac{dv_z}{dt} = F_{mz}(x, z) - 6\pi\eta R_p v_z, \qquad (4.18)$$

where m is the particle mass, and

$$v_x = \frac{dx}{dt}, \qquad (4.19)$$

$$v_z = \frac{dz}{dt}. \tag{4.20}$$

Equations (4.17) and (4.18) constitute a coupled system of first-order differential equations that are solved subject to initial conditions for $x(0), z(0), v_x(0)$, and $v_z(0)$.

Figure 4.7 shows trajectories of 5 identical nanoparticles (10 nm diameter Fe_3O_4) attracted by ultra-high field gradients. These trajectories are obtained by numerically solving equations (4.17) and (4.18) with the Runge-Kutta method (see Appendix A for the Mathematica code) [28] [101]. Large black dots denote initial nanoparticle positions. Particles with positive initial x positions are studied, since the ultra-high field and gradient are symmetric about the z-axis. Each particle trajectory appears linear in the xz plane and is directed towards the transition. However, all particles do not land exactly on the transition (i.e., x = 0). Their final x position on the medium surface depends on their initial position, and there is a distribution of positions around the transition.

Immediately after a particle suspension is injected into the fluid cell, particles start to move toward magnetic transitions. Particles that are attracted onto the medium surface form patterns and diffract light. The diffracted light intensity depends on the particle number and how they are patterned. Within a time t, how many particles reach the magnetic medium surface and where they arrive on the surface depend on their initial positions and trajectories. As time increases, more particles fill in the grating lines. To theoretically predict the diffraction efficiency from the assembled grating as a function of time, Mie scattering theory [153] [22] [97] is employed. Mie scattering theory describes solutions of Maxwell's equations for the scattering of electromagnetic radiation by a sphere, also known as Lorentz-Mie or Lorentz-Mie-Debye solution. It is named after Gustav Mie who studied this problem first in 1908 [153].

To precisely predict the diffraction intensity from all attracted particles that have arbitrary positions on transitions with a finite distribution, a generalized multiparticle
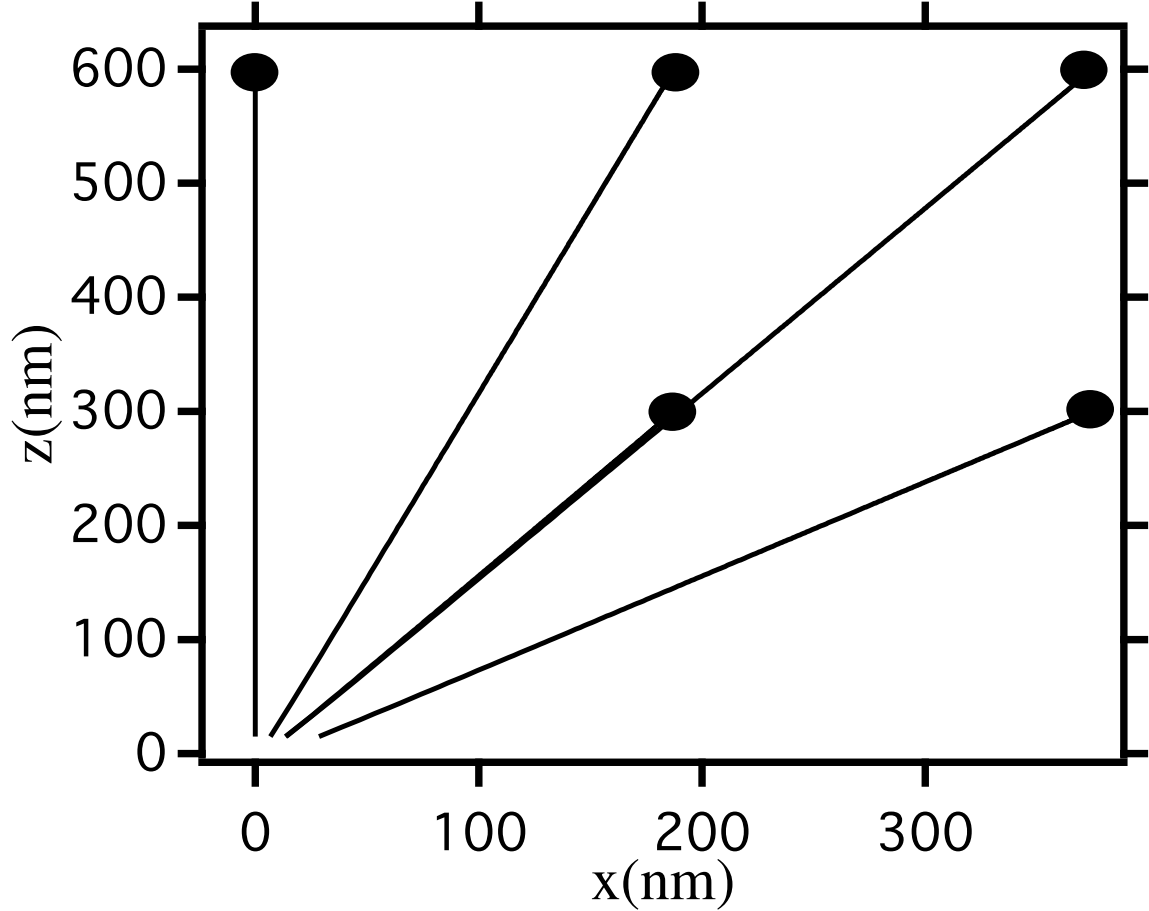
Figure 4.7   Calculated trajectories for 5 identical nanoparticles.

Mie-solution (GMM) [141] [238] [237] is required. The GMM solution describes scattering by ensembles of particles. Here, I present an initial calculation of the diffraction intensity based on the Lortentz-Mie theory, which assumes coated nanoparticles form linear chains of spheres along the x axis with the chain node located above the transition. I first consider the a bisphere system A_1 and A_2 (located at O and O' with radii = R) that are separated by an arbitrary distance d (d $\geq$ 2R) as shown in figure 4.8. The wave vector $\mathbf{k} = 2\pi/\lambda$ of an incident plane wave is contained in the x-z plane and makes an angle α with the z axis. Both spheres scatter waves in all directions. Let $\mathbf{S}_1 = \mathbf{S}_1(\mathrm{kr}, \theta_\mathrm{s}, \phi; \alpha)$ and $\mathbf{S}_2 = \mathbf{S}_2(\mathrm{kr}', \theta'_\mathrm{s}, \phi'; \alpha)$ represent the Lorentz-Mie complex scattering amplitudes of the spheres A_1 and A_2 at positions $(\mathrm{r}, \theta_\mathrm{s}, \phi)$ and $(\mathrm{r}', \theta'_\mathrm{s}, \phi')$ respectively, where ϕ and ϕ' are azimuthal angles. According to the Lorentz-Mie

Figure 4.8   Scattering geometry for the Lorentz-Mie theory.

theory for the noninteracting bisphere, the amplitude of the total scattered electric field $\mathbf{E}_{12}$ at (r, θ_s, ϕ) in the far-field (i.e., $kr, kr' \gg 1$) is [62] [61]

$$\mathbf{E}_{12} = \frac{ie^{ikr}}{kr}\mathbf{S}_1(kr, \theta_s, \phi; \alpha)[1 + e^{ikd(sin\alpha + sin\theta_s)}]. \tag{4.21}$$

Therefore, $|\mathbf{E}_{12}|^2$ is proportional to $1 + \cos[kd(\sin\alpha + \sin\theta_s)]$ and has interference maxima when $kd(\sin\alpha + \sin\theta_s) = 2m\pi$ (m is an integer number), which is essentially equivalent to the diffraction grating equation (4.1), after inserting $k = 2\pi/\lambda$ and $\theta_s = \beta$ in the equation (4.21).

For a linear chain of N spheres (A_j, j = 1, $\cdots$, N) with d_j the distance between A_1 and A_j, using the principle of superposition, the amplitude of the total scattered

81

Figure 4.9   Calculated first order diffraction vs time.

electric field $\mathbf{E}_{tot}$ in the far-field can be expressed as

$$\mathbf{E}_{tot} = \frac{ie^{ikr}}{kr}\mathbf{S}_1[1 + \sum_{j=2}^{N} e^{ikd_j(sin\alpha+sin\beta)}]. \tag{4.22}$$

Similarly, $|\mathbf{E}_{tot}|^2$ has interference maxima when the distance between any neighboring spheres is d_0 and $kd_0(\sin\alpha + \sin\beta) = 2m\pi$. This means the diffraction intensity from N spheres results from the interference of all scattered waves, ,and can be calculated using the equation (4.22). For m =1, $k(\sin\alpha + \sin\beta) = 2\pi/d_0$, which is inserted in

82

the equation (4.22), and thus the first order I_d for arbitrary d_js is given by

$$I_d = \left| \frac{ie^{ikr}}{kr} \mathbf{S}_A [1 + \sum_{j=2}^{N} e^{i2\pi d_j/d_0}] \right|^2.$$ (4.23)

Figure 4.9 shows the first order diffraction intensity calculated using equation (4.23) for the same particle suspensions that are shown in figure 4.5 (a). Each curve has an increasing diffraction intensity with time, and larger concentration particle suspensions produce larger diffraction intensities. In addition, all curves display similar curve shapes as those in figure 4.5 (a). However the curve shapes do not match the experimental curves precisely. Nonetheless, these results demonstrate that the theoretical calculation captures the essence of the nanoparticle self-assembly process and light scattering. A more precise calculation using the GMM solution will be performed in near future.

4.4 Flowing and Non-flowing Fluid Comparison

In the previous section, the fluid of nanoparticle suspensions does not flow during the nanoparticle self-assembly process. In this section, the impact of a flowing fluid that makes on the nanoparticle self-assembly process is investigated. Figure 4.10 (a) and (b) show diffracted intensities as function of time for suspensions NP2_C1, NP2_C0.5, NP2_C0.25, and NP2_C0.125 that flow with 1 mm/s and zero speed respectively.

Comparison analysis in figure 4.10 (a) and (b) show NP2_C0.5, NP2_C0.25, and NP2_C0.125 display similar self-assembly dynamics. The rate of diffraction increases with time are slightly smaller for non-flowing than 1 mm/s flowing. However NP2_C1 appears quite different from other suspensions. For 1 mm/s flow speeds, the diffraction intensity increases with time and then decreases [figure 4.10 (a)]. This behavior is not observed in figure 4.10 (b). This demonstrates that flow of the suspension

83
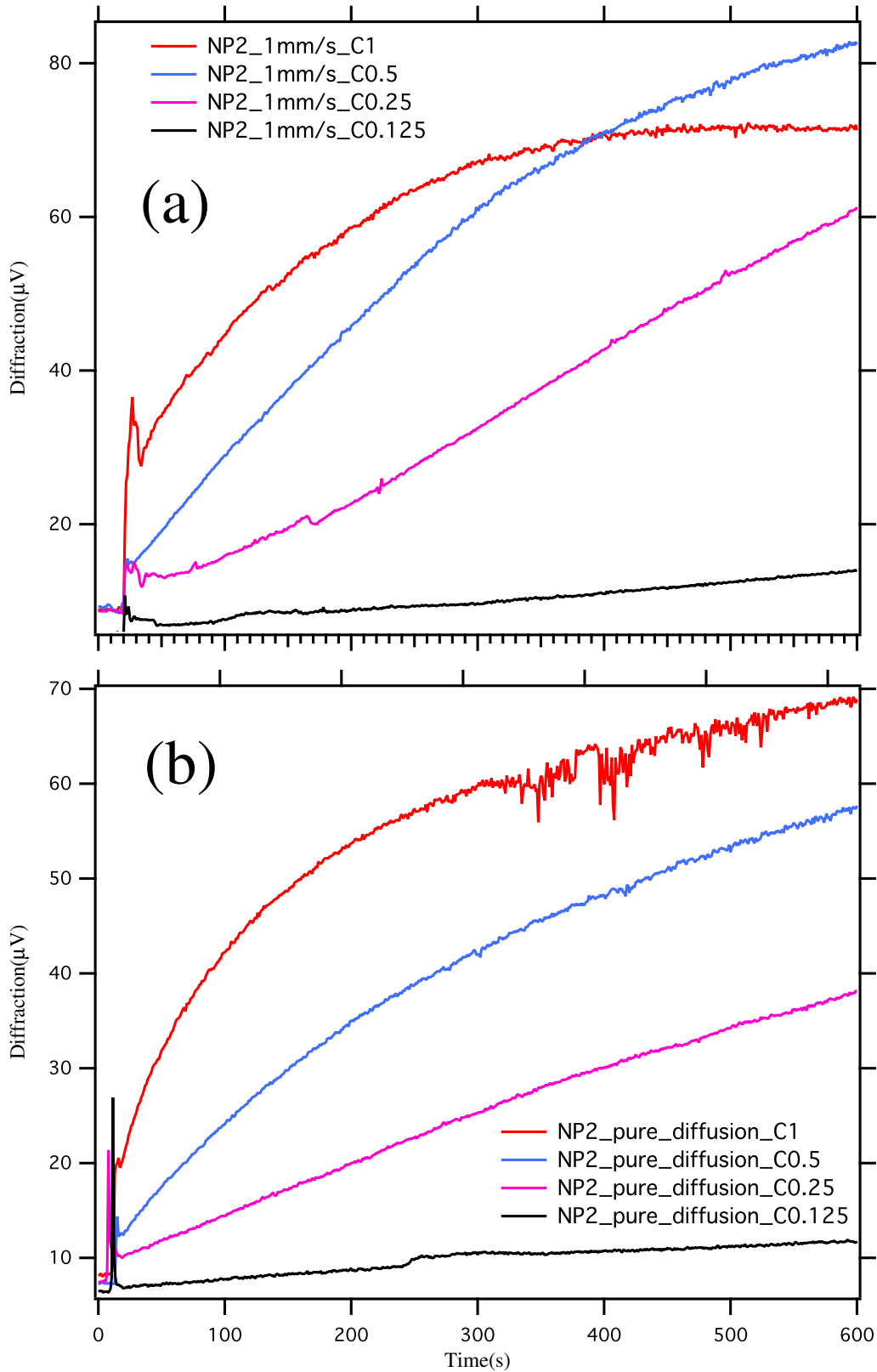
Figure 4.10   First order diffraction vs time for four different concentration particle suspensions NP2_C1, NP2_C0.5, NP2_C0.25, and NP2_C0.125. (a) The fluid speed is 1 mm/s. (b) The fluid does not flow after the fluid injection. The fluctuations of diffraction intensity for NP2_C1 is caused by dirt scattering.

does affect the nanoparticle self-assembly process, but a large impact occurs only for relatively large concentration particles.

CHAPTER 5

NANOPARTICLE SELF-ASSEMBLY PROCESS FOR

DESTABILIZED NANOPARTICLE SUSPENSIONS

In this chapter, I present a versatile approach that can enhance self-assembly of nanoparticles in suspensions onto the magnetic medium surface, based on the experimental apparatus and detection method that are discussed in chapter 4. Here, the nanoparticle self-assembly process can be changed by adding a trigger, i.e., a small volume of the phosphate buffer saline (PBS), to a colloidal suspension that contains anionic nanoparticles, i.e., their surfactants are anionic charges. PBS has a neutral pH and possesses positive and negative ions such as K^+, Na^+, HPO_4^{-2}, and $H_2PO_4^-$. Ions that are added into the nanoparticle suspension decrease the nanoparticle stability and the destabilization effect depends on how many ions are mixed. Nanoparticles that are only slightly destabilized by a small amount of PBS increase the diffraction efficiency dramatically. The amount of PBS is so small that the destabilized nanoparticles do not aggregate and are still colloidally suspended in the fluid. However, the grating self-assembly efficiency decreases as more PBS is added.

5.1 EXPERIMENTAL PROCEDURES

5.1.1 Base Nanoparticle Suspension

The base nanoparticle suspension is created using the following steps. A 20 μL stock solution of EMG-707 ferrofluid (anionic) is added into 5 mL DI water. Immediately the mixture is shaken for 10 s. Another 5 mL DI water is added into the mixture

following a 10 s shaking, and this procedure is repeated until 40 mL mixed suspension is obtained. The base suspension has a 0.001% Fe_3O_4 volume concentration.

5.1.2 Clean Medium and Fluid Cell

Cotton swabs are used to gently clean the coupon surface and fluid cell by first spraying Methanol. A power clean is avoided to reduce possibilities of scratching the medium surface. Then the coupon and fluid cell are blow dried using a Nitrogen gun. This process is repeated until the medium surface is clean, which is checked by investigating the diffraction and scattering intensities from the medium surface.

5.1.3 Mix Base Suspension with PBS

A known volume of PBS (e.g. 25, 50 μL) is added into a 2 mL base nanoparticle suspension. Immediately the fluid is throughly mixed for 10 s using a 2700 RPM Vortex-Gene touch mixer. Two minutes later, this mixed suspension is injected into the fluid cell for data collection.

5.1.4 Collect Diffraction and Scattering Data

Start running the data collection program which reads both the scattering and diffraction intensities. The suspension obtained in the previous section is injected into the fluid cell with a 125 mL/h flowing speed through a syringe pump. The fluid stops flowing immediately after the fluid fills the whole cell.

5.1.5 DLS and Zeta Potential Measurements

DLS and Zeta potential measurements are performed on suspensions obtained in the section 5.1.3. This suspension is loaded into a commercial DLS tool (Malvern, Zetasizer Nano ZS) for collecting DLS and Zeta potential data.

5.2 PBS dependent Diffraction and Scattering

Figure 5.1 (a) shows representative first-order diffraction efficiencies as a function of time for suspensions that are created by mixing a 2 mL base suspension with 0, 25, 50 and 87.5 μL PBS. The nanoparticle self-assembly process is dramatically different depending on PBS Volume. The 0 μL PBS displays a curve shape with a positive curvature, which is similar as those observed for C1, C0.5, C0.25, C0.125, and 22nm nanoparticle suspensions (figure 4.5 and 4.6, chapter 4) [185] [242]. A 25 μL PBS yields a curve with no curvature, i.e., the diffraction efficiency is almost linear with respect to time. The diffraction efficiency at 900 s is $\sim$5x that for no PBS. As the PBS volume is increased to 50 μL, the curve shape appears inverted, i.e., its curvature becomes negative. The diffraction efficiency at 900 s is $\sim$6x that for 0 μL PBS. The rate of diffraction efficiency is smaller than the 25 μL PBS before $\sim$340 s, and becomes larger after $\sim$340 s. And hence, diffraction efficiencies of the 25 μL and 50 μL PBS cross each other at $\sim$ 660 s. A 87.5 μL PBS still further increases the diffraction efficiency yielding a diffraction efficiency at 900 s $\sim$10x that for 0 μL PBS. The curve shape appears similar as the 50 μL PBS.

Figure 5.1 (b) shows representative first-order diffraction efficiencies as a function of time for suspensions that are created by mixing a 2 mL base suspension with 87.5, 150, 175 and 400 μL PBS. A PBS volume over 87.5 μL does not lead to the enhancement, but a decreasing diffraction efficiency. A 150 μL PBS produces a curve shape with zero curvature and the diffraction efficiency at 900 s is smaller than that for 87.5 μL PBS, i.e., $\sim$5x compared with 0 μL PBS. A 175 μL PBS reduces to $\sim$2.5x 0 μL PBS and yields a curve shape with positive curvature, similar to 0 μL PBS. A 400 μL PBS almost does not coat nanoparticles on the medium surface. In summary, the curvature changes in a sequence of positive, zero, negative, zero, positive, zero, as the PBS volume is increased. Similarly, the diffraction efficiency at 900 s is enhanced, reaching a maximum at $\sim$ 87.5 μL PBS, and then decreases to zero eventually as the
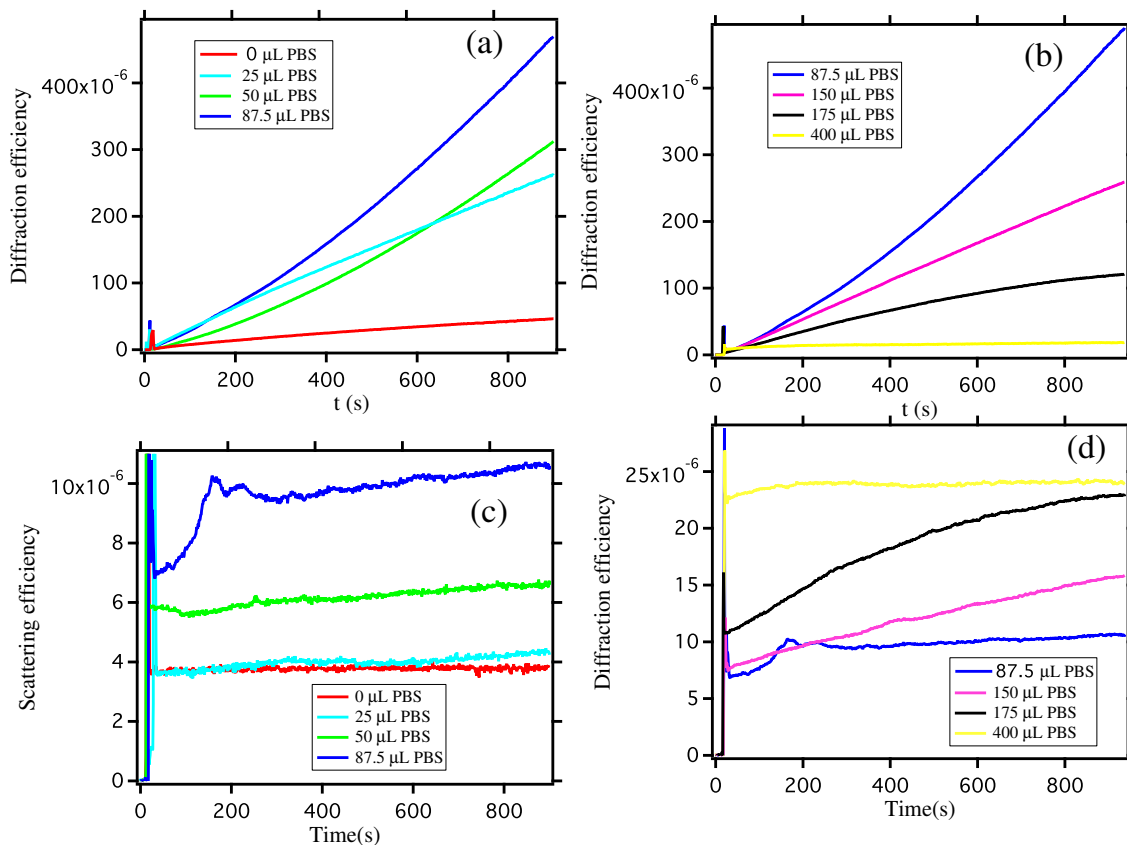
Figure 5.1   First order diffraction efficiency as a function of time for suspensions that are created by (a) mixing 2 mL base suspension with 0 μL, 25 μL, 50 μL, and 87.5 μL PBS. (b) mixing 2 mL base suspension with 87.5 μL, 150 μL, 175 μL, and 400 μL PBS. (c) Scattering intensity as a function of time for same suspensions in (a). (d) Scattering intensity as a function of time for same suspensions in (b).

PBS volume is increased.

Figure 5.1 (c) and (d) show representative scattering intensities as a function of time for the same suspensions as shown in Figure 5.1 (a) and (b) respectively. The scattering intensity remains almost constant with time except for 150 μL and 175 μL PBS. Scattering intensities of both 150 μL and 175 μL suspensions increase with time gradually. This is probably caused by the gradual decrease of nanoparticle colloidal stability while the scattering signal is measured. The reduction in the colloidal stability of nanoparticlces yields larger aggregates of nanoparticles, which produce more scattered light.

Circles in figure 5.2 shows the average scattering efficiency (right axis) as a function of PBS volume. For PBS volumes that are $\leq 125 \ \mu L$, the average scattering efficiency largely remains constant. For a PBS volume that ranges between 125 μL and 250 μL, the average scattering efficiency is almost linear with respect to the PBS volume, and the average scattering efficiency increases as PBS volume increases. However, for PBS volumes > 250 μL, the average scattering efficiency decreases as the PBS volume is increased, while the scattering efficiency also appears largely linear with respect to the PBS volume. Dots in figure 5.2 show the diffraction efficiency at 900 s (left axis) as a function of the PBS volume. The diffraction efficiency at 900 s is dramatically enhanced as a small volume of PBS is added, reaching a maximum when the PBS volume = 87.5 μL, and then decreases quickly as the PBS volume is increased. A 300 μL PBS yields a diffraction efficiency that approximately equals to the 0 μL PBS. More PBS further reduces the diffraction efficiency. A 500 μL PBS almost stops the nanoparticle self-assembly on the medium surface.

5.3 DLS and Zeta Potential Measurements for Nanoparticles Destabilized via PBS

To understand why the diffraction and scattering efficiency behave as shown in figure 5.2. PBS dependent hydrodynamic diameters and Zeta potentials of nanoparticles are determined using experimental procedures discussed in the section 5.1.

Figure 5.3 (a) shows hydrodynamic diameters of suspended nanoparticles (right axis) as a function of the PBS volume from the DLS intensity (green squares), and average size distribution (red triangles) measurements respectively. As a comparison, the scattering efficiency (left axis) obtained from the fluid cell is also shown in figure 5.3 (a). Both Hydrodynamic Diameter$_{\text{intensity}}$ and Hydrodynamic Diameter$_{\text{z-avg}}$ display similar curve shapes as the scattering efficiency, while Hydrodynamic Diameter$_{\text{intensity}}$ matches slightly better. This demonstrates the average scattering intensity measured
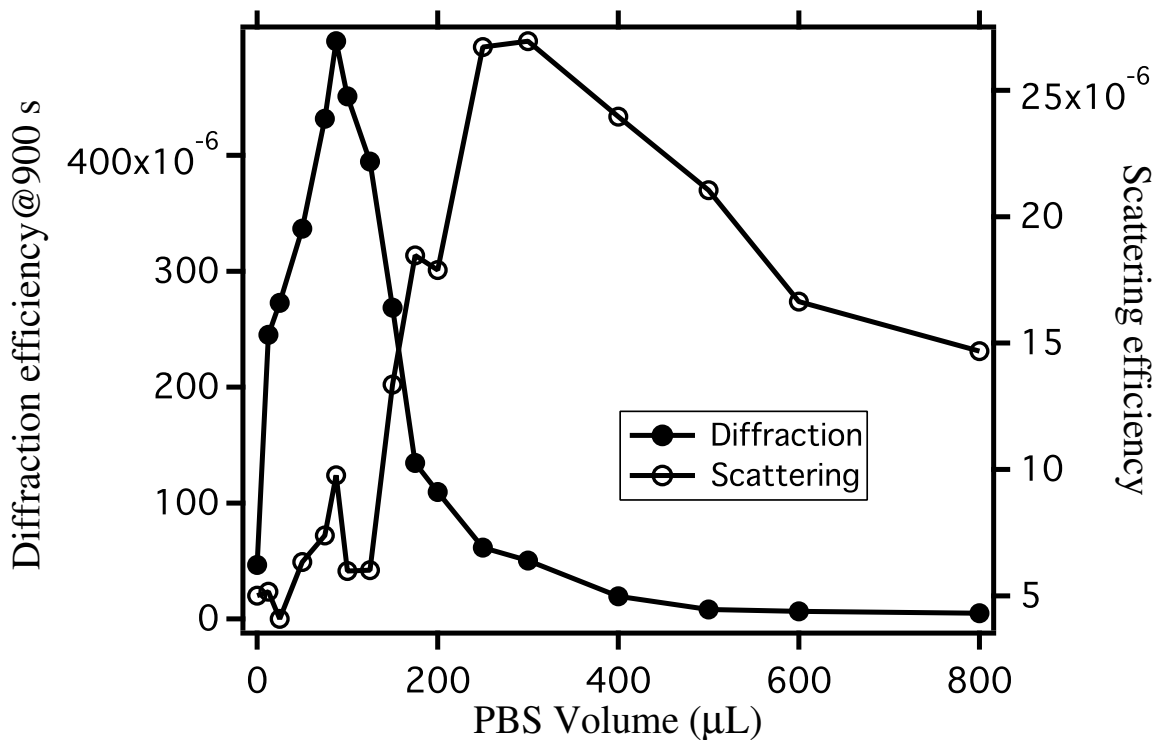
Figure 5.2   Diffraction efficiency at 900 s (left axis) and scattering efficiency (right axis) as a function of the PBS volume.

from nanoparticle suspensions in the fluid cell is proportional to particle hydrodynamic diameters. Therefore, average scattering intensity appear to be an indicator of nanoparticle size as the nanoparticles are suspended in the fluid cell.

Similarly, Figure 5.3 (b) shows Hydrodynamic Diameter$_{\text{intensity}}$ and Hydrodynamic Diameter$_{\text{Z−avg}}$ (right axis), and the diffraction efficiency at 900 s (left axis) as a function of the PBS volume. The diffraction efficiency is strongly enhanced for a PBS volume that ranges between $\sim$25 μL and $\sim$150 μL. But there is little increase in hydrodynamic diameters of particles over the 0 μLPBS. As the particle hydrodynamic diameter increases causing by a larger PBS volume than 150 μL, the diffraction efficiency does not increase, but decreases quickly. This behavior contradicts the intuition that particles with larger hydrodynamic diameters should better self-assemble on the medium surface and would scatter light more intensively. Although I do not understand this behavior
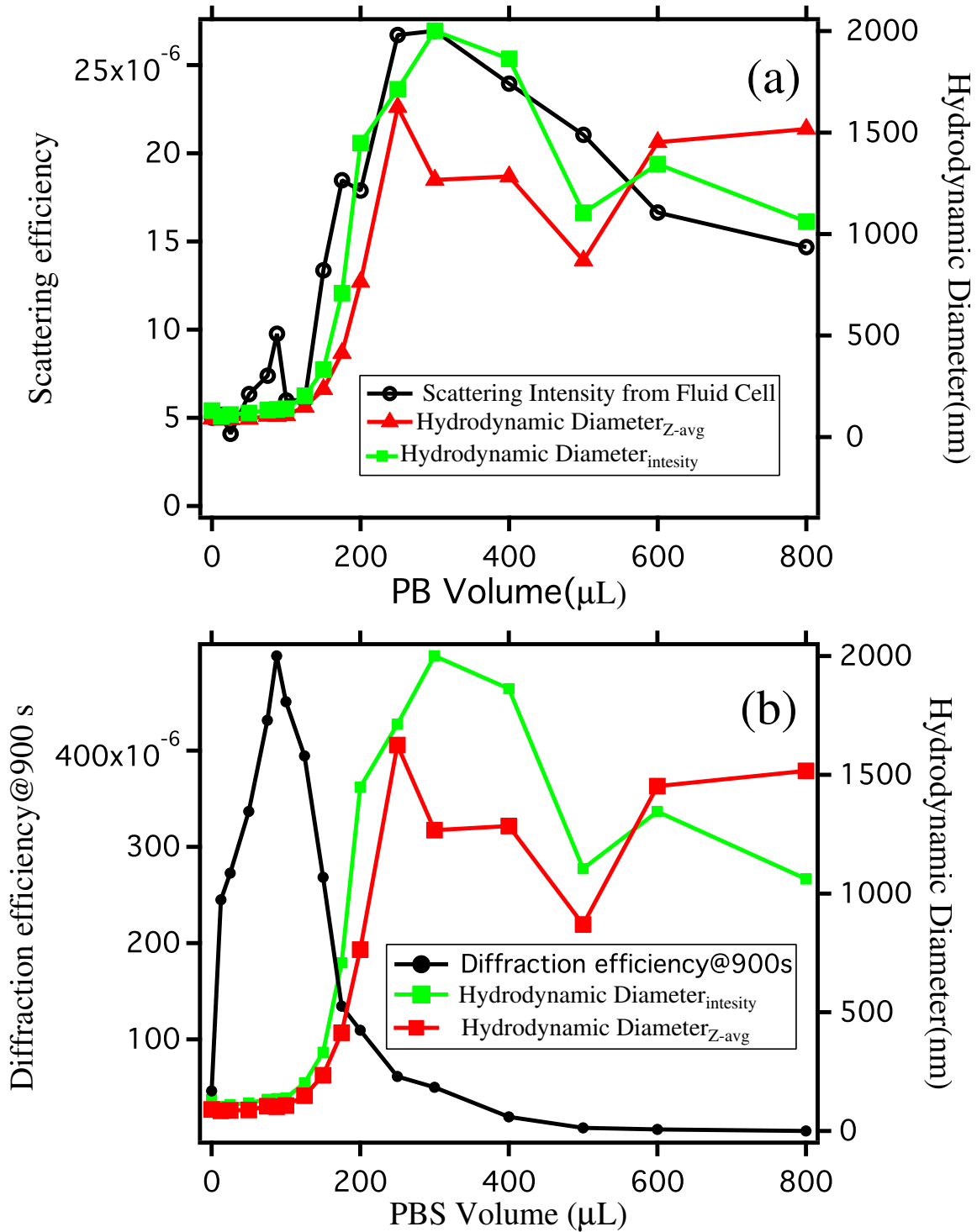
Figure 5.3   Squares in green on the right axis: the hydrodynamic diameter of nanoparticles as a function of the PBS volume that is mixed with the base suspension. Squares (triangles) are determined as the DLS intensity (Z-average) distribution measurement. Circles on the left axis in (a): scattering efficiency vs PBS volume as measured form the fluid cell. Dots on the left axis in (b): diffraction efficiency at 900 s vs PBS volume.

completely yet, this strongly suggests that ultra-high field gradients, together with the destabilization effect caused by small amount of PBS, yield the strong enhancement in the diffraction efficiency. A dramatic decrease in the diffraction efficiency at relatively large PBS volumes may be caused by: (i) nanoparticles aggregate into big particles; (ii) magnetic forces acting on big aggregates are too small to drag the particles onto the medium surface, since the field and field gradient are localized in the range of 0 - 200 nm above the medium surface (figure 2.17, 2.18 and 2.19).

Triangles (right axes) as shown in figure 5.4 display the Zeta potential of nanoparticles as a function of the PBS volume. The scattering efficiency and diffraction efficiency at 900 s are also included in figure 5.4 (a) and (b) (left axes) respectively as comparisons. The surface of these nanoparticles is coated with anions, and thus the Zeta potential is negative. Below the amplitude of Zeta potential is discussed. The base suspension has a 60 mV Zeta potential. A 12.5 μL PBS addition into the base suspension causes the Zeta potential to be $\sim$50 mV. More PBS up to 150 μL does not cause the Zeta potential of nanoparticles to decrease dramatically, but yields a Zeta potential that ranges between 40 and 50 mV. In this range, the Zeta potential is largely linear with the PBS volume, and decreases as the PBS volume is increased. The strong enhancement of the diffraction efficiency occurs in this PBS range [figure 5.4 (b)]. Note that hydrodynamic diameters of these nanoparticles remain same as the 0 μL PBS (figure 5.4). At 250 μL PBS reduces the Zeta potential from 45 to 30 mV and the hydrodynamic diameter grows from $\sim$600 nm to 1500 nm (HydrodynamicDiameter$_{\text{Z}-\text{avg}}$ in figure 5.3), which is dramatic. This indicates the decrease in the diffraction efficiency (comparing with the peak) for $\geq$ 250 μL PBS, is not mainly caused by weaker colloidal stability, but by large particle aggregates ($>$ 1500 nm). This demonstrates that ultrahigh field gradients, together with the destabilization of nanoparticles but without bulk colloid aggregates, can enhance the diffraction efficiency and drive the change in diffraction curve shapes as shown in
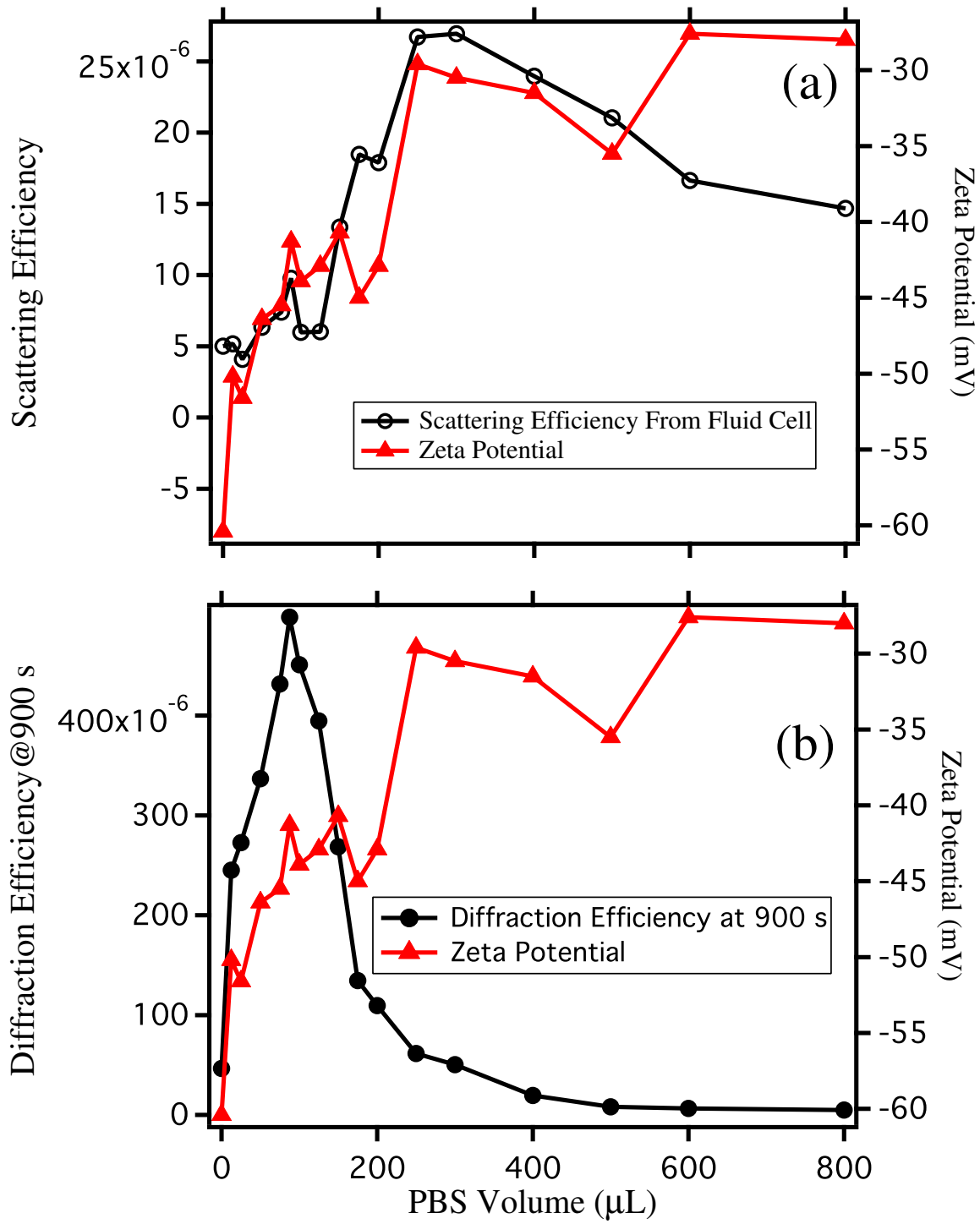
Figure 5.4   Triangles denotes the Zeta potential vs the PBS volume. Circles on the left axis in (a): scattering efficiency vs PBS volume as measured form the fluid cell. Dots on the left axis in (b): diffraction efficiency at 900 s vs PBS volume.

figure 5.1. Weaker stability of particles that leads to the large aggregates, however, does not enhance, but reduces the nanoparticle coating quality dramatically.

CHAPTER 6

SPIN-TRANSFER TORQUE

Previous chapters focus on the nanoparticle self-assembly project. Chapter 6 and 7 describe the spin-transfer torque (STT) project. This chapter introduces ferromagnetism, giant magnetoresistance (GMR), spin injection and STT, and discusses experimental work to investigate ultrafast magnetic switching dynamics using ultrafast STT pulses.

6.1 FERROMAGNETISM AND GIANT MAGNETORESISTANCE

6.1.1 Ferromagnetism and two-current model

Magnetism of materials originates from electron spins, while electrical transport is caused by the motion of electrical charges. Few metallic elements appear ferromagnetic except $3d$ transition metals (Fe, Co, Ni), and heavy rare-earth metals (e.g., Gd, Tb, Dy). In rare-earth ferromagnetic metals, electrons carrying magnetism are $4f$. These $4f$ electrons are located deep inside the atomic core. Therefore, their magnetic moments are well localized within the individual atom, and electrons responsible for electrical transport can be distinguished from the $4f$ electrons for magnetism [158]. However, this distinction does not exist for $3d$ transition metals, where the $3d$ electrons carry magnetism. These $3d$ electrons are located relatively far from the atomic core, and thus considered to be itinerant (i.e., moving among atoms). From a quantum mechanical view, these $3d$ electrons form band structures [34] [24] [20] [158].

The electronic structure of $3d$ transition metals consists mainly of s- and d-orbitals.
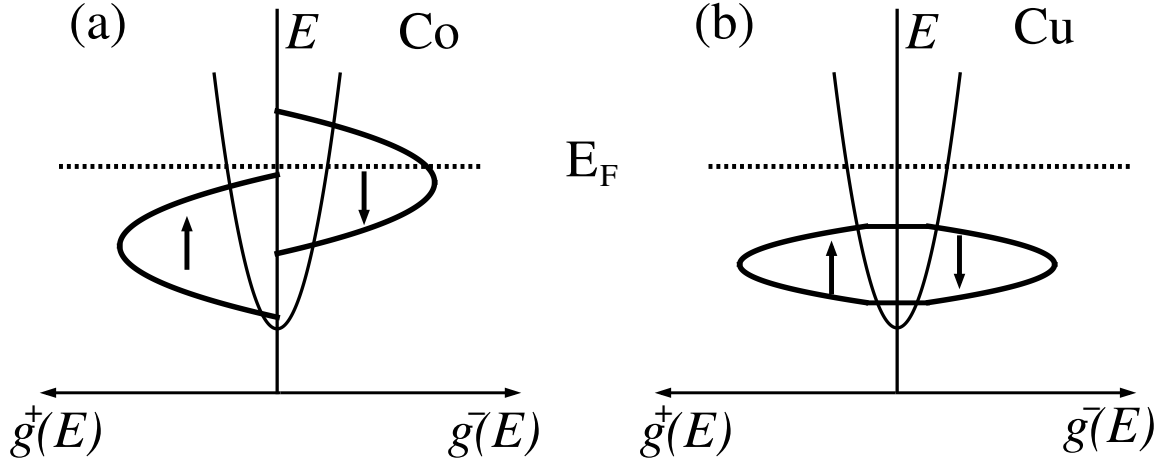
Figure 6.1   (a) and (b) Schematic density of states (DOS) of Co and Cu respectively. Arrows indicate majority (up) and minority (down) spin states, in uniformly magnetized materials. E_F: Fermi energy level.

The relative position of Fermi energy level E_F to s- and d-states depends on the material. Figure 6.1 (a) shows schematic density of states (DOS) of a typical $3d$ transition metal Co, where the horizontal axes represent the DOS for majority [spin up: $g^+(E)$] and minority [spin down: $g^-(E)$] spin states respectively, and the vertical axis denotes the energy E. Electronic structures of both Co and Cu consist of wide s-bands (thin curves in figure 6.1) and narrow d-bands (thick curves in figure 6.1). The d-band splits for spin up and down states. This yields a larger population of spin up electrons than that of spin down electrons. Therefore, ferromagnets show macroscopically spontaneous magnetization [34] [24] [20] [158]. This collectively preferable direction of spins is chosen as the quantization axis $\hat{z}$ (i.e., spin up) in a quantum mechanical representation, and -$\hat{z}$ is the spin down direction. While in normal metals such as Cu, the DOS of s- and d-bands for spin up and down states are equal [figure 6.1 (b)], therefore, normal metals are not ferromagnetic.

The conductance of metals depends on properties of electronic states close to the Fermi surface. For non-magnetic metals (ignoring spin-orbit coupling), all electronic states are spin degenerate, therefore, the scattering probability for a particular electronic state does not depend on its spin state. In ferromagnetic metals, spin-up states

close to the Fermi surface are very different from spin-down states in not only the total number of DOS [figure 6.1 (a)] but also their detailed wavefunction structures [34] [158]. Electrons at different spin states experience different scattering environments in transport, and ferromagnetic metals appear to be more resistive to one type of spin state and more conductive to the other [34] [158]. The electrical conductivity of metals σ is given by the Drude formula [34] [5], i.e.,

$$\sigma = \frac{e^2 n \tau}{m^*} \tag{6.1}$$

where e, n, τ and m are the electrical charge, carrier density, lifetime and effective mass of carriers respectively. In ferromagnets, the Drude formula takes into account the spin dependence in these quantities [158] [248]. Typically n, τ and m are all spin dependent and τ is most spin dependent because τ is strongly affected by spin scattering. τ relates to the mean free path l through $\tau = l/v_F$, where v_F is the Fermi velocity. Typically l is $\ll$ the spin diffusion length and spin angular momentum remains constant approximately over the time scale of τ. Hence, spin up and down electrons can be considered independently in evaluating the scattering lifetime, i.e.,

$$\frac{1}{\tau} = \frac{1}{\tau^\uparrow} + \frac{1}{\tau^\downarrow}, \tag{6.2}$$

where $\tau^\uparrow, \tau^\downarrow$ are the lifetime for spin up and down electrons respectively. $\sigma = \sum_s \sigma_s$, where $s = \uparrow$ or $\downarrow$. This is called the Mott's two-current model [160] [248].

6.1.2 GMR

Magnetoresistance (MR) is a resistance change of specific structures when external magnetic fields are applied. Commonly these specific structures consist of an alternating stack of a few nm thick ferromagnetic (FM) and non-magnetic (NM) layers. Typically ferromagnetic materials are Co, Fe, Ni, and their alloys and normal materials are Cr, Cu and Ag. Some multilayers show large magnetoresistances, which
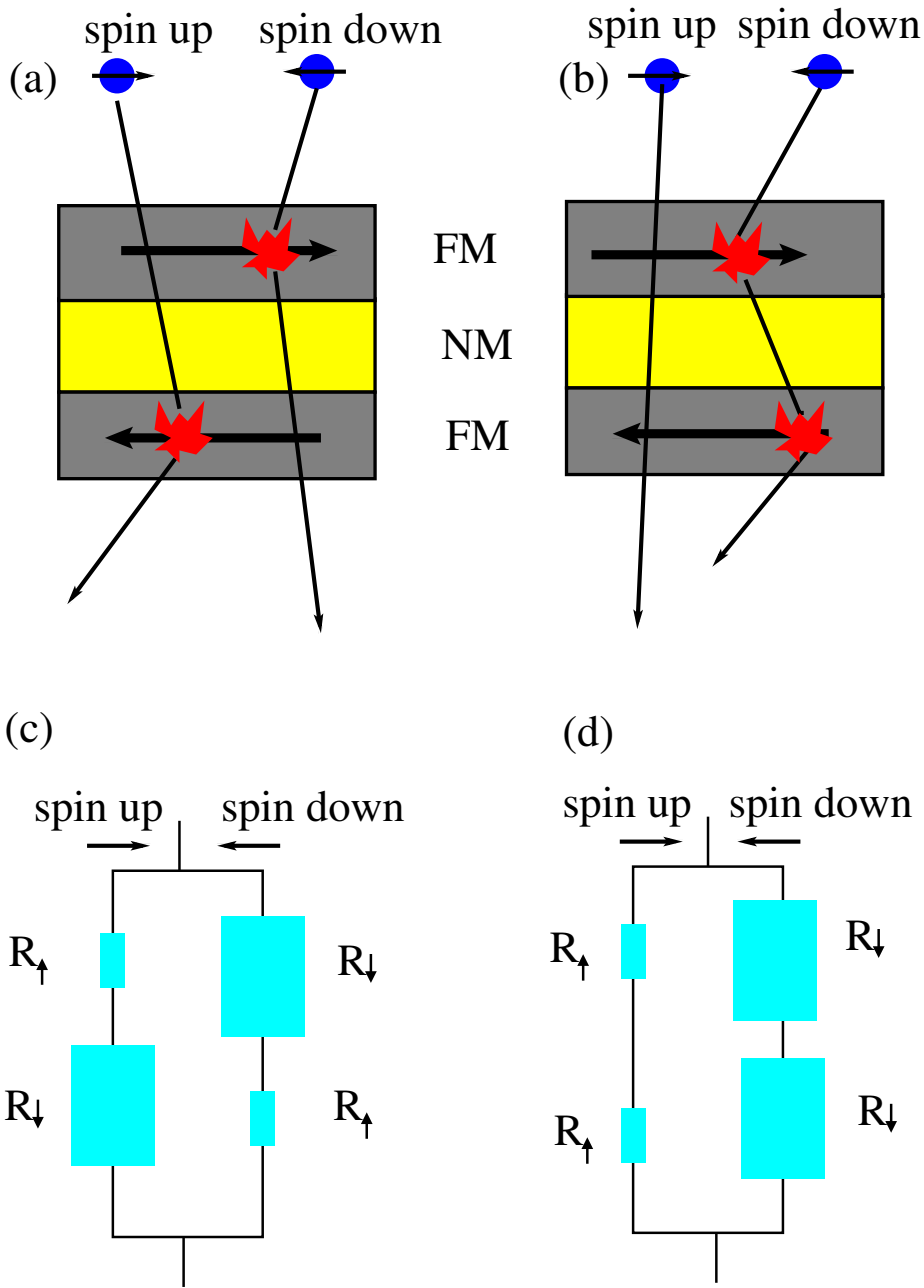
Figure 6.2   Schematic diagram of GMR effect. (a) and (b) FM/NM/FM sandwiches with anti-parallel and parallel magnetizations respectively. (c) and (d) resistance networks for (a) and (b) respectively, according to the two-current model. FM: ferromagnetic. NM: normal.

is called giant MR (GMR) for a metallic NM layer and tunnel MR (TMR) for an insulating NM layer. GMR was first observed in Fe/Cr/Fe multilayers that show a > 50% change in the MR measured at 4.2 K with current in plane [7] [135] [52] [18] [79]. Figure 6.2 (a) shows schematic of a FM/NM/FM trilayer with anti-parallel ferromagnetic magnetizations. Note a dipole field coupling from the two FM layers (inter-layer exchange coupling) favors the anti-parallel alignment of FM magnetizations when no external fields are applied. According to Mott's two-current model [160], [89], spin up electrons transversing the trilayer, i.e., current perpendicular to plane (CPP), have a smaller resistance $R_\uparrow$ than that for spin down electrons $R_\downarrow$, i.e., $R_\uparrow < R_\downarrow$. This trilayer structure can be treated with a resistance network as shown in figure 6.2 (c). The total resistance R_A is expressed as

$$R_A = \frac{R_\uparrow + R_\downarrow}{2}. \tag{6.3}$$

Similarly, figure 6.2 (b) displays the sandwich with parallel ferromagnetic magnetizations, which is treated as a resistance network as shown in figure 6.2 (d). The total resistance R_P is expressed as

$$R_P = \frac{2R_\uparrow R_\downarrow}{R_\uparrow + R_\downarrow}. \tag{6.4}$$

$R_P < R_A$, which explains the magnetoresistance change caused by external fields align the FM magnetizations parallel. In the case that the ferromagnetic magnetizations are not collinear and make a relative angle θ with each other, the total resistance $R(\theta)$ is approximately given by [121]

$$R(\theta) = \frac{R_{AP} + R_P}{2} - \frac{(R_{AP} - R_P)cos\theta}{2}. \tag{6.5}$$

The magnitude of MR is calculated via the MR ratio as

$$MR = \frac{\rho_{AP} - \rho_P}{\rho_{AP}}, \tag{6.6}$$

or

$$MR = \frac{\rho_{AP} - \rho_P}{\rho_P}, \tag{6.7}$$
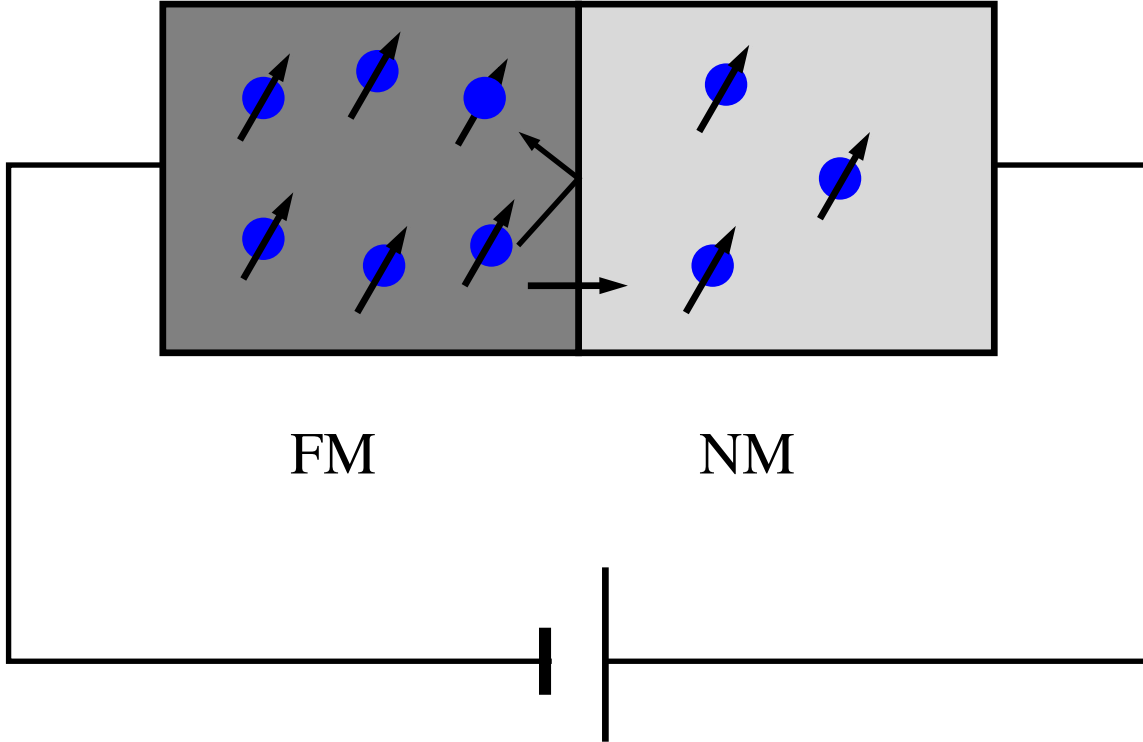
Figure 6.3 Schematic diagram showing spin injection across the interface between the ferromagnet and non-magnetic materials.

where ρ_{AP} and ρ_P are the resistivity in the multilayer with AP and P alignment respectively. Commonly equation (6.7) is used in the literature [158].

6.2   SPIN INJECTION

An electron carries both charge $(-e)$ and spin angular momentum $(\hbar/2)$. A ferromagnet can also be used as a "spin filter". Figure 6.3 shows electrons that are injected into a ferromagnet flow out of the ferromagnet into a non-magnetic material. Electrons passing through the FM/NM interface gain spin imbalance because electrons interact with polarized spins in the ferromagnet and maintain the spin imbalance for a characteristic time (i.e., spin relaxation time) after flowing out the ferromagnet. This current is called a spin current or a spin-polarized current, which carries not only charges, but also a net flow of spins. These spin-polarized electrons are subject

to spin relaxation due to the spin-orbit coupling and diffuse into the non-magnetic material for a characteristic length (i.e, a spin diffusion length). This induces a local spin accumulation in the NM [106] [148] [147] [241]. Johnson and Silsbee [106] are the first to use a ferromagnet to inject spin currents into a NM material and electrically detect the accumulated spin of electrons by a second ferromagnet a few microns away.

6.3 Spin-transfer torque

Figure 6.4 shows schematic of a nanopillar consisting of a FM/NM/FM/NM multilayer (i.e. a spin valve), e.g., Co(10)/Cu(5)/Co(3)/Cu(6). Their thickness in units of nm are enclosed in parentheses. FM1 and FM2 are called the spin polarizer and free layer respectively. Since FM1 is thicker than FM2 and a larger energy is required to switch the FM1 magnetization than that of FM2. The cross section of the nanopillar is on the order of 100 x 100 nm^2. Both the free layer and spin polarizer have single magnetic domains and the magnetization can be treated as a macrospin. A voltage is applied across the nanopillar bottom and top. The electric current is first spin polarized by FM1(i.e., polarizer) and then injected into FM2 (i.e., free layer) through NM1. The current reaching FM2 remains spin polarized since the NM1 thickness is much shorter than the spin diffusion length, which is >100 nm for Cu at room temperature[2, 118]. This spin current exerts a torque on the local magnetic moment of FM2, and this torque is called a spin-transfer torque. The current has a spin angular momentum denoted by $\mathbf{J_1}$ and $\mathbf{J_2}$ in NM1 and NM2 respectively. The exchange interaction between the spin current and the FM2 magnetic moment conserves the total spin angular momentum. Therefore, one obtains

$$\frac{d\mathbf{S_2}}{dt} = \mathbf{J_1} - \mathbf{J_2}. \tag{6.8}$$

This means a decrease in the spin angular momentum of spin current equals an increase in the spin angular momentum of FM2. Assuming electrons passing through
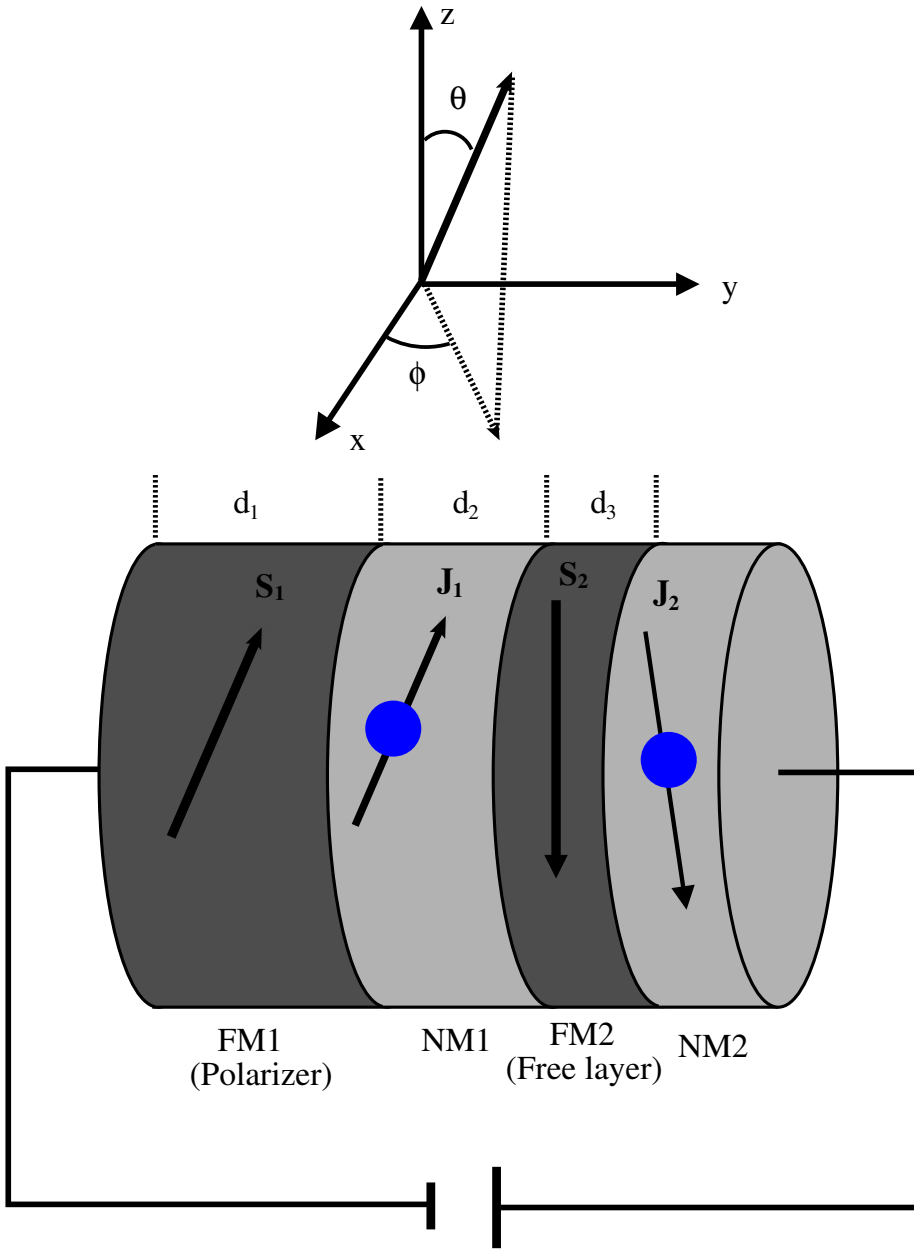
Figure 6.4   Schematic illustration of Spin-transfer torque.

FM1 are spin-polarized along $\mathbf{S}_1$, i.e., $\mathbf{J}_1 \parallel \mathbf{S}_1$ [both are oriented along (θ, ϕ) (figure 6.4)], one can express the spin function of $\mathbf{J_1}$ as (Appendix B)

$$\mathbf{J}_1 = \left| (\theta, \phi) \right\rangle = cos\frac{\theta}{2}\left| \uparrow \right\rangle + sin\frac{\theta}{2}e^{i\phi}\left| \downarrow \right\rangle \quad \text{or} \quad \begin{pmatrix} cos\frac{\theta}{2} \\ sin\frac{\theta}{2}e^{i\phi} \end{pmatrix} \quad (6.9)$$

in the Pauli matrix representation, where $\left| \uparrow \right\rangle$ are $\left| \downarrow \right\rangle$ are the spin eigenstates in the +z and -z direction respectively. Conduction bands of FM2 are split into two bands with direction pointing up and down respectively. Therefore, the wave function of the injected spin current into FM2 has two separated partial waves with different wave vectors $k_\uparrow$ and $k_\downarrow$. The phase acquired on two partial waves after traveling through FM2 (thickness d_3) is $k_\uparrow d_3$ and $k_\downarrow d_3$ respectively. Assuming electrons travel through FM2 with ballistic collision [202] [203] [204], the spin function of spin current is calculated as

$$\mathbf{J}_2 = \begin{pmatrix} e^{ik_\uparrow d_3} & 0 \\ 0 & e^{ik_\downarrow d_3} \end{pmatrix} \begin{pmatrix} cos\frac{\theta}{2} \\ sin\frac{\theta}{2}e^{i\phi} \end{pmatrix} = e^{ik_\uparrow d_3} \begin{pmatrix} cos\frac{\theta}{2} \\ sin\frac{\theta}{2}e^{i[\phi + (k_\downarrow - k_\uparrow)d_3]} \end{pmatrix}. \quad (6.10)$$

Equation (6.10) shows the phase of $\mathbf{S}_2$ has been changed by $(k_\downarrow - k_\uparrow)d_3$, meaning $\mathbf{S}_2$ has precessed around the z axis by $(k_\downarrow - k_\uparrow)d_3$ (units: rad). Since films are polycrystalline and each conduction electron travels along different crystal orientations, the phases and precession angles should be different for different electrons. As a result, the transverse components (x- and y-components) of the injected spins cancel each other [203] [204]. Therefore, in the Cartesian coordinates, the spin current exerts on FM2 a spin-transfer torque that can be expressed as

$$\frac{d\mathbf{S_2}}{dt} = g(\theta)\frac{J^S}{-e}\frac{\hbar}{2}\left[\begin{pmatrix} cos\phi sin\theta \\ sin\phi sin\theta \\ cos\theta \end{pmatrix} - \begin{pmatrix} 0 \\ 0 \\ cos\theta \end{pmatrix} \right] = g(\theta)\frac{J^S}{-e}\frac{\hbar}{2}\mathbf{e}_2 \times \mathbf{e}_1 \times \mathbf{e}_2, \quad (6.11)$$

where $\mathbf{e}_1$ and $\mathbf{e}_2$ are the unit vectors of $\mathbf{S}_1$ and $\mathbf{S}_2$ respectively. J^S is the charge current and $g(\theta)$ represents the STT efficiency that depends on the spin polarization

104

(P) and the relative angle between $\mathbf{S}_1$ and $\mathbf{S}_2$, i.e., θ. Slonczewski proposed a formula for the spin-transfer efficiency, $g(\theta)$, for CPP-GMR junctions by considering a free electron model [202] [203] [204]:

$$g(\theta) = \left[-4 + (P^{-1/2} + P^{1/2})^3(3 + \cos\theta)/4\right]^{-1}. \tag{6.12}$$

6.4 Coherent control of nanomagnet dynamics via ultrafast spin-transfer torque pulses

This section discusses measurements on ultrafast magnetic dynamics in spin valves using a pair of ultrashort STT pulses. This project was conducted with my colleague Samir Garzon. I took most of the data and Samir performed simulations. I greatly appreciate his work that contributed to make this project move forward.

The magnetization orientation of a nanoscale ferromagnet can be manipulated using an electric current via the spin transfer effect [202, 203, 13, 12]: spin angular momentum is transferred from the conduction to the localized electrons, exerting an effective torque on the ferromagnet [113, 211, 223, 161]. Time domain measurements of nanopillar devices at low temperatures have directly shown that magnetization dynamics and reversal occur coherently over a timescale of nanoseconds [128, 35]. By adjusting the shape of a spin torque waveform over a timescale comparable to the free precession period, control of the magnetization dynamics in nanopillar devices should be possible [182, 220, 219]. Here, the coherent control of the free layer magnetization in nanopillar devices, using a pair of current pulses as narrow as 30 ps with adjustable amplitudes and delay, is reported. In contrast with previous measurements where the spin torque is applied throughout a large fraction of a precession cycle [224, 109, 194, 39, 41], in these reported experiments the magnetization evolves freely except for short time intervals when it is driven by the spin torque. By using ultra-short spin torque "impulses" a previously unexplored regime, in which nanomagnet dynamics is strongly affected by the timing of the spin torque pulses with respect

105
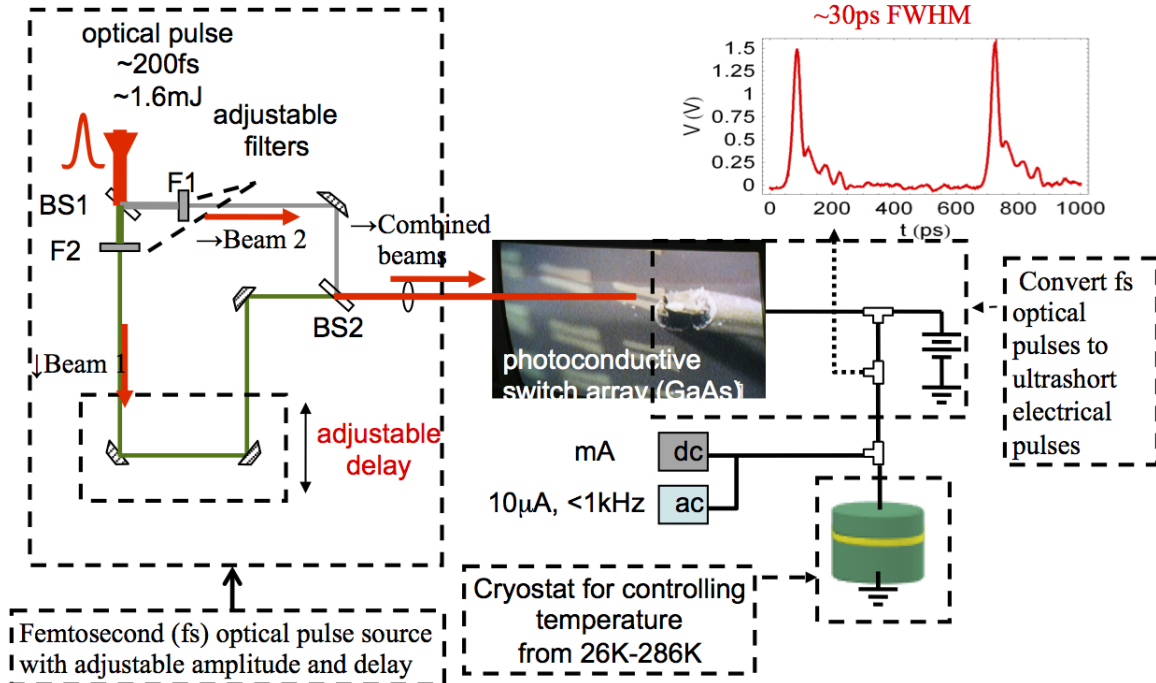
Figure 6.5   Schematic of experimental apparatus.

to the underlying free precession orbits, can be accessed and investigated. Regions where the spin torque "impulses" have the largest effect on the dynamics, thereby increasing the efficiency of nanomagnet switching over longer spin torque pulses, are experimentally mapped. Furthermore, these experiments demonstrate the ability to manipulate the free magnetic moment motion, even exciting large angle precession, and demonstrating room temperature coherent dynamics.

6.4.1   Experimental Setup

Figure 6.5 shows the experimental setup schematically. A femtosecond mode-locked laser in single-shot mode is used to generate either a single pulse or a pair of optical pulses with adjustable amplitudes and time delay t_D, which are then converted to electrical pulses using a LT-GaAs/Au photoconductive switch [6, 206]. To produce the pair of optical pulses with a precise delay, an optical pulse in split into two optical

pulses with a beamsplitter BS1. These two optical pulses are combined together with a second beamsplitter BS2, where their relative time delay is obtained by inserting a linear stage in the optical path of beam 2. Their amplitudes are controlled by optical filters F1 and F2 respectively. Optically-generated electrical pulses can be relatively timed with sub-ps resolution, and since the measurement is independent of the absolute pulse timing, there are no trigger jitter effects. A 40 GHz bias tee is used to inject both the current pulses that induce magnetization dynamics and the ac/dc currents used to measure the resistance and reset the device.

For room temperature measurements, the device is connected with a 40GHz picoprobe. To perform high frequency measurements at low temperature, the device is Au ribbon bonded to a 40GHz interconnect inside the cryostat as shown in figure 6.6. Figure 6.6 (a) shows an image of the cryostat that contains a 40 GHz coaxial cable with both male connectors inside. A thermometer is attached to the cable terminal to monitor the device temperature. Liquid nitrogen and helium can be transferred into the cryostat to cool the device via transfer tubes. Figure 6.6 (b) shows the interconnect that consists of three parts: Cu ground piece, Hermetic seal solder contact, and 2.92 mm female threaded connector [inset to figure 6.6 (b)]. The Hermetic seal solder contact is inserted into the pin hole of the 2.92 mm female connector to join the male connector of the 40 GHz coaxial cable. The Cu piece has inner threads that are used to connect the 2.92 mm female connector and provide the ground connection. The other pin of Hermetic seal solder contact protrudes out of the Cu piece through the ~2 mm diameter pin hole on the other end. Devices are silver painted on the Cu ground piece, and two Au ribbons connect the pin and ground to a device electrically. Figure 6.6 (c) shows an amplified optical image of the spin valve device with two Au ribbons bonded onto two electrodes. Figure 6.6 (d) shows an optical image of the Au bond on the pin of Hermetic seal solder contact. Because Au does not stick well to materials, special care is required to make Au ribbon bonds. I never
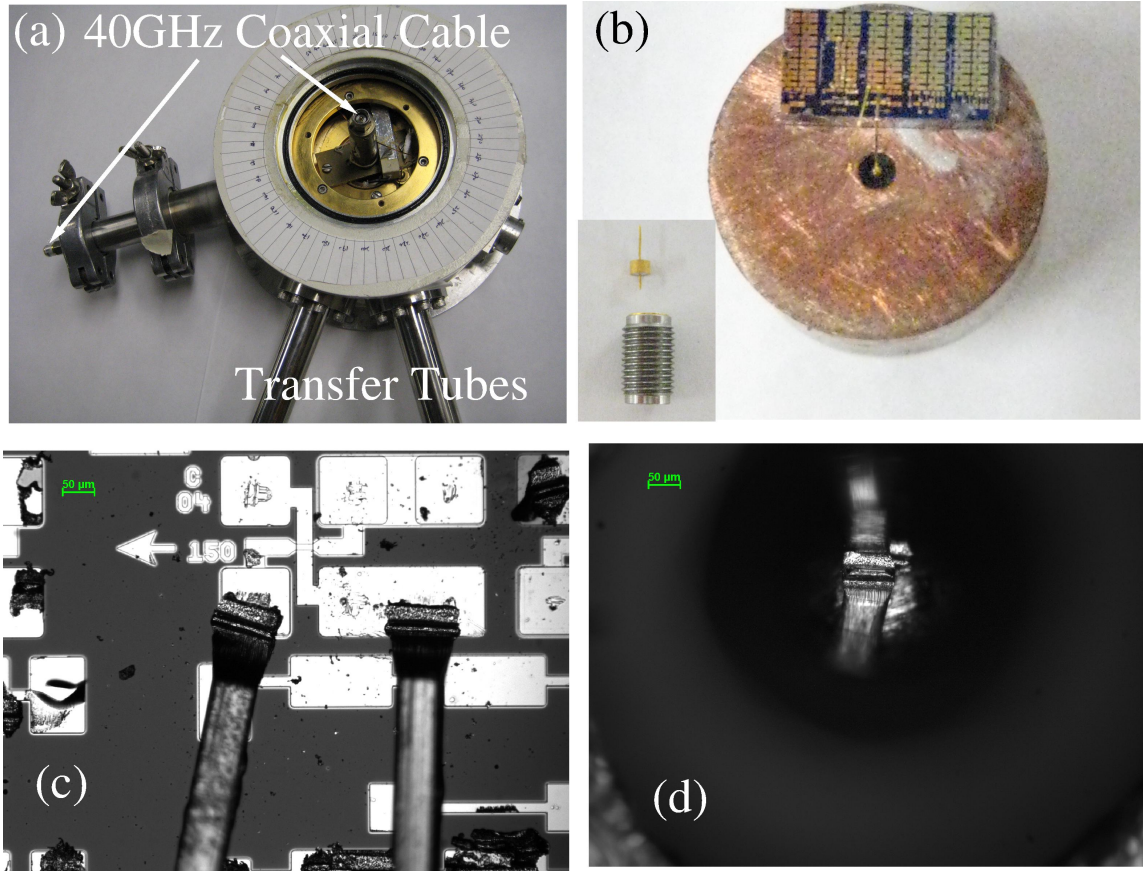
Figure 6.6   Images showing an experimental apparatus for low temperature and high frequency measurements. (a) Cryostat. (b) High frequency interconnect where a spin valve device is Au ribbon bonded on. (c) Image of two Au ribbons that are bonded on a device. (d) Image of a Au ribbon bonded on top of the pin.

succeeded in making Au ribbon bonds when the device and interconnect were at room temperature. Raising the temperature of all components to 65 - 75 °C helps make bonds easier. When all components are at an appropriate temperature (e.g., 70 °C), making Au ribbon bonds on device electrodes was successful most of the time. However making an Au ribbon bond on the pin takes much effort. Major problems are (i) Au ribbon bonds break easily at the bonding site; (ii) Au ribbon bonds do not stick well to the pin, primarily because the pin surface is not flat, but in a pyramid shape. Nonetheless, these problems can be solved by tuning vibration forces and power of the bonder. There are proper power and force making strong Au ribbons that stick as

well. Proper parameters were written in the lab notebook kept with the wire bonder. Bonding order is also an important factor to consider. Since bonding onto the pin is more difficult, a good bond order should bond onto the pin first, and then the device. The reverse order could ruin device electrodes during multiple trials.

Reflection measurements show that typical room temperature pulsewidths at the device are ∼30 ps, but due to cryostat bandwidth limitations the typical pulsewidths are ∼58 ps at 77 K. This pulse width broadening is mainly caused by the impedance mismatch between the coaxial cable and the device including the interconnect and ribbon bonds. However, in devices that are measured the small angle free precession period τ ∼300 ps (calculated from thin film measurements of saturation magnetization M_S and the nominal shape anisotropy) is much larger than the current pulse width τ_ω but comparable to the inter-pulse delay 0 ns $< t_D <$ 2 ns.

6.4.2   Measurement Procedures and Data Acquisition

Measurements of the nanomagnet switching probability (P_S) for single or pair of spin-transfer torque pulses is performed as follows. For each switching attempt, (i) the device is reset to the P state by applying a negative ∼300 ms current step; (ii) the device state is confirmed by measuring the resistance; (iii) a shaped waveform, consisting of either one or two current pulses is used to induce nanomagnet dynamics; and (iv) the final state of the multilayer is probed by measuring its steady state resistance. For all reported measurements the number of repetitions is chosen to ensure that the statistical error is smaller than 2%. It is known that at nonzero temperatures thermal excitations broaden the distribution of orientations of the "free" layer magnetization ($\vec{M}$) around the equilibrium direction. However, reproducibility in nanomagnet switching can be increased by applying transverse fields [39] or through inter-layer coupling [128]. Throughout all measurements in-plane transverse fields $H_\perp$ ∼175 Oe are applied to shift the parallel and anti-parallel fixed points of $\vec{M}$ (blue
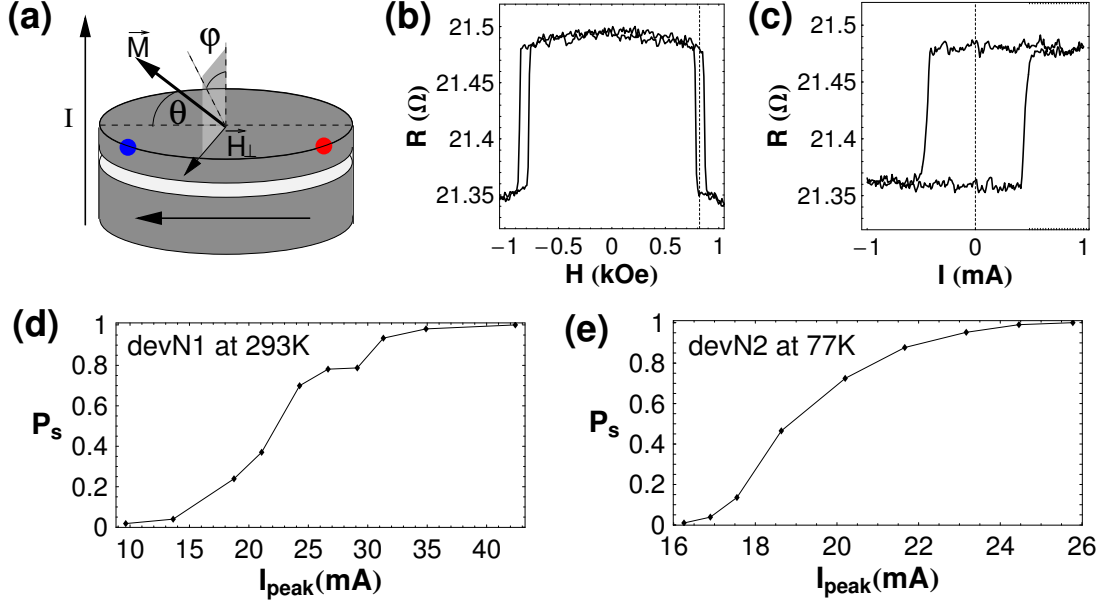
Figure 6.7 (a) Schematic of a type "N" nanopillar device. θ is the polar angle measured from the nanomagnet easy axis and φ is the azimuthal angle measured from the normal to the nanomagnet plane. A transverse field $H_\perp$ is applied to shift the red and blue stable points to a non-collinear configuration. (b) Resistance vs easy axis field for device N2 at room temperature. (c) Resistance vs current for device N2 at room temperature with $H_\parallel$=830 Oe and $H_\perp$=175 Oe. (d) P_S vs. single $\sim$30 ps FWHM pulse amplitude for device N1 at room temperature. (e) P_S vs. single $\sim$58 ps FWHM pulse amplitude for device N2 at 77 K.

and red dot respectively) away from the easy axis [Fig. 6.7(a)] to obtain a nonzero equilibrium angle between polarizer and free layer (non-collinear geometry).

6.4.3   Results and Discussion

Measurements of the type "N" $Co_{90}Fe_{10}$(8.7nm)/Cu(3nm)/$Co_{90}Fe_{10}$(2nm) spin transfer nanopillar devices are discussed. These devices are patterned into $\sim$150nm$\times$75nm ellipses as shown in figure 6.7(a). Antiferromagnetic dipolar field coupling between the thick layer (polarizer) and the "free" layer is canceled by biasing the devices with an easy axis magnetic field $H_\parallel$ $\sim$800 Oe [figure 6.7(b)]. The "free" layer can be switched between low resistance (parallel, P) and high resistance (anti-parallel,

AP) states via a spin-transfer torque from an applied dc current [figure 6.7(c)] with polarity defined in figure 6.7(a). Typical values of the four terminal P state resistance and of the magnetoresistance are 1.3 Ω and 9% respectively. The large resistance values shown in figure 6.7(b) and (c) are due to lead resistance together with inductive impedance in the experimental setup. First, a $\sim$100% P_S with single 30 ps pulses at room temperature is demonstrated. [figure 6.7(d)]. In particular, for devices with dc switching currents comparable to those previously reported [109, 194], a $P_S \approx$100% is achieved with pulse amplitudes two times smaller than expected from the assumption of pulsewidth and amplitude being inversely proportional [124, 138]. These results are supported by macrospin simulations which indicate that for the non-collinear geometry the pulsewidth-current product required for P_S =95% decreases by more than a factor of two when $\tau_w \ll \tau$. The reduction in pulse amplitude occurs because the effect of spin torque produced by longer pulses over a precession cycle is partially canceled. Depending on field bias, temperature, and device anisotropy, P_S shows either stepped [39] [figure 6.7(d)] or smooth [194, 109] [figure 6.7(e)], monotonic increase with increasing pulse amplitude. The stepped increase in P_S, predicted by theoretical simulations and previously observed in similar experiments as a function of pulse width (τ_ω >100 ps) [39], is caused by the underlying free precession orbits.

In order to explore the coherence of nanomagnet evolution, an ultrashort pulse is used to excite the magnetization dynamics, and a second ultrashort pulse of equal amplitude at different instants of the free precession orbit is applied. The switching probability of device N2 as a function of inter-pulse delay at room temperature and 77 K is shown in figure. 6.8(a) and (b). Since incoherent dynamics would lead to a delay-independent switching probability $P_2 = 1 - (1 - P_1)^2$ (with P_1 the single-pulse switching probability), measurement data indicates that coherent nanomagnet dynamics occurs even at room temperature. However, a striking difference between the slow change in P_S at room temperature and the clear oscillations and strong
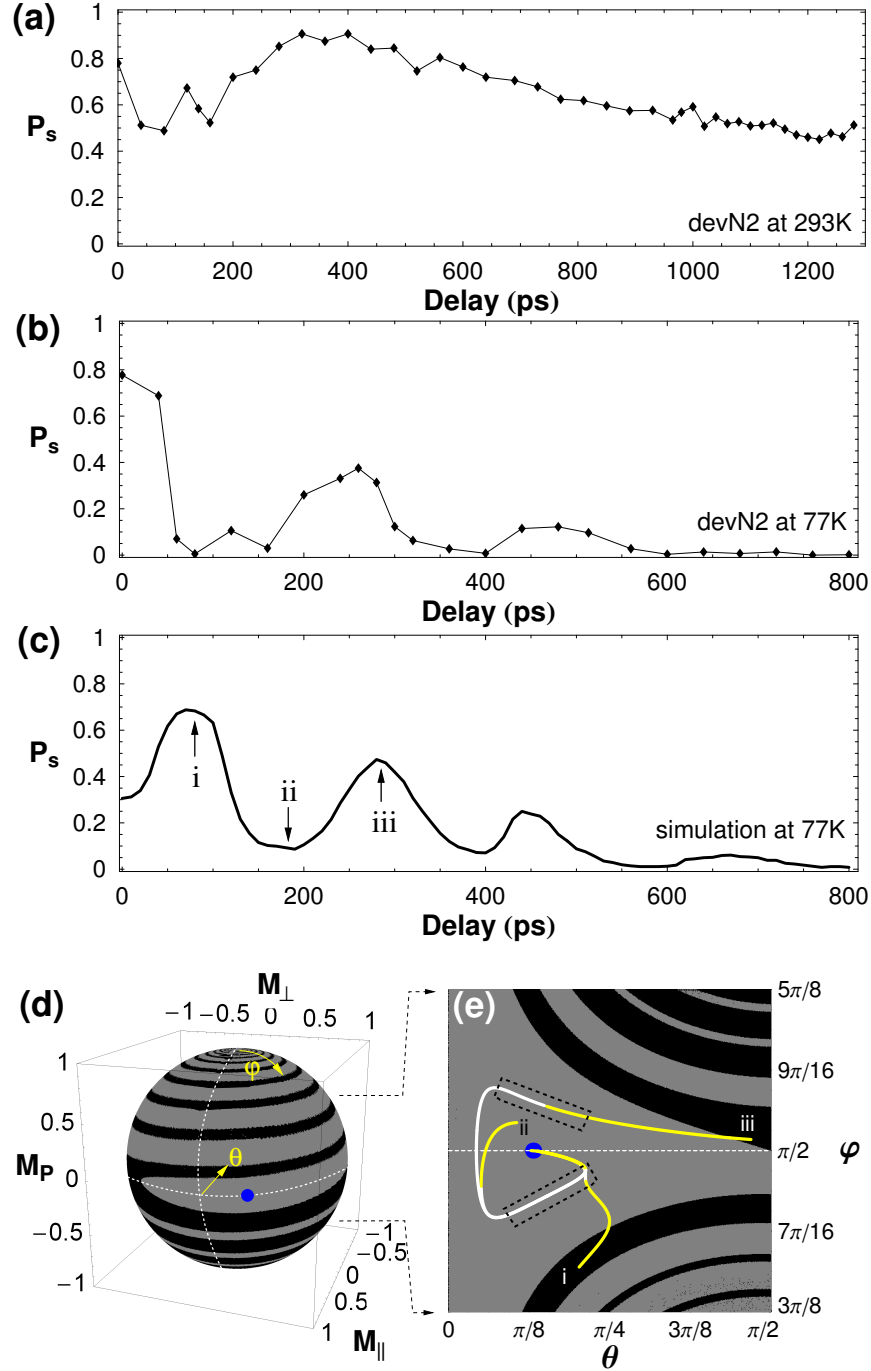
Figure 6.8 P_S of device N2 at (a) 293 K and (b) 77 K as a function of delay between two current pulses. (c) Simulated P_S vs. delay for two equal amplitude 58 ps FWHM pulses at 77K. Labeled regions correspond to the orbits shown in (e). (d) Phase portrait of $\vec{M}$ showing the basins of attraction for the two stable points P (blue) and AP (red, not visible). Initial conditions θ, φ within the gray (black) basin lead to no-switching (switching). (e) $\vec{M}$ trajectories generated by two current pulses of equal amplitude that have been delayed by 90 ps (i), 190 ps (ii), and 280 ps (iii). Rectangles enclose regions where a second pulse has high probability of switching $\vec{M}$.

modulation present at 77 K is observed . The devices described so far (type "N"), with dc switching currents $\sim$0.4 mA, have a small stability factor $\Delta = E_B/k_BT$ (with E_B the energy barrier between P and AP states), and thus are extremely sensitive to thermal effects. At room temperature, the probability of thermally assisted switching increases and the distribution of the initial orientations is much broader. While thermally-assisted switching only increases the baseline of P_S, the broadening of the distribution of initial orientations decreases the reproducibility of the trajectories at each repetition of the experiment, partially averaging out the delay dependence. This averaging explains why at room temperature type "N" devices typically show decay in P_S with increasing delay, and only small amplitude P_S oscillations.

To clearly demonstrate room temperature coherent control, similar measurements on type "E" devices, which have switching currents $\sim$2 mA and higher thermal stability, are performed. These devices (type "E") have an extended bottom layer, and are comprised of $[\text{Ni}_{80}\text{Fe}_{20}(20\text{nm})/ \text{Co}_{90}\text{Fe}_{10}(2\text{nm})]/\text{Cu}(10\text{nm})/\text{Co}_{90}\text{Fe}_{10}(3\text{nm})$, where the extended bottom layer [NiFe/CoFe] decreases the magnetic layer dipolar coupling. Typical traces of P_S as a function of delay are shown in figure 6.9(a) and (b) at room temperature and 77 K. Clear, large amplitude oscillations in P_S can be seen even at room temperature for up to 1 ns. Fourier analysis of the oscillations of device E1 (with nominal dimensions 150$\times$75 nm) at 77 K shows a fundamental period of 120 ps (ω=8.3GHz) and a much smaller 2ω harmonic. Since the precession period is twice the period of the P_S oscillations, $\tau \approx$240 ps for device E1. Similarly, for device E2 with nominal dimensions 160$\times$100 nm, $\tau \approx$330 ps. The precession periods obtained in this way are consistent with estimations based on thin film measurements of M_S and demagnetization coefficients of ellipsoidal nanomagents with the dimensions given above. At room temperature the switching probability of device E2 can be tuned between 4% and 93% by only adjusting the delay between pulses. The enhancement in the switching probability from 60% at zero delay (single pulse) to $\sim$94% at 120
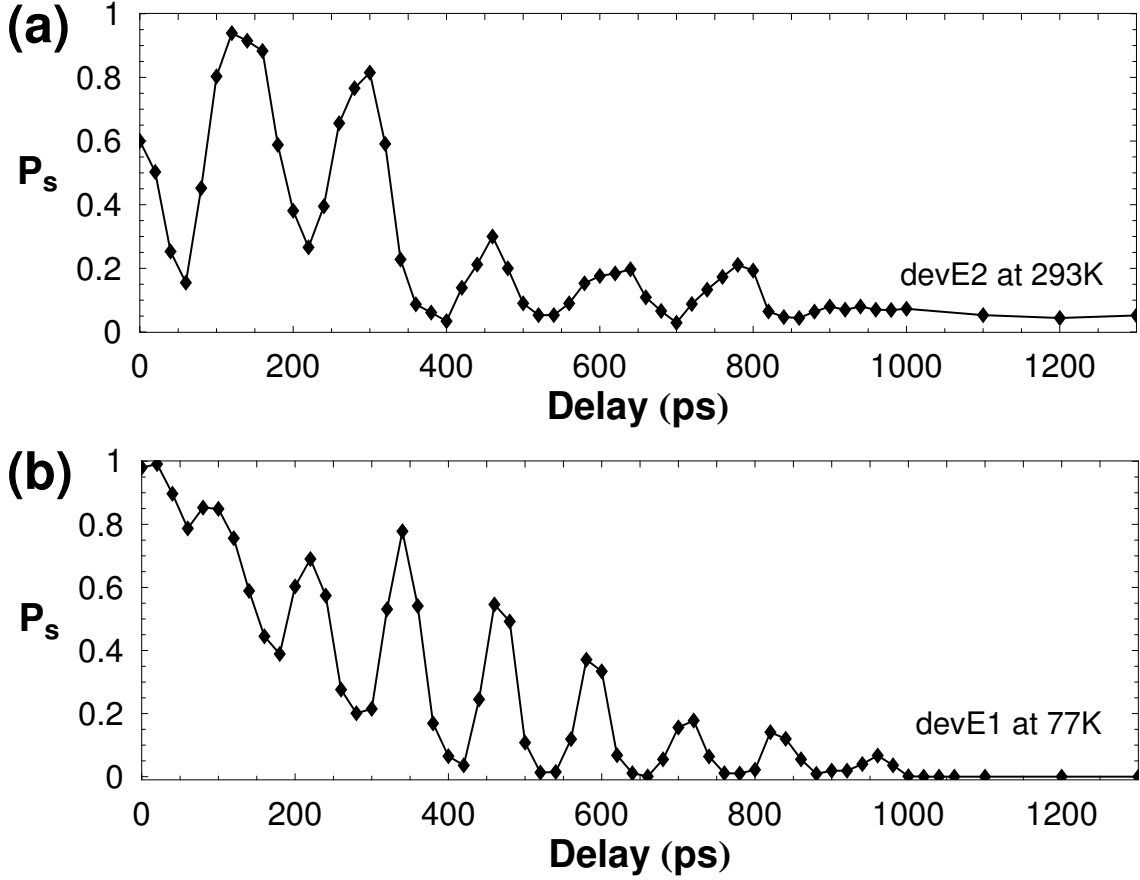
Figure 6.9 P_S vs. delay for extended bottom layer devices (a) E2 at room temperature, and (b) E1 at 77 K.

ps delay [figure 6.9(a)] has been measured while keeping the amplitude of the pulses constant. However, if the total energy delivered by the pulses is kept constant, a more dramatic enhancement in P_S from 10% to 70% at intermediate pulse amplitudes and from 40% to 95% at larger pulse amplitudes is observed. Therefore, multiple current pulses timed with the underlying coherent dynamics require less total energy than a single pulse to reproducibly switch spin transfer devices.

Increased control over the magnetization trajectory can be obtained by adjusting not only the pulses' timing but also their amplitude. We measure the switching probability as a function of the amplitude of a pair of pulses while keeping the delay (185 ps) and relative amplitude ($I_1/I_2 = 1$) constant [figure 6.10(a)]. P_S initially

114
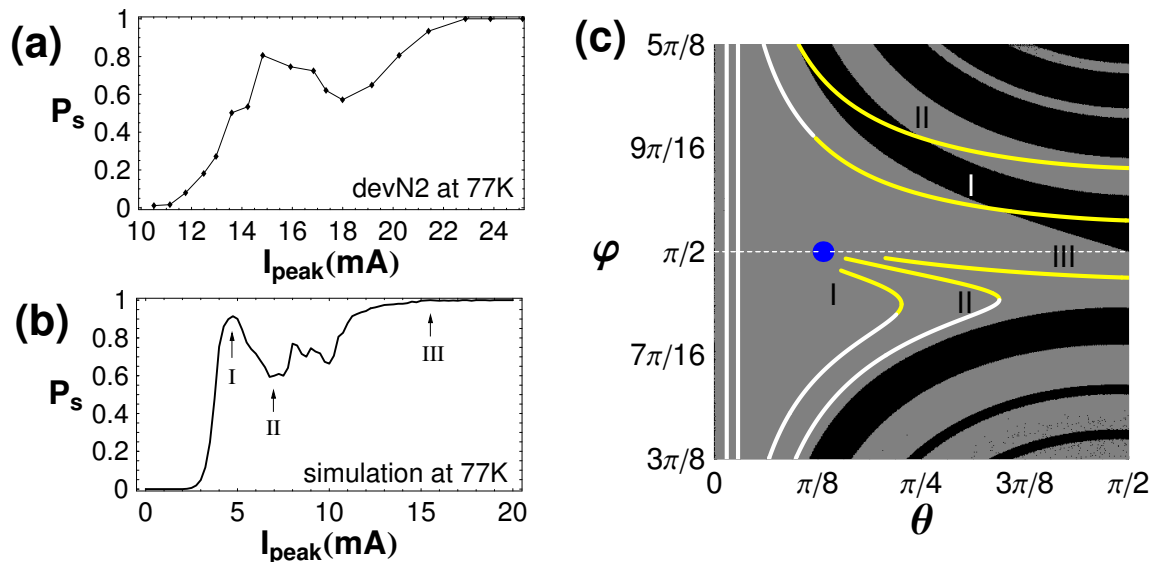
Figure 6.10   (a) P_S vs. pulse pair amplitude at 185 ps delay and 77 K for device N2. (b) Simulated P_S for situation described in (a) using the same parameters as figure 6.8(b). (c) $\vec{M}$ trajectories at labeled regions of (b) corresponding to pulse amplitudes of 4.8 mA (I), 6.8 mA (II), and 15 mA (III). Initial conditions are chosen randomly with a thermal probability distribution.

increases with increasing pulse amplitude, but after 15 mA it decreases from 80% to 55% before finally increasing to ∼100% at 23 mA. This counterintuitive result that increasing the spin torque leads to a decrease in the switching probability is fully consistent with coherent precession and is predicted by our simulations [figure 6.10(b)]. This agreement shows once more that in our system the macro-spin model captures the essence of nanomagnet dynamics. Typical magnetization trajectories at the three labeled regions of figure 6.10(b) are shown in figure 6.10(c). As the amplitude of the pair of pulses is increased from region I to region II [figure 6.10(b)], the state of $\vec{M}$ at the end of the second pulse moves from the black basin to a higher energy gray basin region, therefore decreasing P_S [figure 6.10(c)]. As the amplitude of the pulses is increased further to region III in figure 6.10(b), the first pulse produces enough spin torque to switch $\vec{M}$ [figure 6.10(c)]. These results suggest that by applying multiple short current pulses with controlled amplitudes and delays, the magnetization can be

deliberately moved into larger angle, higher energy orbits.

6.4.4 Simulations

To understand the origin of the oscillations, which are clearly observed at 77 K, theoretical simulations are performed to model the time evolution of the magnetization of a single domain nanomagnet driven by a perpendicular spin current [figure 6.7(a)] by using a modified Landau-Lifshitz-Gilbert equation which includes the Slonckzewski spin torque term with $g(\theta)=$ const [203, 212]. Simulations assume that the magnetization of the polarizer is fixed, and consider the effect of nonzero temperatures only on the distribution of initial orientations of $\vec{M}$ (via a Monte Carlo method) but not on the evolution of $\vec{M}$, which is assumed to be completely deterministic. As shown in figure 6.7(a), $\vec{M}$ is described by θ, the polar angle measured from the nanomagnet easy axis, and φ, the azimuthal angle measured from the normal to the nanomagnet plane [212]. $\vec{M}$ has fixed points at $\varphi = \pi/2$ and $\theta = \arcsin H_\perp/H_k$ with H_k the easy axis anisotropy field. The phase portrait of $\vec{M}$ in the absence of spin torque is shown in figure 6.8(d)[10]. The black and gray regions, which are the basins of attraction for the red and blue minimum energy points, are wrapped around each other, emphasizing the final state's large sensitivity to fluctuations in the initial orientation of $\vec{M}$ (i.e. thermal effects).

Simulations of the delay dependence of P_S for a pair of pulses with equal amplitude at 77 K [figure 6.8(c)] show oscillations with delay that agree qualitatively with our observations [figure 6.8(b)]. Typical trajectories at consecutive maxima and minima of P_S, regions labeled i, ii, and iii, in figure 6.8(c) are shown in figure 6.8(e), where the section $3\pi/8 < \varphi < 5\pi/8$ of the phase portrait shown in figure 6.8(d) has been stretched into a plane. The initial condition and first pulse (in yellow) are equivalent for all trajectories, but the second pulse (also in yellow) is applied at different times ($t_D = $90 ps, 190 ps, and 280 ps). The free evolution between the two pulses is shown

in white. There are two regions (dashed boxes in figure 6.8(e) where the second spin torque pulse can more effectively induce basin boundary crossing and lead to magnetization reversal. As indicated by trajectory ii, a second pulse applied outside of the marked regions can even push $\vec{M}$ closer to the blue fixed point, reducing the effect from the first pulse. These simulations illustrate how in the non-collinear geometry, when a pulse with a width larger than the free precession period is used for nanomagnet switching, partial cancellation of the effect of spin torque occurs, decreasing the switching probability.

CHAPTER 7

EXTENDED WORK ON ULTRAFAST NANOMAGNET

DYNAMICS

In the previous chapter, I discussed coherent control of nanomagnet dynamics using ∼30 ps spin-transfer torque pulses. In this chapter, I present measurements to study magnetic dynamics while the damping is canceled by adding another 5 ns duration pulse that is precisely timed with the two 30 ps STT pulses. A pair of oppositely polarized 30 ps STT pulses with a relative time delay are also generated to investigate the magnetic dynamics. Finally I describe research work that attempts to study nanomagnet demagnetization by combining picosecond STT pulses with femtosecond optical pulses.

7.1 TIME-DOMAIN SAMPLING MEASUREMENTS OF NANOMAGNET DAMPING CANCELLATION VIA SPIN-TRANSFER TORQUE

Spin-polarized electrons passing through a nanomagnet (nanoscale ferromagnet) exert a spin-transfer torque (STT) [202, 13] on the local magnetization. In contrast to external field torques, STT can be largely collinear with the Landau Lifshiftz Gilbert damping torque [179], allowing control over damping [128, 189], in addition to driving precession and switching [223, 113]. Spin torque's ability to coherently cancel the damping torque holds great potential for applications of nanopillars in high stability, low-linewidth microwave oscillators [114]. Whereas for ac driven oscillators the linewidth depends directly on damping, linewidths of dc driven oscillators are domi-

nated by trajectory dephasing [190, 189]. Measuring and understanding the effects of damping and dephasing is critical for minimizing oscillator linewidths and maximizing their power output [95]. At low temperatures, time-domain [128] and ferromagnetic resonance (FMR) measurements [189] of spin-valve nanopillars have demonstrated spin torque induced damping reduction. Here, the damping cancellation at room temperature by using a pulsed time domain technique is demonstrated: two ultrafast (30 ps) spin torque impulses excite nanomagnet dynamics and the switching probability P_S is measured as a function of relative pulse-pulse delay [66]. A comparison in damping cancellation using a 5 ns current pulse and a dc current is made. While both approaches reduce the damping, the trajectory dephasing and thermal switching that occur with dc currents, prevent observing the damping over the full range of spin torque amplitudes where damping cancellation occurs. However, the 5 ns pulse, at amplitudes well above the "dc" critical current, can cancel the effective damping and yield coherent dynamics over a maximum time window of 2.2 ns.

7.1.1 Experimental

Spin-valve nanopillar devices with elliptical cross section are fabricated using e-beam lithography and ion milling. The devices are composed of an extended $Ni_{80}Fe_{20}(20$ nm$)/Co_{90}Fe_{10}(2$ nm$)$ polarizer which provides a large magnetic moment to improve its stability, a 10 nm Cu spacer, and a 3 nm $Co_{90}Fe_{10}$ "free" layer or nanomagnet [Inset to Fig. 7.1(c)]. A typical plot of resistance vs. field is shown in Fig. 7.1(a), where the large vertical arrows indicate free layer switching between P and AP states (largely parallel or anti-parallel to the polarizer). The small dashed and solid arrows represent the orientation of the free layer, $\mathbf{m}$, and polarizer, $\mathbf{m_p}$, respectively. The measured Stoner-Wohlfarth astroid for devices indicates that the polarizer follows the applied field, reversing orientation around zero field [small dips in resistance in Fig. 7.1(a)]. Polarizer reversals near zero field, along with considerable interlayer dipole coupling,

(a)

(b)

(c)

(d)
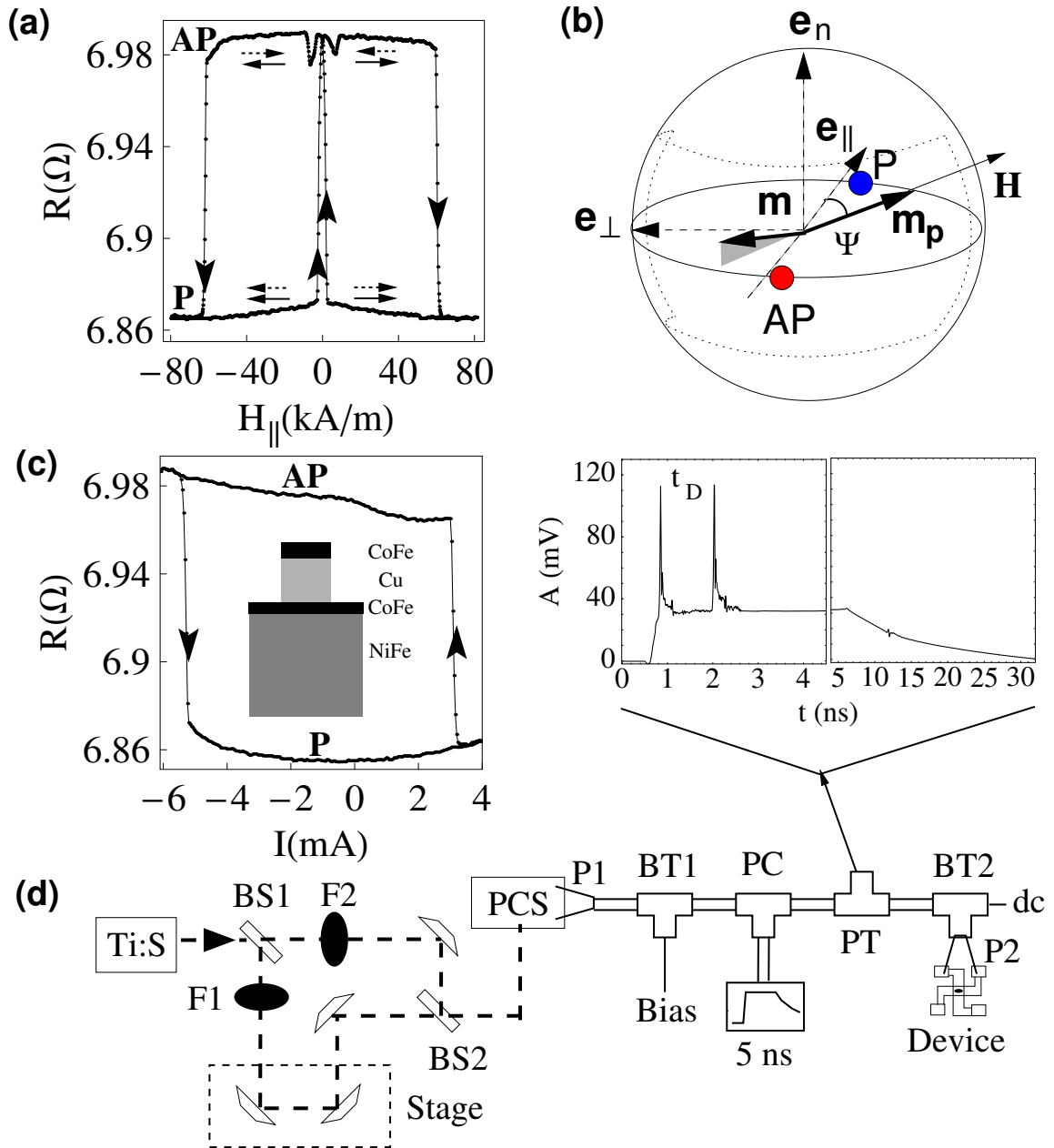
Figure 7.1 **Device characterization and experimental setup.** (a) Resistance vs easy-axis magnetic field, $H_\parallel$, for a typical device at room temperature. (b) Schematic describing the orientation of the polarizer $\mathbf{m_p}$ and P, AP stable points. $\mathbf{m_p}$ tracks the applied field, H. (c) Resistance vs. dc current for device shown in (a) with H=46 kA/m and $\Psi \sim 12$ degrees. Inset: device schematic. (d) Experimental setup for time-resolved measurements of spin torque switching with damping cancellation. Inset: voltage waveform (ultrafast pulse pair plus 5 ns pulse) measured at a pick-off tee before the device.

are responsible for the two symmetric loops at positive and negative fields. For all STT measurements an in-plane magnetic field H at a small angle $\Psi \sim 10$ degrees with respect to the easy axis $\mathbf{e}_\parallel$ [Fig. 7.1(b)] is applied to cancel the polarizer's dipolar field, facilitate AP-P current induced switching, and set the orientation of the polarizer to obtain a non-collinear geometry, increasing switching reproducibility [66]. For the values of H used throughout all experiments the orientations of points P and AP are displaced less than 3 degrees from $\mathbf{e}_\parallel$ due to the easy axis anisotropy of the free layer. Current, defined as positive when flowing across the multilayer from top to bottom [inset to Fig. 7.1(c)] can be used to switch the nanomagnet via STT [179]. A typical resistance vs dc current loop [Fig. 7.1(c)] shows sharp transitions between the P and AP states and a ~ 8 mA wide region of bistability. Four terminal measurements of the P state resistance and magnetoresistance give typical values ~ 1.6 Ω and $\sim 7\%$ respectively. The large two terminal resistance values in Figs. 7.1(a), (c) are due to lead resistance and inductive impedance of the bias tees shown in Fig. 7.1(d).

To generate ultrafast spin torque current pulses an amplified Ti:Sapphire mode-locked laser (120fs FWHM, ~ 1.6mJ per pulse) in single-shot mode is used [Fig. 7.1(d)] . An optical pulse is split into two separate pulses at the first beamsplitter (BS1), with each pulse having independently controlled amplitudes via tunable optical filters (F1, F2). A sub ps resolution variable optical delay t_D between the pulses is produced with a translation stage, after which the beams are recombined at BS2 and focused onto a Au photoconductive switch (PCS) [6]. The two PCS generated electrical pulses (14.9 mA, ~ 30 ps FWHM) are sent through a 40 GHz coplanar-to-coaxial probe (P1) to the PCS bias tee (BT1) with 12 ps risetime and 40V dc switch bias. A power combiner (PC) can add a 25ps risetime, 5 ns duration pulse to the pulse pair, and the resulting signal is then transmitted to the nanomagnet through a 40GHz network which includes a pick-off tee (PT) for pulse monitoring [Fig. 7.1(d)] and a second 40 GHz bias tee (BT2) for injecting dc and low frequency ac currents for

device switching and lock-in amplifier measurement of nanopillar resistance. Device connection is made with a second 40GHz coaxial-to-coplanar probe (P2). For each measurement, the device is reset to the AP state by using a low frequency current ramp, verify the state of the device by measuring its resistance, send a pair of ultrafast pulses together with either a 5ns duration pulse or a dc current, and measure the final state of the device: P or AP.

7.1.2 Results and Discussions

As explained in Ref. [66], the first ultrafast pulse displaces **m** away from AP. After a controlled time delay the second ultrafast pulse displaces **m** once again. By varying the delay the switching efficiency of spin torque at different average orientations of **m** is measured. Hundreds of switching events for each delay are measured to keep the statistical error below 2%. The bandwidth of the technique, currently 40 GHz, depends on the pulse duration and can be extended to over 0.8 THz [162, 226]. Coherent oscillations of P_S with delay are shown in Fig. 7.2(a). Here the oscillating peaks in P_S, always <40%, decrease dramatically after 0.6 ns and disappear before 1 ns.

DC currents together with two ultrafast pulses are applied to decrease the nanomagnet damping via STT [128, 189]. For 0.6 mA dc current [Fig. 7.2(b)], an additional peak at t_D=1.1 ns is observed , while the existing peak amplitudes (at 0.6, 0.78, and 0.94 ns) increase, suggesting that the dc STT indeed reduces the damping. As for zero dc current, here P_S decreases to 0% between successive peaks, meaning that the dc current alone does not cause switching. For 1.6 mA dc currents, just below the "dc switching current" of 1.8 mA [Fig. 7.2(c)], P_S no longer goes to zero at the minima, and although the earlier peak amplitudes again increase, the peaks at 0.94 and 1.1 ns show little to no increase relative to the background. As 1.6 mA is close to the dc switching current, i.e. P_S=100% without ultrafast pulses, the current
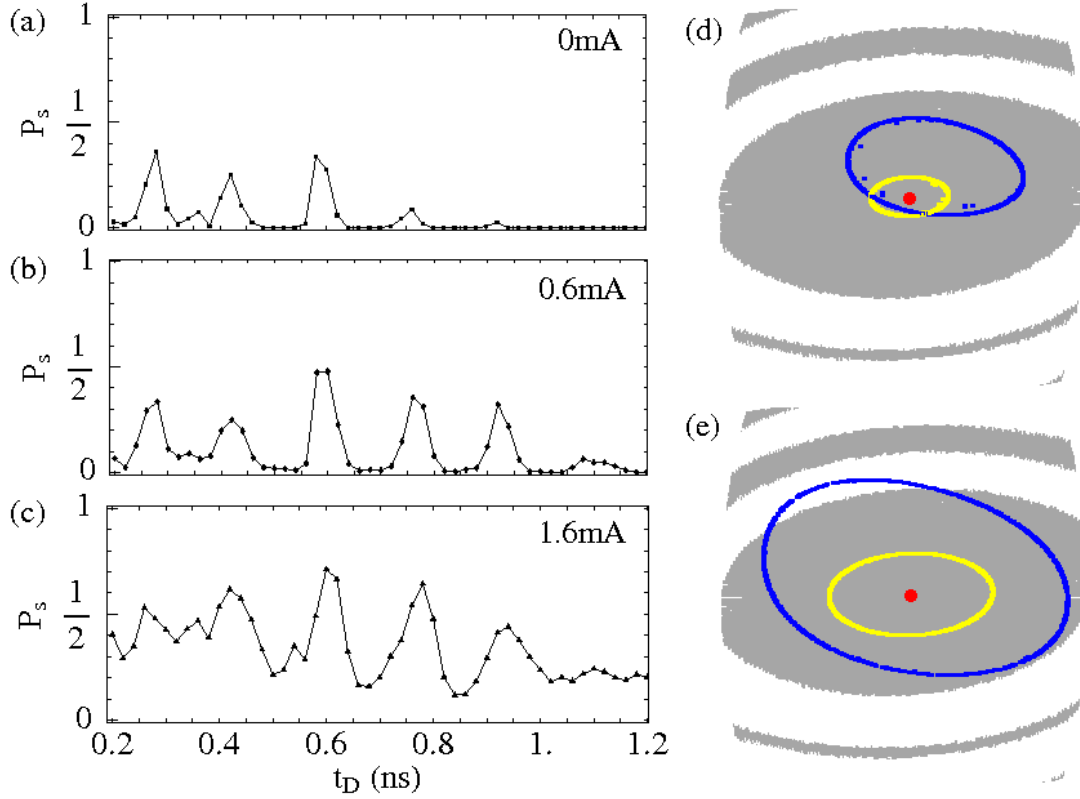
Figure 7.2 **dc current effective damping reduction** (a)-(c) P_S vs delay between two ∼30 ps duration pulses for dc currents of (a) 0 mA, (b) 0.6 mA, and (c) 1.6 mA at room temperature. The "dc switching current", measured using a sweep rate of 0.05 mA/s is ∼1.8mA. (d)-(e) Sections of the free layer moment phase portrait for the dotted region of Fig. 7.1(b) with a dc current. A **m** ensemble long after applying a dc current and the same ensemble just after applying the first ultrafast pulse are respectively shown in yellow and blue. In (d) I_{dc}=1.1 mA, while in (e) I_{dc}=1.2 mA.

cannot be further increased to observe complete elimination of damping. Macrospin simulations shown in Fig. 7.2(d), (e) suggest that long after applying a dc current, the **m** ensemble is uniformly distributed along a stable precessional orbit (yellow), i.e. the individual trajectories are no longer phase coherent with respect to the arrival of the first ultrafast pulse. For small currents the first ultrafast pulse broadens and shifts the dephased **m** ensemble away from AP [blue dots in Fig. 7.2(d)]. Since the ensemble is far from the switching boundary, the second pulse does not always lead to switching and P_S goes to zero at certain delays. For dc currents below the

instability threshold the same behavior is observed. However, for large currents, the first pulse broadens the **m** distribution pushing part of the ensemble near (and even across) the switching boundary [blue dots in Fig. 7.2(e)], and thus the second pulse always leads to nonzero switching probability. In addition, for large dc currents the ensemble is more symmetrically distributed around AP, rather than shifted in a particular direction [compare blue dots in Figs. 7.2(d), (e)], and thus the modulation of P_S with delay will decrease. Therefore trajectory dephasing with dc currents restricts the observation of damping reduction using a time-resolved sampling technique.

To demonstrate coherent damping cancellation and reduce the impact of trajectory dephasing, the dc current is replaced with a 25 ps risetime, 5 ns duration current pulse. The 25 ps risetime allows us to precisely time the first ultrafast pulse with the beginning of the 5 ns pulse throughout all measurements (see inset above Fig. 7.1(d)). As shown in Figs. 7.3(a)-(b), P_S is now measured vs. delay for different 5 ns pulse amplitudes, I_{5ns}. In both cases, I_{5ns} is greater than the "dc" switching current, and in sharp contrast with Figs. 7.2(b)-(c), Figs. 7.3(a)-(b) show near constant amplitude P_S oscillations persisting out to the maximum delay, t_D=2.2 ns. Note in Figs. 7.3(a)-(b), when the 5 ns pulse is used for damping cancellation, as for the 1.6 mA dc bias case, there is a nonzero P_S background. However, for I_{5ns} = 2.16 mA, well above the "dc" switching current, the value of the P_S background is comparable to I_{DC} = 1.6 mA, but the amplitude of the peak at 1.1 ns has increased to 25%, compared with < 10 % for I_{DC} = 1.6 mA. Moreover, in this case, P_S=0% when only the 5 ns pulse is applied. These differences illustrate how the dephasing intrinsic to the dc measurements reduces the visibility of P_S modulation with delay.

For the 5 ns pulse data, three distinct P_S regimes as a function of time are identified: (i) below 0.6 ns, the P_S maxima are irregular and increase with increasing delay, (ii) between 0.6-1 ns the P_S oscillations monotonically decrease with increasing delay, and (iii) above 1 ns the oscillation amplitude is almost constant and shows a

124

minimal decrease at longer t_D. As shown in Fig. 7.3(c), for short delays the $\mathbf{m}$ ensemble resulting from the second pulse is displaced to the second gray non-switching region (blue/dashed line). As t_D increases, the section of the ensemble within the first white switching band gets larger and thus P_S increases (regime i). As t_D increases further [Fig. 7.3(d)], the $\mathbf{m}$ ensemble resulting from the second pulse is not pushed as far away from AP, and the $\mathbf{m}$ ensemble lies between the inner gray and first white band. In this case, P_S decreases monotonically since for larger delays the ensemble has a smaller part in the white switching band (regime ii). Once $\mathbf{m}$ reaches its stable orbit at 1.2 mA, the P_S modulation amplitude is almost constant, with further decay caused by "dephasing" similar to that seen with dc currents (regime iii). These simulations suggest experimental data are consistent with complete damping cancellation over a range of currents.

The analysis ignores thermal effects on the magnetic moment motion. Thermal fluctuations will introduce a stochastic component into the magnetization trajectories, broadening the $\mathbf{m}$ distribution further [25]. This broadening can also contribute to the existence of a nonzero P_S background, and for long delays it will produce additional dephasing of the trajectories and eventually a disappearance of the P_S oscillations.

7.2 ASYMMETRIC DELAY DEPENDENCE IN ULTRAFAST NANOMAGNET DYNAMICS EXCITED BY OPPOSITELY POLARIZED PICOSECOND SPIN TORQUE IMPULSES

Spin-polarized electrons passing through a nanomagnet (nanoscale ferromagnet) exert a spin-transfer torque (STT) [202, 13] on the local magnetization, driving the nanomagnet magnetic precession and switching [223, 113]. This offers a promising writing scheme for high frequency spin torque oscillators and nonvolatile magnetic random access memory (MRAM) devices. Nanosecond STT pulses have been applied to study the nanomagnet switching [2, 40, 111], and two 30 ps STT pulses with equal amplitudes and same polarities can be used to coherently control the mag-
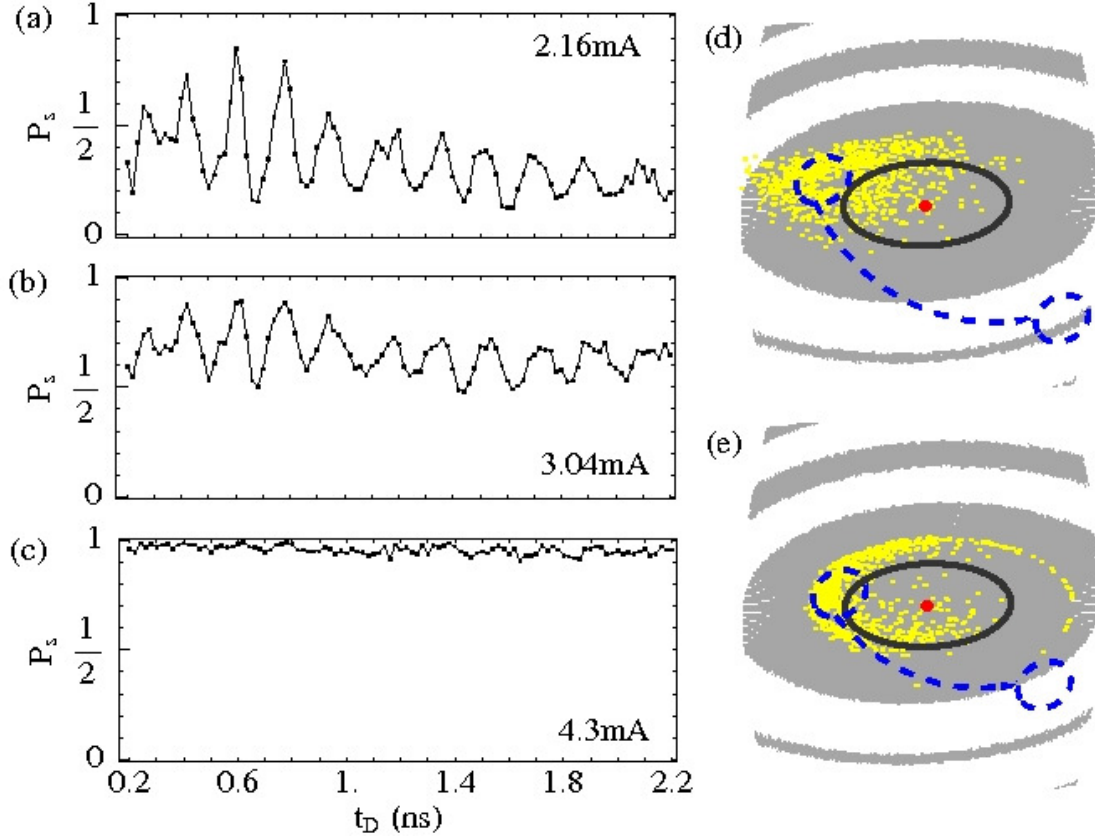
Figure 7.3 **5 ns pulse effective damping reduction** (a)-(b) P_S vs delay for 5ns duration pulse amplitudes of (a) 2.16 mA and (b) 2.71 mA. (c), (d) Sections of the free layer moment phase portrait for the dotted region of Fig. 7.1(b), in the presence of a 1.2 mA 5ns duration pulsed current. Yellow dots represent the **m** ensemble just before the second ultrafast pulse for (c) t_D=140ps and (d) t_D=580 ps. The solid dark line represents a stable orbit at 1.2mA while the blue (dashed) regions schematically represent regimes (i) and (ii) described in the text.

netic dynamics where the switching dynamics is symmetric with respect to interpulse delay [66]. However, by using two oppositely polarized 30 ps STT impulses, the nanomagnet switching dynamics exhibiting asymmetric delay dependence are experimentally demonstrated.

7.2.1   Experimental

Three batches of spin-valve nanopillar devices with nominal elliptical cross sections 150×75nm, 125×75nm and 160×100nm were fabricated using e-beam lithography
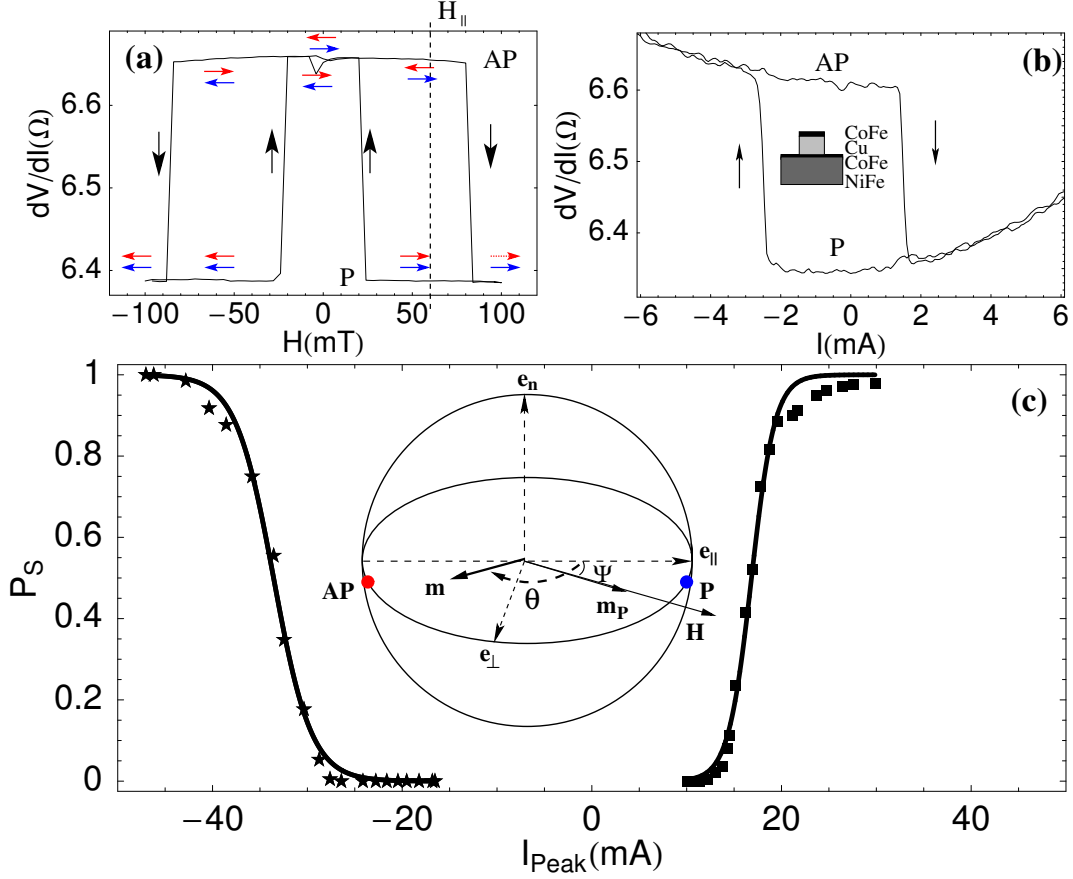
Figure 7.4 **Device characterization.** (a) Resistance vs easy-axis magnetic field, H. (b) Resistance vs dc current with $H_\parallel$=65 mT and $\Psi \sim 8$ degrees. Inset:device schematic. (c) P_S vs single pulse amplitude current for the device in the same configuration shown in (b). Stars (squares) are for negative (positive) pulses. Solid lines are the fit of the data with a Fermi function. Inset: schematic describing the orientation of the polarizer $\mathbf{m_p}$ and P (blue dot), AP (red dot) stable points. θ is the angle that $\mathbf{m}$ makes with $\mathbf{e_\parallel}$. $\mathbf{m_p}$ tracks the applied field, $\mathbf{H}$.

and ion milling. All devices are composed of an extended $Ni_{80}Fe_{20}$ (20 nm)/$Co_{90}Fe_{10}$ (2 nm) polarizer which provides a large magnetic moment to improve its stability, a 10 nm Cu spacer, and a 2 nm $Co_{90}Fe_{10}$ "free" layer or nanomagnet [Inset to Fig. 7.4(b)]. A typical plot of the device resistance vs field is shown in Fig. 7.4(a), where the vertical arrows indicate the free layer switching between P and AP states (largely parallel or anti-parallel to the polarizer). The small red and blue arrows represent the orientation of the free layer, $\mathbf{m}$, and polarizer, $\mathbf{m_p}$, respectively [Inset to Fig. 7.4(c)].

The measured Stoner-Wohlfarth astroid for devices indicates that the polarizer follows the applied field, reversing orientation around zero field [small dips in resistance in Fig. 7.4(a)]. Polarizer reversal near zero field, along with considerable interlayer dipole coupling, are responsible for the two symmetric loops at positive and negative fields. For all STT measurements we apply an in-plane magnetic field $H_\parallel$ [Fig. 7.4(a)] at a small angle $\Psi \sim 8$ degrees with respect to the easy axis $\mathbf{e}_\parallel$ [Inset to Fig. 7.4(c)] to cancel the polarizer's dipolar field, facilitate AP-P current induced switching, and set the orientation of the polarizer to obtain a non-collinear geometry, increasing switching reproducibility [66]. For the values of $H_\parallel$ used throughout all experiments the orientations of points P and AP are displaced less than 5 degrees from $\mathbf{e}_\parallel$ due to the easy axis anisotropy H_K of the free layer. Current, defined as positive when electrons flow across the multilayer from bottom to top [inset to Fig. 7.4(b)], can be used to switch the nanomagnet via STT [179]. A typical resistance vs dc current loop [Fig. 7.4(b)] shows sharp transitions between the P and AP states and a ~ 6 mA wide region of bistability. Four terminal measurements of the P state resistance and magnetoresistance give typical values $\sim 1.85\Omega$ and $\sim 13\%$ respectively. The large two terminal resistance values in Figs. 7.4(a) and (b) are due to lead resistance and inductive impedance of the measurement setup.

Laser pulses [120fs full width at half maximum (FWHM)] in single-shot mode are focused onto two Au photoconductive switches [6] to generate two oppositely polarized ~ 26 ps current pulses. A sub ps resolution variable optical delay t_D between the pulses is produced with a translation stage. The ultrafast electrical pulses are transmitted to the nanomagnet through a 40GHz network. Pulse reflection measurements show the pulse width through the nanomagnet is ≤ 30 ps. For each measurement the device is reset to the AP/P state by using 100ns duration pulses, verify the state of the device by measuring its resistance, wait 100ms, send ultrafast pulses and measure the final state: P or AP. In experiments at least one thousand switching events for

each switching probability (P_S) are measured to keep the statistical error below 1.5%. All measurements are performed at room temperature and all data shown here are from the representative device with 125×75nm cross section. Measurements on other devices show similar behavior qualitatively.

7.2.2 Results and Discussion

First single pulse P_S with respect to pulse amplitudes is measured. Positive pulses attempt to switch **m** from AP to P states (AP-to-P) [Fig. 7.4(b)], and P_S increases monotonically with the pulse amplitude (I_{Peak}) as I_{Peak} is increased over the amplitude threshold of ∼11.4mA. P_S reaches ∼100% at ∼30mA [squares in Fig. 7.4(c)]. P-to-AP switching via single negative pulses is analogous [stars in Fig. 7.4(c)]. However the amplitude threshold for negative pulses is larger than that for positive pulses, since the angular dependence of STT on θ [inset to Fig. 7.4(c)] is not symmetric with respect to the device hard-axis [202]. For both pulse polarities, the data fit better with a Fermi function [solid lines in Fig. 7.4(c)] than a simple exponential function.

A STT waveform consisting of a pair of the oppositely polarized 30 ps pulses (p1 and p2 in the inset to Fig. 7.5) is employed to measure P_S as a function of interpulse delay t_D. In the discussion below I focus on AP-to-P transitions, keep p1 (I_{Peak}=-15.1mA) at t_D=0ps, and scan p2 (I_{Peak}=17mA). For t_D <0 (i.e., p2 arrives before p1), P_S increases monotonically with $|t_D|$ from $|t_{D1}|$=∼80ps to $|t_{D2}|$=∼260ps and then remains constant at 50%, the single p2 P_S alone [stars in Fig. 7.5]. This occurs because p2 attempts to switch **m** to P, while the subsequent p1 endeavors to drive **m** back towards AP, and the eventual **m** state is determined by the magnetic evolution excited by both pulses. Longer relative delay means the less probability that p1 kicks **m** back to AP. This is supported by macrospin simulations using the modified Landau-Lifshitz-Gilbert equation including a Slonczewski spin torque term. In the simulation I consider the effect of 300K temperature on the distribution of initial
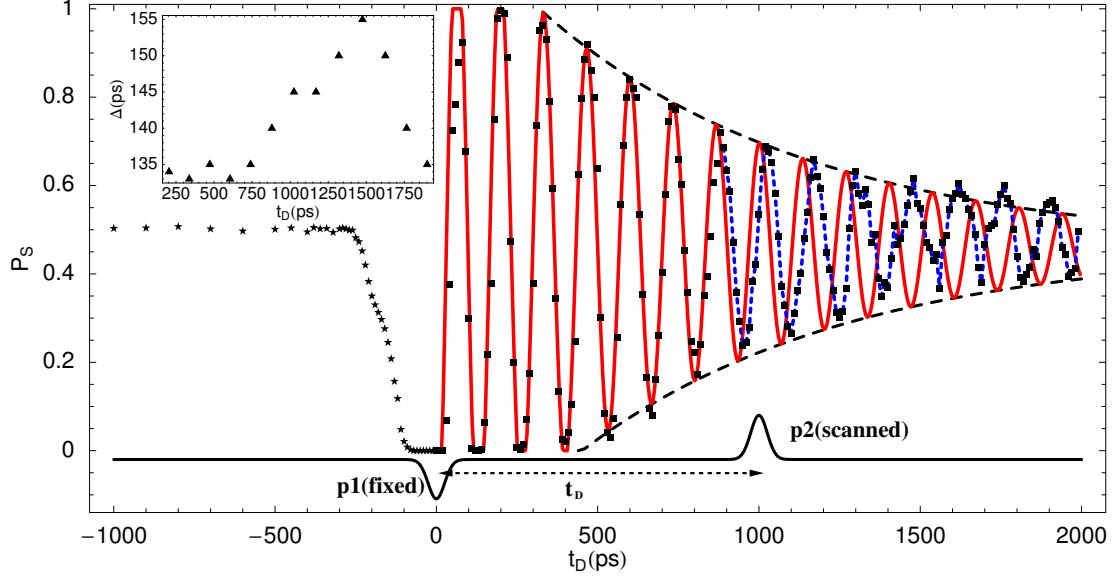
Figure 7.5 **Asymmetric delay dependence in** P_S**.** The device is in the same configuration shown in Fig. 7.4(b). Squares (stars) denote P_S vs t_D for $t_D \geq 0$ (<0) excited by a pulse pair consisting of two oppositely polarized 30 ps pulses, i.e., p1 and p2, as shown in the bottom inset. Red solid line represents the fit. The squares for $t_D \geq 900$ps are joined plotted with the blue dashed line on purpose of guide to eye. Two black dashed lines display envelopes of fit P_S peaks and dips respectively. Top inset: triangles denote the time difference of consecutive peaks vs t_D.

orientations via a Monte Carlo method and the evolution of **m** through stochastic fields. The stochastic field is assumed to obey the Gaussian process, i.e., each spatial component of the stochastic field has a zero mean Gaussian distribution and strength of fluctuations that equals $\sqrt{2\alpha k_B T/[(1+\alpha^2)\gamma M_S V dt]}$, where k_B is the Boltzmann's constant, T=300K, V is the nanomagnet volume and dt is the numerical evolution time step. As shown in Fig. 7.6(a), the black solid line displays the simulated θ evolution of single trajectory in the presence of only p2 starting from 0ps ending up with switching. However if p1 is applied at t_D=120ps (red dashed line) when **m** has not evolved beyond the device hard-axis (i.e., $\theta=\frac{\pi}{2}$), p1 drives **m** back to AP (red solid line). Similarly if p1 arrives at t_D=400ps (blue dashed line) when θ is $< \frac{\pi}{2}$, p1 enlarges θ, but is not able to pull **m** back to AP, and thus a switching event occurs (blue solid line). Depending on the initial condition of **m**, H_K, temperature

130
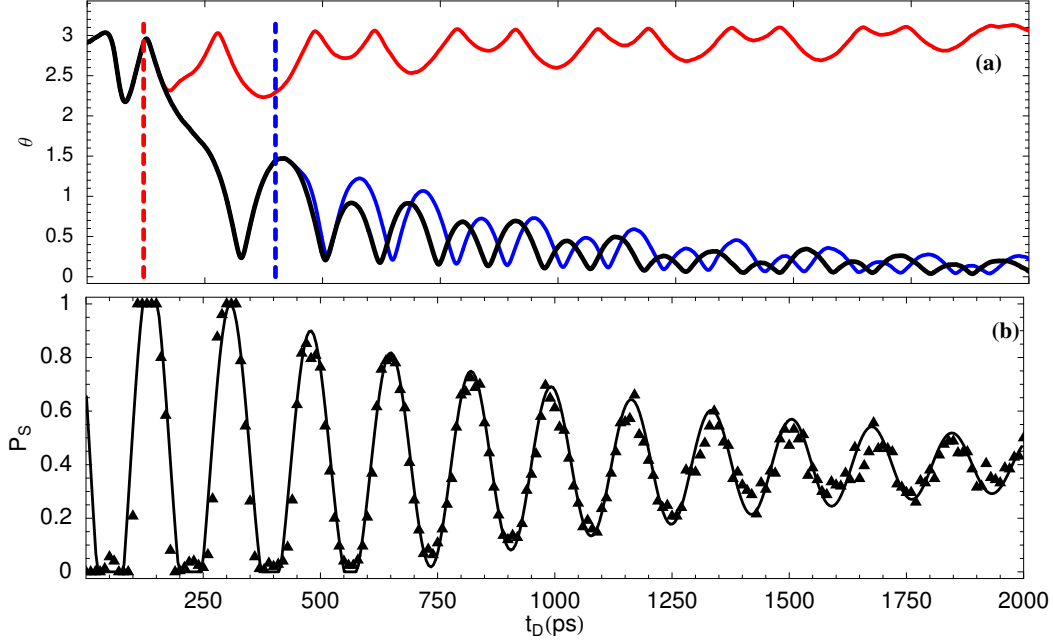
Figure 7.6 **Macrospin simulation results.** (a) Simulated θ vs delay for p2 arrives before p1 ($t_D < 0$). The black line denotes θ for single p2 and red (blue) line for the pulse pair with $|t_D|$ =120ps (400ps). (b) Triangles denote the simulated P_S vs t_D and the solid line represents the fit.

and field bias, in the case of single-p2 switching events, possibilities for p1 to pull **m** back to AP even p1 arrives at a moment when θ is $< \frac{\pi}{2}$ are also observed.

However there is a quite different switching behavior for $t_D > 0$ (i.e., p1 arrives before p2) [squares in Fig. 7.5]. P_S oscillates with decay and strong P_S modulation (0-100%) is present. This is counterintuitive at the first sight, since p1 drives **m** towards AP which should not enhance p2 switching. But the analysis shows p1 displaces **m** away from AP equilibrium, since AP is $\sim$ 13 degrees off from $\mathbf{m_p}$ in the non-collinear geometry [inset to Fig. 7.4(c)]. Then the free precession of **m** around the AP equilibrium is excited. As explained in ref. [66], p2 delivers STT at different instants over the free precessional orbits and the resulting STT efficiency is increased or reduced depending on the timing of p2. And thus decaying oscillations of P_S map the underlying free precessional orbits excited by p1.

131

Simulations of the delay dependence of P_S for $t_D > 0$ display oscillations with decay that agree qualitatively with observations. A typical plot of simulated P_S vs t_D is shown by triangles in Fig. 7.6(b). Simulations also suggest the data can be fit with the phenomenological equation below

$$P_S(t_D) = P_0 + P_A sin[\omega_0(t_D - t_0)]e^{\frac{-(t_D - t_0)}{\tau}} \qquad (7.1)$$

where P_0 is P_S for applying single p2 alone, and P_A, ω, t_0, and τ are fitting parameters, representing the effect of **m** free precession, angular frequency of P_S oscillations, time offset and the magnetic relaxation time. As shown in in Fig. 7.5, the red solid line displays the fit with τ =830ps and 7.46GHz, the fundamental frequency of P_S oscillations. The two black dashed lines represent the envelopes of fit P_S peaks and dips, which match the decay of P_S well. Macrospin simulations show two regions in the phase portrait of **m** where p2 has high probability of switching **m** (see Fig.2 in ref. [66]). The fundamental precessional frequency of **m** is deduced as 3.73GHz (half 7.46GHz). This is consistent with the ferromagnetic resonance frequency (f_{FMR} =3.78GHz) of the device calculated using the demagnetization coefficients of ellipsoidal nanomagnets with the dimensions (125×75×2nm) and the saturation magnetization M_S=1.26T, measured with the perpendicular Magneto-optic Kerr effect (MOKE) on 2nm thick $Co_{90}Fe_{10}$ films. Further analysis of simulations reveals that $\tau = 2/(\alpha\gamma\mu_0 M_S)$ [123] still holds, where γ and μ_0 is the gyromagnetic ratio and the magnetic permeability of the free space respectively. And thus the device damping parameter α is estimated as 0.011.

In addition, as shown in Fig. 7.5, the data demonstrates the coherent magnetic dynamics up to 0.9ns at 293K. However for $t_D > 0.9$ns, P_S shifts gradually from the fit as indicated by the blue dashed line, which does not mean the magnetic dynamics lose coherence completely. The top inset plots the time difference between the consecutive peaks (Δ) with respect to t_D. Δ keeps almost constant (~134ps) for $t_D <$

0.9ns, then increases to 155ps and eventually decreases to ∼135ps. Possible reasons that cause P_S shift are: (i) The ultrafast p1 increases the device temperature by ∼13K based on the estimation of Joule heating effect [49]. Joule heating causes a small reduction of M_S within 30 ps, the subsequent cooling makes M_S increase back to M_S of ambient temperature. This process leads to a blueshift of the frequency (if not negligible) during the free precession, since H_K and the frequency are proportional to M_S and $\sqrt{H_K(H_K + M_S)}$ respectively. Therefore, Joule heating is not the reason for causing the shift of P_S oscillations. (ii) I hypothesize P_S shift is caused by the frequency change due to possible α variations during the free precession as represented by the Eq. (9) in ref. [213]. The maximum ∼155ps Δ corresponds to α = 0.106, where f_{FMR} =3.78GHz is used. This large value of the damping parameter is not reasonable [60] and this possibility is ruled out. (iii) Thermal effects attempt to randomize **m** trajectories during the evolution. However macrospin simulations reveal thermal effects cause indistinguishable or negligible P_S shifts. As demonstrated in Fig. 7.6(b), the triangles match the fit using Eq. 7.1 well without showing distinguishable P_S shifts. More simulations with different device parameters show the similar results. So thermal effects do not play a major role in causing P_S shift. (iiii) This P_S shift may be caused by a process in which a large angle precessional orbit is excited and the orbit changes the shape gradually during the free precession.

7.3 Combine picosecond ultrafast SST pulses with femtosecond optical pulses

This project was proposed to investigate fundamental physics of ultrafast demagnetization in ferromagnets that is caused by a femtosecond optical excitation. Since Beaupaire *et al.* [11] discovered the ultrafast demagnetization of 22 nm Ni films excited by 60 fs optical pulses in 1996, ultrafast demagnetization dynamics has received a great deal of attention and has been demonstrated to occur on 100 fs timescale

[28]. Although ultrafast demagnetization has been studied intensely over the past decades, fundamental questions still remain unanswered. For example, an ultrafast relaxation process is believed to occur through the direct transfer of the spin angular momentum to the lattice. However, the mechanism is still being debated. There is an intense discussion about whether demagnetization can be explained by phonon-mediated spin-flip scattering [125] or by superdiffusive transport of hot electrons [9]. To date, a microscopic description of the physics is still lacking.

Commonly this 100 fs demagnetization timescale is measured using a magneto-optical pump-probe technique. Time-resolved X-Ray absorption spectroscopy, X-Ray magnetic circular dichroism and time-resolved two-photon photoemission have also been employed to study the demagnetization process. To date, there is no ultrafast measurement which specifically probes the conduction electrons that carry spin currents through ferromagnets and generate magnetotransport. In addition, most of these previous studies are performed on sheet films or at best patterned films larger than 500 nm in diameter. Given the fact that all probes to date have been optical, a measurement of the conduction electron spins causing magnetotransport in nano-magnets at these timescales could offer an alternative methodology to uncover the physics behind the demagnetization process. Ultrafast spin transfer can provide this sort of measurement.

7.3.1 Description of Proposed Research

In order to integrate these previously disconnected sub-fields of magnetodynamics: optically driven ultrafast demagnetization with transport-driven spin momntum transfer, I proposed a nanodevice structure, known as a nonlocal spin valve [241]. This nonlocal spin valve device is integrated with a photoconductive switch through a waveguide. Picosecond electrical pulses can be generated via the photoconductive switch and transmitted through the waveguide to the nonlocal spin valve device with-

out broadening their pulse width. Figure 7.7 (a) and (b) show schematically the side and top view of this device respectively. The polarizer (injector) and the free layer (nanomagnet with an elliptical cross section) of the device are laterally spaced, where the Cu spacer is displaced horizontally over a spin diffusion length ($\sim$ 500 - 1000 nm depending on the temperature) between the injector and nanomagnet. A spin current is generated after the current passes through the injector, and remains spin polarized at the nanomagnet. This spin current is confined and thus only transverses through the nanomangnet as the nanomagnet's side is insulated. The spin current interacts with the nanomagnet magnetization and the magnetoresistance of this nonlocal spin valve depends not only on the relative magnetization orientations of the injector and nanomagnet, but also the amplitude of the nanomagnet magnetization. A thin ITO layer on top of the nanomagnet provides both electrical and optical access to the nanomagnet because a thin ITO layer is not only electrically continuous and but also transparent to visible light . Therefore, femtosecond pulses can be focused onto the nanomagnet and excite nanomagnet demagnetization. By precisely timing the picosecond pulse with the femtosecond optical pulse, the nanomagnet demagnetization process can be investigated by measuring the magnetoresistance as a function of the relative time delay between the two pulses. This nonlocal spin valve geometry, instead of a typical spin valve, is proposed to eliminate the heating/demagnetization effect on the injector and Cu spacer from optical pulses. A larger Cu spacer results in smaller optical heating on the injector and long spin diffusion lengths of the Cu spacer can be obtained by cooling the device to low temperatures. The heating on the Cu spacer can be reduced by covering the spacer with SiO_2.

7.3.2   Initial Results

To make progress in achieving the ultimate goal, this experimental research project is divided into several sub-experiments and some initial results are obtained.

Fabrication of Nonlocal Spin Valve

First is the fabrication of a common nonlocal spin valve device, i.e., the nanomagnet as shown in figure 7.7 is replaced by a thin ferromagnetic layer. This is an easy step to verify the fabrication process. Figure 7.8 shows an SEM image of a common nonlocal spin valve. Two ~ 300 nm wide ferromagnets (Co1 and Co2), laterally displaced ~ 500 nm (center-to-center), are patterned with an electron-beam lithography process and sputtered following a lift-off process. A second electron-beam lithography procedure creates patterns of the Cu spacer (~ 200nm wide) and electrodes (Cu Pad 1 - 6).

Side View

(a)

ITO

Injector

SiO$_2$

Cu

Nanomagnet

$\longleftarrow \cdots\cdots$ Spin Diffusion Length $\cdots\cdots \longrightarrow$

(b)

ITO

Injector

SiO$_2$

Cu

Nanomagnet
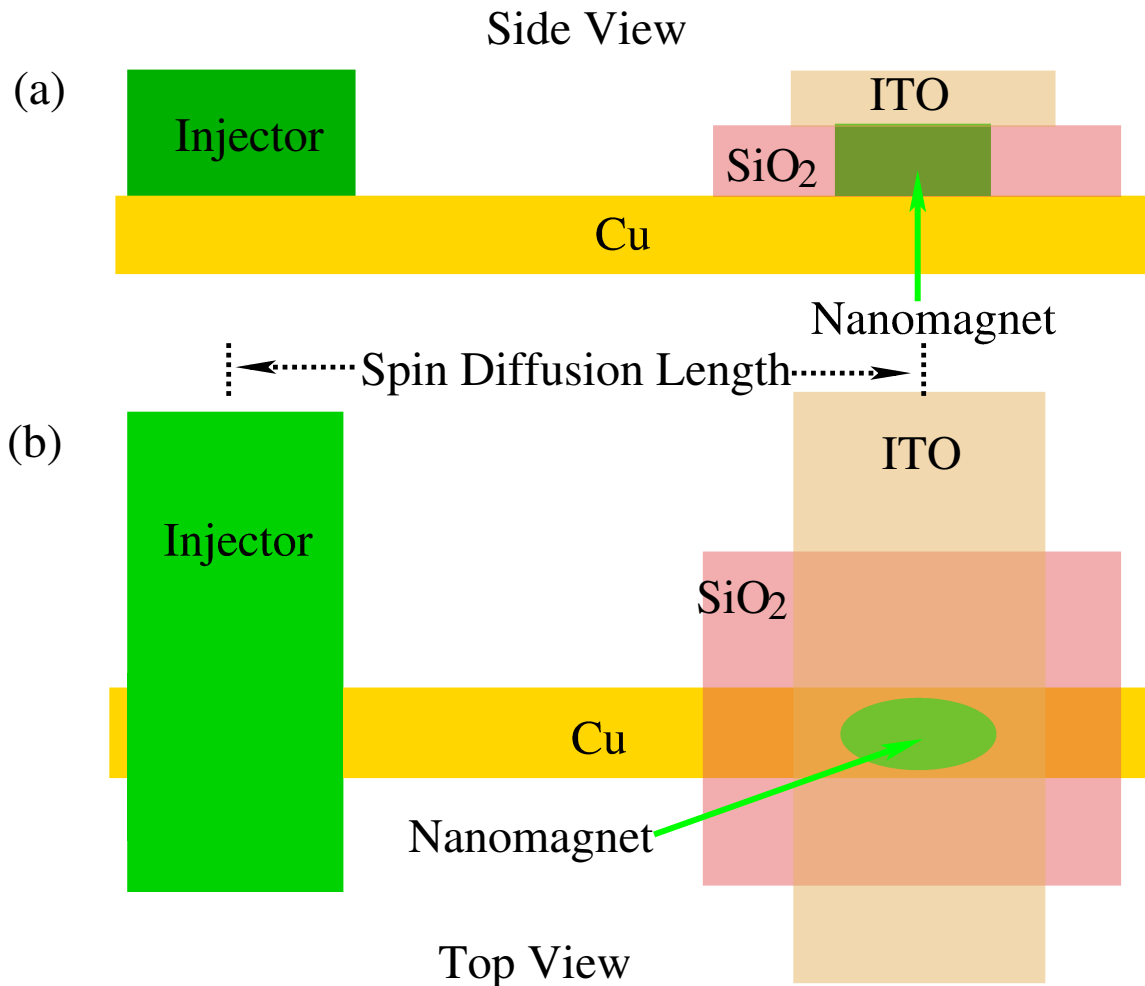
Top View

Figure 7.7   Schematic of a nonlocal spin valve device with optical access. (a) Side view. (b) Top view.

The device was ion milled for 30 s in a chamber with a 1×10^{-8} Torr base pressure (COPRA Plasma source, CCR technology, Germany) before evaporating Cu. Then the device is transferred to a second, attached chamber, to avoid breaking vacuum. Finally, a second lift-off process is performed. AC currents between 10 to 20 μA are injected from Pad 1 to Pad 4. A nonlocal voltage between Pad 2 and Pad 3 is measured using lock-in amplifiers at 11 Hz and 300 K [67] [241]. Other pads are also fabricated to verify electrical connections and contact resistances between Co/Cu junctions. In the steady state an electrical current driven across a Co/Cu junction will lead to a spin accumulation, which is the balance between spins added by the spin current and spins removed by spin relaxation [67] [241]. Spin accumulation in the Cu spacer can act as a source of spin electromotive force which produces a voltage that
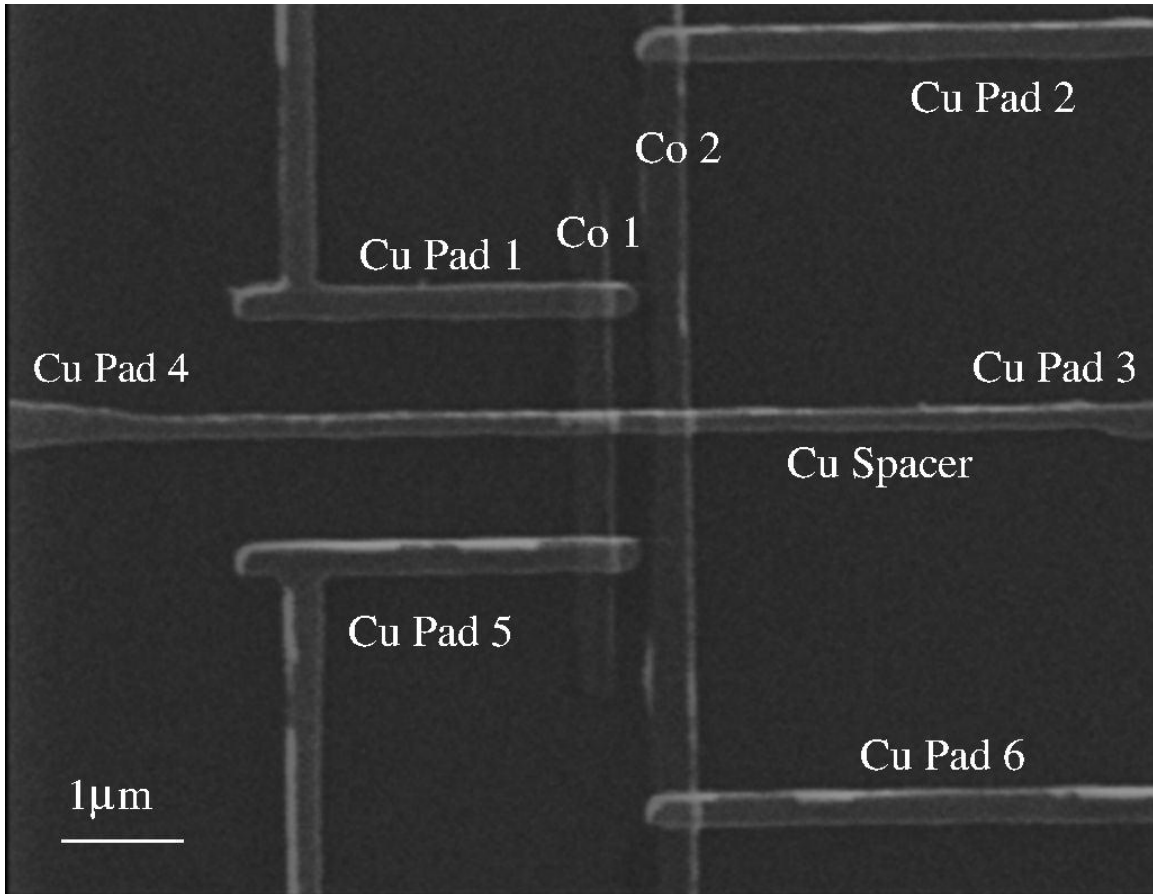
Figure 7.8   SEM image of a common nonlocal spin valve device.

137

is measurable by adding a second ferromagnet Co 2 [106] [200]. Figure 7.9 shows the nonlocal resistance ($R_{nonlocal}$) as a function of magnetic field applied along with the ferromagnets (Co 1 and Co 2). The negative value of $R_{nonlocal}$ is a result of the lock-in phase. The characteristic switching of $R_{nonlocal}$ is caused by one ferromagnet reversing the magnetization and causing the relative orientations of the two ferromagnets to be parallel or antiparallel [67] [241]. The $R_{nonlocal}$ difference ($\Delta R_{nonlocal}$) between the parallel and antiparallel configuration is ~ 0.03 mΩ, which is comparable to previously reported values measured with similar devices [102] [103] [119] [120]. However this $\Delta R_{nonlocal}$ is an order of magnitude smaller than Yang *et al.* reported [241], which is caused by the interface quality between the Co/Cu interface.
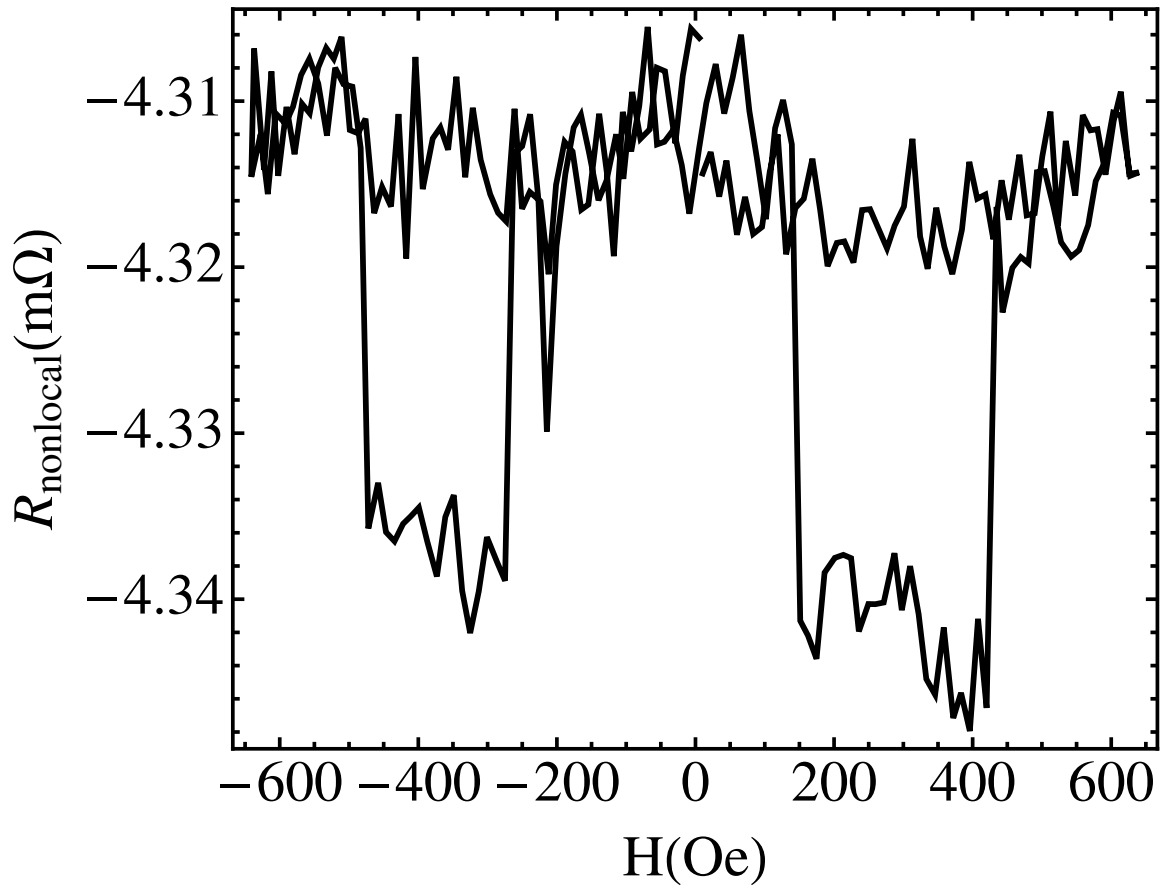
Figure 7.9   Nonlocal Resistance as a function of magnetic field that is applied parallel to ferromagnets.

Optical Microscope Built

Second, an experimental apparatus is required to focus femtosecond optical pulses and locate the focus laser spot onto the nanomagnet precisely, assuming a nanodevice as shown in figure 7.7 has been fabricated. This apparatus consists of a home-made
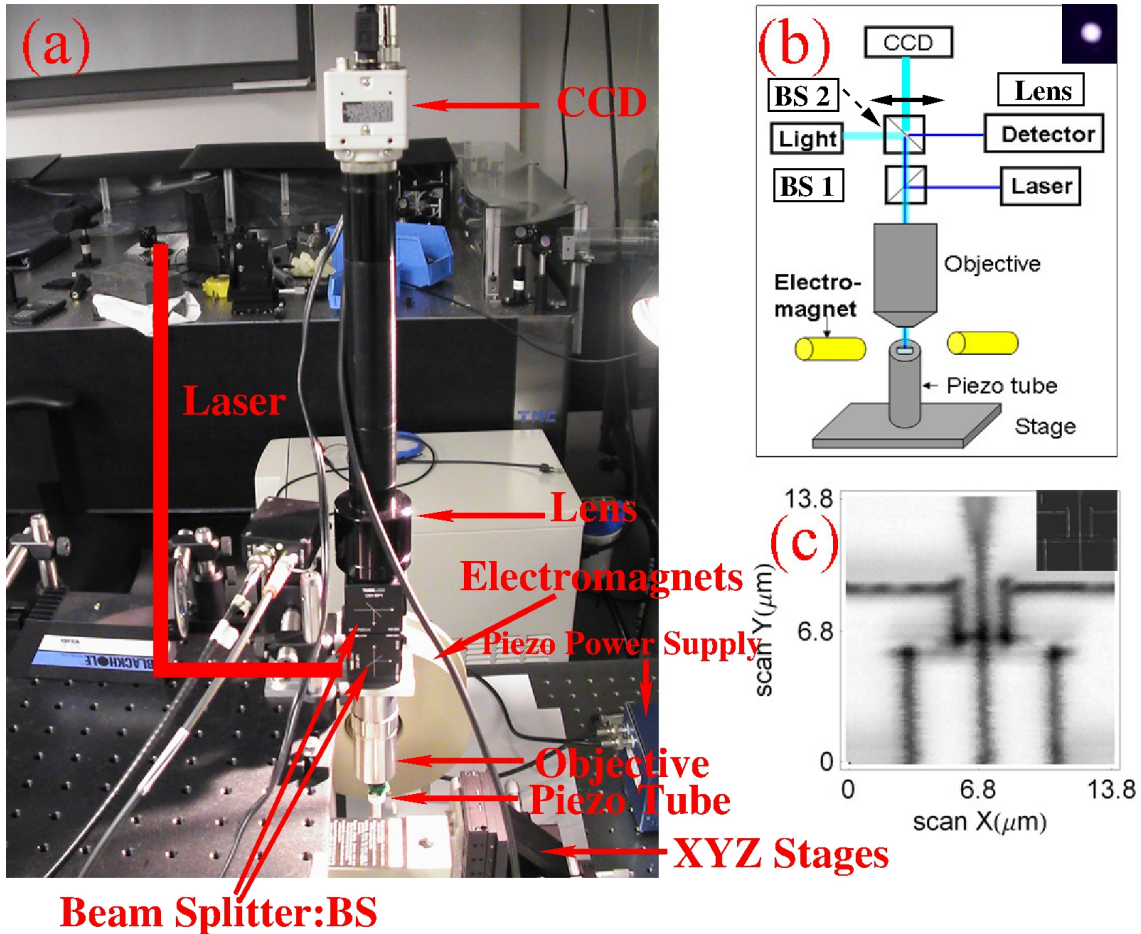
Figure 7.10 (a) Image of an experimental apparatus that is employed to view nonlocal spin valve devices and focus femtosecond optical pulses. (b) Schematic of (a), illustrating how (a) works. Inset: an optical image of a focus laser spot. (c) Image of a nonlocal spin valve device that is measured with laser reflectivity. Inset: SEM image of the device.

optical microscope that is equipped with beamsplitters (BS1 and BS2) to provide optical access. Figure 7.10 (a) shows a real image of the apparatus that I designed and built. Figure 7.10 (b) displays the schematic of figure 7.10 (a) for illustration. A 100X Mitutoyo infinity-corrected long working distance objective (numerical aperture:

NA = 0.9) is employed to optically image devices and focus femtosecond laser pulses [125 fs full width at half maximum (FWHM) with a Gaussian beam]. BS 1 and BS 2 are stacked together and BS 1 is mounted on top of the Mitutoyo lens. Devices are placed on a piezo tube located directly under the Mitutoyo lens. The piezo tube is mounted on a xyz translation stage that provides coarse motion of the devices. Parallel white light is reflected by BS 2, passes BS 1 and into the Mitutoyo lens. The white light reflection from devices passes through BS 1 and BS 2 and is eventually focused onto a CCD camera by another lens. After appropriately positioning the
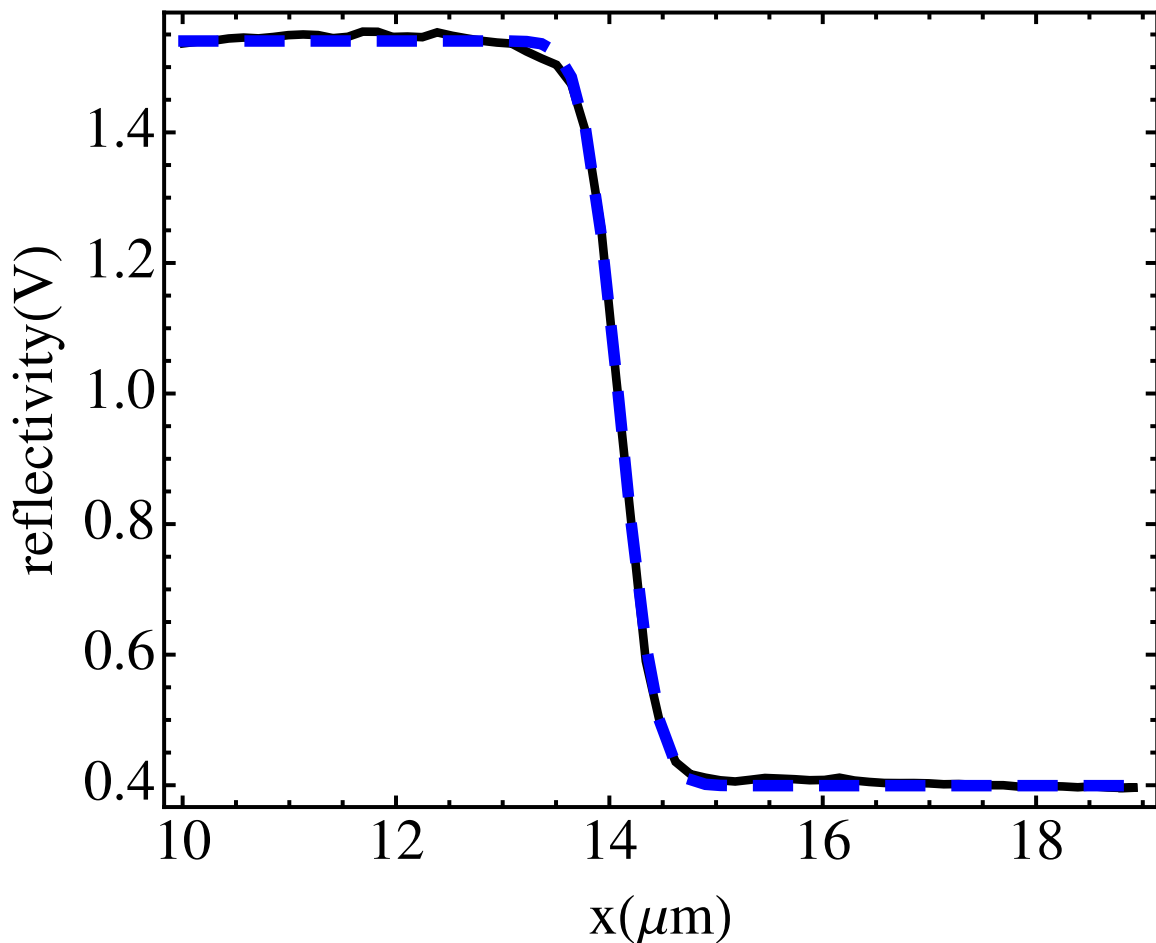
Figure 7.11   Reflectivity as a function of the knife-edge position. Solid (dotted) curve is the measurement data (fit).

device relative to the Mitutoyo lens, i.e., the nanomagnet is in the CCD view, the femtosecond laser beam is aligned with the Mitutoyo lens. An image of the focus

laser spot displays on the CCD camera as shown in inset to figure 7.10 (b). The size of the focus laser spot on devices can be precisely measured using this apparatus. The parallel white light source is replaced with a photodetector that detects the laser intensity reflection from the device. The laser spot size is determined by measuring the laser reflectivity via scanning a knife-edge transversely across the laser beam along the orthogonal direction to the edge, which is called a knife-edge method [75]. A sharp edge of device patterns can be treated as a knife-edge (quasi-knife-edge). The reflectivity of a Gaussian beam from the knife-edge is expressed as [75]

$$I(x) = \frac{I_0}{2}\mathrm{erf}\left[\frac{(x - x_0)}{\sqrt{2}\varnothing}\right], \tag{7.2}$$

where $\varnothing$, and x_0 are the focus laser spot diameter and knife-edge position when the laser spot centers on the knife-edge respectively. I_0 represents the reflectivity difference between the laser spot on and off the knife, and erf(z) is the Gaussian error function defined as [75]

$$\mathrm{erf}(z) = \frac{2}{\sqrt{\pi}}\int_0^z \mathrm{e}^{-t^2} dt. \tag{7.3}$$

A minimum focus spot can be obtained by translating the z stage or moving the z position of the piezo tube.

The solid curve in figure 7.11 shows the laser reflectivity of a focus spot (a 800 nm Gaussian beam) as a function of a quasi-knife-edge position, i.e., a Cu rectangle pattern, where the transverse motion (i.e. in the xy plane) of the quasi-knife-edge is driven by a piezo tube. The data is fitted with equation (7.2) (dotted curve in figure 7.11) obtaining a 1.1 μm diameter laser spot. A 1.1 μm $\varnothing$ is smallest, which can be achieved with the Mitutoyo lens for the 800 nm laser. However, a laser with smaller wavelength (λ) can be employed to shrink the focus spot, since the minimum $\varnothing$ is determined by the Rayleigh criterion [199], i.e.,

$$\varnothing = \frac{1.22\lambda}{2\mathrm{NA}}, \tag{7.4}$$

where λ is the laser wavelength. Equation (7.4) predicts a 1.084 μm $\varnothing$ for 800 nm laser focused by the Mitutoyo lens, which is close to measured, demonstrating this home-made microscope is novel. A 632 nm $\varnothing$, as measured with a quasi-knife-edge, is obtained for the 400 nm laser beam, i.e., the second harmonic generation of the 800 nm laser. This 632 nm $\varnothing$ is a little larger than predicted, which is probably caused by that the 400 nm beam is not well collimated.

After the laser beam is focused on the device, the reflectivity of the focusing spot can be employed to image the device, since patterns of the device act as quasi-knife-edges. Figure 7.10 (c) shows a reflectivity image of a nonlocal spin valve device (inset presents its SEM image) by scanning the device transversely across the laser beam. Therefore, the focus laser spot can be precisely located on the nanomagnet.

On-chip Picosecond Electrical Pulses

Third, an electrical pulse shorter than 30 ps is required to obtain a better resolution for experimental measurements that combine the picosecond and femtosecond pulse together. Verghese *et al.* have made two low-temperature-grown GaAs photoconductive switches that are embedded in a coplanar waveguide [226]. Electrical pulses with 1.2 ps pulse width was generated by illuminating one photoconductive switch with 80 fs optical pulses. I have fabricated the similar device, which produces 4 ps electrical pulses. These pulses have a larger width than Verghese *et al.* made, which may be caused by longer optical pulses illuminating the photoconductive switch (125 fs, as determined by a photo autocorrelation [53] [126] setup I built, as opposed to 80 fs that Verghese *et al.* used). Ultrashort optical pulses with 25 fs width are available in our laboratory to generate electrical pulses as short as 1 ps.
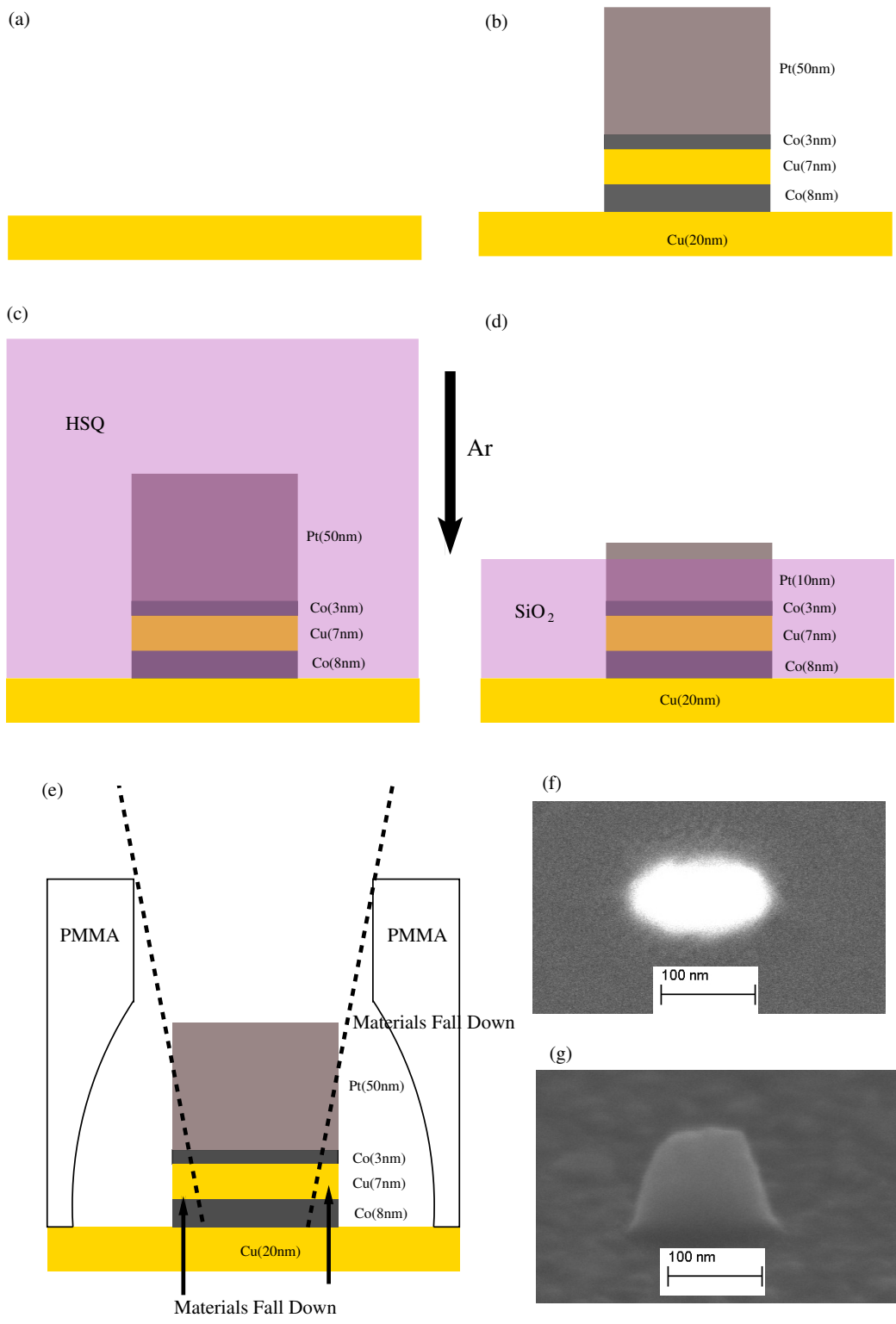
Figure 7.12　Nanopillar fabrication process.

Nanomagnet Fabrication

Fourth is the fabrication of the nanomagnet (figure 7.7). The critical part in the fabrication process is to insulate the nanomagnet side leaving the nanomagnet top open. I made some effort in the nanofabrication, where a spin valve (i.e., a FM/NM/FM sandwich) was chosen to mimic the nanomagnet in the device as the GMR of the spin valve indicates the device quality. The fabrication process is briefly described below. Figure 7.12 (a) shows a 20 nm thick Cu layer that is patterned with optical lithography/lift-off on the wafer. This device is coated with Poly(methyl methacrylate) (PMMA) and a nanohole with an elliptical cross-section (150×100 nm^2) is then created in the PMMA by electron-beam lithography. A 30 s ion milling is used to remove the polymer residue that remains in the nanohole and a multilayer of Co(8 nm)/Cu(7 nm)/Co(2 nm)/Pt(50 nm) are evaporated. A lift-off process leaves a multilayer nanopillar on top of the bottom Cu layer as shown in figure 7.12 (b). Figure 7.12 (f) and (g) show SEM images of a representative nanopillar in the top and side view respectively. A 120 nm thick Hydrogen silsesquioxane (HSQ) (Appendix C), a negative e-beam resist, is spin-coated. HSQ is a flowable, inorganic polymer possessing an effective planarization capacity. The HSQ layer is planarized on the wafer
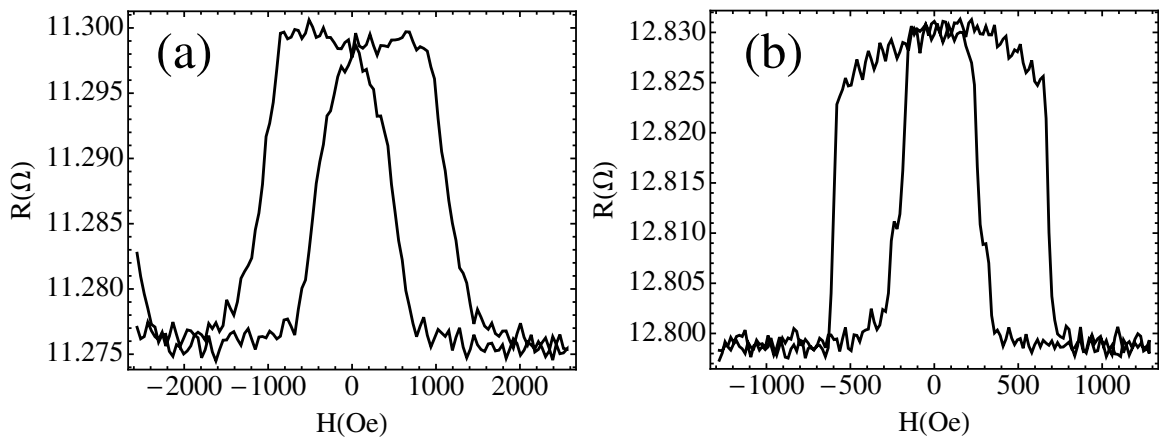
Figure 7.13   MR as a function of applied magnetic field for spin valve devices: (a) device 1 and (b) device 2.

after the spin-coating. A high-dose ($\sim$ 2000 μC/cm^2 for Dr. Webb's Zeiss Ultraplus SEM) e-beam exposure converts the HSQ into SiO$_2$, yielding a 120 nm thick SiO$_2$ [figure 7.12 (c)]. An ion milling (Ar) makes the nanopillar exposed out of the SiO$_2$ keeping the nanopillar side insulated [figure 7.12 (d)]. Finally an optical lithography is used to pattern the top contact electrode of the spin valve.

Figure 7.13 shows the MR as a function of magnetic field applied along the free layer easy-axis for two spin valve devices that are fabricated as discussed above. The device resistance is obtained with two-terminal measurements. The GMR for both devices is $\sim$0.03 Ω, which is only 30% of spin valve devices that have similar materials and dimensions in the literature [66] [121]. This indicates partial current leaks into the electrodes directly, which may be because materials fall down during the multilayer evaporation. Figure 7.12 (e) shows a schematic of the PMMA resist with the nanohole exposed by electron beams. This nanohole has an undercut that is generated by scattered electrons. As the evaporation beam of multilayer materials is not perfectly collimated, materials of the next evaporated layer fall down on sides and mix with the previous layer. This leads to the current leakage. However, this problem can be solved by ion milling a multilayer that has a hard mask (e.g., a Cr nanopillar) on top [3].

Chapter 8

Conclusions and Suggestions for Future Experiments

This dissertation describes a course of experimental research which has attempted to add depth of knowledge to two existing fields of study, i.e., nanoparticle self-assembly and spin-transfer torque. For the point of view of physics, this study has broken new ground in several ways. First, it has helped establish a novel and low-cost nanomanufacturing technology that employes ultra-high field gradients to assemble nanoparticles into complex optical materials. Second, it has performed a first-ever measurement of the nanoparticle self-assembly process using optical diffraction from an all-nanoparticle grating as assembled. This measurement technique is sensitive to colloidal stability of nanoparticles, and thus has a strong potential to be a complementary metrology to DLS measurements. Third, this thesis contains a first-ever discussion and measurement on reliable manipulation of nanomagnet dynamics by employing spin-transfer torque pulses as short as 30 ps.

8.1 Nanoparticle Self-assembly

This thesis demonstrates the nanomanufacturing of an all-nanoparticle diffraction grating that is embedded in a flexible, curved, polymer thin film and its performance in a calibrated optical spectrograph (chapter 3). Appropriate entrance slits could be incorporated to improve spectral resolution, larger gratings could be illuminated, and Rowland circle mounts could be used to reduce aberrations in the diffracted spectrum

[163]. This approach to programmable self-assembly is not limited in terms of how large the line-spacing can be, since larger magnetic patterns can easily be recorded. The minimum line spacing depends on the smallest magnetic pattern that the recording system can support, which is 10 - 30 nm for areal densities from 100 Gbit/in^2 - 1 Tbit/in^2, and will continue to be reduced as magnetic recording technology advances. In principle, grating size is limited by mechanical positioning and the availability of sufficiently large magnetic media materials, however the size and quality of the grating transferred will depend on the polymer properties, and limits to the peeling process. Here different polymers with suitable properties could be employed to potentially create large-scale gratings. Different magnetic media could be used to increase grating thickness, and importantly, different species of nanoparticles with more uniformity and narrow polydispersity could allow better control of groove microstructure, and potentially allow one to create blazed gratings. Future work will include determining how grating efficiency, resolving power, and repeatability depend on parameters of the coating process (e.g. coating time) and nanoparticle magnetic properties. Quantitative measurements of grating scatter and stray light emission will help elucidate the factors that impact absolute efficiency. By combining the unique attributes of nanomaterials with large area reprogrammable patterning, this approach could yield more cost-effective and sustainable materials for optical applications.

This thesis has provided and discussed a novel measurement technique to monitor nanoparticle self-assembly. These measurement results show that diffraction intensity from an all-nanoparticle grating strongly depends on suspension concentration, pH and particle size. Optical diffraction measurements also demonstrate a dramatic change in the diffraction intensity as a result of suspension pH that light scattering does not display. Further, the diffracted signal not only has high sensitivity to particle aggregation, but also detects different time dependence that depends on the colloidal stability of particles. Further, these measurements demonstrate a small volume of

PBS can be used to control the diffraction efficiency and nanoparticle self-assembly process. In addition, this measurement technique appears to be more sensitive to colloidal stability of nanoparticles than the common DLS technique. This is a significant since this technique can offer a complementary metrology or alternative for DLS measurements.

Although I have created an initial theoretical model to interpret the growth of optical diffraction from the assembled grating, a more complex model by including the generalized multiparticle Mie solution is required to better understanding these experimental results. The initial model also requires to be enhanced for explaining the time dependence on the pH and colloidal stability of particle suspensions. In particular, an effort needs to be made in understanding the curvature and optical diffraction dependence on the PBS volume. In addition, a solution or model is urgently needed to interpret why the strong enhancement in optical diffraction occurs only for a small range of the PBS volume, while larger PBS volume does not increase, but decrease the diffraction efficiency dramatically.

Further, using a dipole effective model [63] [64] to describe the nanoparticle magnetization under these ultra-high field gradients remains questionable. The magnetic field in the whole particle volume is not constant due to the large gradients at the disk's surface, therefore, magnetization of the particle may not be uniform. A more accurate model describing how the nanoparticle is magnetized by magnetic fields with ultra-high gradients is needed.

Figuring out why PBS can tune the optical diffraction efficiency will be the major work after my graduation. However, at this stage, more suggestions can be proposed to improve the PTNM technology and further understand the fundamental physics/magnetism in these patterned nanoparticles. For example, (i) different shapes of magnetic patterns consisting only of nanoparticles can be created to manipulate biological cells [245] [222]. (ii) Magnetic particles that are coated with different sur-

factants, e.g., long chains of polymers that provide steric repulsions, can be used to study the particle interaction under these ultra-high field gradients. Understanding how these surfactants interact is critical for utilizing these particles in biological applications such as cell targeted drug delivery [155] [73]. (iii) Magnetic core/Au shell nanoparticles can be employed to enhance the diffraction efficiency and study real-time magnetophoresis of individual nanoparticles under ultra-high field gradients [139]. (iv) Magnetic properties of these nanomanufactured gratings can be studied via diffraction Magneto-optical Kerr Effect (MOKE) (D-MOKE) [78] [193], together with reflection/transmission MOKE and VSM techniques. D-MOKE is supposed to produce a better signal-to-noise [78] than MOKE. Most recently, Dr. Crawford and I have demonstrated that the magnetic properties of these nanomanufactured gratings can be measured magneto-optically.

In addition, magnetic field gradients above transitions on perpendicular magnetic media have also been used to self-assemble nanoparticles. However, a calculation to predict magnetic fields and field gradients above these transitions is needed. Field gradients above transitions on both longitudinal and perpendicular magnetic media could be measured by magnetic force microscopy.

8.2 Spin-transfer torque

This dissertation has demonstrated single ~30 ps pulses switch non-collinear configuration spin valve devices (chapter 6). Furthermore, a pair of short pulses with appropriately adjusted amplitudes and relative timing can: (i) increase the switching probability over its single pulse value while requiring less energy, and (ii) excite the magnetization into large angle precession orbits. However, the distribution of initial orientations of the free layer magnetization $\mathbf{M}$ around its equilibrium direction limits both the switching efficiency and the probability of exciting large angle orbits. Since this distribution depends on the temperature and the energy landscape around the

magnetization equilibrium point, increased switching efficiency and $\sim 100\%$ probability of exciting large angle precession require lower temperatures and higher stability of the energy minimum (which also lead to a higher precession frequency). As these conditions are satisfied, sharper modulation of P_S with pulse amplitude or delay will be observed. To achieve complete control over the magnetization (i.e. to set $\mathbf{M}$ into any desired orbit) requires not only a tight distribution of initial orientations of $\mathbf{M}$ but also multiple ultra-short pulses with precisely adjusted amplitudes and delays.

Experimental measurements also demonstrate coherence at room temperature and 77 K for up to 1 ns. Even though the decaying oscillations in the switching probability completely disappear above 1 ns, this does not imply lack of coherence, as the decay arises mostly due to damping. Further measurements can help distinguish between damping and the long time dephasing of trajectories corresponding to different repetitions of the experiment. Pulsed magnetization control can also be used to study the switching process in a variety of systems, including magnetic tunnel junctions, where a quiet "incubation" period that precedes magnetization switching has been observed [41]. Even though the required ultra-short pulses are not presently available in on-chip sources, our technique suggests an alternative, more efficient mechanism for resonantly pumping microwave oscillators [181, 110], and ultimately, for reversing magnetic memory bits in nanoscale magnetic random access memory (MRAM).

The time domain detection of damping modification in a nanomagnet at room temperature is demonstrated, and in contrast to dc currents, a damping cancellation over a broad range of currents with a precisely-timed 5 ns pulse is achieved. These measurements suggest the possibility to further study thermal dephasing effects in oscillators, both while relaxing towards stable precession, and for times much longer than the precession period. Using time-resolved measurements with two oppositely polarized 30 ps STT impulses, the nanomagnet ultrafast dynamics show asymmetric delay dependence. P_S shows monotonic behavior or oscillations with decay, depending

on order of the two pulses. Macrospin simulations are performed to understand the dynamics and the simulation results show the essence of nanomagnet dynamics is captured. A phenomenological equation is proposed to explain the data of oscillations and decay, and this equation is strongly supported by macrospin simulations.

To date, the ultrafast demagnetization phenomenon is still not well understood. To continue working on the demagnetization project, nanodevices are still required to be fabricated first. A fabrication process using reference [3] is strongly suggested. After that, these devices should be integrated with low temperature grown GaAs conductive switches.

Bibliography

[1] *Iso reference, particle size analysis - photon correlation spectroscopy*, ISO **13321** (1996).

[2] F. J. Albert, N. C. Emley, E. B. Myers, D. C. Ralph, and R. A. Buhrman, *Quantitative study of magnetization reversal by spin-polarized current in magnetic multilayer nanopillars*, Phys. Rev. Lett. **89** (2002), 226802.

[3] Frank Joseph Albert, *The fabrication and measurement of current perpendicular to the plane magnetic nanostructures for the study of the spin transfer effect*, Ph.D. thesis, Cornell University, 2003.

[4] Dmytro Apalkov, Zhitao Diao, Yunfei Ding, and Yiming Huai, *Spin transfer based magnetic storage cells utilizing granular free layers and magnetic memories using such cells*, October 14 2005, US Patent App. 11/251,428.

[5] Neil W. Ashcroft and David N. Mermin, *Solid state physics*, 1 ed., Thomson Learning, Toronto, January 1976.

[6] D. H. Auston, *Picosecond photoconductors: physical properties and applications*, Academic, Orlando, 1984.

[7] Mario Norberto Baibich, JM Broto, Albert Fert, F Nguyen Van Dau, F Petroff, P Etienne, G Creuzet, A Friederich, and J Chazelas, *Giant magnetoresistance of (001) fe/(001) cr magnetic superlattices*, Physical Review Letters **61** (1988), no. 21, 2472.

[8] George Keith Batchelor, *An introduction to fluid dynamics*, Cambridge university press, 2000.

[9] Marco Battiato, Karel Carva, and Peter M Oppeneer, *Superdiffusive spin transport as a mechanism of ultrafast demagnetization*, Physical review letters **105** (2010), no. 2, 027203.

[10] Ya. B. Bazaliy, B. A. Jones, and Shou-Cheng Zhang, *Current-induced magne-*

tization switching in small domains of different anisotropies, Phys. Rev. B **69** (2004), no. 9, 094421.

[11]   E. Beaurepaire, J.-C. Merle, A. Daunois, and J.-Y. Bigot, *Ultrafast spin dynamics in ferromagnetic nickel*, Phys. Rev. Lett. **76** (1996), no. 22, 4250–4253.

[12]   L. Berger, *Low-field magnetoresistance and domain drag in ferromagnets*, J. Appl. Phys. **49** (1978), no. 3, 2156–2161.

[13]   L. Berger, *Emission of spin waves by a magnetic multilayer traversed by a current*, Phys. Rev. B **54** (1996), no. 13, 9353–9358.

[14]   BM Berkovskići, VF Medvedev, and MS Krakov, *Magnetic fluids: engineering applications*, Oxford University Press (Oxford and New York), 1993.

[15]   Bruce J Berne, *Dynamic light scattering: with applications to chemistry, biology and physics*, DoverPublications. com, 1976.

[16]   H Neal Bertram, *Theory of magnetic recording*, Cambridge University Press, 1994.

[17]   Bharat Bhushan, *Tribology issues and opportunities in mems: Proceedings of the nsf/afosr/asme workshop on tribology issues and opportunities in mems held in colombus, ohio, usa, 9-11 november 1997*, Springer, 1998.

[18]   Grünberg Binasch, Peter Grünberg, F Saurenbach, and W Zinn, *Enhanced magnetoresistance in layered magnetic structures with antiferromagnetic interlayer exchange*, Physical review B **39** (1989), 4828–4830.

[19]   Kyle JM Bishop, Christopher E Wilmer, Siowling Soh, and Bartosz A Grzybowski, *Nanoscale forces and their uses in self-assembly*, small **5** (2009), no. 14, 1600–1630.

[20]   Francis Bitter, Trygve Dewey Yensen, and Fritz Zwicky, *Introduction to ferromagnetism*, McGraw-Hill book Company, Incorporated, 1937.

[21]   Andrew K Boal, Faysal Ilhan, Jason E DeRouchey, Thomas Thurn-Albrecht, Thomas P Russell, and Vincent M Rotello, *Self-assembly of nanoparticles into structured spherical and network aggregates*, Nature **404** (2000), no. 6779, 746–748.

[22] Craig F Bohren and Donald R Huffman, *Absorption and scattering of light by small particles*, Wiley. com, 2008.

[23] G Bossis, S Lacis, A Meunier, and O Volkova, *Magnetorheological fluids*, Journal of Magnetism and Magnetic Materials **252** (2002), 224–228.

[24] Richard M Bozorth, *Ferromagnetism*, Ferromagnetism, by Richard M. Bozorth, pp. 992. ISBN 0-7803-1032-2. Wiley-VCH, August 1993. **1** (1993).

[25] William Fuller Brown, *Thermal fluctuations of a single-domain particle*, Phys. Rev. **130** (1963), no. 5, 1677–1686.

[26] Wesley Burgei, Michael J. Pechan, and Herbert Jaeger, *A simple vibrating sample magnetometer for use in a materials physics course*, American Journal of Physics **71** (2003), no. 8, 825–828.

[27] Kurt H Jürgen Buschow and Frank R De Boer, *Physics of magnetism and magnetic materials*, vol. 7, Springer, 2003.

[28] John Charles Butcher, *The numerical analysis of ordinary differential equations: Runge-kutta and general linear methods*, Wiley-Interscience, 1987.

[29] Mark S Chagnon, *Stable ferrofluid compositions and method of making same*, October 26 1982, US Patent 4,356,098.

[30] David Chandler, John D Weeks, Hans C Andersen, et al., *Van der waals picture of liquids, solids, and phase transformations*, Science **220** (1983), no. 4599, 787–794.

[31] E Chen, D Apalkov, Z Diao, A Driskill-Smith, D Druist, D Lottis, V Nikitin, X Tang, S Watts, S Wang, et al., *Advances and future prospects of spin-transfer torque random access memory*, Magnetics, IEEE Transactions on **46** (2010), no. 6, 1873–1878.

[32] Min Chen, Jaemin Kim, J. P. Liu, Hongyou Fan, and Shouheng Sun, *Synthesis of fept nanocubes and their oriented self-assembly*, Journal of the American Chemical Society **128** (2006), no. 22, 7132–7133.

[33] S Chikazumi, S Taketomi, M Ukita, Miyajima Mizukami, H Miyajima, M Setogawa, and Y Kurihara, *Physics of magnetic fluids*, Journal of Magnetism and Magnetic Materials **65** (1987), no. 2, 245–251.

[34] Soshin Chikazumi and Jr, *Physics of Ferromagnetism (International Series of Monographs on Physics)*, Oxford University Press, February 1997.

[35] Y. T. Cui, J. C. Sankey, C. Wang, K. V. Thadani, Z.-P. Li, R. A. Buhrman, and D. C. Ralph, *Resonant spin-transfer-driven switching of magnetic devices assisted by microwave current pulses*, Phys. Rev. B **77** (2008), no. 6, 214440.

[36] Marie-Christine Daniel and Didier Astruc, *Gold nanoparticles: assembly, supramolecular chemistry, quantum-size-related properties, and applications toward biology, catalysis, and nanotechnology*, Chemical reviews **104** (2004), no. 1, 293–346.

[37] SB Darling and SD Bader, *A materials chemistry perspective on nanomagnetism*, Journal of Materials Chemistry **15** (2005), no. 39, 4189–4195.

[38] Sean A Davis, Michael Breulmann, Katja H Rhodes, Baojian Zhang, and Stephen Mann, *Template-directed assembly using nanoparticle building blocks: A nanotectonic approach to organized materials*, Chemistry of materials **13** (2001), no. 10, 3218–3226.

[39] T. Devolder, C. Chappert, J. A. Katine, M. J. Carey, and K. Ito, *Distribution of the magnetization reversal duration in subnanosecond spin-transfer switching*, Phys. Rev. B **75** (2007), no. 6, 064402.

[40] T. Devolder, P. Crozat, J.-V. Kim, C. Chappert, K. Ito, J. A. Katine, and M. J. Carey, *Magnetization switching by spin torque using subnanosecond current pulses assisted by hard axis magnetic fields*, Applied Physics Letters **88** (2006), no. 15, 152502–152502.

[41] T. Devolder, J. Hayakawa, K. Ito, H. Takahashi, S. Ikeda, P. Crozat, N. Zerounian, Joo-Von Kim, C. Chappert, and H. Ohno, *Single-shot time-resolved measurements of nanosecond-scale spin-transfer induced switching: Stochastic versus deterministic aspects*, Phys. Rev. Lett. **100** (2008), no. 5, 057206.

[42] Zhitao Diao, Alex Panchula, Yunfei Ding, Mahendra Pakala, Shengyuan Wang, Zhanjie Li, Dmytro Apalkov, Hideyasu Nagai, Alexander Driskill-Smith, Lien-Chang Wang, et al., *Spin transfer switching in dual mgo magnetic tunnel junctions*, Applied Physics Letters **90** (2007), no. 13, 132508–132508.

[43] Jon Dobson, *Magnetic nanoparticles for drug delivery*, Drug Development Research **67** (2006), no. 1, 55–60.

[44] Yongkang Dong, Liang Chen, and Xiaoyi Bao, *Characterization of the brillouin grating spectra in a polarization-maintaining fiber*, Opt. Express **18** (2010), no. 18, 18960–18967.

[45] Michel Duban, *Improved wadsworth mounting with aspherical holographic grating*, Appl. Opt. **19** (1980), no. 15, 2488–2489.

[46] Julien Dugay, Reasmey P Tan, Anca Meffre, Thomas Blon, Lise-Marie Lacroix, Julian Carrey, Pier F Fazzini, Sébastien Lachaize, Bruno Chaudret, and Marc Respaud, *Room-temperature tunnel magnetoresistance in self-assembled chemically synthesized metallic iron nanoparticles*, Nano letters **11** (2011), no. 12, 5128–5134.

[47] John T Edward, *Molecular volumes and the stokes-einstein equation*, Journal of Chemical Education **47** (1970), no. 4, 261.

[48] Ray Egerton, *Physical Principles of Electron Microscopy*, Kluwer Academic Publishers, Boston, 2005.

[49] N. C. Emley, I. N. Krivorotov, O. Ozatay, A. G. F. Garcia, J. C. Sankey, D. C. Ralph, and R. A. Buhrman, *Time-resolved spin-torque switching and enhanced damping in permalloy/cu/permalloy spin-valve nanopillars*, Phys. Rev. Lett. **96** (2006), 247204.

[50] L. Eurenius, C. Hagglund, E. Olsson, B. Kasemo, and D. Chakarov, *Grating formation by metal-nanoparticle-mediated coupling of light into waveguided modes*, Nat. Photonics **2** (2008), no. 6, 360–364.

[51] WILLIAM G. Fastie, *A small plane grating monochromator*, J. Opt. Soc. Am. **42** (1952), no. 9, 641–647.

[52] Albert Fert, *Nobel lecture: Origin, development, and future of spintronics*, Reviews of Modern Physics **80** (2008), no. 4, 1517.

[53] T Feurer, A Glass, and R Sauerbrey, *Two-photon photoconductivity in sic photodiodes and its application to autocorrelation measurements of femtosecond optical pulses*, Applied Physics B: Lasers and Optics **65** (1997), no. 2, 295–297.

[54] Michael E Fisher and Yan Levin, *Criticality in ionic fluids: Debye-hückel theory, bjerrum, and beyond*, Physical review letters **71** (1993), no. 23, 3826.

[55] S Foner and EJ McNiff, *Very low frequency integrating vibrating sample magnetometer (vlfvsm) with high differential sensitivity in high dc fields*, Review of Scientific Instruments **39** (1968), no. 2, 171–179.

[56] Simon Foner, *Versatile and sensitive vibrating-sample magnetometer*, Review of Scientific Instruments **30** (1959), no. 7, 548–557.

[57] FC Fonseca, GF Goya, RF Jardim, R Muccillo, NLV Carreno, El Longo, and ER Leite, *Superparamagnetism and magnetic properties of ni nanoparticles embedded in sio$_2$*, Physical Review B **66** (2002), no. 10, 104406.

[58] Darren Freeman, Steve Madden, and Barry Luther-Davies, *Fabrication of planar photonic crystals in a chalcogenide glass using a focused ion beam*, Opt. Express **13** (2005), no. 8, 3079–3086.

[59] Barbara J Frisken, *Revisiting the method of cumulants for the analysis of dynamic light-scattering data*, Applied Optics **40** (2001), no. 24, 4087–4091.

[60] G. D. Fuchs, J. C. Sankey, V. S. Pribiag, L. Qian, P. M. Braganca, A. G. F. Garcia, E. M. Ryan, Z.-P. Li, O. Ozatay, D. C. Ralph, and R. A. Buhrman, *Spin-torque ferromagnetic resonance measurements of damping in nanomagnets*, Applied Physics Letters **91** (2007), no. 6, 062507–062507.

[61] K. A. Fuller and G. W. Kattawar, *Consummate solution to the problem of classical electromagnetic scattering by an ensemble of spheres. i: Linear chains*, Opt. Lett. **13** (1988), no. 2, 90–92.

[62] Kirk A. Fuller, George W. Kattawar, and Ru T. Wang, *Electromagnetic scattering from two dielectric spheres: further comparisons between theory and experiment*, Appl. Opt. **25** (1986), no. 15, 2521–2529.

[63] E. P. Furlani, *Analysis of particle transport in a magnetophoretic microsystem*, Journal of Applied Physics **99** (2006), no. 2, 024912–024912.

[64] E. P. Furlani and K. C. Ng, *Nanoscale magnetic biotransport with application to magnetofection*, Phys. Rev. E **77** (2008), 061914.

[65] Edward P Furlani, *Permanent magnet and electromechanical devices [electronic resource]: materials, analysis, and applications*, Access Online via Elsevier, 2001.

[66] Samir Garzon, Longfei Ye, Richard A. Webb, Thomas M. Crawford, Mark Covington, and Shehzaad Kaka, *Coherent control of nanomagnet dynamics via ultrafast spin torque pulses*, Phys. Rev. B **78** (2008), 180401.

[67] Samir Garzon, Igor Žutić, and Richard A Webb, *Temperature-dependent asymmetry of the nonlocal spin-injection resistance: Evidence for spin nonconserving interface scattering*, Physical review letters **94** (2005), no. 17, 176601.

[68] Fabienne Gauffre and Didier Roux, *Studying a new type of surfactant aggregate ("spherulites") as chemical microreactors. a first example: copper ion entrapping and particle synthesis*, Langmuir **15** (1999), no. 11, 3738–3747.

[69] Jianping Ge, Le He, James Goebl, and Yadong Yin, *Assembly of magnetically tunable photonic crystals in nonpolar solvents*, Journal of the American Chemical Society **131** (2009), no. 10, 3484–3486.

[70] Jianping Ge, Yongxing Hu, and Yadong Yin, *Highly tunable superparamagnetic colloidal photonic crystals*, Angewandte Chemie **119** (2007), no. 39, 7572–7575.

[71] Jianping Ge and Yadong Yin, *Magnetically responsive colloidal photonic crystals*, Journal of Materials Chemistry **18** (2008), no. 42, 5041–5045.

[72] David I Gittins, Andrei S Susha, Bjoern Schoeler, and Frank Caruso, *Dense nanoparticulate thin films via gold nanoparticle self-assembly*, Advanced Materials **14** (2002), no. 7, 508–512.

[73] JD Goff, PP Huffstetler, WC Miles, N Pothayee, CM Reinholz, S Ball, RM Davis, and JS Riffle, *Novel phosphonate-functional poly (ethylene oxide)-magnetite nanoparticles form stable colloidal dispersions in phosphate-buffered saline*, Chemistry of Materials **21** (2009), no. 20, 4784–4795.

[74] WI Goldburg, *Dynamic light scattering*, American Journal of Physics **67** (1999), 1152.

[75] Mario González-Cardel, Pedro Arguijo, and Rufino Díaz-Uribe, *Gaussian beam radius measurement with a knife-edge: a polynomial approximation to the inverse error function*, Applied optics **52** (2013), no. 16, 3849–3855.

[76] G. F. Goya, T. S. Berquo, F. C. Fonseca, and M. P. Morales, *Static and dynamic magnetic properties of spherical magnetite nanoparticles*, Journal of Applied Physics **94** (2003), no. 5, 3520–3528.

[77] David Jeffrey Griffiths and Reed College, *Introduction to electrodynamics*, vol. 3, prentice Hall Upper Saddle River, NJ, 1999.

[78] M Grimsditch and P Vavassori, *The diffracted magneto-optic kerr effect: what does it tell you?*, Journal of Physics: Condensed Matter **16** (2004), no. 9, R275.

[79] Peter Grünberg, R Schreiber, Y Pang, MB Brodsky, and H Sowers, *Layered magnetic structures: Evidence for antiferromagnetic coupling of fe layers across cr interlayers*, Physical Review Letters **57** (1986), no. 19, 2442.

[80] Marek Grzelczak, Jan Vermant, Eric M. Furst, and Luis M. Liz-MarzâĽŽ°n, *Directed self-assembly of nanoparticles*, ACS Nano **4** (2010), no. 7, 3591–3605.

[81] Bartosz A Grzybowski, Christopher E Wilmer, Jiwon Kim, Kevin P Browne, and Kyle JM Bishop, *Self-assembly: from crystals to cells*, Soft Matter **5** (2009), no. 6, 1110–1128.

[82] Babu R. Guduri and Adriaan S. Luyt, *Structure and mechanical properties of polycarbonate modified clay nanocomposites*, Journal of Nanoscience and Nanotechnology **8** (2008-04-01T00:00:00), no. 4, 1880–1885.

[83] Zhanhu Guo, H Thomas Hahn, Hongfei Lin, Amar B Karki, and David P Young, *Magnetic and magnetoresistance behaviors of particulate iron/vinyl ester resin nanocomposites*, Journal of Applied Physics **104** (2008), no. 1, 014314–014314.

[84] Ajay Kumar Gupta and Mona Gupta, *Synthesis and surface engineering of iron oxide nanoparticles for biomedical applications*, Biomaterials **26** (2005), no. 18, 3995 – 4021.

[85] Thomas A Halgren, *The representation of van der waals (vdw) interactions in molecular mechanics force fields: potential form, combination rules, and vdw parameters*, Journal of the American Chemical Society **114** (1992), no. 20, 7827–7843.

[86] T. M. Hard, *Laser wavelength selection and output coupling by a grating*, Appl. Opt. **9** (1970), no. 8, 1825–1830.

[87] GEORGE R. Harrison, *The production of diffraction gratings i. development of the ruling art*, J. Opt. Soc. Am. **39** (1949), no. 6, 413–426.

[88] PA Hartley, GD Parfitt, and LB Pollack, *The role of the van der waals force in the agglomeration of powders containing submicron particles*, Powder technology **42** (1985), no. 1, 35–46.

[89] Uwe Hartmann and R Coehoorn, *Magnetic multilayers and giant magnetoresistance: fundamentals and industrial applications*, vol. 37, Springer, 2000.

[90] Marc D Haw, *Colloidal suspensions, brownian motion, molecular reality: a short history*, Journal of physics: condensed matter **14** (2002), no. 33, 7769.

[91] Eugene Hecht, *Optics*, 4th ed., ch. 10, Addison-Wesley, 2001.

[92] Michael C Herman and Kyriakos D Papadopoulos, *Effects of asperities on the van der waals and electric double-layer interactions of two parallel flat plates*, Journal of colloid and interface science **136** (1990), no. 2, 385–392.

[93] Colin M Hessel, Eric J Henderson, and Jonathan GC Veinot, *Hydrogen silsesquioxane: A molecular precursor for nanocrystalline si-sio2 composites and freestanding hydride-surface-terminated silicon nanoparticles*, Chemistry of materials **18** (2006), no. 26, 6139–6146.

[94] Masuo Hosokawa, Kiyoshi Nogi, Makio Naito, and Toyokazu Yokoyama, *Nanoparticle technology handbook*, Elsevier, 2007.

[95] D. Houssameddine, U. Ebels, B. Dieny, K. Garello, J.-P. Michel, B. Delaet, B. Viala, M.-C. Cyrille, J. A. Katine, and D. Mauri, *Temporal coherence of mgo based magnetic tunnel junction spin torque oscillators*, Physical Review Letters **102** (2009), no. 25, 257202.

[96] Yiming Huai, Zhitao Diao, Alex Panchula, Eugene Youjun Chen, Lien-Chang Wang, et al., *Current-switched spin-transfer magnetic devices with reduced spin-transfer switching current density*, September 30 2008, US Patent 7,430,135.

[97] Hendrik Christoffel Hulst and Hendrik C van de Hulst, *Light scattering: by small particles*, Courier Dover Publications, 1957.

[98] W. Hung, W. Cheng, M. Tsai, W. Chung, I. Jiang, and Pochi Yeh, *Laser pulse induced gold nanoparticle gratings*, Appl. Phys. Lett. **93** (2008), no. 6, 061109.

[99] Jacob N Israelachvili, *Intermolecular and surface forces: revised third edition*, Academic press, 2011.

[100] John D. Jackson, *Classical electrodynamics third edition*, third ed., Wiley, August 1998.

[101] Antony Jameson, Wolfgang Schmidt, Eli Turkel, et al., *Numerical solutions of the euler equations by finite volume methods using runge-kutta time-stepping schemes*, AIAA paper **1259** (1981), 1981.

[102] FJ Jedema, AT Filip, and BJ Van Wees, *Electrical spin injection and accumulation at room temperature in an all-metal mesoscopic spin valve*, Nature **410** (2001), no. 6826, 345–348.

[103] FJ Jedema, MS Nijboer, AT Filip, and BJ Van Wees, *Spin injection and spin accumulation in all-metal mesoscopic spin valves*, Physical Review B **67** (2003), no. 8, 085319.

[104] Jianbo Jia, Bingquan Wang, Aiguo Wu, Guangjin Cheng, Zhuang Li, and Shaojun Dong, *A method to construct a third-generation horseradish peroxidase biosensor: self-assembling gold nanoparticles to three-dimensional sol-gel network*, Analytical Chemistry **74** (2002), no. 9, 2217–2223.

[105] Chen Jianrong, Miao Yuqing, He Nongyue, Wu Xiaohua, and Li Sijiao, *Nanotechnology and biosensors*, Biotechnology Advances **22** (2004), no. 7, 505–518.

[106] Mark Johnson and R. H. Silsbee, *Interfacial charge-spin coupling: Injection and detection of spin magnetization in metals*, Phys. Rev. Lett. **55** (1985), 1790–1793.

[107] Mark R Jolly, Jonathan W Bender, and J David Carlson, *Properties and applications of commercial magnetorheological fluids*, Journal of Intelligent Material Systems and Structures **10** (1999), no. 1, 5–13.

[108] Thomas B Jones, *Electromechanics of particles*, Cambridge University Press, 2005.

[109] S. Kaka, M. R. Pufall, W. H. Rippard, T. J. Silva, S. E. Russek, J. A. Katine, and M. Carey, *Spin transfer switching of spin valve nanopillars using nanosecond pulsed currents*, J. Magn. Magn. Mater. **286** (2005), 375–380.

[110] S. Kaka, M.R. Pufall, W.H. Rippard, T.J. Silva, S.E. Russek, and J.A. Katine, *Mutual phase-locking of microwave spin torque nano-oscillators*, Nature **437** (2005), 389–392.

[111] Shehzaad Kaka, Matthew R Pufall, William H Rippard, Thomas J Silva, Stephen E Russek, Jordan A Katine, and Matthew Carey, *Spin transfer switching of spin valve nanopillars using nanosecond pulsed currents*, Journal of magnetism and magnetic materials **286** (2005), 375–380.

[112] Alexander M Kalsin and Bartosz A Grzybowski, *Controlling the growth of "ionic" nanoparticle supracrystals*, Nano letters **7** (2007), no. 4, 1018–1021.

[113] J. A. Katine, F. J. Albert, R. A. Buhrman, E. B. Myers, and D. C. Ralph, *Current-driven magnetization reversal and spin-wave excitations in co / cu / co pillars*, Phys. Rev. Lett. **84** (2000), no. 14, 3149–3152.

[114] J.A. Katine and Eric E. Fullerton, *Device implications of spin-transfer torques*, Journal of Magnetism and Magnetic Materials **320** (2008), no. 7, 1217 – 1226.

[115] M. Kerker, *The scattering of light and other electromagnetic radiation*, first ed., Academic, New York, 1969.

[116] Hee-Cheol Kim, Hendrik Reinhardt, Pierre Hillebrecht, and Norbert A. Hampp, *Photochemical preparation of sub-wavelength heterogeneous laser-induced periodic surface structures*, Advanced Materials **24** (2012), no. 15, 1994–1998.

[117] Hyoki Kim, Jianping Ge, Junhoi Kim, Sung-eun Choi, Hosuk Lee, Howon Lee, Wook Park, Yadong Yin, and Sunghoon Kwon, *Structural colour printing using a magnetically tunable and lithographically fixable photonic crystal*, Nature Photonics **3** (2009), no. 9, 534–540.

[118] T. Kimura, J. Hamrle, and Y. Otani, *Estimation of spin-diffusion length from the magnitude of spin-current absorption: Multiterminal ferromagnetic/nonferromagnetic hybrid structures*, Phys. Rev. B **72** (2005), 014461.

[119] T Kimura, J Hamrle, Y Otani, K Tsukagoshi, and Y Aoyagi, *Spin-dependent boundary resistance in the lateral spin-valve structure*, Applied physics letters **85** (2004), no. 16, 3501–3503.

[120] T Kimura and Y Otani, *Spin transport in lateral ferromagnetic/nonmagnetic hybrid structures*, Journal of Physics: Condensed Matter **19** (2007), no. 16, 165216.

[121] S. I. Kiselev, J. C. Sankey, I. N. Krivorotov, N. C. Emley, R. J. Schoelkopf, R. A. Buhrman, and D. C. Ralph, *Microwave oscillations of a nanomagnet driven by a spin-polarized current*, Nature **425** (2003), 380–383.

162

[122] Fritz Kneubühl, *Diffraction grating spectroscopy*, Appl. Opt. **8** (1969), no. 3, 505–519.

[123] R. H. Koch, J. G. Deak, D. W. Abraham, P. L. Trouilloud, R. A. Altman, Yu Lu, W. J. Gallagher, R. E. Scheuerlein, K. P. Roche, and S. S. P. Parkin, *Magnetization reversal in micron-sized magnetic thin films*, Phys. Rev. Lett. **81** (1998), 4512–4515.

[124] R. H. Koch, J. A. Katine, and J. Z. Sun, *Time-Resolved Reversal of Spin-Transfer Switching in a Nanomagnet*, Phys. Rev. Lett. **92** (2004), no. 8, 088302–+.

[125] B Koopmans, G Malinowski, F Dalla Longa, D Steiauf, M Fähnle, T Roth, M Cinchetti, and M Aeschlimann, *Explaining the paradoxical diversity of ultrafast laser-induced demagnetization*, Nature materials **9** (2009), no. 3, 259–265.

[126] Dennis E Koppel, *Analysis of gaussian light by clipped photocount autocorrelation: the effect of finite sampling times and incomplete spatial coherence*, Journal of Applied Physics **42** (1971), no. 8, 3216–3225.

[127] Maren Krack, Heinrich Hohenberg, Andreas Kornowski, Peter Lindner, Horst Weller, and Stephan Förster, *Nanoparticle-loaded magnetophoretic vesicles*, Journal of the American Chemical Society **130** (2008), no. 23, 7315–7320.

[128] I. N. Krivorotov, N. C. Emley, J. C. Sankey, S. I. Kiselev, D. C. Ralph, and R. A. Buhrman, *Time-Domain Measurements of Nanomagnet Dynamics Driven by Spin-Transfer Torques*, Science **307** (2005), no. 5707, 228–231.

[129] Peter J Krommenhoek and Joseph B Tracy, *Magnetic field-directed self-assembly of magnetic nanoparticle chains in bulk polymers*, Particle & Particle Systems Characterization (2013).

[130] Prashant Kumar, *Directed self-assembly: expectations and achievements*, Nanoscale research letters **5** (2010), no. 9, 1367–1376.

[131] Hans-Joachim Kunze, *Introduction to plasma spectroscopy*, ch. 3, Springer, 2009.

[132] Y Lalatonne, J Richardi, and MP Pileni, *Van der waals versus dipolar forces controlling mesoscopic organizations of magnetic nanocrystals*, Nature materials **3** (2004), no. 2, 121–125.

[133] Horace Lamb, *Hydrodynamics*, Cambridge University Press, 1993.

[134] Jean-Marie Lehn, *Toward self-organization and complex matter*, Science **295** (2002), no. 5564, 2400–2403.

[135] Peter M Levy, Shufeng Zhang, and Albert Fert, *Electrical conductivity of magnetic multilayered structures*, Physical review letters **65** (1990), no. 13, 1643.

[136] Mei Li, Heimo Schnablegger, and Stephen Mann, *Coupled synthesis and self-assembly of nanoparticles to give structures with controlled organization*, Nature **402** (1999), no. 6760, 393–395.

[137] Mingtao Li, Jian Wang, Lei Zhuang, and Stephen Y. Chou, *Fabrication of circular optical structures with a 20 nm minimum feature size using nanoimprint lithography*, Appl. Phys. Lett. **76** (2000), no. 6, 673–675.

[138] Z. Li and S. Zhang, *Magnetization dynamics with a spin-transfer torque*, Phys. Rev. B **68** (2003), no. 2, 024404.

[139] JitKang Lim, Caitlin Lanni, Eric R. Evarts, Frederick Lanni, Robert D. Tilton, and Sara A. Majetich, *Magnetophoresis of nanoparticles*, ACS Nano **5** (2011), no. 1, 217–226.

[140] JitKang Lim, David X. Tan, Frederick Lanni, Robert D. Tilton, and Sara A. Majetich, *Optical imaging and magnetophoresis of nanorods*, J. Magn. Magn. Mater. **321** (2009), no. 10, 1557–1562.

[141] Yu lin Xu, *Electromagnetic scattering by an aggregate of spheres: far field*, Appl. Opt. **36** (1997), no. 36, 9496–9508.

[142] David J Lockhart and Peter S Kim, *Electrostatic screening of charge and dipole interactions with the helix backbone*, Science **260** (1993), no. 5105, 198–202.

[143] Erwin G. Loewen, Michel Nevière, and Daniel Maystre, *On an asymptotic theory of diffraction gratings used in the scalar domain*, J. Opt. Soc. Am. **68** (1978), no. 4, 496–502.

[144] J. Lohau, A. Moser, C. T. Rettner, M. E. Best, and B. D. Terris, *Writing and reading perpendicular magnetic recording media patterned by a focused ion beam*, Appl. Phys. Lett. **78** (2001), no. 7, 990–992.

[145] Ward A Lopes and Heinrich M Jaeger, *Hierarchical self-assembly of metal nanostructures on diblock copolymer scaffolds*, Nature **414** (2001), no. 6865, 735–738.

[146] Johannes Lyklema, *Fundamentals of interface and colloid science: soft colloids*, vol. 5, Access Online via Elsevier, 2005.

[147] Sadamichi Maekawa, *Concepts in spin electronics*, vol. 4, Oxford University Press New York, 2006.

[148] Sadamichi Maekawa and Teruya Shinjo, *Spin dependent transport in magnetic nanostructures*, CRC Press, 2010.

[149] Arif A Mamedov, Artem Belov, Michael Giersig, Nataliya N Mamedova, and Nicholas A Kotov, *Nanorainbows: graded semiconductor films from quantum dots*, Journal of the American Chemical Society **123** (2001), no. 31, 7738–7739.

[150] Ronald Masters, Chunming Hsiech, and Harry L. Pardue, *Advantages of an off-littrow mounting of an echelle grating*, Appl. Opt. **27** (1988), no. 18, 3895–3897.

[151] J.N. McMullin, R.G. DeCorby, and C.J. Haugen, *Theory and simulation of a concave diffraction grating demultiplexer for coarse WDM systems*, J. Lightwave Technol. **20** (2002), no. 4, 758 –765.

[152] André E Merbach and Éva Tóth, *The chemistry of contrast agents in medical magnetic resonance imaging*, Wiley Chichester (W. Sx.) etc., 2001.

[153] Gustav Mie, *Beiträge zur optik trüber medien, speziell kolloidaler metallösungen*, Annalen der physik **330** (1908), no. 3, 377–445.

[154] D Mijatovic, JCT Eijkel, and A Van Den Berg, *Technologies for nanofluidic systems: top-down vs. bottom-up—a review*, Lab on a Chip **5** (2005), no. 5, 492–500.

[155] William C Miles, Jonathan D Goff, Philip P Huffstetler, Christian M Reinholz, Nikorn Pothayee, Beth L Caba, John S Boyd, Richey M Davis, and JS Riffle, *Synthesis and colloidal properties of polyether- magnetite complexes in water and phosphate-buffered saline*, Langmuir **25** (2008), no. 2, 803–813.

[156] K Mistry, M Armstrong, C Auth, S Cea, T Coan, T Ghani, T Hoffmann, A Murthy, J Sandford, R Shaheed, et al., *Delaying forever: Uniaxial strained*

silicon transistors in a 90nm cmos technology, VLSI Technology, 2004. Digest of Technical Papers. 2004 Symposium on, IEEE, 2004, pp. 50–51.

[157] Prashant Mohanpuria, Nisha K Rana, and Sudesh Kumar Yadav, *Biosynthesis of nanoparticles: technological concepts and future applications*, Journal of Nanoparticle Research **10** (2008), no. 3, 507–517.

[158] Allan H Morrish, *The physical principles of magnetism*, The Physical Principles of Magnetism, by Allan H. Morrish, pp. 696. ISBN 0-7803-6029-X. Wiley-VCH, January 2001. **1** (2001).

[159] Andreas Moser, Kentaro Takano, David T Margulies, Manfred Albrecht, Yoshiaki Sonobe, Yoshihiro Ikeda, Shouheng Sun, and Eric E Fullerton, *Magnetic recording: advancing into the future*, Journal of Physics D: Applied Physics **35** (2002), no. 19, R157.

[160] NF Mott, *The electrical conductivity of transition metals*, Proceedings of the Royal Society of London. Series A, Mathematical and Physical Sciences **153** (1936), no. 880, 699–717.

[161] E. B. Myers, D. C. Ralph, J. A. Katine, R. N. Louie, and R. A. Buhrman, *Current-Induced Switching of Domains in Magnetic Multilayer Devices*, Science **285** (1999), no. 5429, 867–870.

[162] T. Nagatsuma, T. Shibata, E. Sano, and A. Iwata, *Subpicosecond sampling using a noncontact electro-optic probe*, Journal of Applied Physics **66** (1989), no. 9, 4001–4009.

[163] T. NAMIOKA, *Theory of the concave grating.*, J. Opt. Soc. Am. **49** (1959), no. 5, 446–460.

[164] Takeshi Namioka and Masato Koike, *Aspheric wave-front recording optics for holographic gratings*, Appl. Opt. **34** (1995), no. 13, 2180–2186.

[165] L. Neel, Ann. Geophys. **5** (1949), 99.

[166] Tobias Neuberger, Bernhard Schöpf, Heinrich Hofmann, Margarete Hofmann, and Brigitte von Rechenberg, *Superparamagnetic nanoparticles for biomedical applications: possibilities and limitations of a new drug delivery system*, Journal of Magnetism and Magnetic Materials **293** (2005), no. 1, 483–496.

[167] Zhihong Nie, Alla Petukhova, and Eugenia Kumacheva, *Properties and emerging applications of self-assembled structures made from inorganic nanoparticles*, Nature nanotechnology **5** (2009), no. 1, 15–25.

[168] DL Olynick, B Cord, A Schipotinin, DF Ogletree, and PJ Schuck, *Electron-beam exposure mechanisms in hydrogen silsesquioxane investigated by vibrational spectroscopy and in situ electron-beam-induced desorption*, Journal of Vacuum Science & Technology B: Microelectronics and Nanometer Structures **28** (2010), 581.

[169] Christopher Palmer and Erwin Loewen, *Diffraction grating handbook*, 6 ed., Newport Corporation, 2005.

[170] Wolfgang J Parak, Teresa Pellegrino, Christine M Micheel, Daniele Gerion, Shara C Williams, and A Paul Alivisatos, *Conformation of oligonucleotides attached to gold nanocrystals probed by gel electrophoresis*, Nano Letters **3** (2003), no. 1, 33–36.

[171] Robert Pecora, *Dynamic light scattering: applications of photon correlation spectroscopy*, Springer, 1985.

[172] Frank L Pedrotti, Leno S Pedrotti, and Leno M Pedrotti, *Introduction to optics*, third ed., Prentice Hall, 2007.

[173] Marie-Paule Pileni, *Nanocrystal self-assemblies: fabrication and collective properties*, The Journal of Physical Chemistry B **105** (2001), no. 17, 3358–3371.

[174] Kenneth S Pitzer and Guillermo Mayorga, *Thermodynamics of electrolytes. ii. activity and osmotic coefficients for strong electrolytes with one or both ions univalent*, The Journal of Physical Chemistry **77** (1973), no. 19, 2300–2308.

[175] Bin Qi, Longfei Ye, Roland Stone, Cindi Dennis, Thomas M. Crawford, and O. Thompson Mefford, *Influence of ligand-precursor molar ratio on the size evolution of modifiable iron oxide nanoparticles*, The Journal of Physical Chemistry C **117** (2013), no. 10, 5429–5435.

[176] K Raj, B Moskowitz, and R Casciari, *Advances in ferrofluid technology*, Journal of Magnetism and Magnetic Materials **149** (1995), no. 1, 174–180.

[177] K Raj and R Moskowitz, *Commercial applications of ferrofluids*, Journal of Magnetism and Magnetic Materials **85** (1990), no. 1, 233–245.

[178] DC Ralph and Mark D Stiles, *Spin transfer torques*, Journal of Magnetism and Magnetic Materials **320** (2008), no. 7, 1190–1216.

[179] D.C. Ralph and M.D. Stiles, *Spin transfer torques*, Journal of Magnetism and Magnetic Materials **320** (2008), no. 7, 1190 – 1216.

[180] Rohit K Rana, Vinit S Murthy, Jie Yu, and Michael S Wong, *Nanoparticle self-assembly of hierarchically ordered microcapsule structures*, Advanced Materials **17** (2005), no. 9, 1145–1150.

[181] W. H. Rippard, M. R. Pufall, S. Kaka, S. E. Russek, and T. J. Silva, *Direct-current induced dynamics in co[sub 90]fe[sub 10]/ni[sub 80]fe[sub 20] point contacts*, Phys. Rev. Lett. **92** (2004), no. 2, 027201.

[182] K. Rivkin and J. B. Ketterson, *Switching spin valves using rf currents*, Appl. Phys. Lett. **88** (2006), no. 19, 192515.

[183] LA Rosen, JC Baygents, and DA Saville, *The interpretation of dielectric response measurements on colloidal dispersions using the dynamic stern layer model*, The Journal of chemical physics **98** (1993), 4183.

[184] Ronald E Rosenzweig, *Ferrohydrodynamics*, Courier Dover Publications, 1997.

[185] John W Rutter, *Geometry of curves*, CRC Press, 2000.

[186] Y Sahoo, M Cheon, S Wang, H Luo, EP Furlani, and PN Prasad, *Field-directed self-assembly of magnetic nanoparticles*, The Journal of Physical Chemistry B **108** (2004), no. 11, 3380–3383.

[187] Yudhisthira Sahoo, Alireza Goodarzi, Mark T Swihart, Tymish Y Ohulchanskyy, Navjot Kaur, Edward P Furlani, and Paras N Prasad, *Aqueous ferrofluid of magnetite nanoparticles: fluorescence labeling and magnetophoretic control*, The Journal of Physical Chemistry B **109** (2005), no. 9, 3879–3885.

[188] Jun John Sakurai, *San fu tuan, modern quantum mechanics*, 1985.

[189] J. C. Sankey, P. M. Braganca, A. G. F. Garcia, I. N. Krivorotov, R. A. Buhrman, and D. C. Ralph, *Spin-transfer-driven ferromagnetic resonance of individual nanomagnets*, Physical Review Letters **96** (2006), no. 22, 227601.

[190] J. C. Sankey, I. N. Krivorotov, S. I. Kiselev, P. M. Braganca, N. C. Emley, R. A. Buhrman, and D. C. Ralph, *Mechanisms limiting the coherence time of spontaneous magnetic oscillations driven by dc spin-polarized currents*, Phys. Rev. B **72** (2005), no. 22, 224427.

[191] Sankar Das Sarma, *Spintronics: A new class of device based on electron spin, rather than on charge, may yield the next generation of microelectronics*, American Scientist **89** (2001), no. 6, 516–523.

[192] C Scherer and AM Figueiredo Neto, *Ferrofluids: properties and applications*, Brazilian Journal of Physics **35** (2005), no. 3A, 718–727.

[193] Till Schmitte, Kurt Westerholt, and Hartmut Zabel, *Magneto-optical kerr effect in the diffracted light of fe gratings*, Journal of applied physics **92** (2002), no. 8, 4524–4530.

[194] M. L. Schneider, M. R. Pufall, W. H. Rippard, S. E. Russek, and J. A. Katine, *Thermal effects on the critical current of spin torque switching in spin valve nanopillars*, Appl. Phys. Lett. **90** (2007), no. 9, 092504.

[195] Gerhard A Schumacher and Theodorus GM van de Ven, *Brownian motion of charged colloidal particles surrounded by electric double layers*, Faraday Discuss. Chem. Soc. **83** (1987), 75–85.

[196] Iuliana E. Sendroiu and Robert M. Corn, *Nanoparticle diffraction gratings for DNA detection on photopatterned glass substrates*, Biointerphases **3** (2008), no. 3, FD23–FD29.

[197] ARTHUR B. Shafer, LAWRENCE R. Megill, and LEANN Droppleman, *Optimization of the czerny-turner spectrometer*, J. Opt. Soc. Am. **54** (1964), no. 7, 879–886.

[198] F Sharaf, SA Mansour, and AMY El-Lawindy, *Mechanical and relaxation properties of< i> γ</i>-irradiated pva doped with ferrous sulphate*, Polymer degradation and stability **66** (1999), no. 2, 173–177.

[199] Anthony E Siegman, *Lasers*, vol. 37, University Science Books, 1986.

[200] RH Silsbee, *Novel method for the study of spin transport in conductors*, Bull. Magn. Reson **2** (1980), 284–285.

[201] Srikanth Singamaneni, Valery N. Bliznyuk, Christian Binek, and Evgeny Y. Tsymbal, *Magnetic nanoparticles: recent advances in synthesis, self-assembly and applications*, J. Mater. Chem. **21** (2011), 16819–16845.

[202] J. C. Slonczewski, *Current-driven excitation of magnetic multilayers*, J. Magn. Magn. Mater. **159** (1996), L1–L7.

[203] J. C. Slonczewski, *Excitation of spin waves by an electric current*, J. Magn. Magn. Mater. **195** (1999), 261–268.

[204] J. C. Slonczewski, *Currents and torques in metallic magnetic multilayers*, Journal of Magnetism and Magnetic Materials **247** (2002), 324–338.

[205] Charles Ray Smith, *Bound states in a debye-hückel potential*, Physical Review **134** (1964), no. 5A, A1235.

[206] F. W. Smith, H. Q. Le, V. Diadiuk, M. A. Hollis, A. R. Calawa, S. Gupta, M. Frankel, D. R. Dykaar, G. A. Mourou, and T. Y. Hsiang, *Picosecond gaas-based photoconductive optoelectronic detectors*, Appl. Phys. Lett. **54** (1989), no. 10, 890–892.

[207] T Solmajer and Ernest L Mehler, *Electrostatic screening in molecular dynamics simulations*, Protein engineering **4** (1991), no. 8, 911–917.

[208] Jason A Stammen, Stephen Williams, David N Ku, and Robert E Guldberg, *Mechanical properties of a novel pva hydrogel in shear and unconfined compression*, Biomaterials **22** (2001), no. 8, 799–806.

[209] Mark D Stiles and Jacques Miltat, *Spin-transfer torque and dynamics*, Spin dynamics in confined magnetic structures III, Springer, 2006, pp. 225–308.

[210] MD Stiles and A Zangwill, *Anatomy of spin-transfer torque*, Physical Review B **66** (2002), no. 1, 014407.

[211] J. Z. Sun, *Current-driven magnetic switching in manganite trilayer junctions*, J. Magn. Magn. Mater. **202** (1999), 157–162.

[212] J. Z. Sun, *Spin-current interaction with a monodomain magnetic body: A model study*, Phys. Rev. B **62** (2000), no. 1, 570–578.

[213] N. X. Sun, S. X. Wang, T. J. Silva, and A. B. Kos, *High-frequency behavior and damping of Fe-Co-N-based high-saturation soft magnetic films*, IEEE Transactions on Magnetics **38** (2002), 146–150.

[214] Shouheng Sun, *Recent advances in chemical synthesis, self-assembly, and applications of fept nanoparticles*, Advanced Materials **18** (2006), no. 4, 393–403.

[215] Shouheng Sun, CB Murray, Dieter Weller, Liesl Folks, and Andreas Moser, *Monodisperse fept nanoparticles and ferromagnetic fept nanocrystal superlattices*, Science **287** (2000), no. 5460, 1989–1992.

[216] M. Takayasu, R. Gerber, and F. J. Friedlaender, *Magnetic separation of submicron particles*, IEEE Trans. Magn. **19** (1983), no. 5, 2112–2114.

[217] Gilles Tarjus and Daniel Kivelson, *Breakdown of the stokes–einstein relation in supercooled liquids*, The Journal of chemical physics **103** (1995), 3071.

[218] Markus Templin, Achim Franck, Alexander Du Chesne, Heike Leist, Yuanming Zhang, Ralph Ulrich, Volker Schädler, and Ulrich Wiesner, *Organically modified aluminosilicate mesostructures from block copolymer phases*, Science **278** (1997), no. 5344, 1795–1798.

[219] L. Thomas, M. Hayashi, X. Jiang, R. Moriya, C. Rettner, and S. Parkin, *Resonant amplification of magnetic domain-wall motion by a train of current pulses*, Science **315** (2007), 1553–.

[220] L. Thomas, M. Hayashi, X. Jiang, R. Moriya, C. Rettner, and S.S.P. Parkin, *Oscillatory dependence of current-driven magnetic domain wall motion on current pulse length*, Nature **443** (2006), 197–200.

[221] Walther Tscharnuter, *Photon correlation spectroscopy in particle sizing*, Encyclopedia of analytical chemistry (2000).

[222] Peter Tseng, Jack W Judy, and Dino Di Carlo, *Magnetic nanoparticle-mediated massively parallel mechanical modulation of single-cell behavior*, Nature methods (2012).

[223] M. Tsoi, A. G. M. Jansen, J. Bass, W.-C. Chiang, M. Seck, V. Tsoi, and P. Wyder, *Excitation of a magnetic multilayer by an electric current*, Phys. Rev. Lett. **80** (1998), no. 19, 4281–4284.

[224] A. A. Tulapurkar, T. Devolder, K. Yagami, P. Crozat, C. Chappert, A. Fukushima, and Y. Suzuki, *Subnanosecond magnetization reversal in magnetic nanopillars by spin angular momentum transfer*, Appl. Phys. Lett. **85** (2004), 5358–5360.

[225] Abraham Ulman, *Langmuir-blodgett films*, The Handbook of Surface Imiging and Visualization (1995), 277.

[226] S. Verghese, N. Zamdmer, Qing Hu, and A. Förster, *Cryogenic picosecond sampling using fiber-coupled photoconductive switches*, Applied Physics Letters **70** (1997), no. 20, 2644–2646.

[227] EJ Evert Johannes Willem Verwey, J Th G Overbeek, and J Th Jan Theodoor Gerard Overbeek, *Theory of the stability of lyophobic colloids*, DoverPublications. com, 1999.

[228] Kristina Vondermassen, Joern Bongers, Andreas Mueller, and Heiner Versmold, *Brownian motion: A tool to determine the pair potential between colloid particles*, Langmuir **10** (1994), no. 5, 1351–1353.

[229] Yukihisa Wada, Shinichiro Totoki, Masayuki Watanabe, Naoji Moriya, Yoshio Tsunazawa, and Haruo Shimaoka, *Nanoparticle size analysis with relaxation of induced grating by dielectrophoresis*, Opt. Express **14** (2006), no. 12, 5755–5764.

[230] F. L. O. Wadsworth, *The modern spectroscope.xv. on the use and mounting of the concave grating as an analyzing or direct comparison spectroscope*, Astrophys. J. **3** (1896), 47.

[231] Shan X. Wang and Alexander M. Taratorin, *Magnetic information storage technology*, first ed., Academic Press, 1999.

[232] W. Wernsdorfer, E. Bonet Orozco, K. Hasselbach, A. Benoit, B. Barbara, N. Demoncy, A. Loiseau, H. Pascard, and D. Mailly, *Experimental evidence of the néel-brown model of magnetization reversal*, Phys. Rev. Lett. **78** (1997), 1791–1794.

[233] George M Whitesides and Bartosz Grzybowski, *Self-assembly at all scales*, Science **295** (2002), no. 5564, 2418–2421.

[234] Erich P Wohlfarth, *Handbook of magnetic materials: A handbook on the properties of magnetically ordered substances*, vol. 2, Access Online via Elsevier, 1980.

172

[235] SA Wolf, DD Awschalom, RA Buhrman, JM Daughton, S Von Molnar, ML Roukes, A Yu Chtchelkanova, and DM Treger, *Spintronics: A spin-based electronics vision for the future*, Science **294** (2001), no. 5546, 1488–1495.

[236] Renliang Xu, *Shear plane and hydrodynamic diameter of microspheres in suspension*, Langmuir **14** (1998), no. 10, 2593–2597.

[237] Yu-Lin Xu, *Scattering of electromagnetic waves by periodic particle arrays*, J. Opt. Soc. Am. A **30** (2013), no. 6, 1053–1068.

[238] Yu-lin Xu and BAS Gustafson, *A generalized multiparticle mie-solution: further experimental verification*, Journal of Quantitative Spectroscopy and Radiative Transfer **70** (2001), no. 4, 395–419.

[239] Hao Yan, Sung Ha Park, Gleb Finkelstein, John H Reif, and Thomas H LaBean, *Dna-templated self-assembly of protein arrays and highly conductive nanowires*, Science **301** (2003), no. 5641, 1882–1884.

[240] Chang-Chung Yang and Wen-Chang Chen, *The structures and properties of hydrogen silsesquioxane (hsq) films produced by thermal curing*, Journal of Materials Chemistry **12** (2002), no. 4, 1138–1141.

[241] Tao Yang, Takashi Kimura, and Yoshichika Otani, *Giant spin-accumulation signal and pure spin-current-induced reversible magnetization switching*, Nature Physics **4** (2008), no. 11, 851–854.

[242] L. Ye, B. Qi, T. Pearson, Y. Cordeau, O. T. Mefford, C. Rinaldi, and T. M. Crawford, *Real time monitoring of superparamagnetic nanoparticle self-assembly on surfaces of magnetic recording media*, Submitted to Journal of Applied Physics (2014).

[243] L. Ye, B. Terry, O. T. Mefford, C. Rinaldi, and T. M. Crawford, *All-nanoparticle concave diffraction grating fabricated by self-assembly onto magnetically-recorded templates*, Opt. Express **21** (2013), no. 1, 1066–1075.

[244] C.X. Yu and D.T. Neilson, *Diffraction-grating-based (de)multiplexer using image plane transformations*, Selected Topics in Quantum Electronics, IEEE Journal of **8** (2002), no. 6, 1194 – 1201.

[245] Vitalii Zablotskii, Alexandr Dejneka, Šárka Kubinová, Damien Le-Roy, Frédéric Dumas-Bouchiat, Dominique Givord, Nora M Dempsey, and Eva Syková, *Life*

on magnets: Stem cell networking on micro-magnet arrays, PloS one **8** (2013), no. 8, e70416.

[246] Zhenli Zhang, Mark A Horsch, Monica H Lamm, and Sharon C Glotzer, *Tethered nano building blocks: Toward a conceptual framework for nanoparticle self-assembly*, Nano Letters **3** (2003), no. 10, 1341–1346.

[247] CF Zukoski and DA Saville, *The interpretation of electrokinetic measurements using a dynamic model of the stern layer: I. the dynamic model*, Journal of colloid and interface science **114** (1986), no. 1, 32–44.

[248] Igor Žutić, Jaroslav Fabian, and S Das Sarma, *Spintronics: Fundamentals and applications*, Reviews of modern physics **76** (2004), no. 2, 323.

Appendix A

Mathematica Code for Calculating Nanoparticle Trajectories and Diffracted Intensities

path = "draft_manuscript/";

Mr $= 450 10^3$; (*A/m*)

$a = 10$; (* Transition parameter in nm*)

$\delta = 30$; (*media thickness in nm*)

(*x : downtrack, $z$perpendicular, $z = 0$meansthecenterofdiskthickness*)

Hx[x_, z_] $= \frac{-Mr}{\pi}(\text{ArcTan}[x, a + z + \delta/2] - \text{ArcTan}[x, a + z - \delta/2])$;

Hz[x_, z_] $= \frac{Mr}{2\pi}\text{Log}\left[\frac{(a+z-\delta/2)^2+x^2}{(a+z+\delta/2)^2+x^2}\right]$;

HGxx[x_, z_] $= D[\text{Hx}[x, z], x]$;

HGxz[x_, z_] $= D[\text{Hx}[x, z], z]$;

HGzx[x_, z_] $= D[\text{Hz}[x, z], x]$;

HGzz[x_, z_] $= D[\text{Hz}[x, z], z]$;

ff[Ha_, Msp_]:=If[Ha $<$ Msp/3, 3, Msp/Ha];

Vp[Rp_]:=Rp$^3 \times 4 \times$ Pi/3; (*Rp in nm*)

Fmx[x_, z_, Rp_, Msp_]:=μ0Vp[Rp]ff [Sqrt [Hx[x, z]^2 + Hz[x, z]^2] , Msp]

$(Hx[x, z]HGxx[x, z] + Hz[x, z]HGxz[x, z]); (\text{*Furlani\_JAP\_2006eqn15};$

$Forceunitsarecancelledwithmassm\text{*})$

$Fmz[x\_, z\_, Rp\_, Msp\_] := \mu 0 Vp[Rp] ff \left[Sqrt\left[Hx[x, z]^2 + Hz[x, z]^2\right], Msp\right]$

$(Hx[x, z]HGzx[x, z] + Hz[x, z]HGzz[x, z]); (\text{*Furlani\_JAP\_2006eqn15};$

$Forceunitsarecancelledwithmassm\text{*})$

MAGNETIC FORCES AND DRAG FORCE

$k = 1.38 \ 10^{-23};$

$\epsilon = 1000;$

$T = 300;$

$\mu 0 = 4 \times Pi \times 10^{-7};$

$Msp = 0.56/\mu 0; (\text{*in} A/m \text{*})$

$R1 = 5; (\text{*nm*})$

$R2 = 50; (\text{*nm*})$

$R = (R1 + R2)/2;$

$Fmx[0.01, R1, R1, Msp] \times 10^{-18} \times 10^{12}$

$Fmz[0.01, R1, R1, Msp] \times 10^{-18} \times 10^{12}$

$datax = \{\};$

$x0 = -375;$

$xstep = 5;$

$Rstep = 50;$

$For[R1 = 5, R1 \leq 260, R1 = R1 + Rstep,$

$Fx = Table\left[\{x, Fmx[x, R1 + \delta/2, R1, Msp]10^{-6}\}, \{x, x0, -x0, xstep\}\right];$

$datax = Append[datax, Fx];$

$]$

$forcex = ListPlot[datax, Frame \rightarrow True, Joined \rightarrow True,$

PlotStyle → {{Red, AbsoluteThickness[3]}, {Green, AbsoluteThickness[3]},

{Blue, AbsoluteThickness[3]}, {Pink, AbsoluteThickness[3]},

{Yellow, AbsoluteThickness[3]}, {Black, AbsoluteThickness[3]}},

FrameLabel → {{"Fx(pN)", None}, {"x(nm)", None}}, LabelStyle → Directive[24],

PlotLegends →

SwatchLegend[{"Z:5nm", "Z:55nm", "Z:105nm", "Z:155nm", "Z:205nm", "Z:255nm"},

LegendMarkerSize → 30], PlotRange → {All, All}, ImageSize → 600]

dataz = {};

x0 = −375;

xstep = 5;

Rstep = 50;

For[R1 = 5, R1 ≤ 260, R1 = R1 + Rstep,

Fz = Table $\left[\left\{x, \text{Fmz}[x, R1 + \delta/2, R1, \text{Msp}]10^{-6}\right\}, \{x, x0, -x0, \text{xstep}\}\right]$;

dataz = Append[dataz, Fz];

]

forcez = ListPlot[dataz, Frame → True, Joined → True,

PlotStyle → {{Red, AbsoluteThickness[3]}, {Green, AbsoluteThickness[3]},

{Blue, AbsoluteThickness[3]}, {Pink, AbsoluteThickness[3]},

{Yellow, AbsoluteThickness[3]}, {Black, AbsoluteThickness[3]}},

FrameLabel → {{"Fz(pN)", None}, {"x(nm)", None}}, LabelStyle → Directive[24],

PlotLegends →

SwatchLegend[{"Z:5nm", "Z:55nm", "Z:105nm", "Z:155nm", "Z:205nm", "Z:255nm"},

LegendMarkerSize → 30], PlotRange → {All, All}, ImageSize → 600]

General

time $= 600$; (*Coating time*)

$\mu 0 = 4 \times \mathrm{Pi} \times 10^{-7}$;

$\mathrm{Msp} = 0.56/\mu 0$; (*particle $\mathrm{Saturation} M; \mathrm{in} A/m$*)

$\mathrm{R1} = 5$; (*particle radium; in nm*)

$\rho = 5.175$; (*particle density; $g/cm3$*)

$\mathrm{vp} = 4\mathrm{Pi}/3 * \mathrm{R1}^3 10^{-27}$; (* particle volume of NP in m3*)

$m = \rho 10^3 \mathrm{vp} 10^{18}$; (*particle mass, multiply 10^{18} to compensate the force units;

in kg*)

$\eta = 0.001$; (*fluid viscosity; Ns/m2*)

$\mathrm{vol} = 40 * 0.02\ 10^{-6} 10^{-3}$;

(*total volume of partilces from 40uLEMG707 stock solutions; in m3*)

$n = \mathrm{vol}\big/\left(4\mathrm{Pi}/3\mathrm{R1}^3 10^{-27}\right)$; (*NP # in 40uL EMG 707 stock solutions*)

$\mathrm{conc} = n/40$; (*not used in the trajectory simulations; in 1/mL*)

$d = \sqrt[3]{40\ 10^{21}/n}$; (*size of cube side/NP,

assume NP occupies the space of a cube in diluted fluid; in nm*)

$\mathrm{x0} = -375$; (*half of the transition cell in x direction; in nm*)

$\mathrm{h0} = 0.5$; (*height of fluid cell; in mm*)

(*Look for farest NP that can reach disk drive surface within coating time;

in nm*)

$\mathrm{t0} = \mathrm{time2}$;

zi $= 0.1\ 10^6 + \delta/2$; (*know particle at zi will not reach the disk surface*)

xi $= 0$;

step $= d$;

spacing $= 750$; (*gratingspacing; innm*)

(*find max zi that could reach disk drive*)

end $= d$;

While[!NumericQ[end],

Clear[sol];

sol $=$

First[NDSolve[{$x"[t] ==$ Fmx[$x[t], z[t], $R1, Msp]/$m$ - 6Pi\eta$R1$x'[t]/m$,

$z"[t] ==$ Fmz[$x[t], z[t], $R1, Msp]/$m$ - 6Pi\eta$R1$z'[t]/m, x[0] ==$ xi,

$z[0] ==$ zi$, x'[0] == 0, z'[0] == 0$}, {x, z}, {$t, 0, $t0},

Method $\rightarrow$ {"EventLocator", "Event" $\rightarrow z[t] - \delta/2$,

"EventAction" $:\rightarrow$ Throw[end $= t$, "StopIntegration"], "Direction" $\rightarrow -1$,

"EventLocationMethod" $\rightarrow$ "LinearInterpolation"}]];

zi $=$ zi $-$ step;

]; (*NumericallysolveforNewton's2ndlaw*)

zi $=$ zi $+ d$;

Concentration1 $= 40$ uL/40 mL

(*AssigninitalNPpositionsin2_D($i.e., x - z$plane)assuminginitial

uniformdistributionrandomly; $x = $ equalgrid, first$z$random, other$z = $equalgrid*)

xi $= 50000$; (*xi/spacing $= $numberofgratinglines*)

xx $=$ Table[0, {i, Floor[xi/d] $+ 1$}, {j, Floor[zi/d] $+ 1$}];

zz $=$ Table[0, {i, Floor[xi/d] $+ 1$}, {j, Floor[zi/d] $+ 1$}];

(*arrays for NP intitial postions*)

zz1 = {}; (*for debug usage*)

For[$i = 1, i \leq$ Floor[xi/d] + 1, i++,

For[$j = 1, j \leq$ Floor[zi/d] + 1, j++,

If[$i == 1$, xx[[i, j]] = dRandomReal[], temp = Mod[($i - 1$)d + xx[[1, j]], spacing];

xx[[i, j]] = If[temp $\leq$ spacing/2, temp, temp $-$ spacing];];

If[$j == 1$, zz[[i, j]] = dRandomReal[] + δ/2; zz1 = Append[zz1, zz[[i, j]]],

zz[[i, j]] = zz[[$i, 1$]] + d($j - 1$)];

];

]; (*Allparticlepositionsaretreatedin$a$singletransition,

sincealltransitionsaretranslatedbygratingspacing;

Initialpositionsaresimplified.Morecomplexmethodwillbeusedtobetter

simulateinititalpositions*)

(*calculate the trajectory for each NP*)

tkey = {}; (*time for NP to reach the disk surface*)

tindex = {}; (*only for debug usage*)

xkey1 = {}; (*x position for NP to reach the surface*)

CTkey = Timing[For[$i = 1, i \leq$ Floor[xi/d] + 1, i++,

For[$j = 1, j \leq$ Floor[zi/d] + 1, j++,

sol = First[NDSolve[{x"[t] == Fmx[x[t], z[t], R1, Msp]/m $-$ 6PiηR1x'[t]/m,

z"[t] == Fmz[x[t], z[t], R1, Msp]/m $-$ 6PiηR1z'[t]/m, x[0] == xx[[i, j]],

z[0] == zz[[i, j]], x'[0] == 0, z'[0] == 0}, {x, z}, {$t, 0, $t0},

Method $\rightarrow$ {"EventLocator", "Event" $\rightarrow$ z[t] $-$ δ/2,

"EventAction" :$\rightarrow$ Throw[endt = t, "StopIntegration"], "Direction" $\rightarrow$ -1,

"EventLocationMethod" $\rightarrow$ "LinearInterpolation"}]];

tkey = Append[tkey, endt];

xkey1 = Append[xkey1, Evaluate[x[endt]/.sol]];

```
tindex = Append[tindex, {xx[[i, j]], zz[[i, j]], endt}]
];
];
];


(*calculate NPs within time t*)
bins = BinCounts[tkey, 0.1];
NP = {};
For[i = 1, i ≤ 9, i++,
tempdata = Take[bins, {1, i}];
NP = Append[NP, {i0.1, Total[tempdata]}];
];
bins = BinCounts[tkey, 1];
For[i = 1, i ≤ Length[bins], i++,
tempdata = Take[bins, {1, i}];
NP = Append[NP, {i, Total[tempdata]}];
];


(*Calculate Intensity within time t *)
xds1 = Table[{}, {i, 1, time, 1}];
nps1 = Table[0, {i, 1, time, 1}];
For[j = 1, j ≤ time, j = j + 1,
For[i = 1, i ≤ Length[tkey], i = i + 1,
If[tkey[[i]] < j, nps1[[j]] = nps1[[j]] + 1;
xds1[[j]] = Append[xds1[[j]], xkey1[[i]]]];
];
];
```

```
intesity1 = Table[{i, 0}, {i, 1, time, 1}];

For[j = 1, j ≤ time, j = j + 1,

tempI = 0;

For[i = 1, i ≤ Length[xds1[[j]]], i++,

tempI = tempI + E^(I2Pi(spacing + xds1[[j, i]])/spacing);

];

intesity1[[j, 2]] = Abs[tempI]^2;

];


xds10 = Table[{}, {i, 0.1, 0.9, 0.1}]; (*CalculateIntensityfor t < 1*)

intesity10 = Table[{i, 0}, {i, 0.1, 0.9, 0.1}];

For[j = 1, j ≤ Length[intesity10], j = j + 1,

For[i = 1, i ≤ Length[tkey], i = i + 1,

If[tkey[[i]] < intesity10[[j, 1]], xds10[[j]] = Append[xds10[[j]], xkey1[[i]]]];

];

];

For[j = 1, j ≤ Length[intesity10], j = j + 1,

tempI = 0;

For[i = 1, i ≤ Length[xds10[[j]]], i++,

tempI = tempI + E^(I2Pi(spacing + xds10[[j, i]])/spacing);

];

intesity10[[j, 2]] = Abs[tempI]^2;

]

intesity100 = Join[intesity10, intesity1];
```

Concentration1/2

d2 $= d\sqrt[3]{2}$;

(*AssignNPgridsassuminginitialuniformdistributionrandomly; $x =$ equalgrid,

first$z$random, other$z =$ equalgrid*)

xi $= 50000$;

(*zi $= 6113.34;$ *)

xx2 $=$ Table[0, $\{i,$ Floor[xi/d2] $+ 1\}, \{j,$ Floor[zi/d2] $+ 1\}$];

zz2 $=$ Table[0, $\{i,$ Floor[xi/d2] $+ 1\}, \{j,$ Floor[zi/d2] $+ 1\}$];

zz3 $= \{\}$;

For[$i = 1, i \leq$ Floor[xi/d2] $+ 1, i{+}{+}$,

For[$j = 1, j \leq$ Floor[zi/d2] $+ 1, j{+}{+}$,

If[$i == 1$, xx2[[i, j]] $=$ d2RandomReal[], temp $=$ Mod[($i - 1$)d2 $+$ xx2[[1, j]], spacing];

xx2[[i, j]] $=$ If[temp $\leq$ spacing/2, temp, temp $-$ spacing];];

If[$j == 1$, zz2[[i, j]] $=$ d2 RandomReal[] $+ \delta/2$; zz3 $=$ Append[zz3, zz2[[i, j]]],

zz2[[i, j]] $=$ zz2[[$i, 1$]] $+$ d2($j - 1$)];

];

];

(*calculatethetrajectoryforeachNPforconc1/2*)

tkey2 $= \{\}$;

tindex2 $= \{\}$;

xkey2 $= \{\}$;

CTkey2 $=$ Timing[For[$i = 1, i \leq$ Floor[xi/d2] $+ 1, i{+}{+}$,

For[$j = 1, j \leq$ Floor[zi/d2] $+ 1, j{+}{+}$,

sol $=$ First[NDSolve[$\{x''[t] ==$ Fmx[$x[t], z[t],$ R1, Msp]$/m - 6$PiηR1$x'[t]/m$,

$z"[t] == \mathrm{Fmz}[x[t], z[t], \mathrm{R1}, \mathrm{Msp}]/m - 6\mathrm{Pi}\eta \mathrm{R1}z'[t]/m,$

$x[0] == \mathrm{xx2}[[i, j]], z[0] == \mathrm{zz2}[[i, j]], x'[0] == 0, z'[0] == 0\},$

$\{x, z\}, \{t, 0, \mathrm{t0}\}, \mathrm{Method} \to \{\text{``EventLocator''}, \text{``Event''} \to z[t] - \delta/2,$

$\text{``EventAction''} :\to \mathrm{Throw}[\mathrm{endt} = t, \text{``StopIntegration''}], \text{``Direction''} \to -1,$

$\text{``EventLocationMethod''} \to \text{``LinearInterpolation''}\}]];$

tkey2 = Append[tkey2, endt];

xkey2 = Append[xkey2, Evaluate[x[endt]/.sol]];

tindex2 = Append[tindex2, $\{\mathrm{xx2}[[i, j]], \mathrm{zz2}[[i, j]], \mathrm{endt}\}$]

];

];

];

bins2 = BinCounts[tkey2, 0.1];

NP2 = {};

For[$i = 1, i \leq 9, i$++,

tempdata = Take[bins2, $\{1, i\}$];

NP2 = Append[NP2, $\{i0.1, \mathrm{Total}[\mathrm{tempdata}]\}$];

];

bins2 = BinCounts[tkey2, 1];

For[$i = 1, i \leq$ Length[bins2], i++,

tempdata = Take[bins2, $\{1, i\}$];

NP2 = Append[NP2, $\{i, \mathrm{Total}[\mathrm{tempdata}]\}$];

];

xds2 = Table[{}, $\{i, 1, \mathrm{time}, 1\}$];

nps2 = Table[0, $\{i, 1, \mathrm{time}, 1\}$];

For[$j = 1, j \leq \mathrm{time}, j = j + 1,$

```
For[i = 1, i ≤ Length[tkey2], i = i + 1,

If[tkey2[[i]] < j, nps2[[j]] = nps2[[j]] + 1;

xds2[[j]] = Append[xds2[[j]], xkey2[[i]]]];

];

];

intesity2 = Table[{i, 0}, {i, 1, time, 1}];

For[j = 1, j ≤ time, j = j + 1,

tempI = 0;

For[i = 1, i ≤ Length[xds2[[j]]], i++,

tempI = tempI + E^(I2Pi(spacing + xds2[[j, i]])/spacing);

];

intesity2[[j, 2]] = Abs[tempI]^2;

];


xds20 = Table[{}, {i, 0.1, 0.9, 0.1}];

intesity20 = Table[{i, 0}, {i, 0.1, 0.9, 0.1}];

For[j = 1, j ≤ Length[intesity20], j = j + 1,

For[i = 1, i ≤ Length[tkey2], i = i + 1,

If[tkey2[[i]] < intesity20[[j, 1]], xds20[[j]] = Append[xds20[[j]], xkey2[[i]]]];

];

];

For[j = 1, j ≤ Length[intesity20], j = j + 1,

tempI = 0;

For[i = 1, i ≤ Length[xds20[[j]]], i++,

tempI = tempI + E^(I2Pi(spacing + xds20[[j, i]])/spacing);

];

intesity20[[j, 2]] = Abs[tempI]^2; ;
```

]

intesity200 = Join[intesity20, intesity2];

Concentration1/4

d3 = $d \big/ \sqrt[3]{1/4}$;

xi = 50000;

(*zi = 6113.34; *)

xx3 = Table[0, {i, Floor[xi/d3] + 1}, {j, Floor[zi/d3] + 1}];

zz33 = Table[0, {i, Floor[xi/d3] + 1}, {j, Floor[zi/d3] + 1}];

zz34 = {};

For[$i = 1, i \leq$ Floor[xi/d3] + 1, i++,

For[$j = 1, j \leq$ Floor[zi/d3] + 1, j++,

If[$i == 1$, xx3[[i, j]] = d3RandomReal[], temp = Mod[$(i - 1)$d3 + xx3[[$1, j$]], spacing];

xx3[[i, j]] = If[temp $\leq$ spacing/2, temp, temp $-$ spacing];];

If[$j == 1$, zz33[[i, j]] = d3 RandomReal[] + δ/2; zz34 = Append[zz34, zz33[[i, j]]],

zz33[[i, j]] = zz33[[$i, 1$]] + d3$(j - 1)$];

];

];

(*calculatethetrajectoryforeachNPforconc1/4*)

tkey3 = {};

tindex3 = {};

xkey3 = {};

CTkey3 = Timing[For[$i = 1, i \leq$ Floor[xi/d3] + 1, i++,

For[$j = 1, j \leq$ Floor[zi/d3] + 1, j++,

```
sol = First[NDSolve[{x''[t] == Fmx[x[t], z[t], R1, Msp]/m − 6PiηR1x'[t]/m,

z''[t] == Fmz[x[t], z[t], R1, Msp]/m − 6PiηR1z'[t]/m,

x[0] == xx3[[i, j]], z[0] == zz33[[i, j]], x'[0] == 0, z'[0] == 0},

{x, z}, {t, 0, t0}, Method → {"EventLocator", "Event" → z[t] − δ/2,

"EventAction" :→ Throw[endt = t, "StopIntegration"], "Direction" → −1,

"EventLocationMethod" → "LinearInterpolation"}]];

tkey3 = Append[tkey3, endt];

xkey3 = Append[xkey3, Evaluate[x[endt]/.sol]];

tindex3 = Append[tindex3, {xx3[[i, j]], zz33[[i, j]], endt}]

];

];

];


bins3 = BinCounts[tkey3, 0.1];

NP3 = {};

For[i = 1, i ≤ 9, i++,

tempdata = Take[bins3, {1, i}];

NP3 = Append[NP3, {i0.1, Total[tempdata]}];

];

bins3 = BinCounts[tkey3, 1];

For[i = 1, i ≤ Length[bins3], i++,

tempdata = Take[bins3, {1, i}];

NP3 = Append[NP3, {i, Total[tempdata]}];

];


xds3 = Table[{}, {i, 1, time, 1}];

nps3 = Table[0, {i, 1, time, 1}];
```

```
For[j = 1, j ≤ time, j = j + 1,
For[i = 1, i ≤ Length[tkey3], i = i + 1,
If[tkey3[[i]] < j, nps3[[j]] = nps3[[j]] + 1;
xds3[[j]] = Append[xds3[[j]], xkey3[[i]]]];
];
];
intesity3 = Table[{i, 0}, {i, 1, time, 1}];
For[j = 1, j ≤ time, j = j + 1,
tempI = 0;
For[i = 1, i ≤ Length[xds3[[j]]], i++,
tempI = tempI + E^(I2Pi(spacing + xds3[[j, i]])/spacing);
];
intesity3[[j, 2]] = Abs[tempI]^2;
];


xds30 = Table[{}, {i, 0.1, 0.9, 0.1}];
intesity30 = Table[{i, 0}, {i, 0.1, 0.9, 0.1}];
For[j = 1, j ≤ Length[intesity30], j = j + 1,
For[i = 1, i ≤ Length[tkey3], i = i + 1,
If[tkey3[[i]] < intesity30[[j, 1]], xds30[[j]] = Append[xds30[[j]], xkey3[[i]]]];
];
];
For[j = 1, j ≤ Length[intesity30], j = j + 1,
tempI = 0;
For[i = 1, i ≤ Length[xds30[[j]]], i++,
tempI = tempI + E^(I2Pi(spacing + xds30[[j, i]])/spacing);
];
```

intesity30[[j, 2]] = Abs[tempI]^2;

]

intesity300 = Join[intesity30, intesity3];

Concentration1/8

d4 = $d \big/ \sqrt[3]{1/8}$;

xi = 50000;

(*zi = 6113.34; *)

xx4 = Table[0, {i, Floor[xi/d4] + 1}, {j, Floor[zi/d4] + 1}];

zz43 = Table[0, {i, Floor[xi/d4] + 1}, {j, Floor[zi/d4] + 1}];

zz44 = {};

For[i = 1, $i \leq$ Floor[xi/d4] + 1, i++,

For[j = 1, $j \leq$ Floor[zi/d4] + 1, j++,

If[i == 1, xx4[[i, j]] = d4RandomReal[], temp = Mod[(i − 1)d4 + xx4[[1, j]], spacing];

xx4[[i, j]] = If[temp $\leq$ spacing/2, temp, temp − spacing];];

If[j == 1, zz43[[i, j]] = d4 RandomReal[] + δ/2; zz44 = Append[zz44, zz43[[i, j]]],

zz43[[i, j]] = zz43[[i, 1]] + d4(j − 1)];

];

];

(*calculatethetrajectoryforeachNPforconc1/8*)

tkey4 = {};

tindex4 = {};

xkey4 = {};

CTkey4 = Timing[For[i = 1, $i \leq$ Floor[xi/d4] + 1, i++,

189

For[$j = 1, j \leq$ Floor[zi/d4] $+ 1, j$++,

sol $=$ First[NDSolve[{$x''[t] ==$ Fmx[$x[t], z[t]$, R1, Msp]/$m - 6$PiηR1$x'[t]/m$,

$z''[t] ==$ Fmz[$x[t], z[t]$, R1, Msp]/$m - 6$PiηR1$z'[t]/m$,

$x[0] ==$ xx4[[i, j]], $z[0] ==$ zz43[[i, j]], $x'[0] == 0, z'[0] == 0$},

{x, z}, {$t, 0,$ t0}, Method $\rightarrow$ {"EventLocator", "Event" $\rightarrow z[t] - \delta/2$,

"EventAction" $:\rightarrow$ Throw[endt $= t$, "StopIntegration"], "Direction" $\rightarrow -1$,

"EventLocationMethod" $\rightarrow$ "LinearInterpolation"}]];

tkey4 $=$ Append[tkey4, endt];

xkey4 $=$ Append[xkey4, Evaluate[x[endt]/.sol]];

tindex4 $=$ Append[tindex4, {xx4[[i, j]], zz43[[i, j]], endt}]

];

];

];

bins4 $=$ BinCounts[tkey4, 0.1];

NP4 $=$ {};

For[$i = 1, i \leq 9, i$++,

tempdata $=$ Take[bins4, {1, i}];

NP4 $=$ Append[NP4, {i0.1, Total[tempdata]}];

];

bins4 $=$ BinCounts[tkey4, 1];

For[$i = 1, i \leq$ Length[bins4], i++,

tempdata $=$ Take[bins4, {1, i}];

NP4 $=$ Append[NP4, {i, Total[tempdata]}];

];

xds4 $=$ Table[{}, {$i, 1,$ time, 1}];

```
nps4 = Table[0, {i, 1, time, 1}];

For[j = 1, j ≤ time, j = j + 1,

For[i = 1, i ≤ Length[tkey4], i = i + 1,

If[tkey4[[i]] < j, nps4[[j]] = nps4[[j]] + 1;

xds4[[j]] = Append[xds4[[j]], xkey4[[i]]]];

];

];




intesity4 = Table[{i, 0}, {i, 1, time, 1}];




For[j = 1, j ≤ time, j = j + 1,

tempI = 0;

For[i = 1, i ≤ Length[xds4[[j]]], i++,

tempI = tempI + E^(I 2 Pi(spacing + xds4[[j, i]])/spacing);

];

intesity4[[j, 2]] = Abs[tempI]^2; ;

];




xds40 = Table[{}, {i, 0.1, 0.9, 0.1}];

intesity40 = Table[{i, 0}, {i, 0.1, 0.9, 0.1}];

For[j = 1, j ≤ Length[intesity40], j = j + 1,

For[i = 1, i ≤ Length[tkey4], i = i + 1,

If[tkey4[[i]] < intesity40[[j, 1]], xds40[[j]] = Append[xds40[[j]], xkey4[[i]]]];

];

];

For[j = 1, j ≤ Length[intesity40], j = j + 1,
```

```
tempI = 0;

For[i = 1, i ≤ Length[xds40[[j]]], i++,

tempI = tempI + E^(I2Pi(spacing + xds40[[j, i]])/spacing);

];

intesity40[[j, 2]] = Abs[tempI]^2;

]

intesity400 = Join[intesity40, intesity4];
```

Appendix B

Derivation of Spin Function for an arbitrarily

orientated spin

A spin $\mathbf{S}$ is oriented along (θ, ϕ) in the polar coordinates as shown in figure B.1. $\big|(\theta, \phi)\big\rangle$ is the spin function. The problem becomes to solve for the eigenvalues $(\lambda\hbar/2)$ and eigenstates of the operator $\mathbf{S} \cdot \hat{\mathbf{n}}$, i.e,

$$\mathbf{S} \cdot \hat{\mathbf{n}}\big|(\theta, \phi)\big\rangle = \lambda\frac{\hbar}{2}\big|(\theta, \phi)\big\rangle, \tag{B.1}$$

where $\hat{\mathbf{n}}$ is the unit vector along $\mathbf{S}$. Using the Pauli matrices, one obtains

$$\mathbf{S} \cdot \hat{\mathbf{n}} = \frac{\hbar}{2}\sigma_n = \frac{\hbar}{2}(\sigma_x n_x + \sigma_y n_y + \sigma_z n_z), \tag{B.2}$$

where $n_x = \sin\theta\cos\phi$, $n_y = \sin\theta\sin\phi$, $n_z = \cos\theta$, and

$$\sigma_x = \begin{pmatrix} 0 & 1 \\ 1 & 0 \end{pmatrix}, \qquad \sigma_y = \begin{pmatrix} 0 & -i \\ i & 0 \end{pmatrix}, \qquad \sigma_z = \begin{pmatrix} 1 & 0 \\ 0 & -1 \end{pmatrix}. \tag{B.3}$$

Therefore,

$$\mathbf{S} \cdot \hat{\mathbf{n}} = \frac{\hbar}{2}\begin{pmatrix} n_z & n_x - in_y \\ n_x + in_y & -n_z \end{pmatrix} = \frac{\hbar}{2}\begin{pmatrix} \cos\theta & \sin\theta\mathrm{e}^{-i\phi} \\ \sin\theta\mathrm{e}^{i\phi} & -\cos\theta \end{pmatrix}. \tag{B.4}$$

Write the spin function as

$$\big|(\theta, \phi)\big\rangle = \begin{pmatrix} C1 \\ C2 \end{pmatrix}, \tag{B.5}$$

where $C1$ and $C2$ are both complex numbers. Equation (B.1) becomes
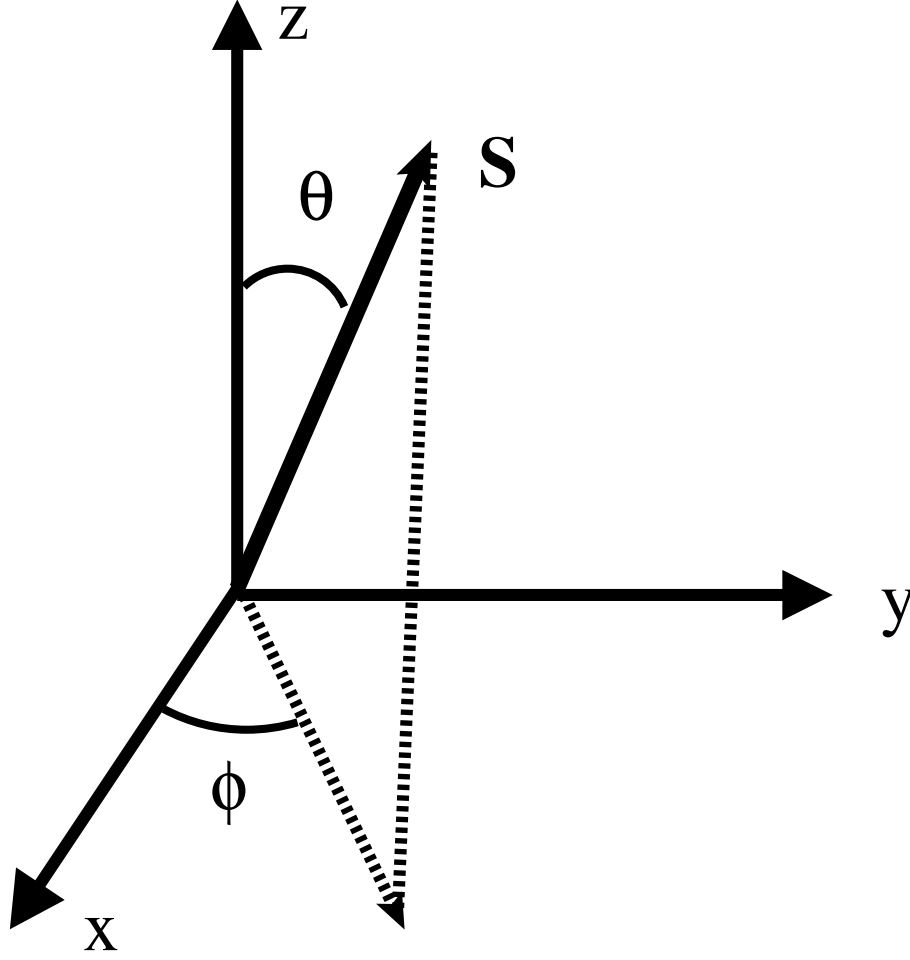
Figure B.1   Schematic illustration of coordinates.

$$\sigma_n \begin{pmatrix} C1 \\ C2 \end{pmatrix} = \begin{pmatrix} \cos\theta & \sin\theta e^{-i\phi} \\ \sin\theta e^{i\phi} & -\cos\theta \end{pmatrix} \begin{pmatrix} C1 \\ C2 \end{pmatrix} = \lambda \begin{pmatrix} C1 \\ C2 \end{pmatrix}, \qquad (B.6)$$

i.e.,

$$(\sigma_n - \lambda) \begin{pmatrix} C1 \\ C2 \end{pmatrix} = \begin{pmatrix} \cos\theta - \lambda & \sin\theta e^{-i\phi} \\ \sin\theta e^{i\phi} & -(\cos\theta + \lambda) \end{pmatrix} \begin{pmatrix} C1 \\ C2 \end{pmatrix} = 0. \qquad (B.7)$$

One obtains

$$\begin{cases} (\cos\theta - \lambda)C1 + \sin\theta e^{-i\phi}C2 = 0, \\ \sin\theta e^{i\phi}C1 - (\cos\theta + \lambda)C2 = 0. \end{cases} \qquad (B.8)$$

For $C1$ and $C2$ are not both 0, equation (B.8) leads to

$$det(\sigma_n - \lambda) = \begin{vmatrix} \cos\theta - \lambda & \sin\theta e^{-i\phi} \\ \sin\theta e^{i\phi} & -(\cos\theta + \lambda) \end{vmatrix} = 0, \qquad (\text{B.9})$$

which yields $\lambda = \pm 1$. Insert λ into equation (B.8) and obtain

$$\left|(\theta, \phi)\right\rangle = \begin{pmatrix} \cos\frac{\theta}{2} \\ \sin\frac{\theta}{2}e^{i\phi} \end{pmatrix}, \qquad (\text{B.10})$$

for $\lambda = 1$, and

$$\left|(\theta, \phi)\right\rangle = \begin{pmatrix} \sin\frac{\theta}{2} \\ -\cos\frac{\theta}{2}e^{i\phi} \end{pmatrix}, \qquad (\text{B.11})$$

for $\lambda = -1$.

Appendix C

Hydrogen silsesquioxane (HSQ)

HSQ is a flowable, inorganic polymer that was first developed by Dow Corning for use as a spin-on insulator, and designed to replace current deposition processes for interlayer dielectrics in the semiconductor industry. Its low level of contamination, low dielectric constant, excellent gap fill, and very low defect density make it widely used in the semiconductor industry, nanolithography and nanoscience application. HSQ has been used as a high-resolution negative tone electron-beam resist ($<$ 10 nm) [168].
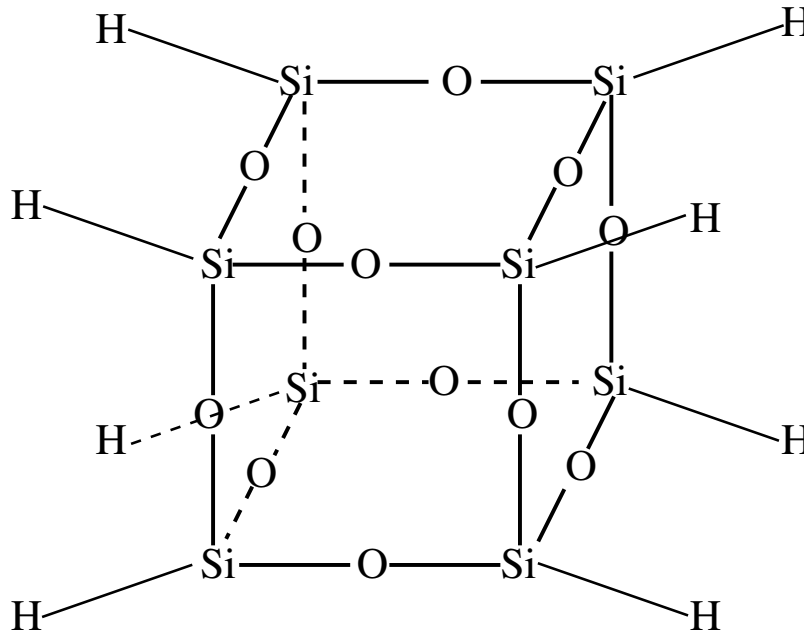

Figure C.1   Chemical structure of HSQ [240] [93].

Understanding the HSQ chemical structure is critical to understand how it behaves as a negative e-beam resist. HSQ molecules have a cage-like structure containing eight

Si atoms, twelve O atoms, and eight H atoms (figure C.1). It has been suggested that HSQ's sensitivity to an electron beam comes from the Si-H bond, which is much weaker than the Si-O bond, and is severed during e-beam exposures. Once cut, it is believed that the free bond on the Si, also called a radical site, reacts with local moisture. Radical sites on neighboring cages become bridged with oxygen that originates from the water absorbed, forming an Si-OH bond. This Si-OH bond is unstable and decomposes into a stable Si-O-Si bond. This final step crosslinks the cages forming a mechanically strong SiO_2 film.